ELECTRONIC AND OPTICAL PROPERTIES OF SEMICONDUCTORS

Influence of rapid high-temperature anneals on the photoluminescence of erbium-doped GaN in the wavelength interval 1.0−1.6 μm

V. Yu. Davydov, V. V. Lundin, A. N. Smirnov, N. A. Sobolev, and A. S. Usikov

A. F. Ioffe Physicotechnical Institute, Russian Academy of Sciences, 194021 St. Petersburg, Russia

A. M. Emel'yanov

St. Petersburg State Technical University, 195251 St. Petersburg, Russia

M. I. Makoviĭchuk and E. O. Parshin

Institute of Microelectronics, Russian Academy of Sciences, 150007 Yaroslav, Russia

(Submitted April 20, 1998; accepted for publication April 23, 1998)
Fiz. Tekh. Poluprovodn. **33**, 3–8 (January 1999)

The influence of rapid-anneal conditions and subsequent coimplantation of oxygen ions on the photoluminescence of erbium ions implanted with an energy of 1 MeV and dose of $5\times10^{14}\,\mathrm{cm}^{-2}$ in MOCVD-grown GaN films is investigated. The erbium photoluminescence intensity at a wavelength ~1.54 μm increases as the fixed-time (15 s) anneal temperature is raised from 700 °C to 1300 °C. The erbium photoluminescence intensity can be increased by the coimplantation of oxygen ions at anneal temperatures in the indicated range below 900 °C. The transformation of the crystal structure of the samples as a result of erbium-ion implantation and subsequent anneals is investigated by Raman spectroscopy. © *1999 American Institute of Physics.* [S1063-7826(99)00101-5]

INTRODUCTION

The growing appeal of research on the luminescence of semiconductors doped with rare-earth elements stems from their promising potential for applications in optoelectronic devices. Gallium nitride is a promising material in this regard. Most of the investigations to date have been directed toward erbium-doped GaN. This choice is dictated by the fact that radiative transitions of electrons from the first excited state $^4I_{13/2}$ of the Er^{3+} ion to the ground state $^4I_{15/2}$ lie in the range of wavelengths λ corresponding to minimum losses and minimum dispersion in optical fibers ($\lambda\sim1.54$ μm) used in fiber-optic communications devices.

In the majority of the studies erbium has been introduced into GaN by ion implantation. Appreciable photoluminescence from Er^{3+} in GaN has been observed only after high-temperature anneals of the implanted samples. The influence of the conditions attending such anneals on the photoluminescence of Er^{3+} has been investigated previously at anneal temperatures $T_0\leqslant1000$ °C with long anneal times (of the order of several tens of minutes).[1–7] As mentioned in Ref. 2, anneals at temperatures above 1000 °C have been avoided because of the risk of damage to the surface of GaN. An analysis of the anneal conditions in Refs. 1–4 shows that as T_0 is raised for Er-implanted GaN (GaN:Er), the photoluminescence of Er^{3+} increases to $T_0=1000$ °C. When oxygen has been implanted in GaN along with Er [GaN:(Er, O) samples] at a concentration 5–10 times the Er concentration, the graph of the photoluminescence intensity (I^{PL}) of Er^{3+} as a function of T_0 has acquired a maximum at $T_0=800$ °C (Refs. 1,3, and 4). The objective of our study is to investigate photoluminescence in the wavelength range $\lambda\sim1.0-1.6$ μm for GaN:Er and GaN:(Er, O) samples after shorter anneals and over a wider range of temperatures than in previous papers: 700–1300 °C.

EXPERIMENTAL CONDITIONS

Undoped *n*-type GaN films with a carrier density $n\sim10^{18}\,\mathrm{cm}^{-3}$ and a thickness of 1.2 μm were grown on the (0001) surfaces of sapphire substrates by metal-organic vapor chemical deposition (MOCVD). The growth procedure entailed the deposition of a GaN buffer layer having a thickness of approximately 200 nm at a low temperature (500 °C), followed by the growth of a GaN epitaxial layer at a high temperature (1040 °C).[8] Erbium ions with an energy $E=1$ MeV and dose $D=5\times10^{14}\,\mathrm{cm}^{-2}$ and oxygen with $E=0.115$ MeV and $D=5\times10^{15}\,\mathrm{cm}^{-2}$ were implanted at room temperature. The calculated projected range of the ions is ~0.25 μm. The implanted samples were oven-treated to achieve a rapid thermal anneal at $T_0=700-1300$ °C for a time $t=15-400$ s in a nitrogen stream. The samples were warmed by halogen lamps. In our experiments, therefore, the warmup time to room temperature was always much shorter than the anneal time.

Radiation from a halogen lamp, selected by a bandpass light filter of SZS-24 optical glass, was used to excite photoluminescence. The transmission (T) spectrum of the light

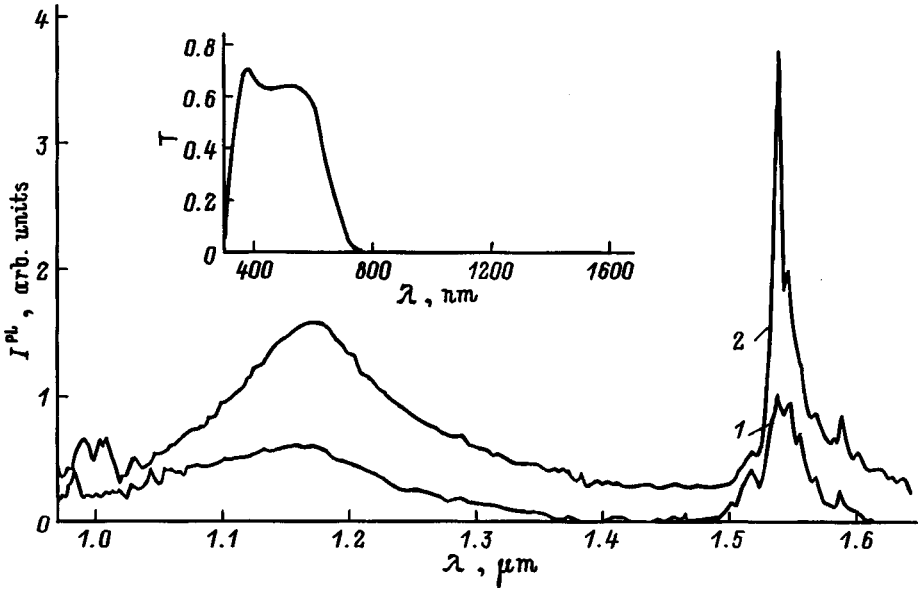

FIG. 1. Photoluminescence spectra of a GaN:Er sample after a 400-s anneal at a temperature of 1300 °C. Measurement temperature: (*1*) 300 K; (*2*) 80 K. As a visual aid, the spectrum *1* is shifted upward by 0.25 arb. units. Inset: transmission *T* spectrum of the SZS-24 optical glass light filter.

filter in the wavelength interval 0.3–1.65 μm is shown in the inset to Fig. 1. The power of the radiation focused by a lens system onto the sample was held at a constant value ~50 mW in all the experiments. The photoluminescence was recorded by means of a monochromator with 3-nm resolution and an InGaAs photodetector operating at room temperature. The light beam from the halogen lamp was modulated by a sector chopper at a frequency of 18 Hz. The detector photocurrent pulses were transformed into an ac voltage, which was recorded by a selective voltmeter. The crystal structure of the erbium-implanted samples was investigated by Raman spectroscopy. This method is one of the few by which it is possible to detect changes in the crystal lattices of the investigated objects in both short-range and long-range orders. The Raman spectra were measured on an automated spectral instrument utilizing a double-grating monochromator. The $\lambda = 488$ nm line of an argon laser was used for excitation, and the power of the exciting radiation on the sample was 30 mW in a spot of diameter 50 μm. All the polarized spectra were recorded in ''back-reflection geometry'' at room temperature. The detector was a cooled photomultiplier in conjunction with a photon counting system.

RESULTS AND DISCUSSION

Figure 1 shows the photoluminescence spectra, measured at 300 K and 80 K, for a GaN:Er sample annealed at 1300 °C for 400 s. In addition to the emission peak with a maximum at $\lambda = 1.538$ μm due to transitions of electrons from the first excited state $^4I_{13/2}$ to the ground level $^4I_{15/2}$ of the Er^{3+} ion, the spectra also contain a broad luminescence band in the interval $\lambda \sim 1.0$–1.4 μm with a maximum at $\lambda \approx 1.17$ μm and a series of small peaks in the vicinity of $\lambda \approx 1$ μm, which can be attributed to electron transitions from the second excited state $^4I_{11/2}$ of the Er^{3+} ion to the ground state $^4I_{15/2}$ (Ref. 2). The broad emission band in the interval $\lambda \sim 1.0$–1.4 μm is associated with photoluminescence at defects in the GaN, because it is observed after the implantation of both erbium and neodymium[2] or chromium[5] ions. We should mentioned that we have not detected any significant differences in the nature of the photoluminescence spectra of GaN:Er and GaN:(Er, O) samples. For the sample in Fig. 1 the photoluminescence intensity at $\lambda = 1.538$ μm increases by a factor of 3.5 when the temperature is lowered from 300 K to 80 K. This factor increases by a factor of 3.9 for a similarly annealed GaN:(Er, O) sample. The intensity of the defect-induced band at the maximum more than doubles for both types of samples after cooldown from 300 K to 80 K.

Figure 2 shows graphs of the photoluminescence intensity of Er^{3+} ions at $\lambda = 1.538$ μm and of defects at $\lambda = 1.17$ μm plotted as a function of the anneal temperature for an anneal time $t = 15$ s for GaN:Er and GaN:(Er, O) samples, measured at 300 K. It is evident from Fig. 2 that the photoluminescence intensity for Er^{3+} increases as T_0 is raised from 700 °C to 1300 °C. At $T_0 < 900$ °C the photoluminescence in the GaN:(Er, O) sample is higher than in the GaN:Er sample, but the opposite relation between the intensities is observed at $T_0 > 900$ °C. Strong emission from defects begins to show up at $T_0 > 1100$ °C and increases as the anneal temperature is raised.

Figure 3 shows graphs of the photoluminescence intensity at $\lambda = 1.538$ μm and 1.17 μm as a function of the anneal time of GaN:Er and GaN:(Er, O) samples at 1300 °C, measured at 300 K. It is evident that the maximum photoluminescence signal at $\lambda = 1.538$ μm for the GaN:Er sample is already observed at $t = 15$ s, whereas for the GaN:(Er, O) sample the photoluminescence intensity increases with the anneal time. For both types of samples the defect-related luminescence intensity increases significantly as the anneal time is increased.

The Raman spectra obtained here can be used to trace the structural transformation of the implanted layer as the anneal temperature is raised. Figure 4 (curve *1*) shows the Raman spectrum of a nonimplanted GaN sample. According to the selection rules for the Raman spectrum of hexagonal GaN in our experimental scattering geometry (here the *z* axis

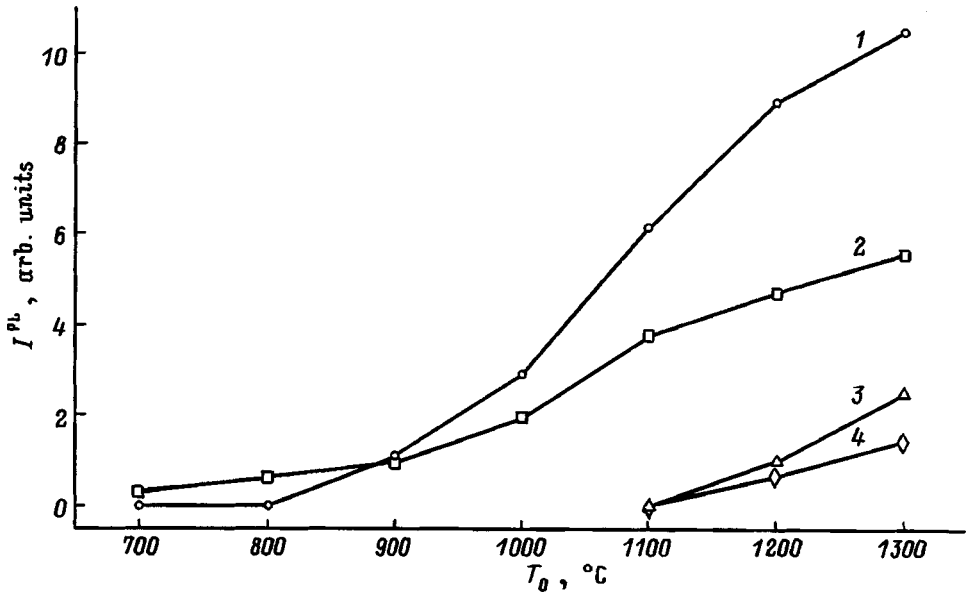

FIG. 2. Photoluminescence intensity at 300 K, wavelengths $\lambda = 1.538\ \mu$m (*1, 2*) and $\lambda = 1.17\ \mu$m (*3, 4*), versus anneal temperature of GaN:Er (*1, 3*) and GaN:(Er, O) (*2, 4*) at a constant anneal time $t = 15$ s.

coincides with the optical axis of the GaN layer), three lines should be observed. Two of them correspond to nonpolar optical phonons of symmetry E_2, and their frequencies for the unstrained GaN layer are $E_2^{(1)} = 145\,\mathrm{cm}^{-1}$ and $E_2^{(2)} = 568\,\mathrm{cm}^{-1}$, respectively.[9] The third line corresponds to the longitudinal component of a polar phonon of symmetry $A_1(LO)$. Its frequency is close to $A_1(LO) = 735\,\mathrm{cm}^{-1}$ for samples having a carrier density $n \sim 1 \times 10^{16}\,\mathrm{cm}^{-3}$ and increases as the carrier density in the sample increases. The Raman spectrum represented by curve *1* is fully consistent with the selection rules for the first-order spectrum of hexagonal GaN. Investigations in other scattering geometries have also exhibited a good match of the experimental results with the selection rules for the hexagonal modification. The investigated sample can therefore be classified as an epitaxial layer of hexagonal GaN with the optical axis directed along the normal to the plane of the substrate. On the other hand, the small upward shift of the phonon frequencies indicates that the GaN is subjected to a stress of the order of 0.3 GPa, which has the character of a compressive stress in the plane of the layer. An estimation of the carrier density from the position of the line $A_1(LO) = 740\,\mathrm{cm}^{-1}$ gives $n = 3 \times 10^{17}\,\mathrm{cm}^{-3}$. The difference in the densities n determined from capacitance-voltage measurements and estimated from Raman data indicate nonuniformity in the distribution of charge carriers in the sample volume.

Curve *2* in Fig. 4 represents the Raman spectrum of a GaN:Er sample. This spectrum is extremely different from curve *1*, being characterized by broad bands in the interval $50 - 750\,\mathrm{cm}^{-1}$ instead of the sharp lines obtained for the nonimplanted sample. The translational symmetry of the lattice is known to gradually disappear in implantation as the dose is increased. As a result, relaxation of the wave vector selection rules takes place, and the spectra of the implanted samples acquire bands associated with phonon modes activated by disorder. A progressive reduction in the intensity of the first-order Raman phonon modes is observed simultaneously. In the final analysis, at large doses the Raman spectrum of the implanted samples reflects the density of vibrational states of the investigated sample.[10] The phonon density of states is one of the fundamental characteristics of a material. As a rule, relevant information is obtained from neutron scattering data. However, the current literature does not contain any such data, because GaN single crystals of the dimensions required for neutron experiments do not exist. Karch *et al.*[11] have calculated the dispersion of the phonon branches in relation to the Brillouin zone from first principles for hexagonal GaN and have used their phonon dispersion data to reconstruct the phonon density of states. A comparison of curve *2* in Fig. 4 with the phonon density-of-states function given in Ref. 11 reveals very good correlation between the two curves in the region of dispersion of both acoustic and optical phonons. The fact that the Raman spectrum obtained for a GaN:Er sample actually reflects the single-phonon density-of-states function of GaN is evidence of total relaxation of the wave vector selection rules as a result of the high defect level of the lattice.

Curves *3–5* in Fig. 4 represent the Raman spectra ob-

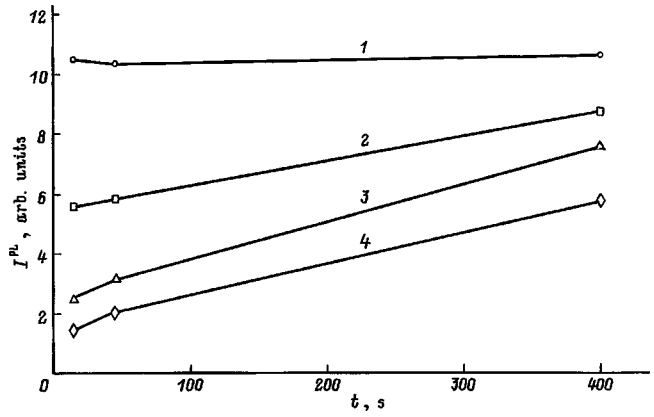

FIG. 3. Photoluminescence intensity at 300 K, wavelengths $\lambda = 1.538\ \mu$m (*1, 2*) and $\lambda = 1.17\ \mu$m (*3, 4*), versus anneal time of GaN:Er (*1, 3*) and GaN:(Er, O) (*2, 4*) at a constant anneal temperature $T_0 = 1300$ °C.

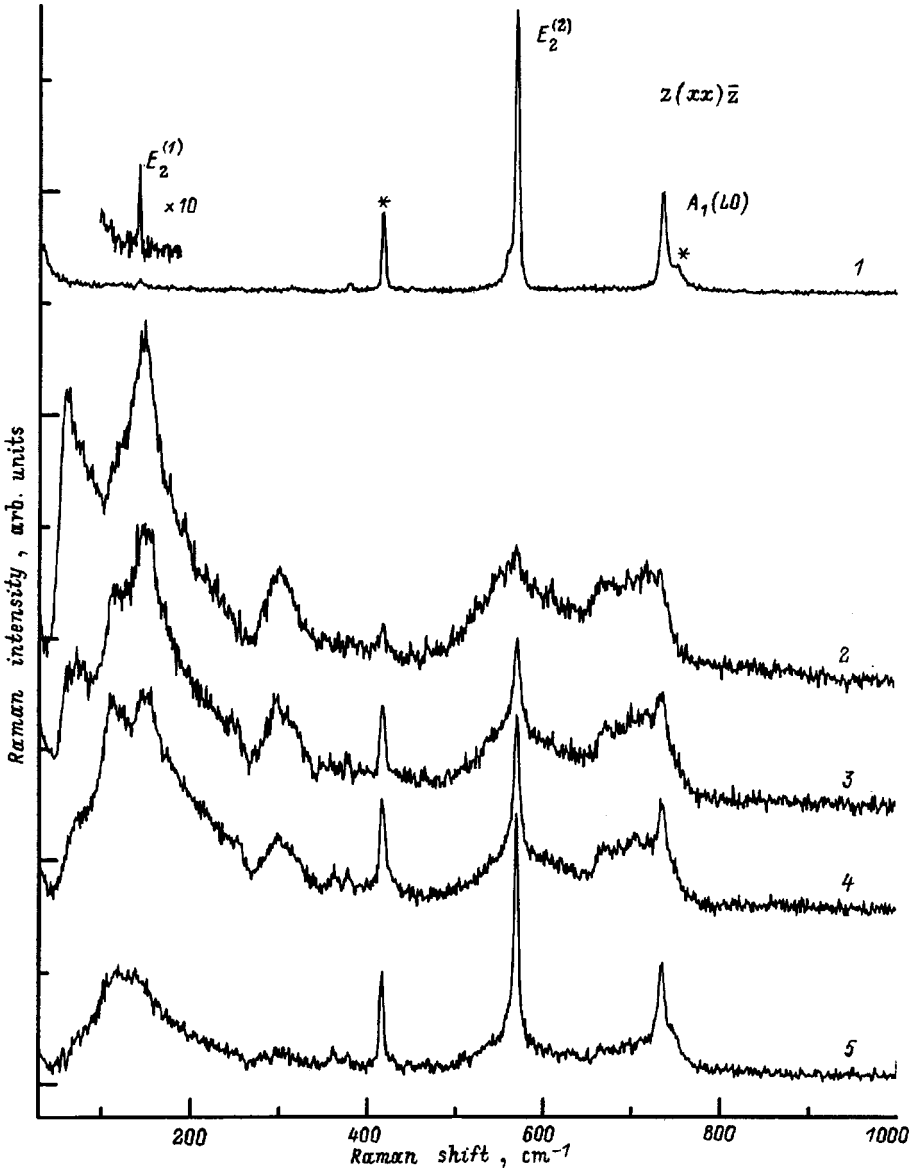

FIG. 4. Raman scattering spectrum. (*1*) Nonimplanted GaN sample (the lines of the Al_2O_3 substrate are marked with stars); (*2*) GaN:Er sample before anneal; (*3–5*) GaN:Er sample after anneals at: $T_0=700\,^\circ$C, $t=15$ s (*3*); $T_0=1000\,^\circ$C, $t=15$ s (*4*); $T_0=1300\,^\circ$C, $t=400$ s (*5*).

tained from a GaN:Er sample annealed for a time $t=15$ s at temperatures $T_0=700\,^\circ$C and $1000\,^\circ$C and for $t=400$ s at $T_0=1300\,^\circ$C, respectively. It is clearly evident that annealing at $T_0=700\,^\circ$C causes sharp lines to appear at once in the Raman spectrum near 568 cm^{-1} and 740 cm^{-1}, where they are associated with phonons of symmetry E_2^2 and $A_1(LO)$ at the center of the Brillouin zone. The onset of lines corresponding to long-wavelength phonons in the Raman spectrum indicates the beginning of the restoration of long-range order in the lattice as a result of the annealing procedure. With a further increase in the anneal temperature (see curves *4* and *5*) the intensities of the phonon lines of symmetry E_2^2 and $A_1(LO)$ continue to increase, and the intensities of the bands associated with phonon modes activated by disorder in the lattice decrease. However, it is evident from a comparison of curves *1* and *5* that even a 400-s anneal at $T_0=1300\,^\circ$C has not fully restored the crystal structure. This result is indicated by the presence in spectrum *5* of a band in the range of acoustic phonons with a maximum near 130 cm^{-1}. This band can be identified with the onset in the first-order Raman spectrum of forbidden acoustic phonons at the boundary of the Brillouin zone as a result of disruption of the ideal lattice by defects. Traces of bands associated with phonon modes activated by disorder in the lattice are also observed in the range of dispersion of optical phonons ($500-750$ cm^{-1}).

On the whole, the transformation of the spectra of annealed GaN:(Er, O) samples is very close to the pattern shown in Fig. 4. It should be noted, however, that in the spectrum of GaN:Er samples, beginning at $T_0=1000\,^\circ$C, a line appears at a frequency close to 360 cm^{-1}, and its intensity increases as the anneal temperature is raised. In the spectra of annealed GaN:(Er, O) samples the intensity of this feature is almost an order of magnitude weaker. We note that the indicated line does not exist in the spectrum of the as-grown sample, but we have observed the emergence of precisely the same line in the spectra of GaN:Mg samples (irradiation energy 100 keV, dose 5×10^{15} cm^{-2}) annealed in a nitrogen atmosphere at $T_0=1000\,^\circ$C and higher. The nature and specific characteristics of the behavior of the Raman line

occurring near $360\,\mathrm{cm}^{-1}$ in the spectrum of annealed GaN implanted with various ions is currently under investigation.

CONCLUSIONS

In summary, the results of the study show that rapid (of the order of a few tens of seconds) postimplant anneals at temperatures $1000\,^{\circ}\mathrm{C} < T_0 \leqslant 1300\,^{\circ}\mathrm{C}$ can be used to fabricate light-emitting structures from erbium-doped GaN. The maximum photoluminescence signal at $\lambda \sim 1.54\,\mu\mathrm{m}$ is obtained in the sample without additional coimplantation of oxygen after an anneal at $T_0 = 1300\,^{\circ}\mathrm{C}$ with durations $15 \leqslant t \leqslant 400\,\mathrm{s}$. The intensity of the photoluminescence of erbium attains saturation when the anneal conditions are such that the defects of crystal structure induced by erbium implantation are not completely removed.

This work has been supported in part by the International Science and Technology Center (Grant 168) and by a combined grant from the International Association for the Promotion of Cooperation with Scientists from the Independent States of the Former Soviet Union and the Russian Fund for Fundamental Research (INTAS-RFFI Grant 95-0531).

[1] J. T. Torvik, C. H. Qiu, R. J. Feuerstein, J. I. Pankove, and F. Namavar, J. Appl. Phys. **81**, 6343 (1997).
[2] E. Silkowski, Y. K. Yeo, R. L. Hengehold, B. Goldenberg, and G. S. Pomrenke, Mater. Res. Soc. Symp. Proc. **422**, 69 (1996).
[3] E. Silkowski, Y. K. Yeo, R. L. Hengehold, and L. R. Everitt, Mater. Sci. Forum **258–263**, 1577 (1997).
[4] J. T. Torvik, R. J. Feuerstein, C. H. Qiu, M. W. Leksono, J. I. Pankove, and F. Namavar, Mater. Res. Soc. Symp. Proc. **422**, 199 (1996).
[5] S. Kim, S. J. Rhee, D. A. Turnbull, E. E. Reuter, X. Li, J. J. Coleman, and S. G. Bishop, Appl. Phys. Lett. **71**, 231 (1997).
[6] S. Kim, S. J. Rhee, D. A. Turnbull, X. Li, J. J. Coleman, and S. G. Bishop, Appl. Phys. Lett. **71**, 2662 (1997).
[7] Myo Thaik, U. Hömmerich, R. N. Schwartz, R. G. Wilson, and J. M. Zavada, Appl. Phys. Lett. **71**, 2641 (1997).
[8] W. V. Lundin, B. V. Pushnyi, A. S. Usikov, M. E. Gaevski, and A. V. Sakharov, in *Institute of Physics Conference Series* 155 (IOP Publ., London, 1997), Chap. 3, p. 319.
[9] V. Yu. Davydov, N. S. Averkiev, I. N. Goncharuk, D. K. Nelson, I. P. Nikitina, A. S. Polkovnikov, A. N. Smirnov, M. A. Jacobson, and O. K. Semchinova, J. Appl. Phys. **82**, 5097 (1997).
[10] M. Cardona, in *Light Scattering in Solids II* (*Topics in Applied Physics*, Vol. 50), edited by M. Cardona and G. Gubtherodt (Springer, Berlin, 1982) 50, p. 117.
[11] K. Karch, J.-M. Wagner, and F. Bechstedt, Phys. Rev. B **57**, 7043 (1998).

Translated by James S. Wood

Influence of the energy transport of electrons by optical phonon emission on the superluminescence and reversible bleaching of a thin GaAs layer excited by a strong picosecond light pulse

I. L. Bronevoĭ and A. N. Krivonosov

Institute of Radio Engineering and Electronics, Russian Academy of Sciences, 103907 Moscow, Russia
(Submitted May 19, 1998; accepted for publication May 20, 1998)
Fiz. Tekh. Poluprovodn. **33**, 13–18 (January 1999)

The dependence of the superluminescence and optical bleaching of GaAs during the interband absorption of a strong picosecond light pulse on the photon energy $\hbar\omega_{ex}$ of the exciting pulse is investigated experimentally. The bleaching (transmission enhancement, i.e., greater transparency) mainly reflects the density of the photogenerated electron-hole plasma. Several events are observed when the distance between the energy level at which electrons are generated and the level from which they undergo stimulated recombination is a multiple of the longitudinal optical phonon energy. These events are: 1) amplification of recombination superluminescence; 2) slowing of the increase in optical bleaching as $\hbar\omega_{ex}$ is increased; and 3) an increase in the shift of the edge of the emission spectrum toward longer wavelengths. These phenomena are qualitatively attributed to an increase in the fraction of transitions involving the emission of *LO* phonons in the energy transport of electrons toward the bottom of the conduction band and to the influence of this process on the heating of the electron-hole plasma and the density of nonequilibrium *LO* phonons. © *1999 American Institute of Physics.* [S1063-7826(99)00301-4]

The emission of longitudinal optical (*LO*) phonons by electrons can sometimes contribute significantly to the energy transport of electrons in GaAs. This connection has surfaced previously, for example, in experimental studies of the energy relaxation of fast electrons (see Refs. 1–3 and others). Such experiments have been carried out at low temperatures. The distribution of electrons in the conduction band occurred below the energy level at which electrons were photogenerated. Transitions of photogenerated electrons to lower energy levels through the emission of *LO* phonons resulted in the formation of ''phonon'' oscillations of the energy distribution of electrons in the conduction band. The oscillations were situated at some distance from the level where electrons are generated, in the direction toward the bottom of the conduction band. The period of the oscillations was equal to the longitudinal optical phonon energy $\hbar\omega_{LO}$. In typical situations phonon oscillations in GaAs have been analyzed from the hot photoluminescence spectra at carrier densities $\sim 10^{15}-10^{16}\,\mathrm{cm}^{-3}$, i.e., when the energy relaxation of fast electrons is dominated by *LO* phonon emission processes. As the density of the electron-hole plasma (EHP) increases, the development of phonon oscillations should be prevented by an increase in the probability Γ_c of an electron escaping from the initial state as a result of interaction with the EHP. According to Kash,[4] the probability Γ_c of an electron escaping from an initial state with, say, an energy of 0.3 eV increases linearly with the density of the EHP and already at $n=p=8\times10^{16}\,\mathrm{cm}^{-3}$ becomes commensurate with the probability of an electron emitting an *LO* phonon (without the EHP) $\Gamma_{e-LO}=5.6\times10^{12}\,\mathrm{s}^{-1}$ (see also Ref. 5). When the density of the EHP increases above $2\times10^{17}\,\mathrm{cm}^{-3}$, the development of phonon oscillations must be further inhibited by stronger screening against the interaction of electrons with *LO* phonons.[6]

Previously[7] we have experimentally observed a different type of phonon oscillations in the carrier energy distribution from the kind described above. These oscillations were observed for a sample at room temperature with electron and hole densities $n=p>10^{18}\,\mathrm{cm}^{-3}$. The energy levels at which the photogeneration of electrons took place were situated inside (rather than above as in Refs. 1–3) the energy distribution of electrons in the conduction band. In Ref. 7 oscillations appeared during the vigorous energy transport of photogenerated electrons toward the bottom of the conduction band with the simultaneous (in a picosecond time interval) generation of an EHP and strong recombination superluminescence. The oscillations were observed most clearly in the interval from the bottom of the conduction band to the energy levels at which electrons are generated. In lieu of an appropriate quantitative theory the onset of such oscillations were interpreted qualitatively as follows. Superluminescence recombination results in depletion of the population of electrons in the local region of energy states at the bottom of the conduction band (see, e.g., Ref. 8). The frequency of electron transitions into the depletion region with the emission of an *LO* phonon is found to be higher than the frequency of escape of electrons from this region with the absorption of an *LO* phonon. As a result of this inequality, repeated regions of depletion of the electron population of the energy levels are formed in the conduction band with a repetition period $\hbar\omega_{LO}$. It can be concluded from Ref. 7 that electron-phonon interaction (although weakened by screening[6]) is appreciable

in the energy transport of a dense EHP, initiated by superluminescence recombination. This conclusion is confirmed in the present study, where we have observed experimentally that the energy transport of electrons by the emission of *LO* phonons produces certain changes in the superluminescence and optical bleaching (transmission enhancement) of GaAs. The character of these changes fosters the assumption that such transport also influences the density of the photogenerated EHP and the density of nonequilibrium *LO* phonons. We note in addition to the foregoing that electron-*LO* phonon interaction in GaAs has also occurred in Raman scattering[9] when the EHP generated by a picosecond light pulse had a density of $(1-9)\times 10^{18}\,\mathrm{cm}^{-3}$.

The investigated sample was an $Al_{0.22}Ga_{0.78}As$–$GaAs$–$Al_{0.4}Ga_{0.6}As$ heterostructure with layer thicknesses of $1.2-1.6-1.2\,\mu$m, respectively, grown by molecular-beam epitaxy on a GaAs (100)–substrate. The width of the x-ray diffraction reflection curve, equal to 29 arcsec, characterizes the degree of defectiveness of the GaAs lattice. The concentration of phonon impurities in the heterostructure was $<10^{15}\,\mathrm{cm}^{-3}$. The substrate was etched on a 4×4-mm area. The $Al_xGa_{1-x}As$ layers, which were designed to stabilize surface recombination and provide mechanical strength, were transparent to our experimental light beam with $\hbar\omega<1.7$ eV. A double-layer antireflection coating of SiO_2 and Si_3N_4 was deposited on the sample, thereby reducing the reflection of normally incident light from the surface to no more than 2% in the actual environment of our experiments. Bleaching was measured by the excite-probe technique, as in Ref. 10, at a fixed probe-beam photon energy $\hbar\omega_p>\hbar\omega_{\mathrm{ex}}$. The exciting (ex) and probe (p) light pulses both had a duration of 14 ps and a spectral width (at the base) ~ 6 meV. The degree of bleaching was characterized by the ratio $\log(T^1/T^0)$ (T is the transmittance of the sample, and the superscripts 1 and 0 indicate the excitation and nonexcitation, respectively), which was calculated from the results of measurements of the time-integrated energies of the probe and exciting pulses. The bleaching $\log(T^1/T^0)$ is proportional to the sum of the nonequilibrium-carrier populations of the energy levels associated with direct interband optical transition.[10] The time-integrated spectra of superluminescent radiation (generated in the photoexcitation of GaAs for a duration in the picosecond range[11,12] and investigated, e.g., in Ref. 13) were measured as in Ref. 7.

Figure 1 shows the dependence, measured in our study, of the energy W_s^M at the maximum of the sample superluminescence spectrum on the photon energy $\hbar\omega_{\mathrm{ex}}$ of the exciting light. The energy density of the exciting pulse $D_{\mathrm{ex}}=1$ arb. unit and the diameter of the focal spot of the exciting beam $F=0.5$ mm were held constant in the measurement of the dependence $W_s^M(\hbar\omega_{\mathrm{ex}})$. Features in the form of steplike local prominences were observed on the $W_s^M(\hbar\omega_{\mathrm{ex}})$ curve (Fig. 1). In addition, we observed a feature on the $W_s^M(\hbar\omega_{\mathrm{ex}})$ curve in the interval $\hbar\omega_{\mathrm{ex}}\approx 1.49-1.54$ eV for a pulse energy density $D_{\mathrm{ex}}\sim 0.3$ arb. unit and a spot diameter $F=0.65$ mm (see Fig. 1) (inconsequential technical differences in the optical systems preclude a more accurate comparison of the pulse energy densities in measurements with $F=0.5$ mm and 0.65 mm). The above-mentioned features were no longer observed in the measurement of $W_s^M(\hbar\omega_{\mathrm{ex}})$ after major reductions in the diameter F and the energy density D_{ex} (which weaken superluminescence[13,14]), for example, to $F=0.35$ mm and $D_{\mathrm{ex}}\sim 0.1$ arb. unit. The antireflection coating on the sample surface ruled out light interference as the explanation for the features on the $W_s^M(\hbar\omega_{\mathrm{ex}})$ curve in Fig. 1. They are probably evidence of an increase in the superluminescence energy W_s^M due to an increase in the fraction of transitions with the emission of *LO* phonons in the energy transport of electrons toward the bottom of the conduction band, induced by recombination superluminescence. In accordance with this assumption, the points of maximum local amplification of radiation [corresponding to maxima of the negative curvature of the $W_s^M(\hbar\omega_{\mathrm{ex}})$ curve] occur in Fig. 1 at photon energies $\hbar\omega_{\mathrm{ex},k}\approx\hbar\omega_s^m+k\Delta$ (indicated by the ''*kLO*'' arrows), where $\hbar\omega_s^m$ is the photon energy at which the maximum of the emission spectrum is situated, $\Delta=\hbar\Omega_{LO}(1+m_e/m_h)=40$ meV, $\hbar\Omega_{LO}=36$ eV is the longitudinal optical phonon energy, $m_e=0.067m_0$ and $m_h=0.5m_0$ are the effective masses of the electron and the heavy hole, respectively, and $k=1,2,3$. In the absorption of photons $\hbar\omega_{\mathrm{ex},k}$ the distance between the energy level at which electrons are generated and the level at which they recombine at the maximum rate is equal to $k\hbar\omega_{LO}$. The positions of maximum curvature of the $W_s^M(\hbar\omega_{\mathrm{ex}})$ curve were determined from the positions of the minima of the function $d^2(W_s^M)/d(\hbar\omega_{\mathrm{ex}})^2=f(\hbar\omega_{\mathrm{ex}})$, also shown in Fig. 1. The (*3LO*) maxima of the two $W_s^M(\hbar\omega_{\mathrm{ex}})$ curves measured for spot diameters $F=0.5$ mm and 0.65 mm (see Fig. 1) were observed for somewhat different values of $\hbar\omega_{\mathrm{ex},3}$ corresponding to equally different emission photon energies $\hbar\omega_s^m\approx\hbar\omega_{\mathrm{ex},3}-3\Delta$.

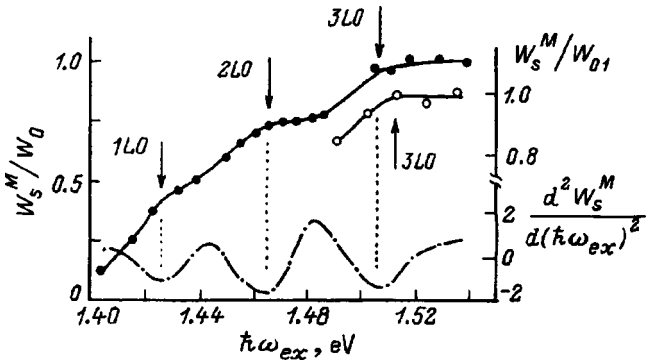

FIG. 1. Energy W_s^M at the maximum of the superluminescence spectrum of GaAs versus exciting photon energy $\hbar\omega_{\mathrm{ex}}$. (●) $F=0.5$ mm, $D_{\mathrm{ex}}=1$ arb. unit; (○) $F=0.65$ mm, $D_{\mathrm{ex}}\sim 0.3$ arb. unit. The normalized energy W_0 is equal to the value of the energy W_s^M measured for an exciting photon energy $\hbar\omega_{\mathrm{ex}}=1.538$ eV and a spot diameter $F=0.5$ mm; accordingly, the normalized energy W_{01} is the same for $\hbar\omega_{\mathrm{ex}}=1.535$ eV and $F=0.65$ mm. The dot-dashed curve represent the graph of $d^2(W_s^M)/d(\hbar\omega_{\mathrm{ex}})^2=f(\hbar\omega_{\mathrm{ex}})$. In all the figures the solid curve is drawn as a visual aid.

The amplification (increase in energy) of superluminescence by the recombination of electrons transported to the bottom of the conduction band through the emission of *LO* phonons is also manifested in oscillations of the width of the radiation spectrum (FWHM) $\Delta\hbar\omega_s$ as a function of $\hbar\omega_{\mathrm{ex}}$ (Fig. 2). The oscillations are attributable to the fact that if

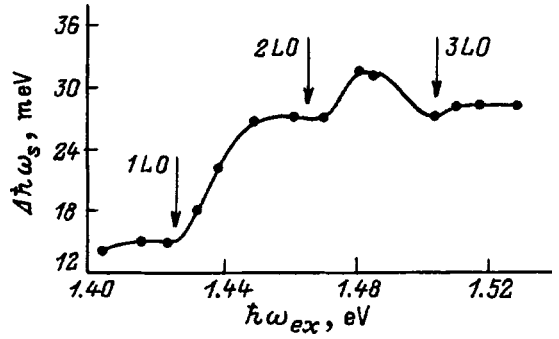

FIG. 2. Width $\Delta\hbar\omega_s$ of the emission spectrum of GaAs versus exciting photon energy $\hbar\omega_{ex}$ for $F=0.5$ mm and $D_{ex}=1$ arb. unit.

such superluminescence amplification (for a fixed exciting pulse) is distributed nonuniformly along its spectrum and is predominant, for example, on a side slope of the emission spectrum, the result is a certain broadening of the emission spectrum relative to the case (for an exciting pulse with the photon energy $\hbar\omega_{ex,k}$) where amplification takes place predominantly in the vicinity of the peak of the spectrum. The emission spectral features shown in Fig. 3 are consistent with the hypothesis that the amplification of superluminescence is distributed nonuniformly along its spectrum for a fixed exciting pulse, and that the region of predominant amplification shifts along the emission spectrum as $\hbar\omega_{ex}$ is varied. A prominence (indicated by the 2*LO* arrow) is observed on the more gradual, short-wavelength slope of spectrum *I* in the vicinity of the photon energy $\hbar\omega_s\approx\hbar\omega_{ex}-2\Delta$. This kind of prominence on the emission spectrum can be interpreted as the amplification of superluminescence due to electron transport in the conduction band by the emission of *LO* phonons (referred to from now on as *LO* transport). For spectrum *II* in the same figure radiation with a photon energy $\hbar\omega_s\approx\hbar\omega_{ex}-2\Delta$ (indicated by the 2*LO* arrow) now takes place on the steeper, long-wavelength slope of the spectrum, where it is more complicated to identify the kind of small additional amplification noted for spectrum *I*. However, such amplification can be discerned from the occurrence of corresponding local minima on the graphs of $d^2(W_s)/d(\hbar\omega_s)^2=f(\hbar\omega_s)$ (see Fig. 3). This assumption is supported by the observation of local minima at emission photon energies $\hbar\omega_s\approx\hbar\omega_{ex}-2\Delta$, indicated by 2*LO* arrows, on graphs *1* and *2* in Fig. 3, which represent the indicated dependence for spectra *I* and *II*. For the emission spectra that occur, for example, at lower exciting photon energies $\hbar\omega_{ex}$ the amplification of the radiation (due to the *LO* transport of electrons) in the region of photon energies $\hbar\omega_s\approx\hbar\omega_{ex}-\Delta$ can be attributed to the onset of a local minimum on curve *3* at $\hbar\omega_s=1.405$ eV and the greater depth of the minimum of curve *4* at $\hbar\omega_s=1.385$ eV than for curves *3* and *5*. The spectral positions of these minima are shifted relative to the photon energies $\hbar\omega_s\approx\hbar\omega_{ex}-\Delta$ (indicated by 1*LO* arrows in Fig. 3), most likely on account of inaccuracy in determining the profile of the spectrum and also the finite width of the spectrum of the exciting light. The greater depth of the minimum at $\hbar\omega_s=1.385$ eV for curve *4* than for curves *3* and *5* ties in with the fact that the amplification of radiation, by increasing

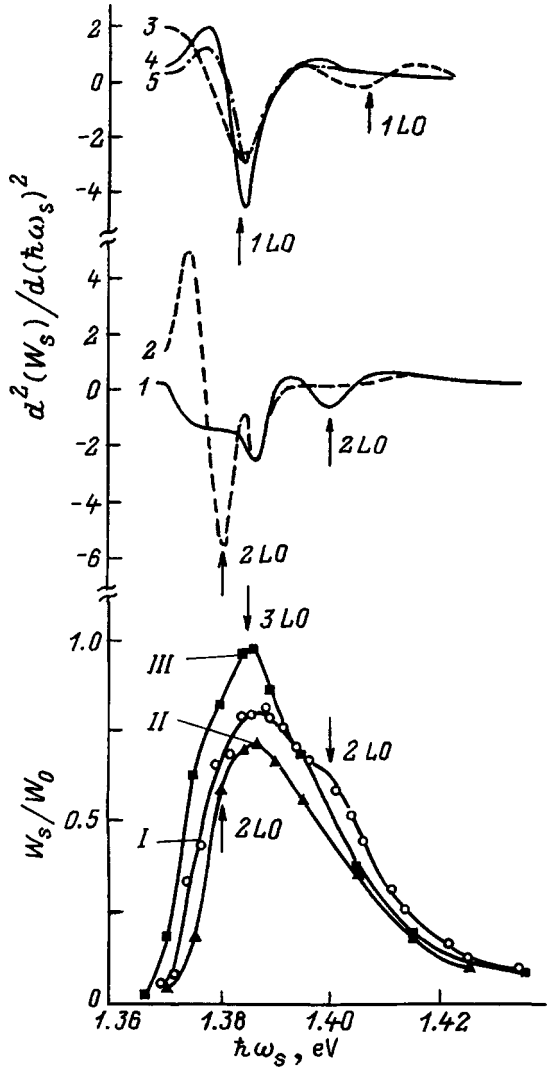

FIG. 3. Emission spectra of GaAs (represented by curves *I–III*) measured for $F=0.5$ mm and $D_{ex}=1$ arb. unit. (*I*) $\hbar\omega_{ex}=1.481$ eV; (*II*) 1.46 eV (*III*) 1.504 eV. Curves *1–5* are graphs of $d^2(W_s)/d(\hbar\omega_{ex})^2=f(\hbar\omega_{ex})$ obtained by differentiating the emission spectra measured at: (*1*) $\hbar\omega_{ex}=1.481$ eV; (*2*) 1.46 eV (*3*) 1.449 eV (*4*) 1.423 eV (*5*) 1.415 eV.

the amplitude of the spectrum, makes the peak of the spectrum sharper, i.e., increases the curvature of the peak. The same is true in regard to spectrum *III* in Fig. 3, where the peak lies in the vicinity of the photon energy $\hbar\omega_s\approx\hbar\omega_{ex}-3\Delta$ (indicated by a 3*LO* arrow). However, for the emission spectra obtained at higher exciting photon energies than spectrum *III* (measured at $\hbar\omega_{ex}=1.504$ eV) the amplification on the side slope of the spectrum at $\hbar\omega_s\approx\hbar\omega_{ex}-3\Delta$ no longer shows up with sufficient contrast (possibly because of the large curvature of the slopes of the spectra). Accordingly, oscillations of the $\Delta\hbar\omega_s(\hbar\omega_{ex})$ curve in this interval of photon energies $\hbar\omega_{ex}$ are now almost unobservable.

When $\hbar\omega_{ex}=\hbar\omega_{ex,k}$, some of the photogenerated electrons emit *LO* phonons and transfer to levels with a depleted carrier population, which correspond to the previously reported[7] phonon oscillations of the electron energy distribution. This process is conducive to the enhancement of electron transport by the emission of *LO* phonons and presumably to an increase in the density of these phonons.

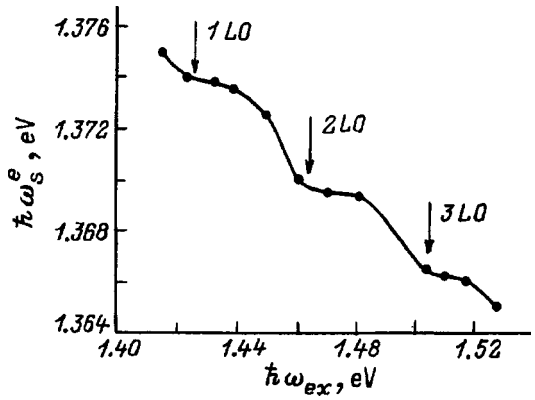

FIG. 4. Position of the long-wavelength edge $\hbar\omega_s^e$ of the emission spectrum versus $\hbar\omega_{ex}$ for $F=0.5$ mm and $D_{ex}=1$ arb. unit ($\hbar\omega_s^e$ is the photon energy at which the radiation energy at the long-wavelength edge of the emission spectrum is equal to 0.04).

According to Ref. 15, the increase in the *LO* phonon density, for example, when the temperature of the crystal lattice of GaAs increases, has the effect of narrowing the band gap E_g by virtue of electron-phonon interaction. Accordingly, the increase in the density of generated nonequilibrium *LO* phonons when $\hbar\omega_{ex}=\hbar\omega_{ex,k}$ could further narrow the band gap. This assumption is consistent with the observed nonuniform shift of the long-wavelength edge of the emission spectrum as $\hbar\omega_{ex}$ increases. This behavior is illustrated in Fig. 4, which shows how the photon energy $\hbar\omega_c^e$, for which the radiation energy at the long-wavelength edge of the spectrum is equal to 0.04, varies as $\hbar\omega_{ex}$ varies.

Figure 5 shows the optical bleaching measured during the exciting pulse at a fixed probe-beam photon energy $\hbar\omega_p>\hbar\omega_{ex}$ as a function of $\hbar\omega_{ex}$. A comparison with the

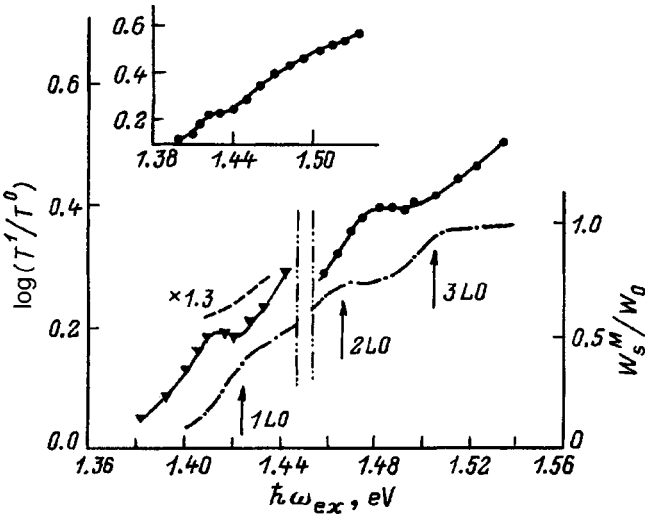

FIG. 5. Optical bleaching of GaAs versus $\hbar\omega_{ex}$ for a probe pulse photon energy $\hbar\omega_p=1.557$ eV and $D_{ex}=1$ arb. unit. Black triangles — $\tau_d=6$ ps, $F=0.56$ mm; (●) $\tau_d=0$, $F=0.5$ mm; here τ_d is the lag time of the probe pulse relative to the exciting pulse. The dot-dashed curve represents the graph of $W_s^M=f(\hbar\omega_{ex})$ (taken from Fig. 1), the dashed curve is the calculated graph of $\log(T^1/T^0)=f(\hbar\omega_{ex})$ at an exciting beam intensity 250 MW/cm^2 (taken from Ref. 22). Inset: Bleaching of GaAs versus $\hbar\omega_{ex}$ for $\tau_d=12$ ps, $F=0.5$ mm, $D_{ex}=1$ arb. unit, and $\hbar\omega_p=1.557$ eV.

$W_s^M(\hbar\omega_{ex})$ curve reveals that in approximately identical intervals of $\hbar\omega_{ex}$ the graphs of the radiation amplitude and bleaching as functions of $\hbar\omega_{ex}$ have curvatures of opposite sign. This means that as the amplification of radiation with increasing excitation energy $\hbar\omega_{ex}$ slows down, the bleaching begins to increase more rapidly; when the radiation energy begins to increase more rapidly, the bleaching increases more slowly. In other words, as $\hbar\omega_{ex}$ is increased, the variation of the growth rates of the radiation energy W_s^M and the bleaching factor have opposite signs for equal values of $\hbar\omega_{ex}$.

The observed correlation between the variations of the bleaching and the radiation energy W_s^M is tentatively explained as follows. The density of the EHP is controlled by recombination superluminescence and approximately (neglecting deviations from a quasiequilibrium distribution) satisfies the condition $\mu_e-\mu_h=E_g$ (see Refs. 8, 10, and 16), where μ_e and μ_h are the Fermi quasilevels of electrons and holes, respectively, and E_g is the width of the band gap. Under these conditions the density of the EHP increases or decreases according to whether the temperature of the EHP increases or decreases.[16–18] We note that this behavior produces approximately reversible changes in the density of the EHP and, accordingly, in the bleaching as the intensity of the exciting light pulse is varied (see Refs. 16 and 17). The EHP is heated by in-gap absorption of both the exciting light[17–19] and the superluminescent radiation[20,21] and also by the involvement of electrons with energies lower than the average conduction band electron energy in superluminescence recombination.[10,20,22] When electron transport by the emission of *LO* phonons (and the radiation energy W_s^M in accordance with Fig. 1) increases as $\hbar\omega_{ex}$ approaches $\hbar\omega_{ex,k}$ from below, the transfer of energy from the EHP to the lattice by the emission of *LO* phonons is intensified. Accordingly, the heating of the EHP as $\hbar\omega_{ex}$ is increased and the concomitant (heating-controlled) increase in the density of the EHP slow down. The variation of the EHP density mainly determines the variation of the bleaching in the presence of superluminescence, as shown in Ref. 16. Consequently, the above-described mechanism of slowing of the growth of the EHP density as $\hbar\omega_{ex}$ approaches $\hbar\omega_{ex,k}$ from below also accounts for the corresponding variation of the bleaching. As $\hbar\omega_{ex}$ is increased above the energy $\hbar\omega_{ex,k}$, the situation becomes the opposite of before. Electron transport by the emission of *LO* phonons (and the increase in the radiation energy W_s^M in accordance with Fig. 1) diminishes. The transfer of energy from the EHP to the lattice by the emission of *LO* phonons diminishes as well. Accordingly, the heating of the EHP as $\hbar\omega_{ex}$ is increased and the concomitant increases in the density of the EHP and the bleaching become more pronounced. It is interesting to note that in Ref. 23, when superluminescence-induced Raman scattering of the exciting light with the participation of plasmons led to the amplification of superluminescence, the bleaching (and, accordingly, the density of the EHP) increased as a result of the more intense heating of the EHP.

It is possible that the above-proposed explanation of the observed correlation between the variations of the bleaching

and the radiation energy W_s^M does not cover all the bases. However, a more scrupulous investigation of this problem taking into account, for example, the variation of the light amplification spectrum in GaAs as the heating of the EHP varies, etc., will require further experiments.

The dashed curve in Fig. 5 shows a characteristic profile of the bleaching as a function of $\hbar\omega_{ex}<1.44$ eV, calculated in Ref. 22 on the assumption that the difference in the energies at which an electron is created and recombines persists in the EHP after recombination of the electron. The calculated bleaching curve clearly exhibits a continuous increase in the bleaching as the $\hbar\omega_{ex}$ is increased. On the experimental curve the bleaching scarcely increases at all in the interval $\hbar\omega_{ex}\approx 1.409-1.425$ eV, and in fact even a small local minimum is observed at $\hbar\omega_{ex,k=1}=1.423$ eV. Beginning with $\hbar\omega_{ex}\approx 1.409-1.425$ eV, the measured bleaching increases with increasing $\hbar\omega_{ex}$ more rapidly than on the calculated curve. This difference in the calculated and experimental curves has been observed previously,[22] where it became more and more conspicuous as the energy density of the exciting pulse D_{ex} was increased. The difference between the calculated and experimental curves can now be attributed to the previously discussed slowing of the growth of the EHP density and bleaching due to the enhancement of electron transport with the emission of *LO* phonons as $\hbar\omega_{ex}$ approaches $\hbar\omega_{ex,k=1}$ from below.

The inset in Fig. 5 shows the dependence of the bleaching on $\hbar\omega_{ex}$, measured for a lag time of the probe pulse from the exciting pulse $\tau_d=12$ ps. It is evident that prominent features (anomalies in the form of local curvature variations) do not exist in the range $\hbar\omega_{ex}>1.44$ eV, and the anomaly (deviation from the calculated curve[22]) in the vicinity of $\hbar\omega_{ex1}$ becomes less distinct, and as the energy D_{ex} decreases, this anomaly is no longer observed.[22] A residual bleaching level, which does not depend on $\hbar\omega_{ex}>E_g$, is attained ~ 20 ps after excitation ceases.[10] Consequently, the anomalies on the curve representing the bleaching as a function of $\hbar\omega_{ex}$ disappear as the intensity of the exciting beam decreases (as τ_d increases). We note that the phonon oscillations in the carrier energy distribution in Ref. 7, mentioned at the beginning of the present article, also occurred as the energy of the exciting pulse was increased.

On the whole, the experimental results obtained here and in Ref. 7 indicate that *LO* phonon emission processes can contribute significantly to the energy transport of photogenerated electrons, induced by strong superluminescence, in GaAs. According to the interpretation set forth in the two studies, the participation of these processes in energy transport can have a certain influence on superluminescence, the heating and concentration of the electron-hole plasma, the energy distribution of electrons, degree of optical bleaching, and the density of nonequilibrium *LO* phonons.

This work has received financial support form the Russian Fund for Fundamental Research (Project 98-02-17377) and the State Committee for Science and Technology of Russia.

The authors are deeply indebted to Yu. D. Kalafati, V. I. Perel', and G. N. Shkerdin for a detailed discussion of the results and for helpful consultations.

[1] D. N. Mirlin, I. Ya. Karlik, L. P. Nikitin, I. I. Reshina, and V. F. Sapega, Solid State Commun. **37**, 757 (1981).
[2] C. L. Petersen and S. A. Lyon, Phys. Rev. Lett. **65**, 760 (1990).
[3] D. N. Mirlin and V. I. Perel', in *Spectroscopy of Nonequilibrium Electrons and Photons*, edited by C. V. Shank and B. P. Zakharchenya (Elsevier Science Publishers B.V., 1992) p. 269.
[4] J. A. Kash, Phys. Rev. B **40**, 3455 (1989).
[5] O. I. Imambecov and S. E. Kumekov, in *All-Union Conference on Physics of Semiconductors*, Vol. 2 (ELM Publishers, Baku, 1982) p. 204.
[6] S. E. Kumekov and V. I. Perel', Fiz. Tekh. Poluprovodn. **16**, 2001 (1982) [Sov. Phys. Semicond. **16**, 1291 (1982)].
[7] I. L. Bronevoi, A. N. Krivonosov, and V. I. Perel', Solid State Commun. **94**, 805 (1995).
[8] I. L. Bronevoi, A. N. Krivonosov, and T. A. Nalet, Solid State Commun. **98**, 903 (1996).
[9] C. L. Collins and P. Y. Yu, Solid State Commun. **51**, 123 (1984).
[10] N. N. Ageeva, I. L. Bronevoi, E. G. Dyadyushkin, V. A. Mironov, S. E. Kumekov, and V. I. Perel', Solid State Commun. **72**, 625 (1989).
[11] D. Hulin, M. Joffre, A. Migus, J. L. Oudar, J. Dubard, and F. Alexandre, J. Phys. (France) **48**, 267 (1987).
[12] N. N. Ageeva, I. L. Bronevoĭ, E. G. Dyadyushkin, and B. S. Yavich, JETP Lett. **48**, 276 (1988).
[13] I. L. Bronevoĭ and A. N. Krivonosov, Fiz. Tekh. Poluprovodn. **32**, 537 (1998) [Semiconductors **32**, 479 (1998)].
[14] L. W. Casperson, J. Appl. **48**, 256 (1977).
[15] Y. P. Varshni, Physica **34**, 149 (1967); M. B. Panish and H. C. Casey, J. Appl. Phys. **40**, 163 (1969).
[16] N. N. Ageeva, I. L. Bronevoi, V. A. Mironov, S. E. Kumekov, and V. I. Perel', in *Mode–Locked Lasers and Ultrafast Phenomena*, edited by G. B. Altshuler, Proc. SPIE **1842**, 70 (1992).
[17] I. L. Bronevoĭ, S. E. Kumekov, and V. I. Perel', JETP Lett. **43**, 473 (1986).
[18] N. N. Ageeva, V. A. Borisov, I. L. Bronevoi, V. A. Mironov, S. E. Kumekov, V. I. Perel', and B. S. Yavich, Solid State Commun. **75**, 167 (1990).
[19] S. E. Kumekov and V. I. Perel', JETP Lett. **50**, 495 (1989).
[20] Yu. D. Kalafati and V. I. Kokin, Zh. Éksp. Teor. Fiz. **99**, 1793 (1991) [Sov. Phys. JETP **72**, 1003 (1991)].
[21] I. L. Bronevoĭ and A. N. Krivonosov, Fiz. Tekh. Poluprovodn. **32**, 542 (1998) [Semiconductors **32**, 484 (1998)].
[22] N. N. Ageeva, I. L. Bronevoi, V. A. Mironov, S. E. Kumekov, and V. I. Perel', Solid State Commun. **81**, 969 (1992).
[23] I. L. Bronevoi, A. N. Krivonosov, and V. I. Perel', Solid State Commun. **94**, 363 (1995).

Translated by James S. Wood

Effect of ion implantation on redistribution of erbium during solid-phase epitaxial crystallization of silicon

O. V. Aleksandrov, Yu. A. Nikolaev, and N. A. Sobolev

A. F. Ioffe Physicotechnical Institute, Russian Academy of Sciences, 194021 St. Petersburg, Russia
(Submitted June 2, 1998; accepted for publication June 6, 1998)
Fiz. Tekh. Poluprovodn. **33**, 114–118 (January 1999)

It is known that Er-ion implantation and O-ion coimplantation into an amorphized Si layer affect the final Er concentration profile when the layer is subjected to solid-phase epitaxial (SPE) crystallization. This paper discusses how this effect depends on dose, energy, temperature, and the parameters of the segregation model, i. e., the transition layer width L and the coordinate dependence of the segregation coefficient $k(x)$. Increasing the Er implantation dose as well as decreasing the implantation energy and temperature cause L to decrease and the segregation coefficient k to increase more rapidly at the initial stage of SPE crystallization. These phenomena could be due to increased defect formation in the amorphous implanted layer. Additional O coimplantation leads to similar changes in L and $k(x)$, due to Er–O complex formation. © *1999 American Institute of Physics.* [S1063-7826(99)02401-1]

INTRODUCTION

One way to make light-emitting structures based on Si:Er is to implant Er ions with subsequent thermal annealing.[1] A promising approach to obtaining higher concentrations of optically and electrically active Er centers is to use doses that exceed the threshold for amorphization.[2] In the course of annealing, the amorphous α-layer is converted into a single crystal c-layer via the mechanism of solid-phase epitaxial (SPE) crystallization. In the process, the initial concentration profile of implanted impurities is strongly modified, due to segregation of impurities at the moving α/c-boundary.[3] Prior to this paper, there have been no studies of how the redistribution of Er changes as the implantation conditions change. In Ref. 4 we proposed a segregation model for the redistribution of Er impurities during SPE crystallization of silicon layers amorphized by implantation. The parameters of the model were the width of the transition layer and the segregation coefficient, which depended on coordinates.

Our goal in this study was to investigate how ion implantation conditions affect the redistribution of Er during SPE crystallization and the parameters of the segregation model.

EXPERIMENTAL CONDITIONS

Polished silicon films with (100) orientation were implanted using the ''high-voltage engineering Europe B2K'' apparatus. The energy of the Er ions varied from 0.5 to 2 MeV, with doses ranging from 4×10^{14} to $3.2\times10^{15}\,\mathrm{cm}^{-2}$. Target temperatures during the implantation were 77 or 300 K. Along with the Er ions, O ions were implanted with energies from 70 to 280 keV and doses in the range 4×10^{15} to $3.2\times10^{16}\,\mathrm{cm}^{-2}$. The energy of the O ions was chosen in such a way that their range coincided with the range of the Er ions. The films were then thermally annealed at temperatures of 620 and 900° for 0.5 to 3 h in a chlorine-containing atmosphere consisting of a mixture of 1 mole % of carbon tetrachloride in a flux of oxygen.[4]

The depth profile of the impurity concentration distribution before and after thermal annealing was measured by secondary ion mass spectrometry on the ''Cameca IMS 4f'' apparatus. The change in the profile as a result of SPE crystallization was analyzed using the segregation model of Ref. 4. In this model, the coordinate dependence of the segregation coefficient was described by the expression

$$k(x)=k_0k_s/\{k_0+(k_s-k_0)\exp[-(x_a-x)/L]\}, \tag{1}$$

where k_0 and k_s are the initial and maximum values of the segregation coefficient, respectively; x_a is the position of the minimum at the inflection point of the Er concentration profile, which appears after thermal annealing, x is the local coordinate measured from the sample surface, and L is the width of the transition layer. The parameters k_s and L are chosen so as to obtain the best agreement between calculated profiles and experimental ones. The initial value of the segregation coefficient is determined from the expression

$$k_0=C(x_a)L/\int_0^L C_0(y)\,dy, \tag{2}$$

where $C(x_a)$ is the concentration of impurities in the recrystallized layer for $x=x_a$, $C_0(y)$ is the initial distribution of impurities after implantation, and $y=x_a-x$ is the local coordinate of the recrystallized layer.

RESULTS OF EXPERIMENT AND DISCUSSION

The effect of implantation temperature on the segregation redistribution of Er was investigated for ions with a fixed energy of 0.5 MeV. Figure 1 shows the concentration profile of erbium at implantation temperatures $T_i=77$ K (curves *1* and *2*) and $T_i=300$ K (curve *4*), measured before SPE crystallization at 620 °C (curve *1*) and afterward (curves

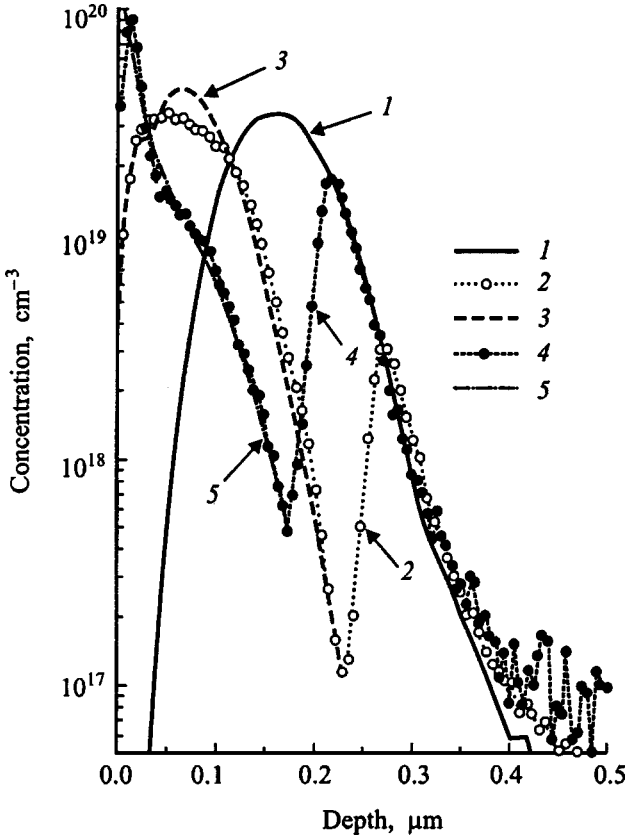

FIG. 1. Effect of erbium ion implantation temperature ($E_{Er}=0.5$ MeV, $D_{Er}=4\times10^{14}$ cm^{-2}) on the Er concentration profile before (*1*) and after annealing (*2* and *4*) at a temperature $T_a=620$ °C for $t_a=60$ min. Implantation temperature T_i, K: *1, 2* — 77, *4* — 300. The parameters for theoretical curves 3 and 5 were $k_s=2.5$; L, nm: *3* — 31, *5* — 42.

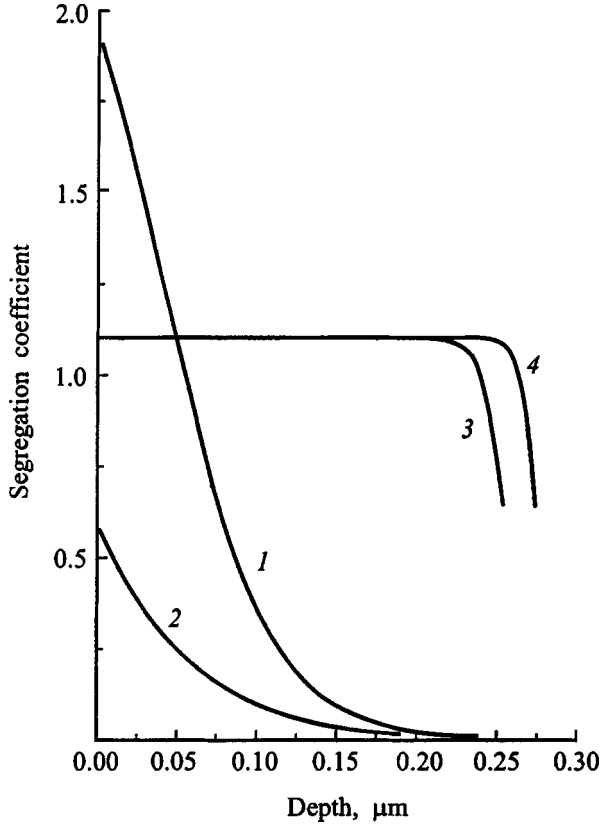

FIG. 2. Dependence of the segregation coefficient on distance into the layer ($E_{Er}=0.5$ MeV, $T_a=620$ °C, $t_a=60$ min). Implantation temperature T_i, K: *1* — 77, *2–4* — 300. Er ion dose, cm^{-2}: *1–3* — 4×10^{14}, *4* — 8×10^{14} cm^{-2}. O ion dose, cm^{-2}: *1, 2* — 0, *3* — 4×10^{15}, *4* — 8×10^{15}.

2 and *4*). It is clear from the figure that as the target temperature increases (1), the thickness of the amorphized layer initially decreases from 0.24 to 0.17 μm, and (2) the character of the Er redistribution near the surface changes. At $T_i=77$ K the Er concentration decreases towards the surface, whereas for $T_i=300$ K it increases. The calculated functions 3 and 5 describe the corresponding experimental profiles well for the following values of the parameter L: 31 nm at $T_i=77$ K and 42 nm at $T_i=300$ K. The corresponding dependences of the segregation coefficient $k(x)$ on the depth at which the layer is located are given in Fig. 2 (curves *1* and *2*). It is clear from the figure that at $T_i=77$ K (curve 1) the segregation coefficient exceeds 1 as we approach the surface, whereas at $T_i=300$ K (curve *2*) it does not reach 1, i.e., the Er concentration decreases near the surface in the first case due to segregation of the Er by trapping in the recrystallized *c* layer, and accumulates at the surface in the second case due to segregation-driven outflow of Er.

Changing the anneal time at 620 °C from 0.5 to 3 hours and adding a subsequent anneal at 900 °C had virtually no effect on the character of Er redistribution, the parameters k_0 and k_s of the coordinate dependence $k(x)$, or the width of the transition layer L (see Table I). These results indicate that the time it takes the crystallization front to travel from $x=x_a$ to the surface is much less than the anneal time. According to the data of Ref. 5, the transit time for the crystallization front is roughly 3 min. The subsequent anneal at 900 °C has no effect because of the small value of the diffusion coefficient for Er in the recrystallized layer ($\sim10^{-15}$ cm^2/s at 900 °C according to the estimates of Ref. 6). These facts also explain why the portion of the Er profile located in the single-crystal substrate is unaffected by annealing (see Fig. 1).

We also studied the effect of implantation dose on the character of Er redistribution and the segregation parameters of the model for an ion energy of 1.0 MeV. Figure 3 also shows the concentration profiles of Er before and after annealing for implantation doses of 4×10^{14} and 8×10^{14} cm^{-2}; the function $k(x)$ is plotted in Fig. 4 (curves *1–4*). It is clear from Fig. 3 that increasing the implantation dose increases the slope of the Er concentration at the initial stage of SPE crystallization (curves *2* and *5*). This is due to the rate of increase of the function $k(x)$ at this stage, assuming that the rate of SPE crystallization is constant (see Fig. 4, curves *1* and *2*). Increasing the dose of Er ions from 4×10^{14} to 3.2×10^{15} cm^{-2} decreases the parameter L from 65 to 40 nm. As we approach the surface, the segregation coefficients exceed 1 and approach a constant level $k(x)\approx k_s=1.3-1.7$.

The effect of an additional oxygen implantation on the redistribution of Er ions implanted at energies of 0.5 and 1 MeV was studied for oxygen doses exceeding the erbium dose by an order of magnitude. The Er concentration profiles

TABLE I. Effect of anneal time and temperature on the parameters of the segregation model ($E_{Er}=0.5$ MeV, $D_{Er}=4\times10^{14}$ cm^{-2}).

Sample label	T_i, K	T_a, °C/t_a, min	x_a, μm	k_0	k_s	L, μm
104	300	620/30	0.215	5.4×10^{-3}	2.5	27
98	300	620/60	0.24	4.7×10^{-3}	2.5	27
141	300	620/180	0.22	1.2×10^{-2}	2.5	31
320	77	620/60 + 900/30	0.23	6.0×10^{-3}	2.5	32
102	300	620/60 +900/30	0.21	1.9×10^{-2}	2.5	35

after implantation of O ions with subsequent SPE crystallization are shown in Fig. 5, and the corresponding functions $k(x)$ are shown in Fig. 2 (curves *3* and *4*) and Fig. 4 (curves *5–8*). It is clear from these figures that coimplantation of oxygen usually leads to an increase of k_0, and always leads to an abrupt increase in the rate of growth of the Er concentration and the segregation coefficient at the initial stages of SPE crystallization. During subsequent SPE crystallization, the Er redistribution is described satisfactorily by a coordinate-independent segregation coefficient $k(x)\approx k_s=1.1-1.5$. The parameter L decreases from 48 to 9 nm for $E_{Er}=0.5$ MeV and from 40–65 nm to 14–18 for $E_{Er}=1$ eV. Note that coimplantation of O ions has virtually no effect on the position of the α/c-boundary, which corresponds to the position of the maximum at the inflection point of the Er profile concentration.

For a fixed implantation dose we found that the energy of the implanted ions affects the erbium redistribution profile. When the energy of the Er ions is increased from 0.5 to 1 MeV, the parameter L increases from 27–48 nm to 52–65 nm. Although coimplantation of oxygen leads to a decrease in the width of the transition layer, the tendency for L to increase with increasing erbium energy is maintained. The width of this layer is roughly 9 nm for $E_{Er}=0.5$ MeV, 16 nm for $E_{Er}=1.0$ MeV, and 31 nm for $E_{Er}=2.0$ MeV. The magnitude of the ion energy was found to have no significant

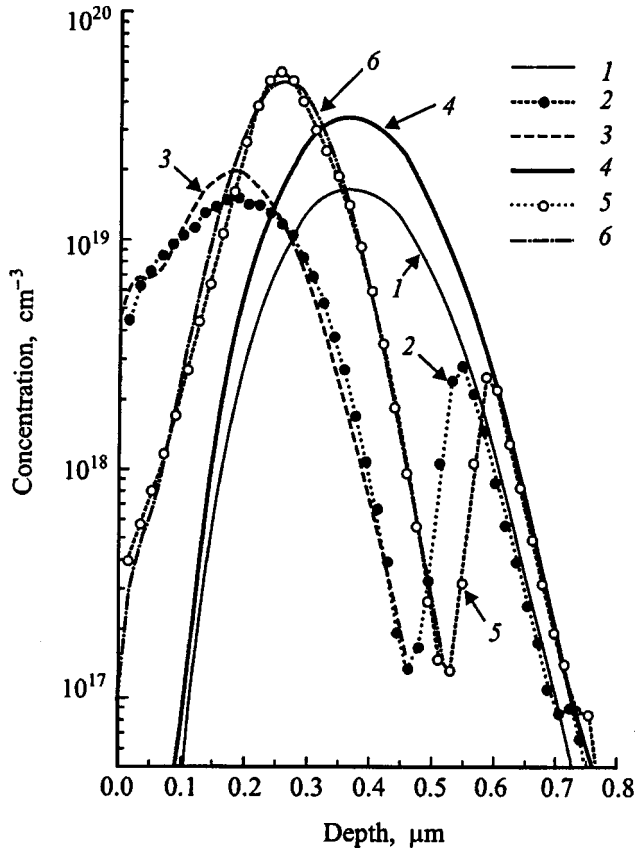

FIG. 3. Effect of erbium ion implantation temperature ($E_{Er}=1$ MeV, 300 K) on the Er concentration profile before (*1* and *4*) and after annealing (*2* and *5*) at a temperature $T_a=620$ °C for $t_a=60$ min. Er ion dose, cm^{-2}: *1, 2*— 4×10^{14}, *4, 5*— 8×10^{14}. Parameters for theoretical curves *3* and *6*: L, μm: *3* — 65, *6* — 52; k_s: *3* — 1.3, *6* — 1.7.

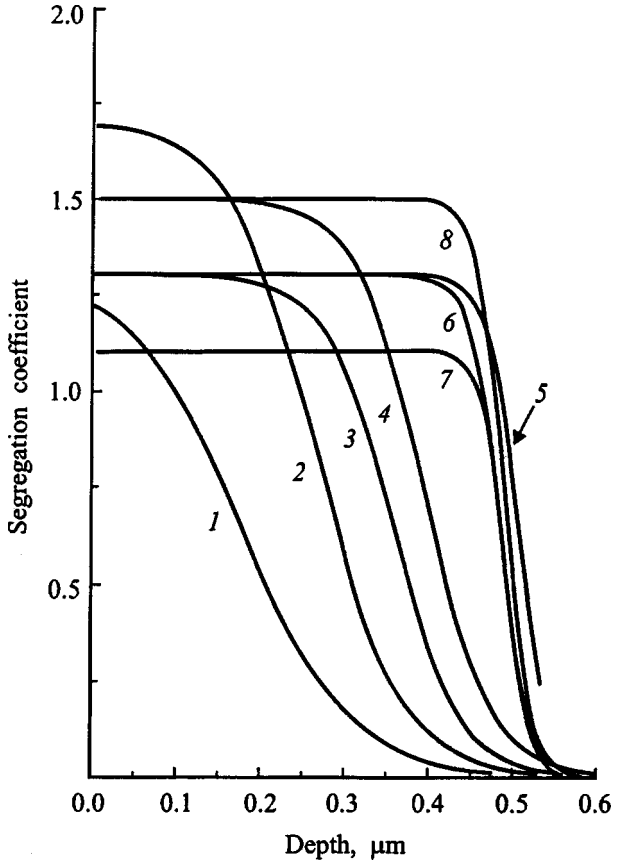

FIG. 4. Dependence of the segregation coefficient on distance into the layer ($E_{Er}=1$ MeV, $E_O=135$ keV, $T_a=620$ °C, $t_a=60$ min). Er ion dose, cm^{-2}: *1, 5* — 4×10^{14}, *2, 6* — 8×10^{14}, *3, 7* — 1.6×10^{15}, *4, 8* — 3.2×10^{15}; O ion dose, cm^{-2}: *1–4* — 0, *5* — 4×10^{15}, *6* — 8×10^{15}, *7* — 1.6×10^{16}, *8* — 3.2×10^{16}.

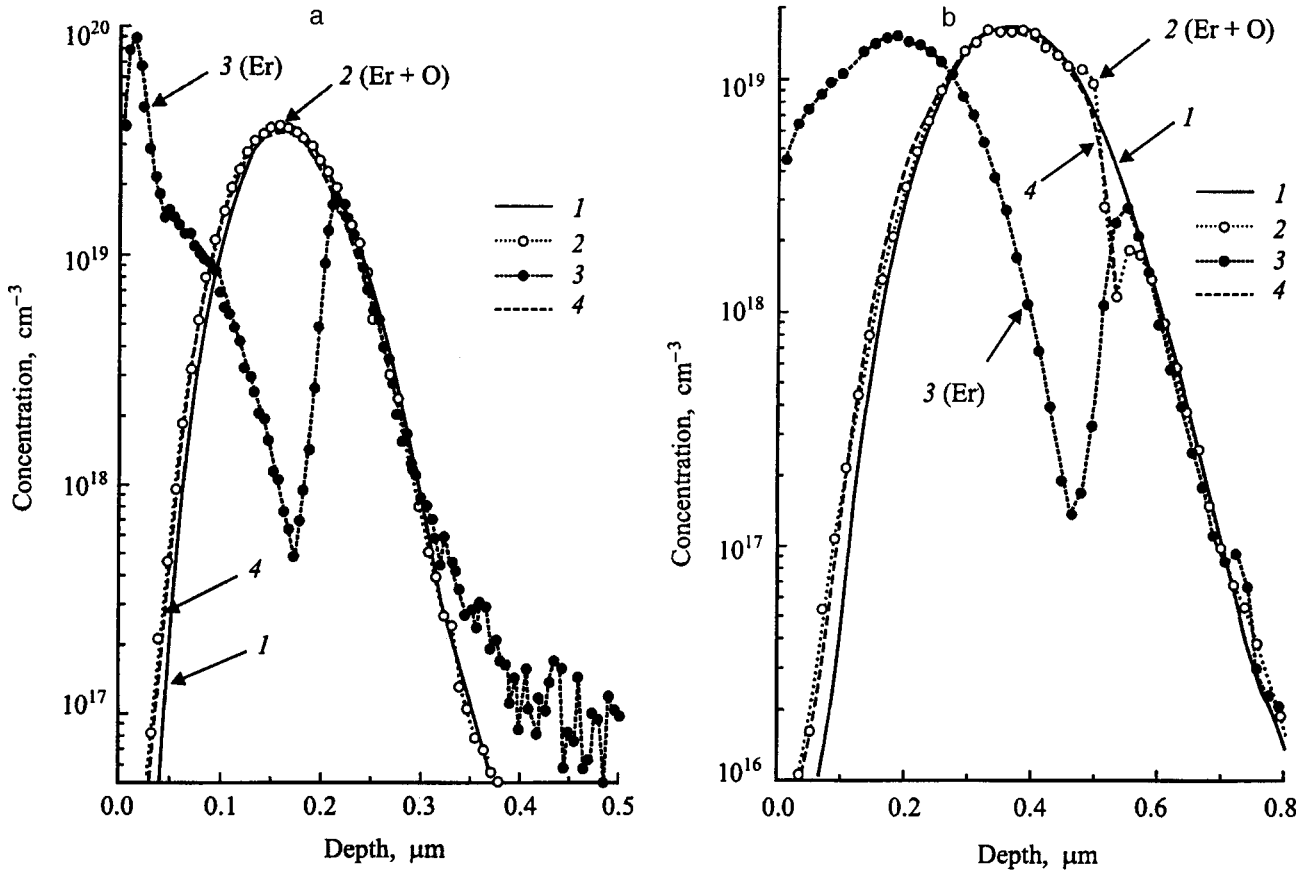

FIG. 5. Effect of coimplantation of oxygen ions on the Er concentration profile before (*1*) and after annealing (*2* and *3*) at a temperature $T_a = 620\,^{\circ}\mathrm{C}$ for $t_a = 60$ min. O ion dose, cm^{-2}: *1*, *3* — 0, *2* — 4×10^{15}. Experimental conditions: *a* — $E_{\mathrm{Er}} = 0.5$ MeV, $D_{\mathrm{Er}} = 4\times10^{14}$ cm^{-2}, $E_{\mathrm{O}} = 70$ keV (theoretical curve *4* was plotted using $L = 7$ nm, $k_s = 1.1$); *b* — $E_{\mathrm{Er}} = 1$ MeV, $D_{\mathrm{Er}} = 4\times10^{14}$ cm^{-2}, $E_{\mathrm{O}} = 280$ keV (theoretical curve *4* was plotted using $L = 18$ nm, $k_s = 1.3$).

effect on the initial and final values of the segregation coefficient.

All the parameters of the ion implantation process under study were found to affect the character of the segregation-induced redistribution of Er strongly, changing the rate of growth of the Er concentration at the initial stage and the character of the impurity distribution near the surface during the final stage of SPE crystallization. These changes, which are well described in the framework of the segregation model,[4] are explained by the change in the width of the transition layer L, which determines the rate of increase of the segregation coefficient, both with thickness of the recrystallized layer and with the maximum value of the segregation coefficient k_s which controls the character of the segregation near the surface. The width of the transition layer decreases with decreasing temperature, increasing dose, and increasing implantation energy. All of these parameters of the implantation process affect the change in the defect content of the implanted layer: increases in the implantation dose and decreases in the energy and temperature of implantation are accompanied by an increase in the local concentration of implantation defects introduced into the single-crystal substrate. When the threshold for amorphization is reached, the implanted layer is amorphized. Subsequent increases in the implantation dose lead to an increase in the defect content of the already amorphized layer. Evidence for this behavior is, e.g., the appearance and growth in the density of states of transverse acoustic phonons in the wave number range around 200 cm^{-1} in the Raman scattering spectra of light with increasing dose.[7]

Coimplantation of O ions was found to abruptly increase $k(x)$ at the initial phase of SPE crystallization and to decrease L. Since co-implantation of O ions does not lead to an increase in the thickness of the amorphized layer, the reason for the growth in k and decrease of L is probably not so much a decrease in defect content of the α-layer as it is a manifestation of the chemical nature of oxygen atoms, for example, their ability to form Er-O complexes.[8,9] An increase in the Er segregation coefficient when O ions are coimplanted was observed previously in Ref. 10, and is explained either by the formation of Er-O complexes, which lower the conversion enthalpy of Er from the α- to the *c*-layer, or by a decrease in the density of Er traps in the amorphous layer.

Thus, we have established that all the ion implantation conditions discussed here—temperature, dose, and energy, as well as co-implantation with O ions—have a significant effect on the segregation redistribution of Er during SPE crystallization. Using our segregation model, it is possible to parametrize this effect in terms of three quantities: the width of the transition layer L, and the initial and final values of the segregation coefficient. The decrease of L is connected with accumulation of defects in the amorphized implantation

layer, and with the formation of Er-O complexes when Er and O ions are coimplanted.

We wish to thank E. O. Parshin and A. V. Shestakov for doing the implantation and to Yu. A. Kudryashev for measuring the concentration profiles.

This work was supported in part by ISTC (Grant 168), CRDF (Grant 235), and the Russian Fund for Fundamental Research (Grant 96-02-17901).

[1] H. Ennen, J. Schneider, G. Pomrenke, and A. Axmann, Appl. Phys. Lett. **43**, 943 (1983).
[2] N. A. Sobolev, Fiz. Tekh. Poluprovodn. **29**, 1153 (1995) [Semiconductors **29**, 595 (1995)].
[3] W. P. Gillin, Z. Jingping, and B. J. Sealy, Solid State Commun. **77**, 907 (1991).
[4] O. V. Aleksandrov, Yu. A. Nikolaev, and N. A. Sobolev, Fiz. Tekh. Poluprovodn. **32**, 1420 (1998) [Semiconductors **32**, 1266 (1998)].
[5] L. Chepregi, E. F. Kennedy, J. W. Mayer, and T. W. Sigmon, J. Appl. Phys. **49**, 3906 (1978).
[6] F. Y. G. Ren, J. Michel, Q. Sun Paduano, B. Zheng, H. Kitagawa, D. C. Jacobson, J. M. Poate, and L. C. Kimerling, Mater. Res. Soc. Symp. Proc. **301**, 87 (1993).
[7] T. Motooka, Thin Solid Films **272**, 235 (1996).
[8] D. L. Adler, D. C. Jacobson, D. J. Eaglesham, M. A. Marcus, J. L. Benton, J. M. Poate, and P. H. Citrin, Appl. Phys. Lett. **61**, 2181 (1992).
[9] V. F. Masterov, F. S. Nasredinov, P. P. Seregin, E. I. Terukov, and M. M. Mezdrogina, Fiz. Tekh. Poluprovodn. **32**, 708 (1998) [Semiconductors **32**, 696 (1998)].
[10] J. S. Custer, A. Polman, and H. M. Pinxtern, J. Appl. Phys. **75**, 2809 (1994).

Translated by Frank J. Crowne

Fano effect in the magnetoabsorption spectra of gallium arsenide

D. V. Vasilenko, N. V. Luk'yanova, and R. P. Seĭsyan

A. F. Ioffe Physicotechnical Institute, Russian Academy of Sciences, 194021 St. Petersburg, Russia
(Submitted March 26, 1998; accepted for publication May 25, 1998)
Fiz. Tekh. Poluprovodn. **33**, 19–24 (January 1999)

The magnetooptic absorption spectra of high-quality homoepitaxial GaAs layers in a magnetic field B up to 7.5 T at $T=1.7$ K are investigated. It is shown that the Fano effect is involved in the formation of certain lines of the magnetooptic spectrum. The parameters of the phenomenological Fano function are determined. It is shown that polariton effects of the diamagnetic exciton play a significant role in the investigated processes. © *1999 American Institute of Physics.* [S1063-7826(99)00401-9]

1. INTRODUCTION

The magnetoabsorption spectra of bulk crystals are known to be formed (see, e.g., Ref. 1) by a set of diamagnetic exciton series ''linked'' to corresponding transitions between Landau subbands that act as dissociation edges. Because of the strong anisotropy of the motion of electrons and holes along and across the magnetic field in this case, each series in strong fields acquires a form typical of a one-dimensional quantum state and inherent, for example, in the optical absorption of quantum wires. This pattern was first successfully observed in InSb crystals,[2] where the Elliott–Loudon strong-field condition ($\beta \gg 1$, where $\beta=\hbar\Omega/2\mathrm{Ry}^*$; Ω is the sum of the electron and hole cyclotron frequencies, and Ry* is the exciton binding energy) is easily attained for the exciton ground state by virtue of the smallness of the exciton binding energy and the proper effective mass of the electron. It becomes clear that the same is true for crystals in which the Elliott–Loudon condition for the ground state can no longer be satisfied, but where excited exciton states are observed prior to the application of a magnetic field. Here the Elliott–Loudon condition holds primarily for excited states having a lower binding energy and greater radius, and the magnetooptic spectrum is formed by a scheme similar to that of the ''Rydberg'' states of atoms and molecules.[3] The first successful observations of such spectra were reported in the early seventies.[4,5] They are characterized by a set of very narrow spectral features far greater in number than the expected number of lines (judging from the spectra of allowed transitions between Landau subbands). The composition and structure of the spectra have been found to result from the superposition of a whole series of effects, which could not be properly interpreted until comparatively recently, whereupon a method was devised and substantiated for calculating the binding energy of diamagnetic excitons. Certainly one instance of these puzzling and until recently unfathomable phenomena is the extremely unusual shape of certain lines of the magnetoabsorption spectrum with their distinctive long-wavelength ''tail'' and sharp cutoff, sinking deeply into phonon absorption from the short-wavelength side. There have been recent attempts to attribute this nature of the spectral lines to the Franz–Keldysh effect for diamagnetic excitons[6] or, similarly, to the presence of a region of negative effective mass of one of the series of the Landau level for heavy holes and, accordingly, the diamagnetic exciton series.[5] A possible relationship of this phenomenon to the onset of the Fano effect in semiconductors has been reported recently.[7] Having access to ultrathin samples of extremely perfect GaAs crystals, we have thought it might be feasible to test this possibility by comparing with other versions.

2. SAMPLES AND EXPERIMENTAL TECHNIQUE

We have investigated samples of high-quality pure GaAs [$n<5\times10^{14}\,\mathrm{cm}^{-3}$, $\mu_{77}=(1-1.5)\times10^5\,\mathrm{cm}^2/(\mathrm{V}\cdot\mathrm{s})$] grown by vapor-phase epitaxy on a (100)-oriented GaAs substrate. The samples were reduced to a ''prequantum'' thickness of $4.4-0.3\,\mu$m by chemical etching of the thicker epitaxial layer. Samples of this series have also been used for experiments to investigate the temperature dependence of the linewidth[8] and the thickness dependence of the amplitude and total absorption[9] for the ground state of the exciton series. The results of Refs. 8 and 9 clearly demonstrate the exciton-polariton character of low-temperature energy transfer over the entire central region of the cross section of the sample exclusive of zones of thickness of the order of $0.1\,\mu$m associated with surface layers up to temperatures of the order of 105 K. Polariton transfer effects vanish at $T>105$ K (Ref. 8) and also at $T=1.7$ K, but only in regions exposed to the strong, nonuniform electric field created by the charge of surface states.[9] Either effect is attributable to an increase in dissipative damping, so that for $\Gamma>\Gamma_c$, where Γ_c is the critical damping, $\Gamma_c=2E_m(2\kappa\Delta_{LT}/Mc^2)^{1/2}$, the spatial dispersion of excitons is suppressed (here E_m is the exciton resonance energy, Δ_{LT} is the longitudinal-transverse splitting, κ is the dielectric constant, and M is the translational exciton mass). Thus, the overall pattern of the low-temperature ''absorption'' of such ''prequantum'' objects is governed by competition between the magnitude of the absorption in three thickness zones of the sample: two outer surface zones characterized by maximum absorption, which depends on the strength of the exciton oscillators or the longitudinal-transverse splitting Δ_{LT}, and a middle zone, in which ''true'' absorption is nonexistent, but the variations of

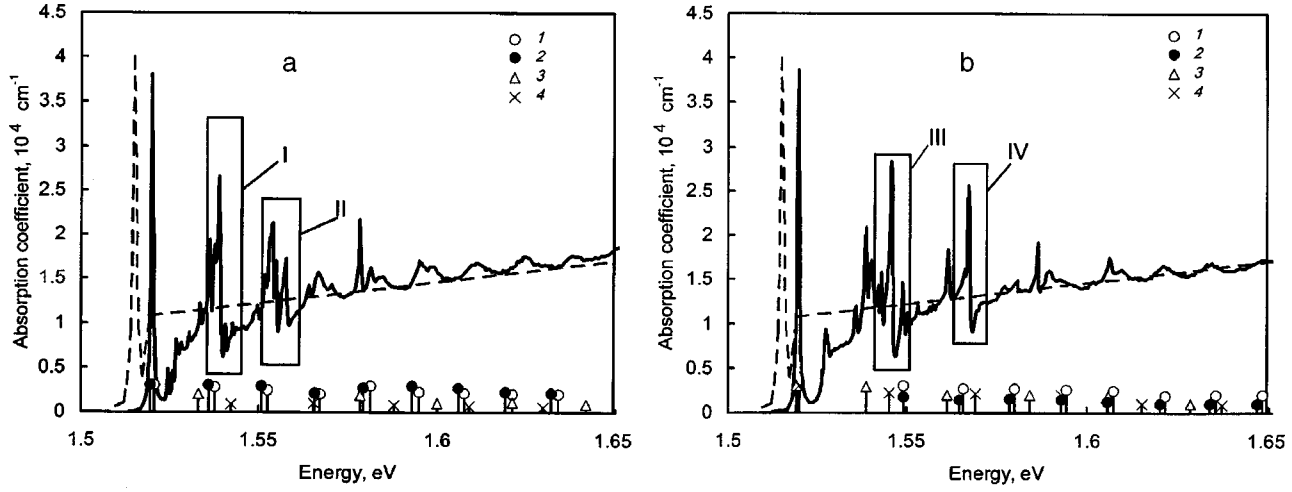

FIG. 1. Spectra of the magnetoabsorption coefficient of GaAs (Faraday geometry) at $T=1.7$ K and $B=7.5$ T. (a) Right-circular polarization, calculated transition energies: (*1*) $a^-(l)a^c(l-1)$; (*2*) $b^-(l)b^c(l-1)$; (*3*) $a^+(l)a^c(l-1)$; (*4*) $b^+(l)b^c(l-1)$, where $l=1,2,\ldots$ are the hole Landau numbers, which increase with increasing energy, the longest-wavelength transition corresponding to $l=1$. (b) Left-circular polarization, calculated transition energies: (*1*) $a^-(l)a^c(l+1)$; (*2*) $b^-(l)b^c(l+1)$; (*3*) $a^+(l)a^c(l+1)$; (*4*) $b^+(l)b^c(l+1)$; the longest-wavelength transition corresponds to $l=1$ for a^- and b^- and to $l=-1$ for a^+ and b^+. The dashed lines represent spectrum in zero magnetic field. The rectangular boxes frame the lines analyzed in the text: (I) $a^-(2)a^c(1)$; (II) $a^-(3)a^c(2)$; (III) $b^+(0)b^c(1)$; (IV) $b^+(1)b^c(2)$. The superscripts $+$, $-$, and c refer to the light-hole, heavy-hole, and electron magnetic subbands, respectively (see Refs. 11 and 5).

the optical transmission of a sample that complies with the ''prequantum'' condition, i.e., has a thickness commensurate with or smaller than the ballistic length of an exciton polariton, is determined entirely by the magnitude and variation of the real dissipative damping. For our magnetooptical experiments we have selected upper-limit ''prequantum'' samples, i.e., samples having thicknesses $d=3-4$ μm. To estimate the physical sample thickness, we used the known value of the absorption coefficient at $B=0$ in the continuum region, where polariton effects are eliminated by dissociation of the bound state. Here the thickness d of the crystal can be estimated as $d=D/\alpha^*$, where D is the measured optical density at $E=1.525$ eV, and $\alpha^*=8\times10^3$ cm^{-1} (Ref. 5). Optical measurements were performed in a liquid-helium medium at a temperature of 1.7 K. The magnetooptic absorption spectra were determined for a broad range of magnetic fields (up to 7.5 T) with irradiation by left-handed circularly polarized (LCP) and right-handed circularly polarized (RCP) light. The free-form technique of packing and performing experiments on the samples without any kind of attachment or adhesive is described in Ref. 5.

3. ''QUANTITATIVE'' OSCILLATORY MAGNETOABSORPTION SPECTRUM OF GaAs

The general appearance of the resulting magnetoabsorption spectra for the two circular polarizations in Faraday geometry at $B=7.5$ T is shown in Fig. 1. We note that the spectra shown here are quantitative, having been plotted to show the values of the absorption coefficient but bearing in mind that the possible polariton nature of the detected lines partially detracts from the real meaning of the ordinate scale, because formally an optical polariton is nonabsorbing, and the given data must be interpreted as a conditional absorption calculated from the transmittance of the sample in the same manner as the true absorption. The spectra are quite typical of the magnetooptics of ''Rydberg'' exciton states, when at least one excited state ($n_0=2$) is detected at $B=0$ in addition to theground state. They are similar to those observed initially in early studies[4,5] and later in Ref. 10. Up to photon energies exceeding the band gap by one or even two factors the longitudinal optical photon energy $\hbar\Omega_{LO}$ the spectrum consists of a set of very narrow lines having a half-width (FWHM) smaller than 1 meV. Only at energies $h\nu>E_g+2\hbar\Omega_{LO}$ does the magnetoabsorption spectrum lose its fine structure and begin to resemble ''oscillatory'' magnetoabsorption. It is interesting to note that while thinner samples with $d<1$ μm can be used to exhibit spectra unique in their width, which can extend up to $h\nu>E_g+\Delta_0$, where Δ_0 is the spin-orbit splitting, in no way are they distinguished by the presence of such a fine structure of lines in the range $h\nu<E_g+2\hbar\Omega_{LO}$. A method for calculating the binding energies of diamagnetic excitons in connection with various transitions between Landau subbands has been proposed and tested in the example of InP crystals.[3] In the final analysis, this method essentially entails the numerical solution of the one-dimensional Schrödinger equation and provides remarkable agreement between theory and experiment for photon energies $h\nu>E_g(B)$, setting the stage for the totally rigorous analysis of elements of the band structure and its parameters. We have used the method of Ref. 3 and achieved good agreement for the principal spectral lines of GaAs. The positions of the transitions between Landau subbands in this case are calculated using modified Pidgeon–Brown equations (see Ref. 5). A theoretical spectrum representing the spectrum of transitions between Landau subbands is given along the energy axes of Figs. 1a and 1b; the spectrum in each case is shifted toward lower energies by amounts equal to the diamagnetic exciton binding energies. It is evident from the figure that by and large the deviations from the theoretical spectrum plotted in this way do not exceed an amount of the

order of 1 meV with the exception of energy intervals in which electron-phonon coupling is highly pronounced.[12,1] If we then look at the absorption spectrum recorded at $B=0$ (dashed curves in Figs. 1a and 1b), we see that in the vicinity of E_g this spectrum is not equivalent to the frequency-integrated magnetooptic spectrum, as predicted by magnetoabsorption theory (see Ref. 5) without regard for polariton effects.

Our processing of the spectra enables us to identify with certainty the parts of the spectra in which we observe unusual behavior of the spectral lines, i.e., behavior that does not fit into conventional notions of exciton magnetoabsorption spectra. There are at least five such spectral regions associated with the strongest transitions: $a^-(2)a^c(1)$, $a^-(3)a^c(2)$ and $b^+(0)b^c(1)$, $b^+(1)b^c(2)$, $b^+(2)b^c(3)$ in the RCP and LCP spectra, respectively. An unusual feature is the sharp cutoff of a line on the short-wavelength side and its deep penetration into phonon absorption, along with the extended ''tail'' on the long-wavelength side. On the other hand, only symmetric behavior could be expected from an exciton line in general, and the sawtooth profile of the density of states of free carriers in a strong magnetic field is known to exhibit the opposite trend (see, e.g., Ref. 5). An especially strange feature, however, is the formation of a relatively deep ''pit'' in the continuous spectrum near the short-wavelength wings of the lines. We also note that a greater number of such features can be observed in weaker magnetic fields, beginning with the long-wavelength side and skipping the first line of the spectrum. Interestingly, this first line, in contrast with those that follow, is totally symmetric.

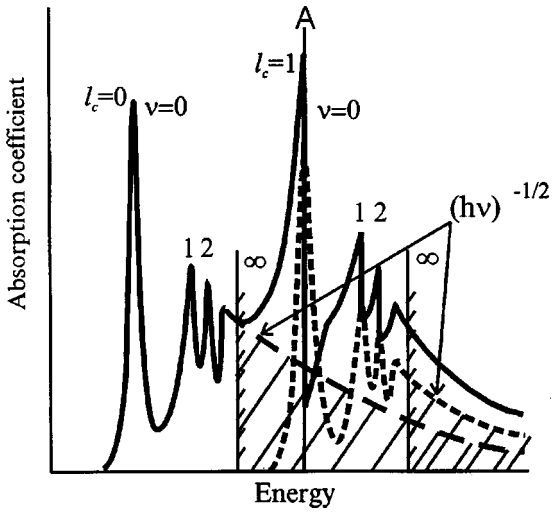

FIG. 2. Schematic representation of the formation of the spectrum of diamagnetic excitons and variations of the line shape in connection with the Fano effect (interference of the discrete line of the diamagnetic exciton ground state is constructive to the left of line A and destructive to the right of line A). The regions of spectra of the continuum and their boundaries are shown hatched; $\nu=0, 1, 2$ are the principal quantum numbers of the one-dimensional exciton.

4. LINE SHAPE ANALYSIS IN TERMS OF THE FANO EFFECT

Fano[13] has investigated the many-particle problem of interaction between continuum states and a discrete level and has demonstrated the existence of constructive-destructive interference between states, which has the effect of distorting the spectral profiles of both the discrete line and the continuum. The Fano effect has been observed in atomic and nuclear spectroscopy in cases where the discrete and continuous spectra overlap. In this situation the probability of transition from an arbitrary initial state to a continuum has a characteristic dependence, which can be described as follows in application to, for example, a discrete level near $\varepsilon=0$:

$$V=\frac{(\varepsilon+q)^2}{(1+\varepsilon^2)}, \tag{1}$$

where ε is the dimensionless transition energy in the discrete spectrum in units of linewidth, and q is a quantity proportional to the ratio of the amplitudes (matrix elements) of transition between states of the discrete spectrum and transition in the continuous spectrum. Bearing in mind the general character of the interband magnetooptic spectrum as having been formed by the superposition of individual diamagnetic exciton series associated with optically active combinations of four sequences of quantum states in the valence band $(a^{\pm}, b^{\pm})$ and two such sequences in the conduction band (a^c, b^c), we can expect multiple superpositions of discrete lines on the continua associated with four groups of diamagnetic excitons for each polarization. Each series of diamagnetic excitons, taken separately, comprises a sequence of discrete lines, a quasicontinuum consisting of merged discrete states, and a true continuum that is an inverse square-root function of the photon energy. Figure 2 shows our postulated pattern of superposition of the first two series of diamagnetic excitons for the transitions $b^+(-1)b^c(0)$ and $b^+(0)b^c(1)$, which are dominant in the beginning of the LCP spectrum. Also shown here is a schematic representation of the spectral changes resulting from the Fano effect. The scheme most nearly approximates the actually observed pattern of an LCP spectrum in which the discrete diamagnetic exciton levels associated with the state $b^+(0)b^c(1)$ overlap the continuum of the state $b^+(-1)b^c(0)$. For local modeling of the experimental data we have used the phenomenological Fano function in the form

$$f(E)=\frac{[(E-\Omega)/\Gamma-q]^2}{1+[(E-\Omega)/\Gamma]^2}, \tag{2}$$

where Ω is the energy of the corresponding resonance, and Γ is the linewidth. The parameters of the Fano resonances have been determined by curve fitting and are summarized in Table I; the phenomenological (fitted) and experimental line shapes are shown in Fig. 3. It follows from an inspection of Table I and Fig. 3 that the agreement is good, especially in light of the appreciable noise generated by series of lines that originate from other types of transitions and are not involved in the interacting system. This consideration is evident in the example the weaker experimental maxima to the left and to the right of the absorption line analyzed in Fig. 3. The resulting data can be used to refine the ''true'' positions of the

TABLE I. Phenomenological parameters of certain magnetooptic absorption lines of GaAs, evaluated by fitting the Fano function to the experimental data.

Polarization	Transition	$E_{\max}$, eV experiment	$E_{\max}$, eV theory	q	Γ, eV
RCP	$a^-(2)a^c(1)$	1.5386	1.5387	-4.38	3.9×10^{-4}
RCP	$a^-(3)a^c(2)$	1.5537	1.5538	-4.10	3.5×10^{-4}
LCP	$b^+(0)b^c(1)$	1.5457	1.5458	-3.18	4.1×10^{-4}
LCP	$b^+(1)b^c(2)$	1.5662	1.5674	-3.57	4.2×10^{-4}

lines, which are shifted 0.1–1.2 meV toward higher energies, to estimate the half-width of the lines Γ as 0.35–0.42 meV, and to ascertain the asymmetry factor $-q$.

5. DISCUSSION OF THE RESULTS

An analysis of the results leaves us no choice but to regard the ideas set forth in Refs. 5 and 6 as to the diamagnetic exciton absorption line shapes observed in GaAs crystals as not fully consistent. Indeed, the phenomenon is observed for both heavy-hole and light-hole transitions, leaving no room to develop the ideas in Ref. 5 associated with the region of negative effective mass of one of the systems of heavy-hole Landau levels ($b^-_{-3/2}$). Not to be overlooked is an explanation based on the possibility of tunneling into diamagnetic exciton states under the influence of an electric field (an effect of the Keldysh–Franz type, first discussed for exciton states by Merkulov and Perel' in Ref. 14) both by virtue of the relative smallness of the regions of the skin-layer field in our samples (according to Ref. 9, we have $2d_{sc}/d<10\%$ in the samples used in our study) and because the ''sawtooth'' line shape clearly observed over the entire extent of the spectra for $h\nu>E_g(B)$ is not observed at all at the first line of the magnetooptic spectra, which does not have a background of continuous states.

Thus, following the results described in the preceding section, we can concur with Ref. 7 and regard the line shapes

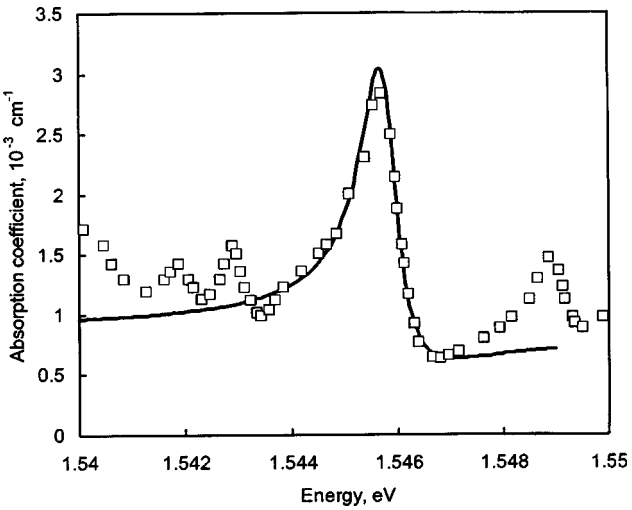

FIG. 3. Example of numerical fitting of the line shape by means of the Fano function. The point symbols represent the experimental data contained in the rectangular box III in Fig. 1b [transition $b^+(0)b^c(1)$], and the solid curve is fitted according to Eq. (2) using the parameters in Table I.

observed in the magnetoabsorption spectra as a consequence of the Fano effect. We note that the Fano effect has been observed in magnetooptic absorption spectra at dozens of spectral lines in much earlier studies,[4,5] but without appropriate interpretation. It is interesting that this effect probably also occurs in the magnetoabsorption of other materials when samples of high perfection are used, for example, in InP (Ref. 3) and in CdTe (Ref. 15). Bellani et al.[16] have demonstrated the extinction of the Fano effect in the magnetooptic spectra of luminescence excitation in GaAs as a result of electrons and holes interacting with longitudinal optical phonons. When the magnetic field is increased until the distance between the corresponding electron Landau levels is equal to the longitudinal optical phonon energy, polaron interaction attains resonance, and one observes anticrossing of the level corresponding to Landau quantum number l_c with the virtual l_c-1 level shifted from the origin by the amount $\hbar\Omega_{LO}$. Now a conspicuous feature is clearly observed on the curves of Γ as a function of $|q|$: They rise, tending to infinity, and the line shape becomes more nearly Lorentzian, shedding its ''sawtooth'' appearance. A similar behavior can be witnessed in the results of Refs. 12 and 17, where the effects of interaction with a longitudinal optical phonon have been studied in detail in GaAs samples of extremely high quality, as well as in our experimental work. The Fano effect is found to be a very universal phenomenon and, as becomes clear, can also be observed in impurity photoionization spectra (see Ref. 18) and in quasi-two-dimensional structures with a relatively broad quantum well.[19] In the latter case an inverse line shape with positive q for the forbidden $LH3E1$ transition can be observed. The absolute value of q increases as the magnetic field is increased, eradicating Fano interference and imparting symmetry to the lines as a result of discrete structure of the continuum (in Faraday geometry).

We note, however, the emergence of a new fact. All the above-described phenomena appear to be observed primarily in samples exhibiting polariton behavior of the discrete exciton lines, when $\Gamma<\Gamma_c$ and, accordingly, spatial dispersion effects are significant. The application of a magnetic field preserves the polariton properties at least for the first diamagnetic exciton series. This result demonstrates that not only does the intensity of the first magnetoabsorption line not increase, as might be expected in connection with magnetic enhancement of the strength of the transition oscillator, but it even decreases in a magnetic field. Observing the behavior of the half-width of lines associated with higher energy states for higher Landau numbers $l_c\geqslant1$, we can assume that the indicated trend remains possible up to energies $h\nu<E_g(B)+2\hbar\Omega_{LO}$, where the condition $\Gamma<\Gamma_c$ most likely still holds. With increasing energy, the dissipative damping increases as a result of the probability of emission of an optical phonon, and the lines begin to broaden considerably, losing their ''fine structure'' at high energies. On the other hand, a magnetic field merely diminishes the dissipative damping, promoting the ''flareup'' of lines. This assertion in all likelihood is supported by the distinct observation of a set of narrow lines in spectra recorded in relatively weak fields $B=(2-3)$ T, when the interval $2\hbar\Omega_{LO}$ contains many magnetooptic transitions, up to $l_c=15-20$.

The polariton nature of the lines of the discrete spectrum breaks down their quantitative relationship with the discrete spectrum. While the intensity of the continuum states is determined entirely by the strength of the transition oscillator, the area of the discrete lines is only a measure of the true dissipative damping, increasing with Γ until the level Γ_c is attained; it then remains constant and corresponds to the strength of the state oscillator. The magneti-field-induced increase in the oscillator strength with the possibility of a simultaneous decrease in the effective linewidth Γ causes the critical threshold $\Gamma=\Gamma_c(B)$ for the observation of exciton-polariton effects with spatial dispersion to shift toward larger values of Γ.

In summary, we can affirm that diamagnetic exciton polariton effects can be involved in the observed phenomena. Their role warrants further careful study. A magnetic field can be used to simulate the behavior of a one-dimensional polariton, specifically under conditions (with respect to the level of active dissipative damping Γ) that are all but inaccessible for as-grown one-dimensional heterostructures, owing to the influence of heterointerfaces and also to internal defects, together with closely spaced barrier defects and nonuniform (geometric) broadening.

6. CONCLUSIONS

We have demonstrated the significant role of the Fano effect in the formation of the magnetoabsorption spectral lines of GaAs. We have analyzed its role in the examples of previous observations of the magnetooptic spectra of GaAs recorded when the Elliott–Loudon strong-field condition is not satisfied and when it is satisfied. We have suggested that ramifications of the Fano effect are very likely to show up in the magnetooptic spectra of other materials and, hence, that it has a certain universality. At the same time, we have called attention to the involvement of exciton-polariton processes in the observed effects and the possibility that they have an independent role, which requires further investigation.

The authors are grateful to G. N. Aliev for helping to obtain the spectra in Fig. 1 and also to U. Rössler for kindly sending us results from T. Hornung's dissertation.

[1] R. P. Seisyan and B. P. Zakharchenya, in *Landau Level Spectroscopy*, edited by E. I. Rashba and G. Landwehr (North-Holland, 1991) p. 345.
[2] L. M. Kanskaya, S. I. Kokhanovskiĭ, R. P. Seĭsyan, and Al. L. Éfros, Fiz. Tekh. Poluprovodn. **15**, 1854 (1981) [Sov. Phys. Semicond. **15**, 1079 (1981)].
[3] S. I. Kokhanovskiĭ, Yu. M. Makushenko, R. P. Seĭsyan, Al. L. Éfros, T. V. Yazeva, and M. A. Abdullaev, Fiz. Tverd. Tela (Leningrad) **33**, 1719 (1991) [Sov. Phys. Solid State **33**, 967 (1991)].
[4] R. P. Seĭsyan, M. A. Abdullaev, and B. P. Zakharchenya, Fiz. Tekh. Poluprovodn. **7**, 957 (1973) [Sov. Phys. Semicond. **7**, 649 (1973)].
[5] R. P. Seĭsyan, *Diamagnetic Exciton Spectroscopy* [in Russian], Nauka, Moscow, 1984.
[6] B. S. Monozon, R P. Seĭsyan, and V. I. Karpov, Fiz. Tekh. Poluprovodn. **9**, 1839 (1975) [Sov. Phys. Semicond. **9**, 1216 (1975)]; B. S. Monozon, Fiz. Tverd. Tela (Leningrad) **18**, 475 (1976) [Sov. Phys. Solid State **18**, 275 (1976)].
[7] S. Glutsch, U. Siegner, M.-A. Mycek, and D. S. Chemla, Phys. Rev. **50**, 170 (1994).
[8] V. A. Kosobukin, R. P. Seisyan, and S. A. Vaganov, Semicond. Sci. Technol. **8**, 1235 (1993).
[9] G. N. Aliev, N. V. Luk'yanova, R. P. Seisyan, M. R. Vladimirova, H. Gibbs, and G. Khitrova, Phys. Status Solidi A **164**, 193 (1993).
[10] L. P. Nikitin, I. B. Rusanov, R. P. Seĭsyan, Al. L. Éfros, and T. V. Yazeva, Fiz. Tekh. Poluprovodn. **16**, 1377 (1982) [Sov. Phys. Semicond. **16**, 883 (1982)].
[11] C. R. Pidgeon and R. N. Brown, Phys. Rev. **146**, 575 (1966).
[12] W. Becker, B. Gerlach, T. Hornung, and R. G. Ulbrich, in *Proceedings of the 18th International Conference on the Physics of Semiconductors*, Vol. 2 (Stockholm, Sweden, 1996), p. 1713.
[13] U. Fano, Phys. Rev. **124**, 1866 (1961).
[14] I. A. Merkulov, Zh. Éksp. Teor. Fiz. **66**, 2314 (1974) [Sov. Phys. JETP **39**, 1140 (1974)].
[15] G. A. Aliev, O. S. Koshchug, A. I. Nesvizhskiĭ, R. P. Seĭsyan, and T. V. Yazeva, Fiz. Tverd. Tela (St. Petersburg) **35**, 1514 (1993) [Phys. Solid State **35**, 764 (1993)].
[16] V. Bellani, L. Vina, E. Perez, R. Hey, and K. Ploog, in *Proceedings of the 18th International Conference on the Physics of Semiconductors*, Vol. 1 (Berlin, 1996), p. 373.
[17] T. Hornung, Ph.D. Thesis (University of Dortmund, 1984); U. Rössler, private communication.
[18] G. Piao, R. A. Lewis, and P. Fisher, Solid State Commun. **75**, 835 (1990).
[19] V. Bellani, E. Perez, S. Zimmermann, L. Vina, R. Hey, and K. Ploog, Solid State Commun. **97**, 459 (1996).

Translated by James S. Wood

Correlation between the material parameters and conditions for the excitation of recombination waves in Si⟨S⟩

M. K. Bakhadyrkhanov, U. Kh. Kurbanova, and N. F. Zikrillaev

Tashkent State Technical University, 700095 Tashkent, Uzbekistan
(Submitted April 1, 1998; accepted for publication May 25, 1998)
Fiz. Tekh. Poluprovodn. **33**, 25–26 (January 1999)

The conditions for the self-excitation of current oscillations in the form of recombination waves in sulfur-doped silicon are investigated as a function of the electrical parameters of Si⟨S⟩ samples. The data reveal regular and reproducible self-excited oscillations with controllable parameters. A distinct correlation is established between the resistivities and the type of conductivity of the Si⟨S⟩ samples, and the parameters for the excitation of recombination waves are determined, specifically, the excitation electric field and temperature. © *1999 American Institute of Physics.* [S1063-7826(99)00501-3]

Many authors have investigated self-excited oscillatory processes in various semiconductor materials.[1–5] An analysis of the data in these papers reveals, despite the acquisition of several interesting results, essentially a failure to exploit the functional capabilities of this important phenomenon in electronics. The dilemma stems from the following factors.

1. The results are difficult to reproduce, and a clear correlation is lacking between the parameters of the material, the excitation conditions, and the parameters of the self-excited current oscillations.

2. Self-excited oscillations are observed in these materials in high electric fields, in a narrow temperature interval, and in illumination by light at a definite wavelength.

3. The amplitude of the self-excited current oscillations and the percentage modulation of the oscillations are small $[I=1-10,\ K=(0.1-30)\%]$.

In view of these considerations, the main objective of the present study is to establish laws governing the variation of the current self-excitation conditions as a function of the parameters of compensated silicon with a view toward generating stable, reproducible oscillations with prescribed and controllable parameters.

We have chosen single-crystalline silicon compensated by sulfur atoms as the object of investigation. This choice is dictated by the availability of a well-developed, reproducible technology for the preparation of such materials.[6,7] For the investigations we used (111)- and (110)-oriented single-crystalline *p*-type silicon, marks KDB-1 and KDB-10, with an oxygen content of $(5-6)\times10^{17}\,\mathrm{cm}^{-3}$. A well-developed technology[8] was used to diffuse S in the Si. The diffusion regimes were chosen in such a way as to yield uniformly doped Si⟨S⟩ samples with various resistivities in the range $\rho=10^2-10^5\,\Omega\cdot\mathrm{cm}$ at $T=300\,\mathrm{K}$ and with both *p*-type and *n*-type conductivities. The self-excited current oscillations were investigated in a cryostat designed so that the temperature, the electric and magnetic fields, the illuminance, and the pressure could be varied between wide limits.[9–12] The self-excited current oscillations were recorded on an S1-48B oscilloscope and an SKI-56 spectrum analyzer, which afforded the possibility of determining the parameters (amplitude and frequency) and waveform of the current oscillations with high accuracy.

The results of the investigations show that self-excited current oscillations of the recombination wave type are observed when the sample is exposed to an electric field in excess of a certain threshold, $E>E_{\mathrm{thr}}$. It has been established that under identical conditions (i.e., for the same temperature and illuminance) the value of E_{thr} is determined mainly by the resistivity of the material. We have therefore investigated self-excited current oscillations in Si⟨S⟩ as a function ρ. It should be noted that three to five samples were prepared for each value of the resistivity to obtain reliable and reproducible results and also to establish a correlation between E_{thr} and ρ. The data show that self-excited current

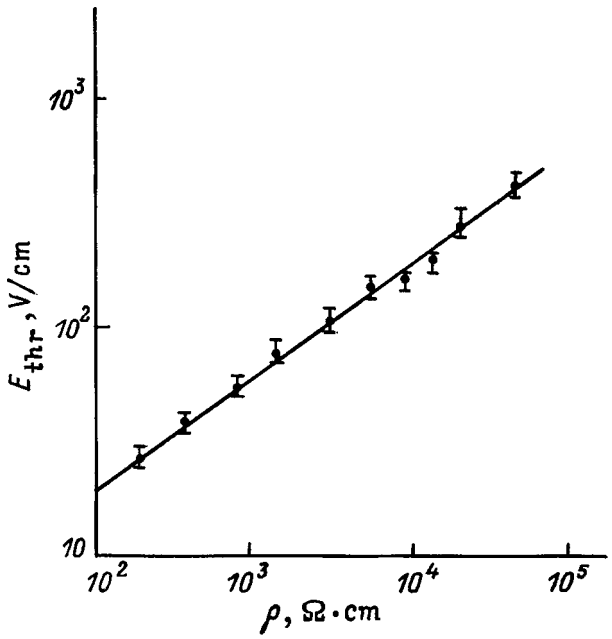

FIG. 1. Dependence of the threshold field E_{thr} for current self-excitation in the form of recombination waves on the resistivity in Si⟨S⟩ samples.

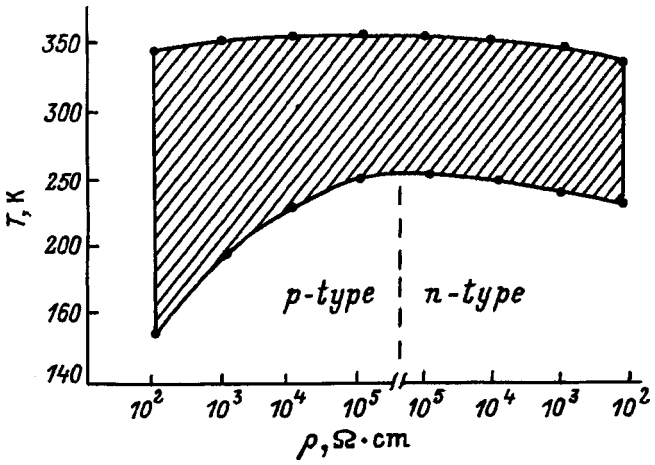

FIG. 2. Temperature domain for the existence of self-excited current oscillation as a function of the resistivity of *p*-type and *n*-type Si⟨S⟩.

oscillations of the recombination wave type are observed over a broad range of resistivities $\rho = 10^2 - 10^5\ \Omega \cdot \mathrm{cm}$ for *p*-type Si⟨S⟩ and in the range $\rho = 10^2 - 10^4\ \Omega \cdot \mathrm{cm}$ for the *n*-type. It is evident from Fig. 1 that the threshold electric field for recombination waves increases linearly with the resistivity, and this dependence can be described by the equation

$$E_{\mathrm{thr}} = E_0(1 + \alpha\rho),$$

where $E_0 = 30\ \mathrm{V/cm}$ is the threshold electric field for a sample with $\rho = 3 \times 10^2\ \Omega \cdot \mathrm{cm}$, and the coefficient α has a value $\alpha = 3.19\ (\Omega \cdot \mathrm{cm})^{-1}$.

It is important to note, in contrast with the recombination wave modes investigated in Si⟨Mn⟩ and Si⟨Zn⟩ samples, that self-excited current oscillations are observed over a fairly broad interval of resistivities of the Si⟨S⟩ samples, and that their threshold field E_{thr} is relatively low. The amplitude and waveform of the self-excited oscillations are stable, and the percentage modulation attains 40% in this case.

The temperature ranges in which self-excited current oscillations exist as a function of the resistivity and type of conductivity of the Si⟨S⟩ samples are shown in Fig. 2. It is evident from the figure that for compensated *p*-type Si⟨S⟩ samples the upper temperature limit for the existence of self-excited current oscillations is essentially independent of ρ and attains $T = 350\ \mathrm{K}$, while the lower limit increases from 160 to 250 K as the resistivity increases from $3 \times 10^2\ \Omega \cdot \mathrm{cm}$ to $10^5\ \Omega \cdot \mathrm{cm}$. In overcompensated *n*-Si⟨S⟩ samples both the upper limit and the lower limit decrease slightly with increasing ρ, and the finite domain of existence of self-excited current oscillations occupies the temperature interval 230–330 K. It should be noted in this regard that reproducible self-excited current oscillations are observed in this temperature interval, independently of the resistivity and the type of conductivity. The dependences of the parameters (amplitude and frequency) on the temperature, the electric field, and the resistivity of the Si⟨S⟩ sample are similar to data in Ref. 13.

In contrast with the data in Refs. 1–11, therefore, for the first time we have established a clear-cut correlation between the excitation conditions, the parameters of the self-excited current oscillations, and the parameters of the material. These investigations are conducive not only to the generation of regular and stable self-excited current oscillations, but also to the reproduction of this phenomenon over a broad range of temperatures and resistivities of silicon, providing a basis for the fabrication of solid-state oscillators with controllable parameters.

[1] N. Holonyak and S. F. Beracgua, Appl. Phys. Lett. **2**, 72 (1963).
[2] S. P. Kal'venas, Fiz. Tekh. Poluprovodn. **9**, 1685 (1975) [Sov. Phys. Semicond. **9**, 1109 (1975)].
[3] S. G. Kalashnikov and G. S. Pado, Fiz. Tekh. Poluprovodn. **3**, 1028 (1969) [Sov. Phys. Semicond. **3**, 864 (1969)].
[4] Yu. I. Zavadskiĭ and B. V. Kornilov, Fiz. Tverd. Tela (Leningrad) **11**, 1494 (1969) [Sov. Phys. Solid State **11**, 1213 (1969)].
[5] M. K. Bakhadyrkhanov, A. A. Tursunov, and K. Khaĭdarov, Fiz. Tekh. Poluprovodn. **14**, 966 (1980) [Sov. Phys. Semicond. **14**, 571 (1980)].
[6] S. G. Kalashnikov and G. S. Pado, Fiz. Tekh. Poluprovodn. **3**, 1028 (1969) [Sov. Phys. Semicond. **3**, 864 (1969)].
[7] I. V. Karpova and S. G. Kalashnikov, Fiz. Tekh. Poluprovodn. **12**, 954 (1978) [Sov. Phys. Semicond. **12**, 563 (1978)].
[8] A. Sh. Abdinov and V. K. Mamedov, Fiz. Tekh. Poluprovodn. **14**, 754 (1980) [Sov. Phys. Semicond. **14**, 442 (1980)].
[9] M. K. Bakhadyrkhanov, B. Z. Sharipov, and Sh. I. Askarov, Pis'ma Zh. Tekh. Fiz. **18**(4), 52 (1992) [Sov. Phys. Tech. Phys. **18**, 115 (1992)].
[10] I. V. Karpova, S. G. Kalashnikov, O. V. Konstantinov, and V. I. Perel', Fiz. Tekh. Poluprovodn. **6**, 1155 (1972) [Sov. Phys. Semicond. **6**, 1011 (1972)].
[11] M. K. Bakhadyrkhanov, Kh. M. Iliev, A. Khamidov, and I. P. Parmankulov, Fiz. Tekh. Poluprovodn. **25**, 1731 (1991) [Sov. Phys. Semicond. **25**, 1041 (1991)].
[12] O. V. Konstantinov and V. I. Perel', Fiz. Tverd. Tela (Leningrad) **6**, 3364 (1964) [Sov. Phys. Solid State **6**, 2691 (1964)].
[13] M. K. Bakhadyrkhanov and U. Kh. Kurbanova, Fiz. Tekh. Poluprovodn. **28**, 1305 (1994) [Semiconductors **28**, 739 (1994)].

Translated by James S. Wood

Self-compensation in PbSe:Tl thin films

V. A. Zykov, T. A. Gavrikova, S. A. Nemov, and P. A. Osipov

St. Petersburg State Technical University, 195251 St. Petersburg, Russia
(Submitted May 25, 1998; accepted for publication May 17, 1998)
Fiz. Tekh. Poluprovodn. **33**, 27–30 (January 1999)

Processes of defect formation are investigated in epitaxial PbSe:Tl films prepared by vacuum evaporation from molecular beams at various condensation temperatures from mixtures with a thallium content of 0–1.6 at. %. It is established that an increase in the content of the acceptor impurity in the film is accompanied by a significant increase in the number of selenium donor vacancies through the self-compensation mechanism. The thallium concentrations in the films are determined, along with the impurity transport coefficients, which vary from 0.82 to 0.44 as the condensation temperature varies from 250 °C to 350 °C. The carrier densities are calculated theoretically as a function of the thallium content in the films. The noticeable discrepancy between theory and experiment for thallium concentrations in the film $N_{\mathrm{Tl}} < 0.3$ at. % is attributed to the presence of growth-induced nonequilibrium donor defects in the sample, whose influence is taken into account by simply substituting their concentration into the electroneutrality equation. Estimates based on self-compensation theory lead to the conclusion that the films must be evaporated at $T_K > 400$ °C to obtain films having a low carrier density. © *1999 American Institute of Physics.* [S1063-7826(99)00601-8]

It is a well-known fact[1] that a thallium impurity in PbSe manifests acceptor properties and produces one hole per impurity atom in the valence band. Self-compensation in equilibrium bulk PbSe:Tl samples has been studied in detail,[2] where it has been shown that the acceptor action of thallium is compensated by solitary, doubly ionized lead donor vacancies. The properties of PbSe:Tl films has been investigated.[3] Film samples differ from the bulk kind primarily in that they are prepared under nonequilibrium conditions. The temperature at which vacuum evaporation is performed is much lower than the homogenizing anneal temperature of bulk samples. The drop in temperature makes it difficult to exhibit the self-compensation effect, because the width of the band gap E_g and the density of states in the bands N_C and N_V decrease. Moreover, bulk diffusion processes are insignificant during the preparation of film samples, and the dominant role is played by diffusion directly onto the growth surface. In Ref. 3 it has been determined from several indirect clues that despite the nonequilibrium growth conditions, the self-compensation effect occurs in PbSe:Tl thin films just as it does in bulk samples. However, a lack of reliable information about the content of the Tl impurity in the PbSe samples made it impossible for the authors of Ref. 3 to carry out a quantitative analysis of the experimental data.

In the present study we have obtained quantitative information about the onset of the self-compensation effect in epitaxial PbSe:Tl films. This information has been acquired by analyzing the dependence of the density of current carriers in the samples on the content of thallium impurity and stoichiometrically excess lead.

We have investigated lead selenide films prepared by vacuum evaporation onto oriented $BaF_2\langle 111\rangle$ substrates by the procedure described in Ref. 4. Two independent sources were used for deposition: a main source containing Tl-doped PbSe and a secondary source containing lead. The molecular vapor streams were mixed directly in the vicinity of the substrate surface. The substrate temperature T_K was 250–400 °C, the temperature of the main source was 700 °C, and the temperature of the secondary lead source T_{Pb} was varied in the range 100–650 °C.

In the first part of the paper we use a procedure described in Ref. 4 to obtain estimates of the concentrations of thallium and electrically active native defects in the PbSe:Tl films. The principal relation used to calculate the corresponding concentrations is the electroneutrality equation, which is written as follows for PbSe:Tl:

$$N_{\mathrm{Tl}}^{-} + 2[V_{\mathrm{Pb}}^{2-}] + n = 2[V_{\mathrm{Se}}^{2+}] + p, \tag{1}$$

where N_{Tl}^{-} is the thallium concentration in the film, $[V_{\mathrm{Pb}}^{2-}]$ and $[V_{\mathrm{Se}}^{2-}]$ are the concentrations of lead and selenium vacancies, and n and p are the densities of electrons and holes, respectively.

In turn, the quantities needed for the calculations have been obtained in experiments to compare the carrier densities in a set of films prepared in identical technological regimes from mixtures with a constant thallium content but different excess lead contents. At sufficiently high doping levels the dependence has at least two characteristic segments for which the carrier density does not depend on the excess lead in the sample. The first corresponds to the part of the region of homogeneity where the relations $N_{\mathrm{Tl}} \gg [V_{\mathrm{Pb}}]$ and $N_{\mathrm{Tl}} \gg [V_{\mathrm{Se}}]$ hold and, accordingly, the electroneutrality condition has the form $N_{\mathrm{Tl}} = p$. The length of this segment increases with the impurity concentration. The second segment, which corresponds to saturation of the carrier density, refers to samples with the limiting excess Pb content (including two-phase samples). Obviously, the impurity concentration is determined from the results of measurements of the

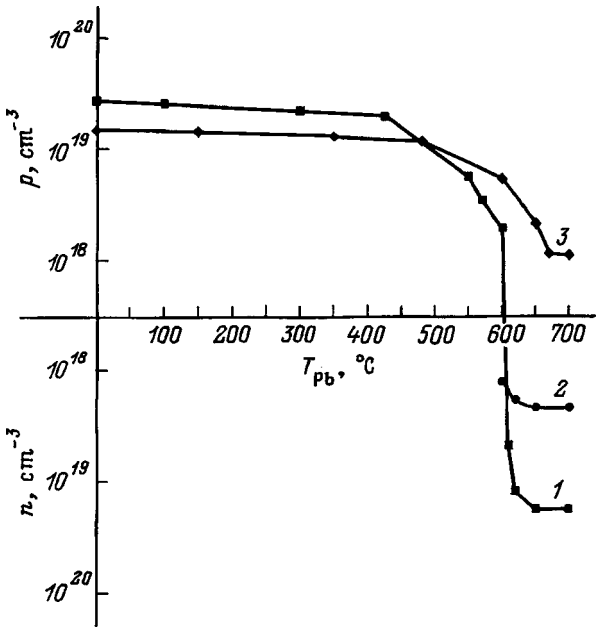

FIG. 1. Density of current carriers in PbSe:Tl:Pb$_{ex}$ versus temperature T_{Pb} of the secondary lead source, $N_{Tl}=0.2$ at. %. Substrate temperature T_K: (*1*) 250 °C; (*2*) 300 °C; (*3*) 350 °C.

carrier density in samples associated with the first interval; the carrier densities in the second segment characterize the self-compensated sample.

The foregoing considerations are illustrated by typical experimental plots, shown in Fig. 1, of the carrier density as a function of the temperature T_{Pb} of the secondary lead source for a set of PbSe:Tl films deposited from a mixture with a 0.2 at. % Tl content. It is evident from the figure that the curves have two constant-density segments: one in the region of low vapor flux densities (at low temperatures T_{Pb}, region I) and the other in the region of high vapor flux densities (high T_{Pb}, region II). In region I the quantity of lead entering the film in the described experiments is much lower than the injected Tl impurity concentration, so that the excess Pb does not influence the carrier density. Also, in this region

$$N_{Tl}^{-} \gg [V_{Se}^{2+}] - [V_{Pb}^{2-}].$$

The quantity $[V_{Se}^{2+}]-[V_{Pb}^{2-}]$ in the experiments on the vacuum evaporation of undoped PbSe films has been estimated as being of the order of $10^{18}\,\mathrm{cm}^{-3}$, i.e., an order of magnitude smaller than the concentration N_{Tl}. This consideration can be used to simplify Eq. (1), which then assumes the form

$$N_{Tl}^{-} = p, \tag{2}$$

i.e., the hole density in segment I is equal to the concentration N_{Tl} in the film.

The saturation level in region I for films prepared from a mixture containing 0.2 at. % thallium is $p=2.8\times10^{19}\,\mathrm{cm}^{-3}$ at a substrate temperature $T_K=250$ °C, $p=2.1\times10^{19}\,\mathrm{cm}^{-3}$ at a substrate temperature $T_K=300$ °C, and $p=1.5\times10^{19}\,\mathrm{cm}^{-3}$ at a substrate temperature $T_K=350$ °C. For a different mixture composition (0.4 at. %Tl) and $T_K=350$ °C we have $N_{Tl}=p=2.8\times10^{19}\,\mathrm{cm}^{-3}$. These data can be used to estimate the transport coefficient of Tl impurity from the mixture into the film for various deposition conditions. The transport coefficient is defined as the ratio of the Tl concentration in the film to its content in the mixture. The calculated mixture-to-film transport coefficients of Tl are 82%, 62%, and 44% at $T_K=250$ °C, 300 °C, and 350 °C, respectively.

We now turn to region II. The interval of saturation in this region characterizes films saturated to the limit with Pb. For films prepared from a mixture with $N_{Tl}=0.2$ at. % the saturation level is $n=1.7\times10^{19}\,\mathrm{cm}^{-3}$ at $T_K=250$ °C, $n=2\times10^{18}\,\mathrm{cm}^{-3}$ at $T_K=300$ °C, and $p=1.1\times10^{19}\,\mathrm{cm}^{-3}$ at $T_K=350$ °C. For films prepared from a mixture with $N_{Tl}=0.4$ at. % the saturation level at $T_K=350$ °C is $p=2\times10^{18}\,\mathrm{cm}^{-3}$.

Using these data, we can calculate the density of defects in the film at various condensation temperatures and thallium impurity contents. For these calculations we use a simplified electroneutrality equation obtained with allowance for the condition $[V_{Se}^{2+}] \gg [V_{Pb}^{2-}]$, which is obvious for the given region and reduces Eq. (1) to the form

$$N_{Tl}^{-} + n = 2[V_{Se}^{2+}] + p. \tag{3}$$

We infer from Eq. (3) that for $N_{Tl}=0.2$ at. % and $T_K=350$ °C the concentration of donor defects is $[V_{Se}^{2+}]=0.67\times10^{19}\,\mathrm{cm}^{-3}$. For $N_{Tl}=0.4$ at. % and $T_K=350$ °C we have $[V_{Se}^{2+}]=1.3\times10^{19}\,\mathrm{cm}^{-3}$. On the other hand, the concentration of native defects, calculated from the phase diagram, is approximately $3\times10^{18}\,\mathrm{cm}^{-3}$ (Ref. 1). These data show that an increase in the thallium concentration in the film increases the concentration of donor defects, which is equivalent to raising the limiting solubility of Pb in a PbSe film by increasing the Tl content. This result is direct evidence of the onset of self-compensation in epitaxial PbSe:Tl:Pb films prepared by vacuum evaporation.

Using the procedure for the determination of N_{Tl} in a film, we attempt to describe qualitatively the characteristic features of self-compensation in PbSe:Tl:Pb films. It follows from the self-compensation theory developed in Ref. 2 that the most complete information about defect-forming processes can be acquired by analyzing the dependence of the carrier density on the thallium content in samples saturated to the limit with lead. Consequently, to investigate the characteristics of self-compensation in PbSe:Tl:Pb films, we have prepared series of such samples with a thallium content in the mixture $N_{Tl}=0-1.8$ at. %. The experiments were carried out at substrate temperatures $T_K=250$ °C and 350 °C. The thallium concentration in the samples was estimated from the Tl concentration in the mixture with allowance for the transport coefficient determined in the preceding sections. We note that precipitations of the second phase (Pb) were observed on the surfaces of all the samples in this series, indicating that the boundary of the region of homogeneity had been approached from the excess-lead side.

The dependence of the carrier density on the thallium content N_{Tl} in samples saturated to the limit with lead at a substrate temperature $T_K=250$ °C is shown in Fig. 2a. It is

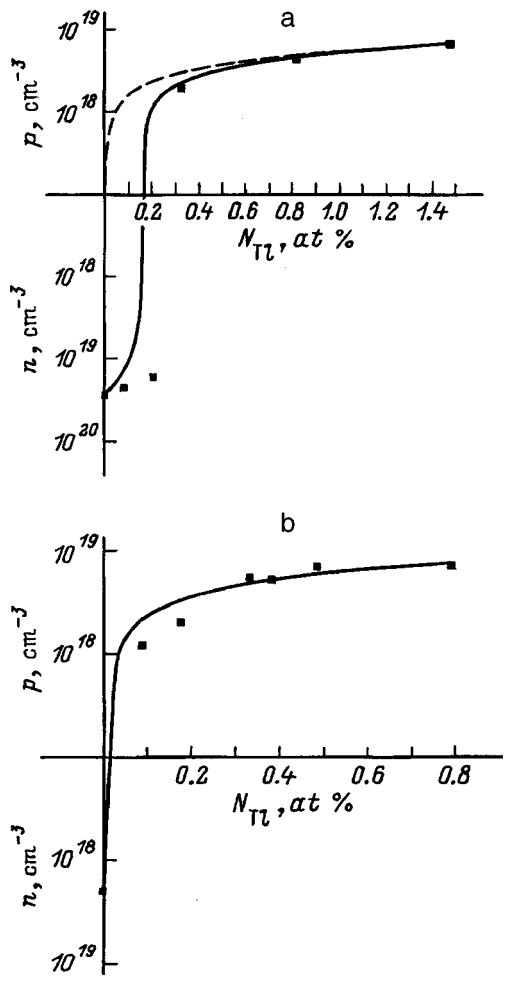

FIG. 2. Carrier density versus thallium concentration N_{Tl} in PbSe:Tl samples saturated to the limit with Pb at different substrate temperatures T_K: (a) 250 °C; (b) 250 °C. The points represent the experimental results, and the curves represent the results obtained by calculations according to the theory in Ref. 2 (dashed curves) and according to the same theory with allowance for additional (nonnative) defects (solid curves).

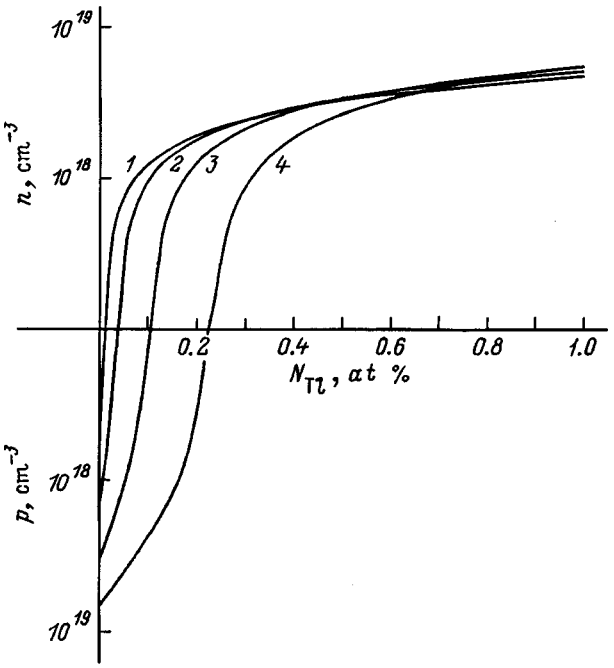

FIG. 3. Calculated curves of the carrier density in PbSe:Tl versus thallium content. Substrate temperature T_K: (*1*) 350 °C; (*2*) 450 °C; (*3*) 550 °C; (*4*) 650 °C.

evident from the figure that the carrier density varies insignificantly in the region of small $N_{\mathrm{Tl}}<0.16$ at. %, electrons are the majority carriers, and their density is of the order of $2.8\times10^{19}\,\mathrm{cm}^{-3}$. When the concentration N_{Tl} in the film is increased above 0.16 at. %, the hole density increases abruptly, and the type of conductivity changes. Now the point of total self-compensation corresponds to $N_{\mathrm{Tl}}\approx0.2$ at. %. The carrier density varies only slightly with a further increase in the thallium concentration. For the given film deposition conditions we have carried out a theoretical calculation using a previously proposed[2] model of self-compensation of the thallium impurity by solitary vacancies. The calculated dependence of the carrier density on the thallium concentration at $T_K=250$ °C is represented by the dashed curve in Fig. 2a. It is evident from the graph that the experimental and theoretical curves are in good agreement for $N_{\mathrm{Tl}}>0.5$ at. %. The main differences in the behavior of the curves is observed at low thallium concentrations. In this range the theoretical calculation predicts that the change in type of conductivity at $T_K=250$ °C takes place at very low thallium concentrations, while for $N_{\mathrm{Tl}}>0.1$ at. % the hole density is large and changes insignificantly. The theory agrees with experiment if we assume that nonequilibrium donor defects are present in the samples, having been formed there as part of the film growth processes. If the nonequilibrium defects are taken into account by simply adding their concentration to the electroneutrality condition

$$N_{\mathrm{Tl}}^{-}+n=p+2[V_{\mathrm{Se}}^{2+}]+N_g\,, \tag{4}$$

where N_g is the concentration of nonequilibrium defects, the experimental and theoretical (dashed curve in Fig. 2a) curves are found to agree, for all practical purposes, over the entire range of N_{Tl}. The concentration of nonequilibrium defects, calculated from the carrier density in undoped lead selenide films saturated to the limit with lead, is equal to $2.8\times10^{19}\,\mathrm{cm}^{-3}$ at a substrate temperature $T_K=250$ °C.

The dependence of the carrier density on N_{Tl} in samples saturated to the limit with lead and prepared at $T_K=350$ °C is shown in Fig. 2b. It is evident from the graph that a sharp increase in the hole density and a change in the type of conductivity are observed as N_{Tl} is increased in the range of low thallium contents. At $N_{\mathrm{Tl}}>0.1$ at. % the hole density increases smoothly as N_{Tl} is increased. We note that all the samples (except the as-grown) exhibit acceptor conductivity and a carrier density of at least $10^{18}\,\mathrm{cm}^{-3}$. A point of total self-compensation has not been observed experimentally in the given series. The concentration of nonequilibrium defects in PbSe:Tl films grown at $T_K=350$ °C is estimated to be $2\times10^{18}\,\mathrm{cm}^{-3}$. Figure 2b also shows the calculated dependence of the carrier density on the thallium content. Clearly, the theoretical and experimental curves are in good agreement for a substrate temperature $T_K=350$ °C. We note that the concentration of nonequilibrium defects decreases considerably as the condensation temperature is raised. For ex-

ample, their concentration at $T_K=250\,°C$ is equal to $2.8\times10^{19}\,cm^{-3}$, and at $T_K=350\,°C$ it is equal to $2\times10^{18}\,cm^{-3}$, i.e., is an order of magnitude lower.

It follows from these data that the experimental curves of the carrier densities as a function of N_{Tl} in epitaxial PbSe:Tl films are satisfactorily described on the basis of the model of impurity self-compensation by solitary vacancies with a simple procedure for taking nonequilibrium defects into account, and the influence of nonequilibrium defects can be disregarded in films prepared at $T_K>350\,°C$. This means that the behavior of $n, p=f(N_{Tl})$ for PbSe:Tl films prepared at $T_K>350\,°C$ can be estimated from the results of calculations using the model of impurity self-compensation by solitary vacancies. The results of such calculations are shown in Fig. 3. An analysis of the curves reveals the following. As T_K is raised, the point of total self-compensation shifts toward higher concentrations N_{Tl}, and the derivative $d(n-p)/dN_{Tl}$ also decreases in the vicinity of this point. We can conclude from this behavior that raising the substrate temperature T_K in the deposition of epitaxial PbSe:Tl films should facilitate the preparation of samples with low carrier densities and improve the reproducibility of the technical results.

In summary, the reported investigations show that the compensation of the doping effects of the thallium impurity in epitaxial PbSe:Tl films is well described by the theory of impurity self-compensation by solitary, doubly ionized vacancies. The discrepancy between theory and experiment at thallium concentrations in the film $N_{Tl}<0.3$ at. % is explained by the presence in the samples of nonequilibrium donor defects associated with growth processes; the influence of these defects is taken into account by simply substituting their concentration into the electroneutrality equation. Estimates based on self-compensation theory lead to the conclusion that the preparation of samples having a low density of current carriers requires evaporation of the films at a substrate temperature $T_K>400\,°C$.

[1] N. Kh. Abrikosov and L. E. Shelimova, *Semiconducting IV–VI compounds* [in Russian] (Nauka, Moscow, 1975).
[2] V. I. Kaĭdanov, Yu. I. Nemov, and Yu. I. Ravich, Fiz. Tekh. Poluprovodn. **28**, 369 (1994) [Semiconductors **28**, 223 (1994)].
[3] T. A. Gavrikova, V. A. Zykov, and S. A. Nemov, Fiz. Tekh. Poluprovodn. **27**, 200 (1993) [Semiconductors **27**, 112 (1993)].
[4] V. A. Zykov, T. A. Gavrikova, S. A. Nemov, and S. A. Rykov, Zh. Prikl. Khim. **71**, 526 (1998).

Translated by James S. Wood

Electronic structure of C_{60} films

V. V. Sobolev and E. L. Busypina

Udmurt State University, 426034 Izhevsk, Russia
(Submitted January 12, 1998; accepted for publication May 28, 1998)
Fiz. Tekh. Poluprovodn. **33**, 31–35 (January 1999)

A complete set of fundamental optical functions of fullerite (C_{60}) films in the range 1.5–7 eV is calculated from the known spectra of the imaginary and real parts of the dielectric permittivity. The total permittivity spectrum is expanded into elementary components. Three main parameters are determined for each component (the energy of the band maximum, the band half-width, and the oscillator strength). An interpretation of these components of the permittivity is proposed on the basis of published theoretical band calculations for fullerite.
 [S1063-7826(99)00701-2]

In recent years there have been many publications on the third (after diamond and graphite) modification of carbon — the giant C_{60} molecule — in the form of a free molecule (fullerene), in solutions, and in the solid state (fullerite) as thin films and small single crystals.[1–5] The absorption spectra of free C_{60} molecules and C_{60} molecules in various solvents as well as the absorption and reflection spectra of fullerite have confirmed that the individuality of the electronic structure of the C_{60} molecule is retained, for the most part, in the crystal.[5–8]

Fullerite C_{60} is the lowest representative of the fullerite C_n group. The properties of fullerites can be modified considerably, including elevation of the superconducting transition temperature to 30 K, by the intercalation of various impurity atoms. It is therefore of fundamental importance to investigate the electronic structure of fullerite over a wide range of intrinsic absorption energies.

The objective of this report is to remedy deficiencies in Refs. 7 and 8, to derive a complete set of optical functions of fullerite in the energy range 1.5–7 eV, and to determine the most complete spectrum of optical transitions and their parameters.

The most accurate spectra of the imaginary part (ε_2) and the real part (ε_1) of the dielectric constant of C_{60} films in the range 1.5–7 eV have been obtained in Ref. 7 from the room-temperature reflection and transmission spectra. The films were deposited on fluorite and fused quartz substrates at a substrate temperature of 393 K. The air-exposed surface of the film changes with time. The spectra of the reflection $R(E)$ from the films through the substrate (Figs. 1 and 2) were therefore used for the calculations of ε_2 and ε_1. We calculate all the remaining optical functions on the basis of the spectra in Ref. 7, using standard equations[9,10] (Fig. 1). The experimental ε_2 spectrum contains maxima at 2.75 eV, 3.55 eV, 4.50 eV, and 5.50 eV, along with a weak band at $\sim$2.05 eV and a step at 2.5 eV. The calculated absorption functions μ (absorption coefficient), k (extinction coefficient), and $E^2\varepsilon_2$ have a similar structure except that the maxima are shifted approximately 0.05 eV toward higher energies, and the absorption coefficient μ is a maximum in the two shortest-wavelength bands. The maxima of the real part of the dielectric consrant ε_1 are situated at 2.4 eV, 3.18 eV, 4.1 eV, and 5.3 eV, i.e., they are shifted approximately 0.3–0.4 eV toward higher energies from the ε_2 maxima. The spectra of the reflection coefficient R and the refractive index n also contain four principal bands; the maxima of n and ε_1 are very close to each other, while the reflection bands are shifted quite far toward higher energies, with the R maxima near the ε_2 maxima. The curve representing the number n_{eff} of valence electrons involved in transitions up to a given energy E closely resemble the ε_2 spectrum, where $n_{\text{eff}} \simeq 0.25$ and 1.5 in the first two long-wavelength transitions ($E < 4$ eV) and $\sim 6-10$ in the next two, strongest transitions ($E \simeq 4.5-5.5$ eV). The maxima of the bulk and surface electron loss characteristics $-\operatorname{Im}\varepsilon^{-1}$ and $-\operatorname{Im}(1+\varepsilon)^{-1}$, situated at $\sim$6.5 eV and 6 eV, are associated with the excitation of π-plasmons[3]; the remaining maxima at 2.8 eV, 3.7 eV, and 4.9 eV and the structures at $\sim$6.1 eV are shifted approximately 0.05–0.5 eV from the ε_2 maxima and are attributable to transitions similar in nature to those identified with the ε_2 maxima.

This complete set of fundamental optical functions of a fullerite C_{60} single crystal in the energy range 1.5–7 eV affords the first graphic evidence of the relationship of their structures and gives them absolute numerical values. It can be used to analyze the spectrum of possible transitions in greater detail and for theoretical calculations of the electronic structure.

Chiu *et al.*[11] have measured the transmission spectrum of a thick (thickness $d = 0.3$ cm) C_{60} single crystal. According to the calculations, allowed direct transitions begin at an energy $E \approx 1.7$ eV (300 K). The experimental data on the absorption spectra of C_{60} thin films in the range 1–6 eV (Ref. 12) are in good agreement with our calculated data on the positions of the maxima of the bands and the values of the absorption coefficient. The spectrum of characteristic electron losses of C_{60} films, obtained with use of high-resolution instrumentation, contains peaks at 2.8 eV, 3.7 eV, and 4.8 eV (Refs. 13 and 14), in good agreement with our calculations. The good agreement between the cited experimental

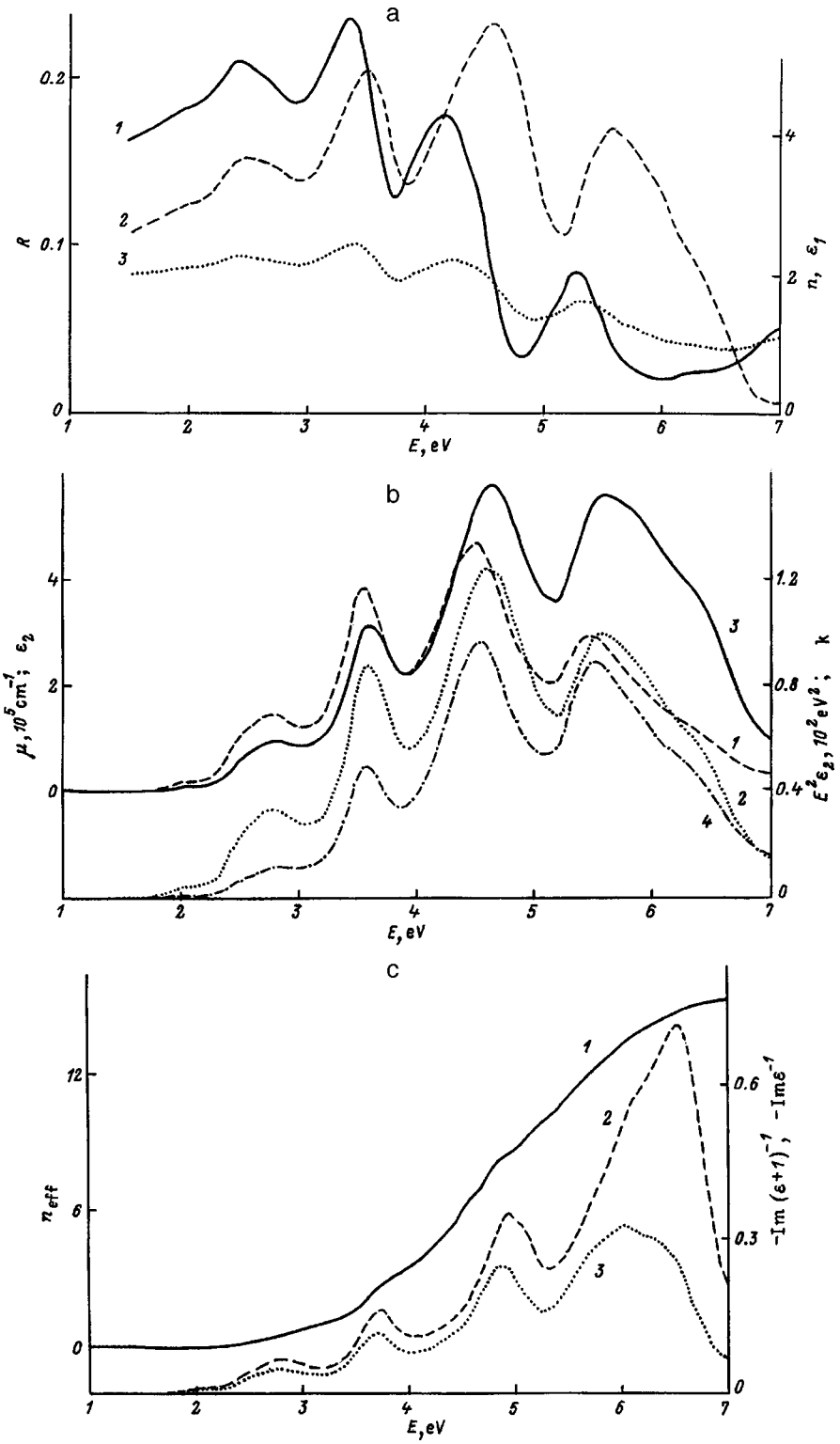

FIG. 1. (a) Experimental ε_1 spectrum (*1*) from Ref. 7 and calculated spectra of R (*2*) and n (*3*). (b) Experimental ε_2 spectrum (*1*) from Ref. 7 and calculated spectra of k (*2*), μ (*3*), and $E^2\varepsilon_2$ (*4*). (c) Calculated spectra of n_{eff} (*1*), $-\text{Im}\,\varepsilon^{-1}$ (*2*), and $-\text{Im}(1+\varepsilon)^{-1}$ (*3*).

data[11–14] and our calculated data for the absorption and characteristic electron loss spectra attest to the reliability of the ε_2 and ε_1 measurements in Ref. 7 and our calculations of the complete set of optical functions for C_{60} films in the range 1.5–7 eV.

We have obtained the following conceptually new information by expanding the total ε_2 curve into components. For this purpose we have relied on the method of Argand diagrams used many times in previous work.[15,10] The spectrum of the total curve is often reconstructed by a set of N symmetric Lorentz oscillators with parameters E_i (energy), H_i (half-width), and f_i (oscillator strength) by fitting $3N$ parameters, despite the obvious ambiguity and excessive number of fitting parameters (e.g., as in Ref. 8, the number of such parameters for ten bands attains 30!). The method of Argand diagrams avoids fitting parameters altogether. Its basic scheme is to treat the spectra of two functions simultaneously: not only the imaginary part of the permittivity, but

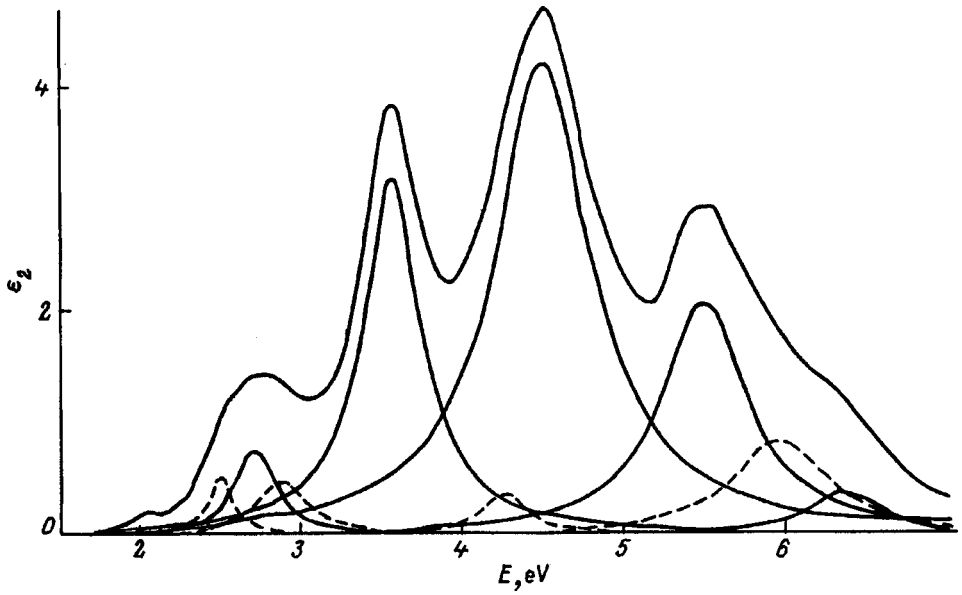

FIG. 2. Total spectrum $\varepsilon_2(E)$ (upper curve) from Ref. 7 and its components for fullerite films.

also its real part. The experimental ε_2 and ε_1 (Ref. 7) are used to expand the ε_2 curve into nine bands (Fig. 2). Naturally, the strongest bands emerge first: E_8 (4.51 eV), E_5 (3.56 eV), and E_9 (5.51 eV), which are clearly structurally observable in the total ε_2 spectrum. Instead of a broad band with a maximum at 2.75 eV and a weak step at $\sim$2.5 eV, we now distinguish the E_2 (2.71 eV) and E_3 (2.89 eV) bands. The E_1, E_7, E_{10}, and E_{11} bands are established in addition to the foregoing. In addition to the energies E_i at which the maxima occur, for all nine of the identified bands we have also determined the half-widths H_i, the oscillator strengths f_i, and the areas of the bands P_i (Table I). To within a constant factor, the band intensities and the oscillator strengths correspond to their areas P_i in the spectrum $\varepsilon_2(E)$. Their absolute values are usually calculated, for simplicity, by averaging over the total number of valence electrons N_v, i.e., dividing by N_v, independently of the transition energy; this case is conveyed through the parameter P_i ($P_i/P_{\max}$). It might be more correct, however, to estimate the oscillator strengths, not in fractions of the total number of valence electrons N_v, but in fractions of only the total number involved in transitions up to a given energy, $n_{\text{eff}}(E)$; the estimates obtained by this method are denoted by f_i in the table.

As a result of these calculations, five more bands, latent in the total ε_2 spectrum, have been established, in addition to the four bands distinctly observed in the total ε_2 curve, and all the parameters of these nine bands (E_i, H_i, f_i, and P_i) have been determined. It should be emphasized that in the conventional approximation where the total dielectric permittivity is represented by the sum of the Lorentz oscillator contributions, the Argand diagram method used by us permits the total ε_2 spectrum to be single-valuedly expanded into a minimal set of bands without any fitting parameters. Transitions that have close energies but are not necessarily similar in nature are summed in each band. They can therefore be further expanded into several components each on the basis of theoretical models postulating the fine structure of the bands.

TABLE I. Energies of the maxima E_i, half-widths H_i, oscillator strengths f_i and S_i, and optical areas $S_i/S_{\max}$ and $P_i/P_{\max}$ of the spectral bands for fullerite C_{60} films.

	E_i, eV		H_i, eV		f_i	$P_i/P_{\max}$	S_i	$S_i/S_{\max}$	
Oscillator (band) No.	Calc.	Ref. 8	Calc.	Ref. 8	Calc.	Ref. 8	Calc.	Ref. 8	Nature of transition
1	(2.5)	(2.41)	0.17	0.05	0.02	0.03	0.002	(0.007)	$h_u \rightarrow t_{1g}$
2	2.75	2.70	0.29	0.30	0.03	0.07	0.174	0.5	$(v_1 \rightarrow c_2)$
3	2.89	(3.2)	0.34	0.20	0.02	0.05	0.015	0.05	$h_g, g_g \rightarrow t_{1u}$
4	⋯	3.49	⋯	0.24	⋯	⋯	0.07	0.2	$(v_2 \rightarrow c_1)$
5	3.55	3.54	0.46	0.30	0.05	0.46	0.33	1	
6	⋯	3.99	⋯	0.13	⋯	⋯	0.01	(0.03)	$h_u \rightarrow h_g$
7	4.26	4.36	0.28	0.47	0	0.04	0.23	0.7	$(v_1 \rightarrow c_3)$
8	4.50	4.54	0.75	0.29	0.06	1	0.27	0.8	
9	5.50	5.50	0.62	0.65	0.03	0.43	0.18	0.55	$h_g, g_g \rightarrow t_{2u}$
10	5.97	5.77	0.69	1.25	0.02	0.19	0.32	0.9	$(v_2 \rightarrow c_2)$
11	6.36	⋯	0.57	⋯	0.01	0.06	⋯	⋯	$g_u, t_{2u} \rightarrow h_g$ $(v_3 \rightarrow c_3)$

Hora *et al.*[8] have recently calculated only the ε_2 spectrum of C_{60} thin films in the range 2.4–6.0 eV using ellipsometric measurements (2–3.4 eV) and reflection spectra (1.4–6.0 eV). The ε_2 spectra in Refs. 7 and 8 exhibit good agreement. The total $\varepsilon_2(E)$ curve in Ref. 8 is reconstructed by means of a set of eleven oscillators with a total of 41 fitting parameters and a formidable general expression for $\varepsilon_2(E)$ in terms of the parameters, including E_i, H_i, and S_i, that govern the band intensities (in the table the E_1, E_3, and E_6 bands are found to be very weak, falling almost within the error limits, and are therefore enclosed in parentheses; the E_1 band lies outside the range of measurement of ε_2, making its identification in Ref. 8 problematic at best). It is interesting to note that the values of E_i for bands 2, 5, 8, and 9, according to our data and the results of Ref. 8, agree to within $\Delta E = 0.01 - 0.03$ eV, whereas for all other bands $\Delta E \approx 0.1 - 0.2$ eV. The half-widths agree for bands 2 and 9 and differ considerably for all other bands. To compare the data on the oscillator strengths f_i in the two papers requires additional reprocessing of the results of Ref. 8 for the parameter S_i. Owing to the closeness of E_i for bands 4 and 5 in Ref. 8 ($\Delta E \simeq 0.05$ eV, they actually need to be joined into a single band 5, and the longest-wavelength band 1 in Ref. 8 is introduced artificially, so that its parameters clearly differ appreciably from our data. Moreover, the reconstruction of the ε_2 curve in the range 2.4–6.0 eV by ten oscillators in Ref. 8 required the artificial introduction of an additional, very strong band in the vicinity of 10 eV, and the authors have attempted to solve the multivalued problem of extrapolating the permittivity spectrum into a broad range of energies where measurements had not been performed [see Eq. (1) in Ref. 8].

The foregoing brief analysis of the characteristic features of the expansion of the ε_2 and ε_1 spectra of fullerite by the method of Argand diagrams and the reconstruction of the ε_2 spectrum using an enormous number of fitting parameters (41!) with the additional use of arbitrary approximations provides a strong case in favor of the first method. The method of Argand diagrams for achieving a parameter-free, single-valued expansion of the spectral curves of ε_2 and ε_1 into elementary components is not yet adequately perfected and serves in effect as a ''zeroth'' approximation to a more sophisticated solution of the problem.

Many papers have been devoted to theoretical calculations of the electronic structure and absorption spectra of C_{60} molecules and crystals.[3,16–21] They are simplified considerably by the unique properties of C_{60} molecules and the known features of their experimental absorption spectra: For the most part the spectra consist of three strong, slightly overlapping bands, whose parameters (E_i, H_i, and f_i) change comparatively little in the order {free molecule $\rightarrow C_{60}$ in solutions $\rightarrow$ crystal}. Consequently, it is assumed at the outset that at least the stronger bands are attributable to small-radius excitons of the Frenkel' type, which are usually typical of molecular crystals.

The uppermost narrow valence band (v_1) of fullerite (total width 0.4 eV) consists of five subbands. Situated below this band, in the intervals 1–2 eV and 2.8–3.8 eV, are a second (v_2) and third (v_3) valence band, which partially exhibit strong dispersion in certain directions of the Brillouin zone. The two lower conduction bands (c_1 and c_2) are also narrow (of width ~ 0.4 eV) and have a triplet structure. Transitions between the bands v_1 and c_1 are forbidden by virtue of their identical odd symmetry; this prohibition is partially lifted by virtue of exciton-phonon and electron-phonon interaction. The longest-wavelength strong transitions are associated with bands v_1 and c_2, which are expected to be followed in rank by transitions of the type $v_2 \rightarrow c_1$, $v_1 \rightarrow c_3$, $v_2 \rightarrow c_2$, and $v_3 \rightarrow c_3$. The last column of Table I presents a conceivable general model of the nature of the absorption and ε_2 bands according to the known results of theoretical calculations in the approximation of molecular terms h_u, h_g, g_u, g_g, t_u and bands. This model provides a satisfactory general explanation for the very complex structure of the established spectrum of transitions in fullerite. A detailed quantitative analysis of the parameters of our established transitions in fullerite will require more sophisticated matching theoretical calculations. On the other hand, the more comprehensive new information that we have obtained here will help to develop substantially more rigorous models of the electronic structure of fullerite and related materials.

The main results of the study are the first-time derivation of a set of fundamental optical functions of fullerite films in the range 1.5–7 eV, the first-time expansion of the total spectrum of the dielectric permittivity into nine transition bands without fitting parameters, and a hypothesis as to the nature of these bands in the Frenkel' exciton model, based on established band calculations.

We are grateful to A. Ya. Vul', V. R. Belosludov, Y. Jwasa, H. Kataura, W. E. Pickett, J. H. Weaver, Y. Wang, T. Tsubo, K. Harigaya, M. Braga, R. Kuzuo, P. A. Thiry, S. Saito, M. K. Kelly, P. Milani, and G. Guizzetti for reprints of articles and surveys.

This work has received support from the Center for Basic Research (St. Petersburg State University).

[1] S. V. Kozyrev and V. V. Rotkin, Fiz. Tekh. Poluprovodn. **27**, 1409 (1993) [Semiconductors **27**, 777 (1993)].
[2] A. V. Eletskiĭ and B. M. Smirnov, Usp. Fiz. Nauk **165**, 977 (1995).
[3] W. E. Pickett, Solid State Phys. **48**, 225 (1994).
[4] T. L. Makarova, J. T. Serenkov, and A. Ya. Vul, Mol. Mater. **7**, 183 (1996).
[5] Y. Iwasa, in *Optical Properties of Low-Dimensional Materials*, edited by T. Ogawa and Y. Kanemitsu (World Scientific Publ., Singapore, 1995), Chap. 7, p. 340.
[6] H. Kataura, N. Jrie, N. Kobayashi, Y. Achiba, K. Kikuchi, and Sh. Yamaguchi, Jpn. J. Appl. Phys. B **32**, L1667 (1993).
[7] H. Kataura, J. Endo, J. Achiba, K. Kikuchi, T. Hanyu, and Sh. Yamaguchi, Jpn. J. Appl. Phys. B **34**, L1467 (1995).
[8] J. Hora, P. Pánek, K. Navrátil, B. Handlířova, J. Humlíček, H. Sitter, and D. Stifter, Phys. Rev. B **54**, 5106 (1996).
[9] V. V. Soboloev and V. V. Nemoshkalenko, *Methods of Computational Physics of the Solid State: Electronic Structure of Semiconductors* (Naukova Dumka, Kiev, 1988).
[10] V. V. Sobolev and V. Val. Sobolev, Fiz. Tverd. Tela (St. Petersburg) **36**, 2560 (1994) [Phys. Solid State **36**, 1393 (1994)].
[11] K.-Ch. Chiu, J.-Sh. Wang, and Ch.-You Lin, J. Appl. Phys. **79**, 1784 (1996).
[12] Y. Wang, J. M. Holden, A. M. Rao, P. S. Eklund, U. D. Venkateswaran *et al.*, Phys. Rev. B **51**, 4547 (1995).
[13] R. Kuzuo, M. Terauchi, M. Tanaka, Y. Saito, and H. Shinohara, Jpn. J. Appl. Phys. A **30**, L1817 (1991).
[14] G. Gensterblum, J. J. Pareaux, P. A. Thiry, R. Caudano, J. P. Vigneron,

Ph. Lambin, A. A. Lucas, and W. Kratschmer, Phys. Rev. Lett. **67**, 2171 (1991).
[15] V. V. Sobolev, *Characteristic Energy Levels of Group IV Solids* [in Russian], Shtiintsa, Kishinev, 1978.
[16] Y.-N. Xu, M.-Z. Huang, and W. Y. Ching, Phys. Rev. B **44**, 1371 (1991).
[17] M. Braga, A. Rosen, and S. Larsson, Z. Phys. D **19**, 435 (1991).
[18] T. Tsubo and K. Nasu, J. Phys. Soc. Jpn. **63**, 2401 (1994).
[19] K. Harigaya and S. Abe, Phys. Rev. B **49**, 16 746 (1994).
[20] A. A. Remova, V. A. Shpakov, U-Hyon Paek, and V. R. Belosludov, Phys. Rev. B **52**, 13 715 (1995).
[21] S. Saito, S. Okada, S. Sawada, and N. Hamada, Phys. Rev. Lett. **75**, 685 (1995).

Translated by James S. Wood

Quasi-gapless semiconductor: *p*-type indium arsenide

M. I. Daunov, I. K. Kamilov, A. B. Magomedov, and A. Sh. Kirakosyan

Institute of Physics, Dagestan Science Center, Russian Academy of Sciences, 367003 Makhachkala, Russia
(Submitted May 5, 1998; accepted for publication June 29, 1998)
Fiz. Tekh. Poluprovodn. **33**, 36–38 (January 1999)

Data on the Hall coefficient R and the resistivity ρ as functions of the magnetic field (to $H=12$ kOe) and electric field (to $E=25$ V/cm) in a heavily doped, compensated semiconductor *p*-type InAs with a density of excess acceptors $N_{\text{ext}}=(N_A-N_D)\simeq 10^{16}\,\text{cm}^{-3}$ and a ratio $N_A/N_D\simeq 0.9$ are used to calculate the characteristic carrier parameters at hydrostatic pressures up to $P=1.5$ Pa and temperatures $T=77.6$ and 300 K. It is found that a deep acceptor band is situated in the tail of the density of states of the conduction band, and a state of the heavily doped, fully compensated semiconductor type is established at low temperatures. © *1999 American Institute of Physics.* [S1063-7826(99)00801-7]

Having analyzed published data on the anomalous kinetic properties of narrow-gap, heavily doped, compensated *p*-type semiconductors $CdSnAs_2\langle Cu\rangle$ (Refs. 1–6), HgCdTe (Ref. 7), InAs with $N_{\text{ext}}<10^{17}\,\text{cm}^{-3}$ (Refs. 8 and 9), and $InSb\langle Cr\rangle$ (Ref. 12), we have come to the conclusion[4–6] that these substances exhibit a common uniformity in their electronic spectra, which is governed, on the one hand, by the presence of a deep acceptor band situated in the tail of the density of states of the conduction band and, on the other, by the influence of a large-scale fluctuating potential. Since the gapless state in these substances is induced by defects, they have come to be known as quasi-gapless semiconductors.[5,6]

In this brief communication we report investigations of certain electrophysical properties of crystals of the heavily doped, compensated semiconductor *p*-InAs with $N_{\text{ext}}\simeq 10^{16}\,\text{cm}^{-3}$ under hydrostatic pressure (Figs. 1–3, Table I).

The experimental procedure, the techniques used to calculate the effective characteristic parameters of the charge carriers — their mobilities μ_c, μ_A, μ_ν and densities n, p_A, p_ν (the subscripts c, A, and ν refer to the conduction, acceptor, and valence bands) — and the model representations pertaining to p-$CdSnAs_2\langle Cu\rangle$ are described in detail in Refs. 1–6. In view of the similarity of the kinetic properties and the common nature of the investigated phenomena in *p*-type $CdSnAs_2\langle Cu\rangle$ and InAs, we discuss them briefly below.

In sample 3 (see Table I) we have $N_{\text{ext}}\simeq N_A$, where N_A is the density of deep-level acceptor centers. The specific nature of the situation and the usefulness of comparing with the data for p-$CdSnAs_2\langle Cu\rangle$ sample 10, which has similar characteristics (see Ref. 5), have prompted us to focus our attention on the kinetic properties of this particular sample.

Known information about the dispersion law and the values of the effective electron mass at the bottom of the conduction band m_c/m_0, the width of the band gap ε_g, and the spin-orbit splitting of the valence bands Δ_s (Refs. 8,9, and 12) are used in the calculations. It has been assumed previously that Δ_s and the effective hole mass with respect to the density of states m_p/m_0 do not depend on the pressure P. The broadening of the deep acceptor level at 300 K has been disregarded.[2] At 300 K, in contrast with $T=77.6$ K, the function $n(P)$ exhibits exponential behavior. It is therefore legitimate to use the ideal-semiconductor dispersion relation for a semiconductor with a fluctuating potential such as the heavily doped, compensated semiconductor *p*-InAs (see Refs. 1, 2, 4, and 5). It follows from the results of a quantitative analysis at 300 K that

$$\begin{aligned} m_c/m_0 &= 0.022+4.34\times 10^{-3}P,\\ \varepsilon_g &= (0.36+9\times 10^{-2}P)\ \text{eV},\\ \varepsilon_A &= (-0.13-9\times 10^{-2}P)\ \text{eV}. \end{aligned} \tag{1}$$

TABLE I. Parameters of the samples.

	Sample No. 3									Sample No. 4		
T, K	P, GPa	R_0, cm^3/C	ρ, $\Omega\cdot\text{cm}$	p_A, $10^{16}\,\text{cm}^{-3}$	μ_A, $\text{cm}^2/(\text{V}\cdot\text{s})$	p_A/n	p_ν/n	μ_c/μ_A	μ_c/μ_ν	P, GPa	R_0, cm^3/C	ρ, $\Omega\cdot\text{cm}$
300	10^{-4}	−4000	1.67	1.84	95.5	$1.4\cdot 10^2$	35.3	88.4	44.0	10^{-4}	−1800	1.53
	1.46	520	3.76	1.84	41.0	$1.4\cdot 10^4$	3500	186	33			
	∞	931	5.81	1.84	10.2	∞	∞	0	0	1.5	135	3.76
77.6	10^{-4}	−3450	9.09	2.26	25.3	915	7	133	18.7	10^{-4}	−3340	4.92
	1.1	−1560	25	2.26	9.03	2570	19.8	179	9.0			
	∞	36000	200	2.26	0	∞	∞		0	1.17	−6432	45.64

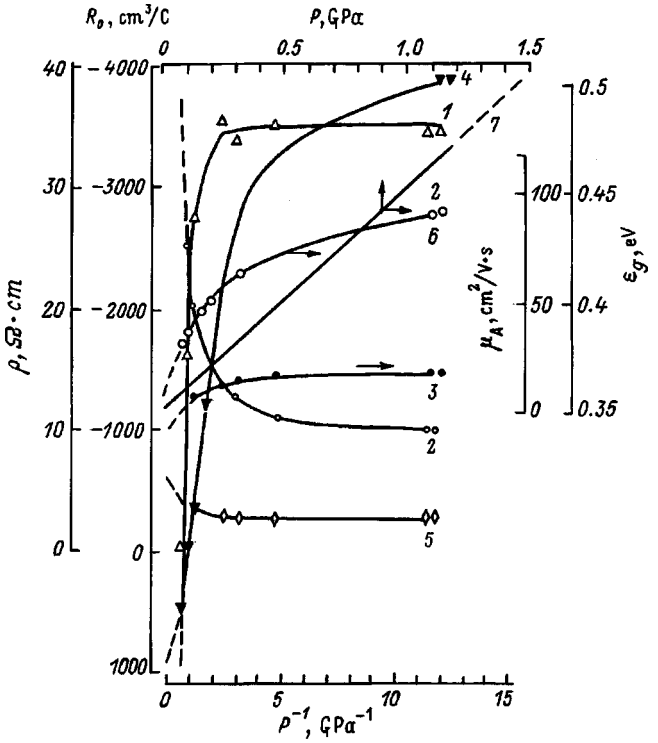

FIG. 1. Dependence of the Hall coefficient in a minimal magnetic field R_0 (*1*, *4*), the resistivityρ (*2*, *5*), the acceptor-band hole mobility μ_A (*3*, *6*), and the width of the band gap ε_g (*7*) at $T=77.6\,K$ (*1–3*) and $T=300\,K$ (*4–7*) on the pressure P in sample 3. The experimental data (point symbols and solid curves) are plotted with the pressure increasing; the dashed curves represent extrapolations.

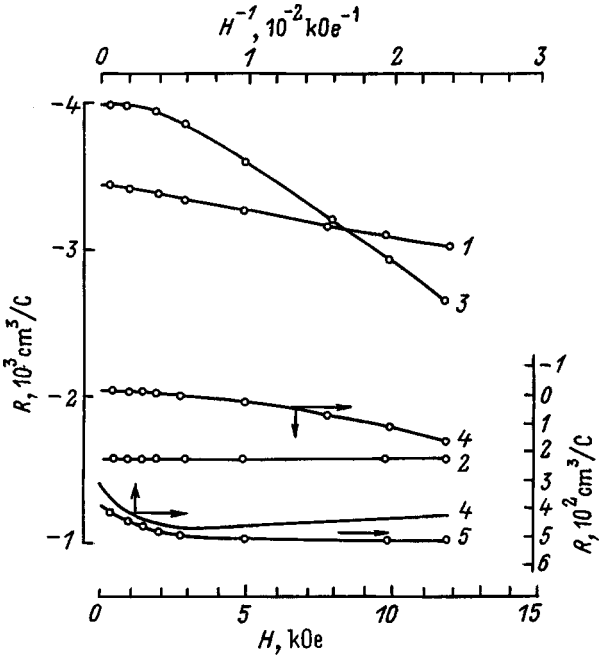

FIG. 2. Experimental (points) and theoretical (curves) magnetic-field dependence of the Hall coefficient R in sample 3 at $T=77.6\,K$ (*1*, *2*) and $T=300\,K$ (*3–5*). Pressure P: (*1*) 0.4 GPa; (*2*) 1.1 GPa; (*3*) 10^{-4} GPa; (*4*) 1.06 GPa; (*5*) 1.4 GPa.

Here the pressure P is expressed in GPa units, and ε_A is the energy of the deep acceptor level (the energy is measured upward from the unperturbed edge of the conduction band).

The relative occupation number of the acceptor band $K_A=(N_A-p_A)/N_A$ decreases from 0.19 to 0 as T decreases from 300 K to 77.6 K, and the Fermi energy varies as

$$\varepsilon_F=(-0.17-9\times10^{-2}P)\ \text{eV}. \tag{2}$$

Together with holes from the valence band, therefore, carriers from the deep acceptor band also take part in the transport processes. The position of the Fermi level is fixed relative to the top of the valence band for hole statistics, because $n\ll p_A, p_\nu$, and the energy interval between the valence and acceptor bands does not depend on the pressure. The resulting values of $d\varepsilon_g/dP$ and $m_p/m_0=0.44$ are consistent with published data.[9,12]

The random oscillations of the potential grow as the temperature is lowered, and below 100 K they attain values of the order of the distance from the unperturbed edge of the conduction band to the Fermi level ''frozen'' in the acceptor band, i.e., a state of the heavily doped, fully compensated semiconductor (HDFCS) type is formed.[4–6] The electron density in this case tends to a finite value in the limit $T\to0$. Moreover, the difference in the dynamics of localization of conduction-band electrons and acceptor-band holes, as observed, for example, in the analogous case in *p*-type $CdSnAs_2\langle Cu\rangle$ (Refs. 1 and 4–6), causes the ratio μ_c/μ_A to increase considerably as the temperature is lowered.

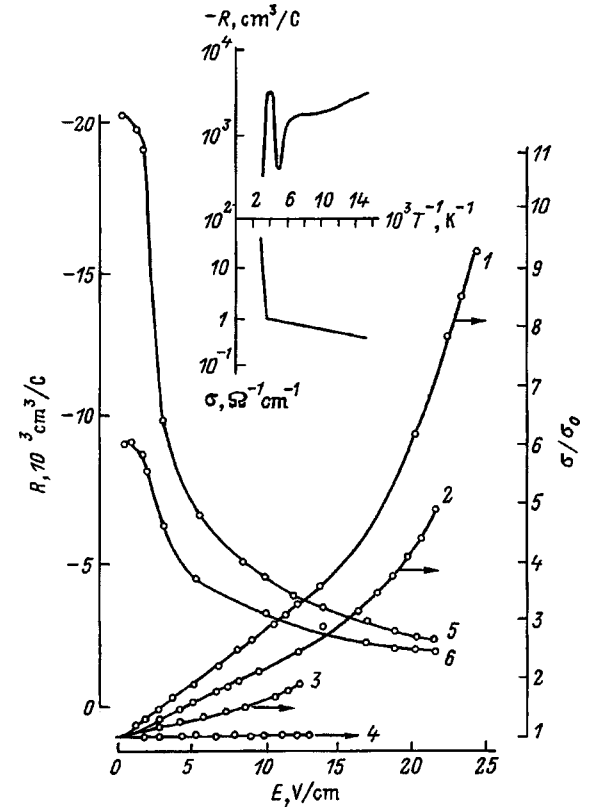

FIG. 3. Electric-field dependence of the electrical conductivity normalized to atmospheric pressure σ/σ_0) (*1–4*) and the Hall coefficient R (*5*, *6*) at $T=77.6\,K$ (*1–3*, *5*, *6*) and $T=300\,K$ (*4*) in sample 4. Pressure P: (*1*, *5*, *6*) 1.05 GPa; (*2*) 0.67 GPa; (*3*) 0.03 GPa; (*4*) 1.42 GPa. Magnetic field H: (*5*) 2 kOe; (*6*) 15 kOe.

For example, the formation of a state of the HDFCS type in a quasi-gapless semiconductor naturally accounts for the negative sign of R and the anomalous behavior of the $R(T)$ curve at low temperatures (Fig. 3).[8,9] We emphasize that the opinion attributing the nature of the anomalous behavior of $R(T)$ and the condition $R<0$ at low temperatures in p-type InAs to the formation of a degenerate n-type surface layer with a bulk density of electrons of the order of $10^{18}\,\mathrm{cm}^{-3}$ (Refs. 7–9) contradicts the pressure curves of the kinetic coefficients (Figs. 1–3). The inversion layer, which is supposed to (according to Ref. 8) envelop the entire surface of the sample, would have to completely shunt its volume, the Hall coefficient could not depend on the pressure, and the resistivity ρ could increase only slightly (not more than 50% at 1 GPa). In closing, we note the timeliness of the proposed model representations in that the influence of the random potential, which is responsible for the formation of a state of the HDFCS type in a quasi-gapless semiconductor is typically ignored in discussions of experimental results.[7,11,13]

The authors are indebted to the Russian Fund for Fundamental Research for support (Project 97-02-16545).

[1] M. I. Daunov, A. B. Magomedov, and V. I. Danilov, Fiz. Tekh. Poluprovodn. **25**, 467 (1991) [Sov. Phys. Semicond. **25**, 282 (1991)].
[2] M. I. Daunov, A. B. Magomedov, and V. I. Danilov, Ukr. Fiz. Zh. **37**, 103 (1992).
[3] M. I. Daunov, K. M. Aliev, and V. I. Danilov, Ukr. Fiz. Zh. **38**, 1811 (1993).
[4] I. K. Kamilov, M. I. Daunov, V. A. Elizarov, and A. B. Magomedov, JETP Lett. **77**, 92 (1993).
[5] M. I. Daunov, I. K. Kamilov, and A. B. Magomedov, JETP Lett. **84**, 309 (1997).
[6] M. I. Daunov, I. K. Kamilov, V. A. Elizarov, A. B. Magomedov, and V. I. Danilov, Dokl. Akad. Nauk **357**, 612 (1997) [Phys. Dokl. **42**, 657 (1997)]; in *Proceedings of the Third All-Russian Conference on the Physics of Semiconductors* [in Russian], Vol. 227 (1997).
[7] I. M. Tsidilkovski, G. I. Harus, and N. G. Shelushinina, Adv. Phys. **34**, 43 (1985).
[8] V. V. Voronkov, E. V. Solov'eva, M. I. Iglitsin, and M. N. Pivovarov, Fiz. Tekh. Poluprovodn. **2**, 1800 (1968) [Sov. Phys. Semicond. **2**, 1499 (1968)].
[9] O. Madelung, *Physics of III-V Compounds* (Wiley, New York, 1964; Mir, Moscow, 1967).
[10] V. V. Popov, M. L. Shubnikov, S. S. Shalyt, and V. V. Kosarev, Fiz. Tekh. Poluprovodn. **11**, 1914 (1977) [Sov. Phys. Semicond. **11**, 1120 (1977)].
[11] V. V. Kosarev, R. R. Parfen'ev, V. V. Popov, and S. S. Shalyt, Fiz. Tverd. Tela (Leningrad) **18**, 489 (1976) [Sov. Phys. Solid State **18**, 282 (1976)].
[12] A. Plitkas, A. Krokus, L. A. Balagurov, and É. M. Omel'yanovskiĭ, Fiz. Tekh. Poluprovodn. **14**, 2123 (1980) [Sov. Phys. Semicond. **14**, 1262 (1980)].
[13] S. G. Gasan-zade, E. A. Sal'kov, and G. A. Shepel'skiĭ, Fiz. Tekh. Poluprovodn. **31**, 35 (1997) [Semiconductors **31**, 29 (1997)].

Translated by James S. Wood

Optical absorption in $PbGa_2Se_4$ single crystals

B. G. Tagiev, N. N. Musaeva, and R. B. Dzhabbarov

Institute of Physics, Academy of Sciences of Azerbaidzhan, 370143 Baku, Azerbaidzhan
(Submitted October 7, 1997; accepted for publication July 1, 1998)
Fiz. Tekh. Poluprovodn. **33**, 39–41 (January 1999)

Optical measurements are performed in a $PbGa_2Se_4$ single crystal. The nature of the optical transitions is determined in the interval of photon energies 2.24–2.46 eV in the temperature range 77–300 K. It is shown that indirect and direct optical transitions take place in the energy intervals 2.28–2.35 eV and 2.35–2.46 eV, corresponding to $E_{gi}=2.228$ eV and $E_{gd}=2.35$ eV, respectively, at 300 K. The temperature coefficients of E_{gi} and E_{gd} are equal to -0.6×10^{-4} eV/K and -4.75×10^{-4} eV/K, respectively.
[S1063-7826(99)00901-1]

INTRODUCTION

The compound $PbGa_2Se_4$ was first synthesized by Eholie et al.[1,2], who confirmed that this semiconductor has an orthorhombic lattice with parameters $a=10.64$ Å, $b=10.94$ Å, $c=6.36$ Å and space group *Bbmm*. This compound ($PbGa_2Se_4$) is photosensitive in the region $0.4-1.4\ \mu$m with a multiplicity of 10^3-10^4 and is a high-resistance semiconductor with a resistivity of approximately $10^{11}\ \Omega\cdot$cm at 300 K.

To ascertain the mechanisms underlying the electronic effects in $PbGa_2Se_4$ single crystals, it is necessary to investigate the electrical and optical properties over a wide range of temperatures and photon energies. To the best of our knowledge, the optical properties of $PbGa_2Se_4$ have not been studied. In this paper we give the results of experimental studies of the optical absorption α in $PbGa_2Se_4$ single crystals.

1. GROWTH OF $PbGa_2Se_4$ SINGLE CRYSTALS

The compound $PbGa_2Se_4$ was synthesized by melting the components together in stoichiometric ratios in evacuated (10^{-5} Torr) quartz cells. Single crystals of $PbGa_2Se_4$ with dimensions $1\times1\times2$ cm were grown by the Bridgman–Stockbarger method. The compound has a layered chain structure. Its color varies from yellowish orange to deep red, depending on the thickness.

2. MEASUREMENT PROCEDURE

The spectral curves $\alpha(h\nu)$ of the $PbGa_2Se_4$ single-crystal samples were measured in the temperature range 77–300 K and photon energies 2.24–2.46 eV. The main component of the instrumentation used for the measurements was an MDR-12 monochromator. Various single-crystal samples having thicknesses of $35-200\ \mu$m were investigated.

3. RESULTS OF THE EXPERIMENTAL STUDIES AND DISCUSSION

The results of the measurements of $\alpha(h\nu)$ for a sample of thickness 35 μm at eight different temperatures are shown in Fig. 1. Similar results have been obtained for the other five samples. It is evident from the figure that the $\alpha(h\nu)$ curves shift toward shorter wavelengths as the temperature is lowered from 300 K to 86 K. In the interval of photon energies 2.24–2.46 eV the absorption coefficient $\alpha(h\nu)$ varies from 1000 cm^{-1} to 2500 cm^{-1}. The $\alpha(h\nu)$ curve is divided into three sections: 1) In the interval of photon energies 2.24–2.28 eV α is almost independent of $h\nu$ or increases relatively little; 2) α increases significantly in the interval 2.28–2.35 eV; 3) α rises sharply in the interval of photon energies 2.35–2.46 eV.

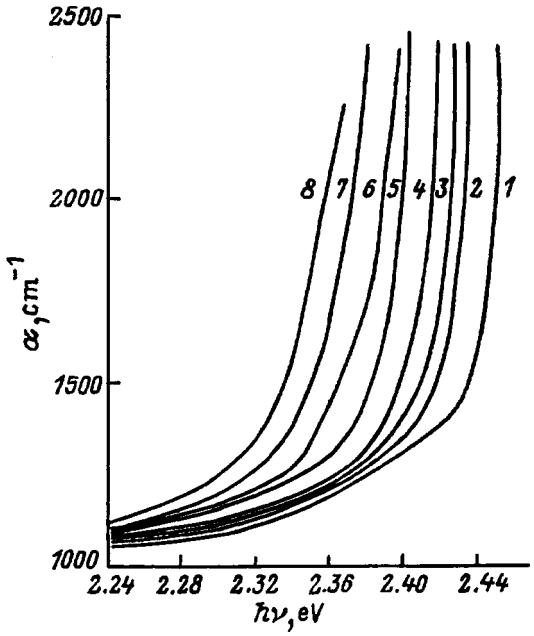

FIG. 1. Spectral curves of the optical absorption coefficient in a $PbGa_2Se_4$ single crystal at various temperatures: (*1*) $T=86$ K; (*2*) 112 K; (*3*) 134 K; (*4*) 157 K; (*5*) 214 K; (*6*) 258 K; (*7*) 271 K; (*8*) 294 K.

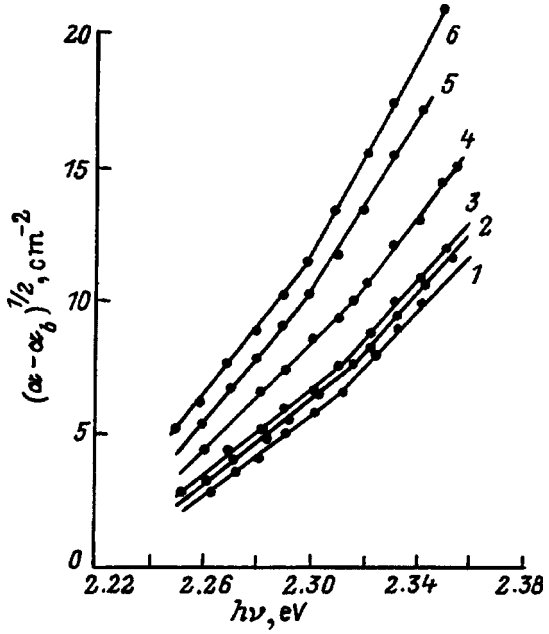

FIG. 2. Graphs of $(\alpha-\alpha_b)^{1/2}\sim h\nu$ at various temperatures: (*1*) $T=86$ K; (*2*) 112 K; (*3*) 134 K; (*4*) 157 K; (*5*) 214 K; (*6*) 258 K; (*7*) 271 K; (*8*) 294 K.

We analyze these results in accordance with the theory of indirect and direct optical transitions.[3–6] The coefficient $\alpha(h\nu)$ can be written in the form

$$\alpha=\alpha_i+\alpha_d+\alpha_b\,, \tag{1}$$

where $\alpha_i\,,\alpha_d\,,$ and α_b are the optical absorption coefficients in indirect and direct transitions and in phonon absorption, respectively. Here phonon absorption is interpreted to mean absorption due to defects, scattering, etc.[3–6]

In analyzing the function $\alpha(h\nu)$, we extrapolate its component α_b, which is independent or only slightly dependent on the photon energy, to higher photon energies and subtract it from the total absorption, i.e., we work with $\alpha-\alpha_b$. Bearing in mind that the dependences of $(\alpha-\alpha_b)^{1/2}$ and $[(\alpha-\alpha_b)^{1/2}h\nu]$ on $h\nu$ are almost identical, we display the experimental data in coordinates $(\alpha-\alpha_b)^{1/2}\sim h\nu$ (Fig. 2). Two linear segments with different slopes are discerned for each curve; the slopes of these segments decrease with decreasing temperature. These segments are attributable to the absorption and emission of phonons, and in this case the optical absorption is given by the equation

$$\alpha(h\nu)=A\left(\frac{(h\nu-E_{gi}+k)^2}{e^{\theta/T}-1}+\frac{(h\nu-E_{gi}-k)^2}{1-e^{\theta/T}}\right), \tag{2}$$

TABLE I.

T, K	E_{gi}, eV	K_e, cm$^{-1/2}$eV^{-1}	K_a, cm$^{-1/2}$eV^{-1}	θ, K	k, eV
86	2.235	105	70	69	0.0060
112	2.234	110	75	86	0.0074
134	2.233	110	80	86	0.0073
157	2.233	110	80	100	0.0086
214	2.231	145	100	159	0.0136
271	2.229	160	125	133	0.0115
294	2.228	185	159	123	0.0105

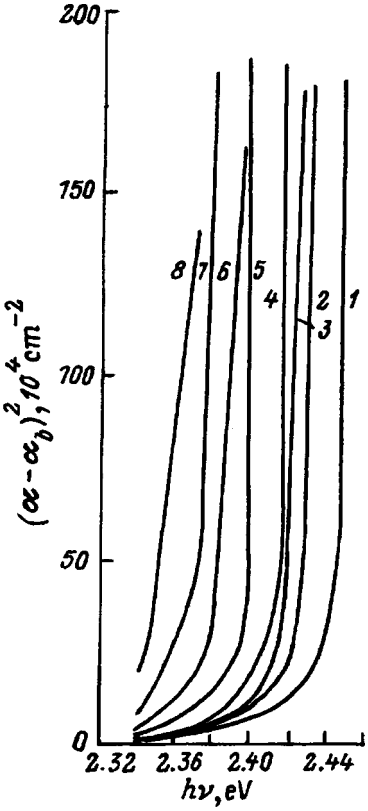

FIG. 3. Graphs of $(\alpha-\alpha_b)^2\sim h\nu$ at various temperatures: (*1*) $T=86$ K; (*2*) 112 K; (*3*) 134 K; (*4*) 157 K; (*5*) 214 K; (*6*) 258 K; (*7*) 271 K; (*8*) 294 K.

where E_{gi} is the width of the band gap in indirect transitions, k is the phonon energy, θ is a characteristic temperature, T is the absolute temperature, and A is a constant which is nearly independent of $h\nu$ and T. If we bear in mind that the first term is associated with phonon absorption (α_a) and the sec-

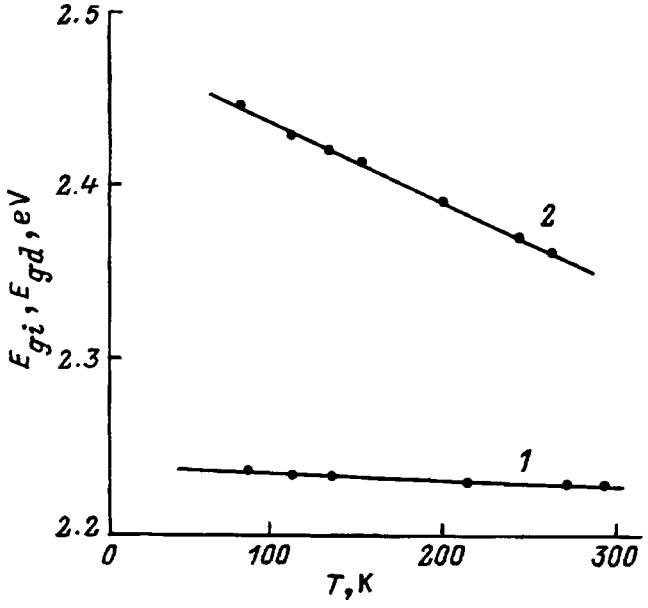

FIG. 4. Temperature dependence of the width of the band gap for direct and indirect transitions: (*1*) E_{gd}; (*2*) E_{gi},

ond term is associated with phonon emission (α_e), the slopes of the lines $\alpha_a^{1/2}=f(h\nu)$ and $\alpha_e^{1/2}=f(h\nu)$ can be determined from the expressions

$$K_a=\left(\frac{A}{e^{\theta/T}-1}\right)^{1/2}, \quad K_e=\left(\frac{A}{1-e^{\theta/T}}\right)^{1/2}. \tag{3}$$

From Eqs. (3) we readily deduce the expression

$$\frac{K_e^2}{K_a^2}=\exp\frac{\theta}{T}. \tag{4}$$

These equations can be used in conjunction with the experimental data at various temperatures to determine E_{gi}, θ, and k, which are given in Table I.

The absorption coefficient rises abruptly at higher energies ($h\nu \geqslant 2.35$ eV). To determine the nature of the optical transitions in a $PbGa_2Se_4$ single crystal, we analyze this interval of photon energies in accordance with Ref. 7. It has been established that the experimental values of the absorption coefficient provide a good fit to a straight line in the coordinates $(\alpha-\alpha_b)^2 \sim f(h\nu)$ (Fig. 3). The linear dependence of $(\alpha-\alpha_b)^2$ on $h\nu$ indicates that the intrinsic absorption edge in $PbGa_2Se_4$ single crystals is formed by direct allowed optical transitions. At different temperatures the width of the band gap is determined by extrapolating the lines $(\alpha-\alpha_b)^2=f(h\nu)$ to the value $(\alpha-\alpha_b)=0$ (Fig. 4).

The temperature dependences of E_{gi} and E_{gd} are shown in Fig. 4, from which we obtain the following values for the temperature coefficients of these quantities: -0.6×10^{-4} eV/K and -4.75×10^{-4} eV/K, respectively.

[1] R. Eholie, I. K. Kom, and J. Flahaut, C.R. Acad. Sci. Ser. C **268**, 700 (1969).
[2] R. Eholie, O. Gorochov, M. Guittard, A. Mazurier, and J. Flahaut, Bull. Soc. Chim. Fr., 747 (1971).
[3] C. Jullien, M. Eddrief, K. Kambas, and M. Balkanski, Thin Solid Films **137**, 27 (1986).
[4] E. Cuerrero, M. Quintero, and J. C. Wolley, J. Phys.: Condens. Matter **2**, 6119 (1990).
[5] A. M. Elkorashy, Phys. Status Solidi B **135**, 707 (1986).
[6] S. Saha, U. Pal *et al.*, Phys. Status Solidi A **114**, 721 (1989).
[7] J. I. Pankove, *Optical Processes in Semiconductors* (Prentice-Hall, Englewood Cliffs, N.J., 1971; Mir, Moscow, 1973).

Translated by James S. Wood

Characteristic features of the temperature dependence of the photoluminescence polarization of {Ga vacancy}–$Sn_{Ga}(Si_{Ga})$ complexes in GaAs produced as a result of resonant polarized excitation

A. A. Gutkin, M. A. Reshchikov, and V. E. Sedov

A. F. Ioffe Physicotechnical Institute, Russian Academy of Sciences, 194021 St. Petersburg, Russia
(Submitted June 29, 1998; accepted for publication July 2, 1998)
Fiz. Tekh. Poluprovodn. **33**, 42–46 (January 1999)

The excitation and induced polarization spectra of the photoluminescence band with the maximum near a photon energy of 1.18 eV in Sn- or Si-doped *n*-GaAs with an electron density $\sim 10^{18}\,\mathrm{cm}^{-3}$ are measured at various temperatures. It is shown that the temperature dependence of the induced polarization of this photoluminescence due to $V_{Ga}Sn_{Ga}$ or $V_{Ga}Si_{Ga}$ complexes in the temperature range 77–230 K is close to the corresponding dependence for $V_{Ga}Te_{As}$ complexes. In addition, a slight decrease in the induced polarization as the temperature is increased, not observed for $V_{Ga}Te_{As}$ complexes, is observed in the range 77–125 K for the investigated complexes. It is hypothesized that the difference is attributable to the existence of excited configurations in the absorbing and emitting states of the $V_{Ga}Sn_{Ga}$ and $V_{Ga}Si_{Ga}$ complexes, where the populations of these configurations in the absorbing state increase with the temperature. The difference between the total energies of the excited and ground configurations of the absorbing state is 10–20 meV for $V_{Ga}Sn_{Ga}$ complexes and 15–30 meV for $V_{Ga}Si_{Ga}$ complexes. © *1999 American Institute of Physics.* [S1063-7826(99)01001-7]

1. INTRODUCTION

The broad photoluminescence band with a maximum near a photon energy of 1.18 eV in *n*-type GaAs is associated with complexes consisting of a Ga vacancy plus a donor and is induced by the recombination of holes trapped by these complexes with electrons from the conduction band or from localized states near its bottom.[1–4] Several characteristics of this photoluminescence in *n*-GaAs doped with various donors (Te, Sn, or Si) are qualitatively identical and quantitatively differ very little.[1–5]

An exception is the dependence of the polarization of low-temperature photoluminescence on the uniaxial pressure (P) along the crystallographic [111] or [110] direction. For $V_{Ga}Sn_{Ga}$ and $V_{Ga}Si_{Ga}$ at liquid-helium temperatures the curves representing this dependence contain a stepped increase in the linear polarization of the photoluminescence for $P \simeq 4-6$ kbar (Refs. 5 and 6), whereas for $V_{Ga}Te_{As}$ a similar variation of the polarization is observed for $P \approx 0$ (Ref. 7). Such a disparity in the behavior of the radiation polarization of the indicated complexes is attributable to a difference in the position of the donor relative to the vacancy in the $V_{Ga}Te_{As}$ and $V_{Ga}Sn_{Ga}$ ($V_{Ga}Si_{Ga}$) complexes. Because of this difference, the three Jahn-Teller equivalent monoclinic configurations of the $V_{Ga}Te_{As}$ complex with a symmetry plane passing through the initial trigonal axis of $V_{Ga}Te_{As}$ is replaced in the $V_{Ga}Sn_{Ga}$ and $V_{Ga}Si_{Ga}$ complexes by a single monoclinic and two triclinic configurations and have different total energies.[5,8] However, the difference in the energies of these configurations is not too great. When uniaxial pressure is applied to the crystal, the axes of the optical dipoles of the higher-energy configurations in certain groups of such complexes with their components in a definite arrangement are closer to the pressure axis than the dipole axis of the ground configuration. In these groups of complexes the difference between the energies of the ground and excited configurations decreases as the pressure P is raised, and when the latter exceeds a certain threshold P_{cr}, whichever configuration had the higher energy for $P=0$ becomes the ground configuration. At low temperatures this behavior stimulates a transition of these groups of complexes into a new configuration (alignment of distortions) and an abrupt change in the radiation polarization of the entire set of complexes in the crystal. In $V_{Ga}Te_{As}$ complexes all three configurations have the same energy for $P=0$, so that the alignment of distortions and the stepped variation of the radiation polarization at low temperatures take place as soon as P becomes greater than zero.

It is important to note that the above-described processes involving transitions between configurations occur in the absorbing state, i.e., the state preceding hole localization at a defect, where the hole subsequently undergoes radiative recombination with an electron. In the emitting state formed after hole capture or after the optical excitation of an electron from the complex into the conduction band, the configuration of the complex is preserved,[9,10] i.e., excited configurations also exist in the emitting state. It is reasonable to expect that the occupation of excited configurations of the absorbing state of $V_{Ga}Sn_{Ga}$ and $V_{Ga}Si_{Ga}$ complexes should also be possible at elevated temperatures and, if their parameters differ appreciably from those of the ground configuration, they should be observed in various phenomena. The observation of such effects could serve as subsequent confirmation of the above-described model of complexes containing a donor in the second coordination sphere of a vacancy and could be

used to acquire information about the properties of their excited configurations. With this objective in mind, we have investigated the temperature curves of the polarization of the photoluminescence of $V_{Ga}Sn_{Ga}$ and $V_{Ga}Si_{Ga}$ complexes excited in resonance by linearly polarized light.

2. DESCRIPTION OF THE EXPERIMENT AND ITS RESULTS

The *n*-type GaAs samples investigated in the present study had an electron density $\sim 10^{18}\,cm^{-3}$ and were cut from an *n*-GaAs:Sn crystal doped during growth by the Czochralski method and from an *n*-GaAs:Si crystal prepared by oriented crystallization. The broad photoluminescence band induced by $V_{Ga}Sn_{Ga}$ and $V_{Ga}Si_{Ga}$ complexes with a maximum at a photon energy ~ 1.18 eV is dominant in such samples in the temperature range 2–200 K when photoluminescence is excited by light in the intrinsic absorption band.

The procedure for the investigation of this band is similar to that used in previous studies.[5,8,10] Its excitation spectra at various temperatures T are shown in Fig. 1. Their behavior with increasing temperature is characterized by a shift into the long-wavelength part of the spectrum and broadening of the long-wavelength edge of the band. It scarcely differs from the behavior of the corresponding spectra of $V_{Ga}Te_{As}$ complexes.[10]

We have measured the photoluminescence polarization resulting from resonance excitation of the complexes by polarized light with a photon energy less than the width of the band gap in an orthogonal scheme where the photoluminescence-exciting light beam propagates along the crystallographic [110] axis, and we have observed photoluminescence in the [001] direction. The electric vector of the emitting light was parallel to the [110] axis. In this experimental geometry the induced polarization of the vacancy-donor complexes in *n*-GaAs at low temperatures is high,[5,8] a fact that can be exploited to determine its slight temperature variations. The degree of induced polarization ρ were measured for radiation in a band of width ~ 50 meV around the photoluminescence maximum induced by the investigated complexes. The distribution of ρ along the excitation spectrum at various temperatures is shown in Fig. 2. If the temperatures are moderately high, saturation is observed in the ρ spectra for emitting light having low photon energies ($\hbar\omega_{ex}$), but then ρ decreases as $\hbar\omega_{ex}$ is increased (Fig. 2). As in the case of $V_{Ga}Te_{As}$ complexes,[10] the polarization ρ at saturation ρ_s can be assumed to correspond to the situation where free holes vulnerable to capture by the complexes are not generated by the emitting light. The temperature dependence of ρ_s in the high-temperature range is shown in Fig. 3. The sharp drop of ρ_s in the high-temperature range resembles the same drop observed for $V_{Ga}Te_{As}$ complexes[10] and is attributable to the thermal emission of holes formed at the complexes when electrons are optically excited in the conduction band and to the subsequent equiprobable recapture of some of these holes by complexes with any orientation of the distortions.[10] This process must be accompanied by a drastic reduction in the photoluminescence intensity of the complexes and an increase in the edge photoluminescence intensity,[10] as has indeed been observed for the investigated samples in the corresponding temperature range. Since the ratio of the intensities of edge photoluminescence to photoluminescence of the complexes are the same in order of magnitude for $V_{Ga}Sn_{Ga}$, $V_{Ga}Si_{Ga}$, and $V_{Ga}Te_{As}$ in samples having the same electron density during the excitation of photoluminescence by interband optical transitions, we can assume that the lifetimes of the emitting state of the complexes are similar. Accordingly, as in the case of $V_{Ga}Te_{As}$ complexes,[10] the fact that a sharp drop in the degree of induced polarization of the photoluminescence of the $V_{Ga}Sn_{Ga}$ and $V_{Ga}Si_{Ga}$ complexes occurs only in the region of thermal emission of holes for complexes in the valence band (activation energy ~ 0.18 eV) implies that the barriers between different configurations of the emitting state of $V_{Ga}Sn_{Ga}$ and $V_{Ga}Si_{Ga}$ are not lower than ~ 0.2 eV.

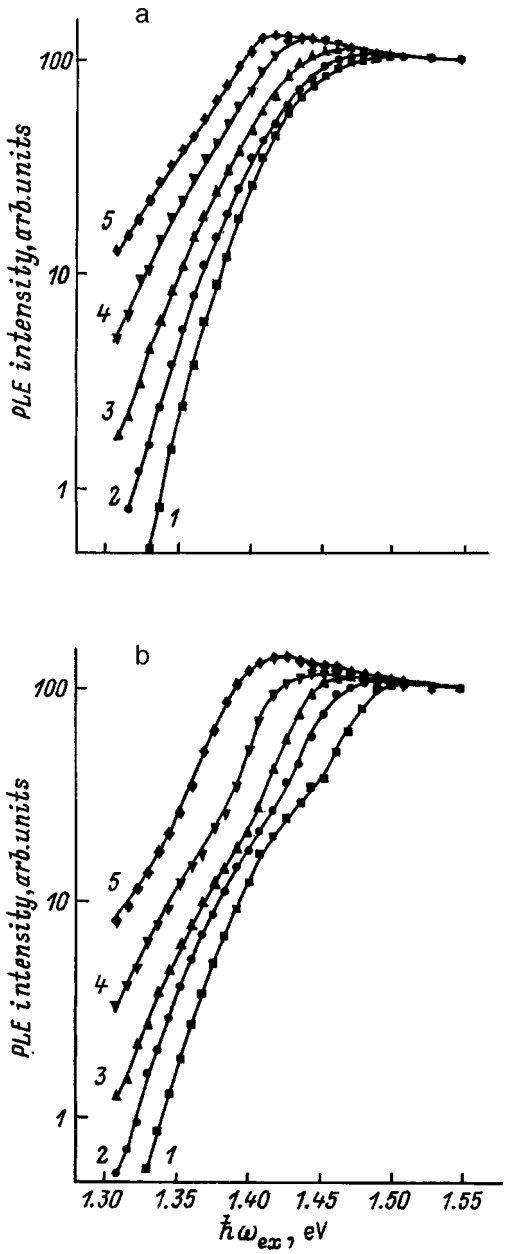

FIG. 1. Photoluminescence excitation spectra of $V_{Ga}Sn_{Ga}$ (a) and $V_{Ga}Si_{Ga}$ (b) complexes. Temperature: (*1*) 78 K; (*2*) 120 K; (*3*) 160 K; (*4*) 200 K; (*5*) 240 K.

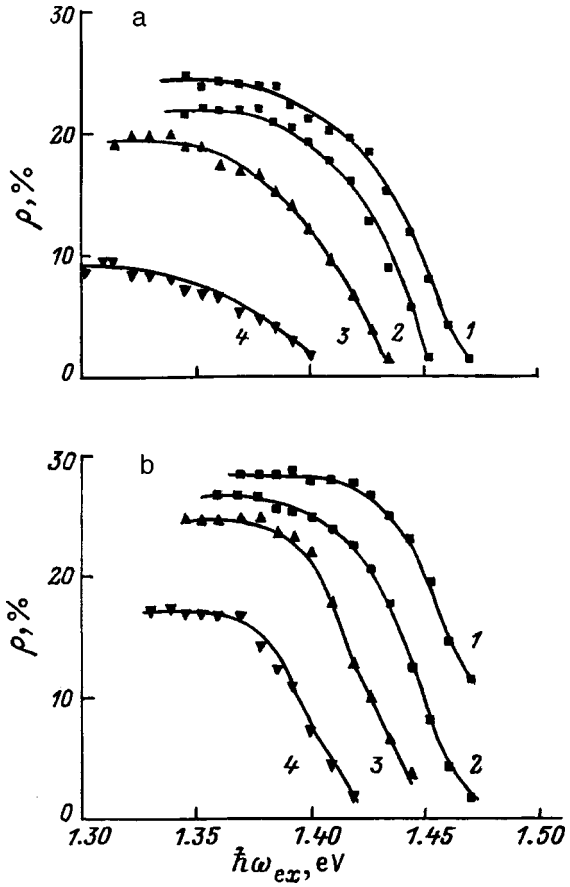

FIG. 2. Distribution of the induced polarization of $V_{Ga}Sn_{Ga}$ (a) and $V_{Ga}Si_{Ga}$ (b) complexes along the excitation spectrum. Temperature: (*1*) 78 K; (*2*) 120 K; (*3*) 160 K; (*4*) 200 K.

In addition to the sharp drop in ρ_s at high temperatures, a slight decrease in ρ_s as T increases is also observed for the $V_{Ga}Sn_{Ga}$ and $V_{Ga}Si_{Ga}$ complexes at medium temperatures (77–120 K); this behavior is nonexistent for $V_{Ga}Te_{As}$ complexes (Fig. 3). As mentioned in the introduction, the difference can be attributed to the existence in the $V_{Ga}Sn_{Ga}$ and $V_{Ga}Si_{Ga}$ complexes of excited configurations of the absorbing state whose energies do not differ too much from the energy of the basic configuration.

3. ANALYSIS OF THE TEMPERATURE DEPENDENCE OF THE DEGREE OF POLARIZATION IN THE TEMPERATURE RANGE UP TO 120 K

To describe the role of excited configurations in the temperature dependence of the induced photoluminescence polarization of the complexes, we consider a model in which the $V_{Ga}Sn_{Ga}$ or $V_{Ga}Si_{Ga}$ complex has one ground configuration, whose symmetry is monoclinic.[8] In this case each complex contains two equivalent excited configurations of triclinic symmetry,[3,8] in which the directions of the optical dipoles are symmetric about a (110) plane containing, in their initial positions, the Ga sublattice sites occupied by V_{Ga} and a donor.[8] This model is thought to be more natural than a previously discussed (see, e.g., Refs. 5 and 6) model in which two triclinic configurations have ground status, and a monoclinic configuration is excited. Since a complex-localized hole is closer to the donor in triclinic configurations than in the ground configuration, the influence of the donor on vacancy-like hole orbitals will be stronger. This fact causes the direction of the optical dipole of the complex to deviate much farther from the [111] axis, which corresponds to the dipole direction of the isolated vacancy subjected to the Jahn–Teller effect, than the same sort of deviation in the ground configuration. As a result, the degree of radiation polarization of the set of complexes present in excited configurations (ρ_2) is smaller than the degree of radiation polarization of the set of complexes in the ground configuration (ρ_1). Because of the relatively low energy of the excited configurations and the large width of the excitation and photoluminescence bands, the complexes situated in these configurations transfer to the emitting state with the absorption of photons of the same energy as complexes situated in the ground configuration, and the recorded part of the photoluminescence band contains radiation from defects situated in

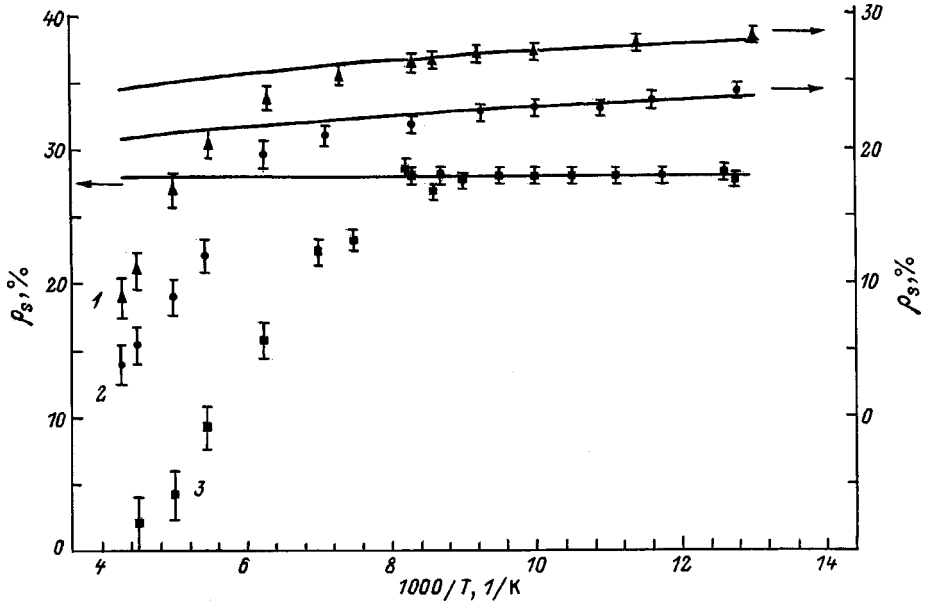

FIG. 3. Temperature dependence of ρ_s for $V_{Ga}Si_{Ga}$ (*1*), $V_{Ga}Sn_{Ga}$ (*2*), and $V_{Ga}Te_{As}$ (*3*) complexes, experimental (points) and calculated from Eq. (1) for the following values of the parameters: (*1*) $\rho_1=29\%$, $\rho_2=0$, $\Delta W_0=16$ meV, $\gamma=0.2$; (*2*) $\rho_1=26\%$, $\rho_2=0$, $\Delta W_0=10$ meV, $\gamma=0.2$; (*3*) $\rho_1=28\%$, $\rho_2=28\%$, $\Delta W_0=0$ meV, $\gamma=1$.

both configurations. Under these conditions the increase in the populations of the excited configurations of the absorbing state with no change in the configuration after excitation should lower the degree of polarization of the total radiation ρ_s measured in the experiments.

Assuming that a Boltzmann distribution of defects in the absorbing state among the various configurations is maintained under the experimental conditions, we readily infer that the degree of polarization of the observed radiation is related to the defect parameters by the equation

$$\rho_s=\frac{\rho_1+2\rho_2\gamma\exp(-\Delta W_0/kT)}{1+2\gamma\exp(-\Delta W_0/kT)}, \tag{1}$$

where ΔW_0 is the difference between the energies of the excited configurations and the ground configuration of the absorbing state, γ is the ratio of the photoluminescence intensities of the sets of defects situated in the excited and ground configurations, subject to the condition of equal defect densities, and k is the Boltzmann constant. The deviation of γ from unity is caused not only by difference in the wave functions of the carrier localized in different configurations, but also by a difference in the excitation and emission spectra of the defects in these configurations. The quantity ρ_1 represents the degree of radiation polarization at liquid-helium temperatures, when the excited configurations are unpopulated, and has been determined previously.[8] For the experimental geometry and emitting light polarization used in the present study we then let $\rho_1=0.26$ for $V_{Ga}Sn_{Ga}$ and $\rho_1=0.29$ for $V_{Ga}Si_{Ga}$. Calculations for defects of triclinic symmetry in the single-dipole approximation (expressions for the degree of polarization in this case are given in Ref. 8) show that ρ_1 cannot be less than zero in our experimental geometry.

The difference between the excited and ground configurations ΔW_0 in Eq. (1) can also be estimated from independent measurements. It has been shown earlier[6] that the photoluminescence polarization ratio r for $V_{Ga}Sn_{Ga}$ complexes in the presence of uniaxial compression along the [111] axis with excitation by light from the intrinsic absorption band at a temperature of 2 K and pressure $P>6$ kbar corresponds to ''saturation'' of the function $r(P)$ after the jump of r at $P=P_{cr}\approx 4.5$ kbar. Consequently, for the group of complexes in which excited (at $P=0$) triclinic configurations of the absorbing state were found to have the lowest energy under the influence of uniaxial compression, only these configurations occur for $P\geqslant 6$ kbar (the Boltzmann filling of other configurations at $T=2$ K is negligible). On the other hand, at $T=77$ K and $P=10$ kbar $r(P)$ attains almost the same value as at $T=2$ K (see Fig. 4b in Ref. 6). This means that at $T=77$ K and $P=10$ kbar the population of the other configurations in the above-indicated group of centers is small. Consequently, allowing for the error of experimental determination of r, which does not exceed $\pm 5\%$, the difference $\Delta W(P=10\text{ kbar})$ between the energies of the triclinic and monoclinic configurations for $P=10$ kbar is negative, and its absolute value is within (2–3) kT ($T=77$ K). On the other hand, for $P=P_{cr}\approx 4.5$ kbar we have $\Delta W(P=P_{cr})=0$ (Refs. 3 and 6), from which, assuming that ΔW varies linearly with the pressure, it follows that

$$\Delta W_0=-\frac{\Delta W(P)}{P-P_{cr}}P_{cr}. \tag{2}$$

Substituting $P_{cr}=4.5$ kbar and $\Delta W(P=10\text{ kbar})$ into Eq. (2), for the $V_{Ga}Sn_{Ga}$ complexes, we obtain

$$1.6kT\lesssim\Delta W_0\lesssim 2.5kT \quad (T=77\text{ K}). \tag{3}$$

Since the Jahn-Teller effect, and not the influence of donors, plays the dominant role in the formation of vacancy-like states of the complex,[5,8] and since the $V_{Ga}Sn_{Ga}$ and $V_{Ga}Si_{Ga}$ complexes do not differ in the position of the donor, it is reasonable to assume that the rates of change of the energies of different configurations as the pressure is varied change only slightly with a change in the chemical nature of the donor. For the $V_{Ga}Si_{Ga}$ complexes ($P_{cr}\approx 6$ kbar for $P\|[111]$; Ref. 5) we then have

$$2kT\lesssim\Delta W_0\lesssim 3.3kT \quad (T=77\text{ K}). \tag{4}$$

Making use of the above estimates, we approximate the experimental $\rho_s(T)$ curves in the temperature range 77–125 K by Eq. (1). We find that the best match between the calculations and experiment is actually achieved when ΔW_0 falls within the limits indicated in expressions (3) and (4) (Fig. 3). In the case of $V_{Ga}Sn_{Ga}$ the consistency of the calculations with the measured dependence within the experimental error limits for $\Delta W_0=10$ meV is obtained for $\rho_2=0-22\%$ as γ is varied from 0.2 to 4, respectively. For $\Delta W_0=16$ meV we have $\rho_2=0-22\%$ and $\gamma=0.4-7$. In the case of $V_{Ga}Si_{Ga}$: for $\Delta W_0=16$ meV we have $\rho_2=0-26\%$ and $\gamma=0.2-6$; for $\Delta W_0=26$ meV we have $\rho_2=0-26\%$ and $\gamma=0.5-13$. For intermediate values of ΔW_0 the ratio γ has intermediate values as well.

These estimates seem reasonable and lead to the conclusion that the given model of $V_{Ga}Sn_{Ga}$ and $V_{Ga}Si_{Ga}$ complexes, which postulates the existence of excited configurations, is capable of explaining the experimentally observed features of the temperature dependence of the induced polarization of the photoluminescence of the complexes.

This work has received partial support from the Russian Fund for Fundamental Research (Grant 98-02-18327).

[1] E. W. Williams, Phys. Rev. **168**, 992 (1968).
[2] V. I. Vovnenko, K. D. Glinchuk, and A. V. Prokhorovich, Fiz. Tekh. Poluprovodn. **10**, 1097 (1976) [Sov. Phys. Semicond. **10**, 652 (1976)].
[3] H. J. Guislain, L. De Wolf, and P. Clauws, J. Electron. Mater. **7**, 83 (1978).
[4] Z. C. Wong, C. J. Li, S. K. Wan, and L. Y. Lin, J. Cryst. Growth **103**, 38 (1990).
[5] N. S. Averkiev, A. A. Gutkin, M. A. Reshchikov, and V. E. Sedov, Fiz. Tekh. Poluprovodn. **30**, 1123 (1996) [Semiconductors **30**, 595 (1996)].
[6] A. A. Gutkin, M. A. Reshchikov, and V. R. Sosnovskiĭ, Fiz. Tekh. Poluprovodn. **27**, 1526 (1993) [Semiconductors **27**, 844 (1993)].
[7] N. S. Averkiev, A. A. Gutkin, E. B. Osipov, M. A. Reshchikov, and V. R. Sosnovskiĭ, Fiz. Tekh. Poluprovodn. **26**, 1269 (1992) [Sov. Phys. Semicond. **26**, 708 (1992)].
[8] A. A. Gutkin, T. Piotrovskiĭ, E. Pultorak, M. A. Reshchikov, and V. E. Sedov, Fiz. Tekh. Poluprovodn. **32**, 40 (1998) [Semiconductors **32**, 33 (1998)].
[9] A. A. Gutkin, M. A. Reshchikow, and V. E. Sedov, Z. Phys. C **200**, 217 (1997).
[10] A. A. Gutkin, M. A. Reshchikov, and V. E. Sedov, Fiz. Tekh. Poluprovodn. **31**, 1062 (1997) [Semiconductors **31**, 908 (1997)].

Translated by James S. Wood

Photoconductivity spectra of CdHgTe crystals with photoactive inclusions

A. I. Vlasenko, Z. K. Vlasenko, and A. V. Lyubchenko

Institute of Semiconductor Physics, Ukrainian Academy of Sciences, 252028 Kiev, Ukraine
(Submitted April 10, 1998; accepted for publication May 12, 1998)
Fiz. Tekh. Poluprovodn. **33**, 47–51 (January 1999)

This paper analyzes how both wide- and narrow-band-gap inclusions in CdHgTe host material affect the generation-recombination behavior of the latter. It is found that the shape of the photoconductivity (PC) spectral characteristic is sensitive to the type of inclusion present in the host: wide-band-gap inclusions lead to additional maxima in the spectral region near the fundamental absorption edge, while narrow-band-gap inclusions wash out the edge at long wavelengths. It is found that the shape of the PC spectra of these nonuniform crystals depends on the magnitude and polarity of the applied bias voltage. A photovoltage which alternates in sign as a function of wavelength and which is similar to the photosensitivity spectra of opposing barriers in graded-gap layers, is observed. © *1999 American Institute of Physics.* [S1063-7826(99)01101-1]

INTRODUCTION

The optimum functional parameters of a semiconductor photoelectric material are generally limited by the degree of structural perfection of the material.[1–3] This is particularly true of narrow-gap semiconducting solid solutions such as CdHgTe, which is characterized by a well-developed system of intrinsic point and extended defects. In Refs. 4–6 it was shown that photosensitivity in these materials is limited by composition fluctuations, inclusions of a second phase, in particular, Te and low-angle Q boundaries. The authors of Ref. 7 established that the mechanism for degradation of CdHgTe is related to decomposition of the solid solution mediated by mass transport and gettering of the mobile component Hg in the strain fields of lattice macrodefects. However, the photoelectric properties of crystals with spatial nonuniformities have not yet been analyzed in detail. In this paper, experimental data on the photoelectric characteristics of CdHgTe crystals with photoactive inclusions are correlated with x-ray data indicating the type of spatial nonuniformity. Here ''photoactive'' inclusions are defined as inclusions whose photoconductivity parameters (generation, recombination, or nonequilirium charge carrier transport) differ from those of the host.

EXPERIMENTAL RESULTS AND ANALYSIS

Because microfluctuations in composition and shallow-impurity doping levels lead to the appearance of ''tails'' in the density of states, they affect the photoconductivity spectrum of a semiconductor primarily by washing-out the long-wavelength edge of the latter. Hence, the effect of microfluctuations on the photosensitivity can be taken into account by introducing an absorption coefficient α associated with transitions between tails of the density of states that is quasi-uniform throughout the volume, and consequently a photogeneration rate G which depends exponentially on $h\nu$ (in accordance with the Urbach rule; see Ref. 8). In this case the lifetimes of nonequilibrium charge carriers τ and their mobilities μ can also be modeled as spatially averaged, spectrally independent quantities, and the influence of diffusion and diffusion-drift microcurrents of nonequilibrium charge carriers can be disregarded.

The electron-probe x-ray spectral microanalysis (Camebax) data shown in Fig. 1 indicate that CdHgTe solid solutions contain inclusions with compositions that differ from the host by higher or lower Hg content (Figs. 1a and 1c) and hence have smaller or larger band gap widths E_g, respectively. They also can contain inclusions of a second phase, for example, Te (Fig. 1b).

In order to analyze the spectral distribution of the photosensitivity of these crystals, we must consider generation-recombination parameters for the host and inclusions separately, taking into account the diffusion- drift exchange of nonequilibrium charge carriers between them. We must also include the properties of the transition layer (at the host-

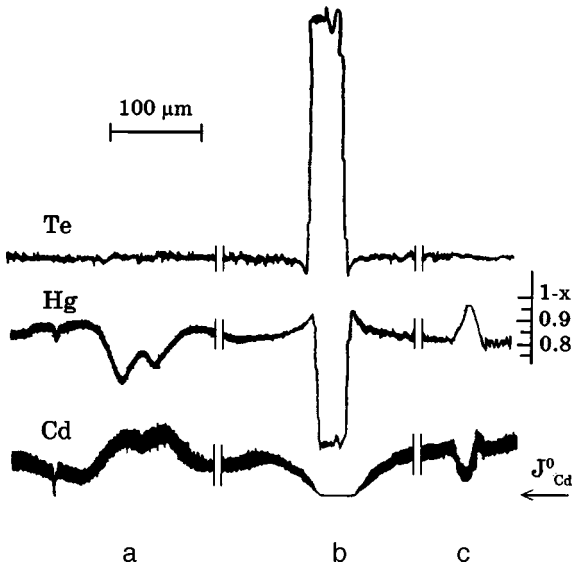

FIG. 1. Distribution of components in nonuniform CdHgTe crystals—Cd, Hg, Te: a) with Cd-rich inclusions, b) with Te inclusions, c) with Hg-rich inclusions. J^0_{Cd} marks the level of zero Cd content.

inclusion boundary), which generally is characterized by an increased density of dislocations (due to lattice parameter mismatch, difference in thermal expansion coefficients, etc.), variations in the concentration of point defects, and residual elastic compressive or tensile strains. These latter perturbations can give rise to a complicated energy band profile, in whose ''trenches'' nonequilibrium charge carriers can undergo strong recombination or heating. The authors of Refs. 4 and 7 demonstrated that when Te inclusions and mechanical damage are present, these regions become so enriched with Hg that the material around them becomes semimetallic, with an increased recombination rate and low photosensitivity. It is natural to assume that these structures will have altered transport parameters for nonequilibrium charge carriers, which determine the carrier mobility in them.

The influence of these regions is even more evident when we take into account their long-range interaction, i.e., the distances over which they perturb the distribution of nonequilibrium charge carriers (L_{eff}). The difference in the parameters for generation, transport, and recombination of nonequilibrium charge carriers in these regions accounts for the appearance of diffusion fluxes, which are usually accompanied by a superimposed drift in the (quasi) electric fields arising from graded-gap (var E_g) or concentration-induced (var n_0) potentials. The spatial distribution of the concentration of nonequilibrium charge carriers $\Delta n(r)$ becomes complicated and depends on the form of the vector field made up of the electric (quasi-electric) fields. While for large inclusions the magnitude of L_{eff} is determined by the diffusion and drift parameters, for small inclusions the geometric size of the latter (see Ref. 9) (more precisely its shape) enters into the problem and must be studied individually for each specific shape.

In the approximation that the nonequilibrium charge carrier distribution arises primarily from diffusion and that no energy barriers exist between host and inclusion, Grigor'ev et al.[6] obtained the following solution to the continuity equation for the distribution $\Delta n_v(r)$:

$$\Delta n_v(r) = G_v\tau_v\left\{1-\frac{r_c}{r}\exp\left(-\frac{r-r_c}{L_v}\right)\times\frac{(1-G_i\tau_i/G_v\tau_v)[r_c/L_i-\tanh(r_c/L_i)]}{r_c/L_i+\tanh(r_c/L_i)[D_v(1+r_c/L_v)/D_i-1]}\right\}, \tag{1}$$

where r is the radius vector, r_c is the radius of the inclusion, D is the diffusion coefficient, and $L_{v,i}=(D_{v,i}\cdot\tau_{v,i})^{1/2}$ (the labels v and i refer to the host volume and inclusion, respectively). The parameters $G_{v,i}\tau_{v,i}$ determine the nonequilibrium charge carrier concentration.

Figure 2 shows curves for the spatial distribution of nonequilibrium charge carriers in a system consisting of a spherical inclusion in a host, calculated using Eq. (1) and various ratios $G_i\tau_i/G_v\tau_v$ for an n-type CdHgTe crystal with $x=0.2$ (here $n_{0v}\approx 3\times10^{14}\,\text{cm}^{-3}$, $\tau_v\approx 6\times10^{-6}$ s, $L_v\approx 50\mu$m, $\tau_i\approx 6\times10^{-7}$ s, $L_i\approx 15\mu$m, and $D_i\approx D_v$).

Decreasing the ratio until $G_i\tau_i/G_v\tau_v<1$ (which makes the inclusion a getter) increases the effective volume over

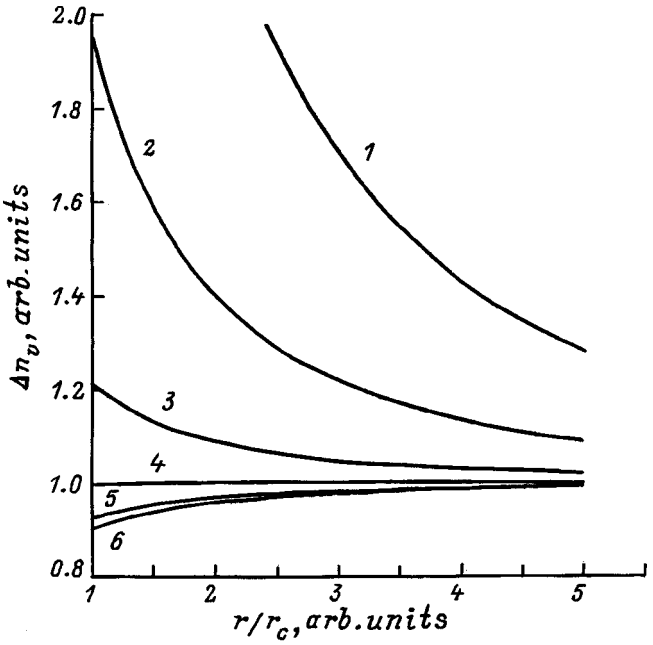

FIG. 2. Relative spatial distributions of nonequilibrium charge carriers in the neighborhood of an inclusion, calculated from Eq. (1) for the following values of the parameter $G_i\tau_i/G_v\tau_v$: *1* — 30, *2* — 10, *3* — 3, *4* — 1, *5* — 0.3, *6* — 0.1.

which the inclusion absorbs nonequilibrium charge carriers from the host. Increasing the ratio until $G_i\tau_i/G_v\tau_v>1$ (which makes the inclusion an injector) increases the effective host volume into which nonequilibrium charge carriers are injected from the inclusion. Note that when $r_c>L_i$, we must take into account diffusion and recombination of nonequilibrium charge carriers within the inclusion, and when $r_c\gg L_i$, all of the nonequilibrium charge carriers generated in the inclusion are injected into the host. Note also the sensitivity of $\Delta n(r)$ to the ratio of parameters D_i/D_v (particularly when the conductivity type of the inclusion is opposite that of the host; in that case D_i and D_v can differ by as much as one to two orders of magnitude). In real situations we must take into account that the distribution $\Delta n(r)$ enters self-consistently into the generation of barriers to recombination of nonequilibrium charge carriers between the host and the inclusion.

In the analysis that follows, we will not take into account the fact that the recombination and transport parameters differ from those of the host in regions immediately adjacent to the inclusions. We will also assume that the inclusions are defined by abrupt boundaries and isolated from one another by the host. When this is not true, the inclusions may form a continuous cluster with a photoconductivity channel in parallel with the host.

Let us first consider material with wide-gap inclusions, i.e., for which $E_{gi}>E_{gv}$ (Figs. 1a and 1b). When such a material is illuminated by photons with energies $h\nu\geqslant E_{gi}$, nonequilibrium charge carriers are generated only in inclusions located a distance l from the surface, where l does not exceed the penetration depth of the light in the corresponding spectral range, i.e., $l<1/\alpha$. It is obvious that in the region where α is saturated for both the host and inclusion compo-

sitions ($\approx 10^{-4}$ cm^{-1}; see Ref. 10) we have $G_i \approx G_v$. When the nonequilibrium charge carrier concentration in the inclusions exceeds that of the host ($G_i\tau_i > G_v\tau_v$, which is possible only for $\tau_i > \tau_v$), the regions adjacent to the inclusion will be enriched with nonequilibrium charge carriers due to their injection from the inclusions (Fig. 2, curves *1–3*) (when a continuous cluster forms, the inclusions themselves can contribute to the photoconductivity). Subsequent recombination of nonequilibrium charge carriers can take place both in the skin layer, with a lifetime τ_s determined by recombination at the surface which defines the inclusion shape, and within the bulk of the host with the bulk lifetime τ_v, which generally exceeds τ_s.[11,12] When the crystal is illuminated by photons with energies $E_{gv} < h\nu < E_{gi}$, the inclusions passively transmit this light into the depth of the crystal (the transparency channel), where nonequilibrium charge carriers are generated and recombine in host layers adjacent to the inclusions over distances $\approx 1/\alpha$, as in the previous case, with lifetime τ_v. This can happen when the sizes of the wide-gap inclusions, and consequently the distances from the surface to points where the nonequilibrium charge carriers are generated, exceed a distance $l_s = (D_v\tau_s)^{1/2}$, which, based on the estimates of Ref. 12, can be as large as 15–20 μm for surface recombination velocities $s \approx 10^3$ cm/s.

Grigor'ev *et al.*[6] noted that a host illuminated through transparent wide-gap inclusions by photons with energies $h\nu > 2E_g$ can have its quantum yield β increased via collisional generation. In CdHgTe with $E_g \approx 0.1$ eV this effect begins to appear for $h\nu \geqslant 0.5$ eV.[13]

The phenomena listed above can make the crystal photosensitive in the spectral range $h\nu > E_{gv}$ and cause the photoconductivity spectral characteristic to become nonmonotonic, with additional maxima at $h\nu \approx E_{gi}$. Note that this can happen only when recombination forces the surface of the host- inclusion boundary to be neutral. When the surface recombination velocity at the inclusion boundary is high ($s_i \gg 1$), the inclusions play the role of sinks for nonequilibrium charge carriers both on the inclusion side and on the host side, and the photosensitivity decreases over the entire spectral range.[4]

For $h\nu \leqslant E_{gv}$, the photoconductivity should develop an exponential edge derived from the Urbach absorption edge as long as there are no narrow-gap inclusions.

Figure 3 shows photoconductivity spectra at various temperatures for a crystal containing wide-gap CdHgTe and Te inclusions in the surface region (Figs. 1a and 1b for a probe depth of 2–3 μm). The maxima in the vicinity of the fundamental absorption edge are associated with photoactivity of these inclusions. The maxima in the range $\lambda = 3 - 4$ μm correspond to E_g for Te (or CdHgTe with $x = 0.4$). Also noteworthy are the maxima in the range $\lambda = 0.8 - 1$ μm, which are quite commonly seen in these crystals and correspond to compositions with E_g close to CdTe. With increasing T and the conversion of the material conductivity to intrinsic, the carrier lifetimes in the host and inclusions approach one another, which changes the photoconductivity spectral profile. The spectral sensitivity of these maxima to changes in T differs from that of the long-wavelength maximum, which is explained by the different coefficients

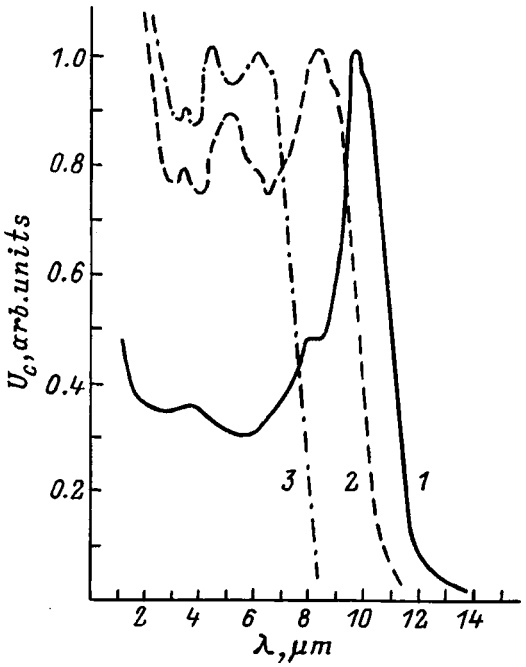

FIG. 3. Photosensitivity spectral distribution U_c for a sample with wide-gap inclusions and Te inclusions. T, K: *1* — 85, *2* — 145, *3* — 300.

dE_g/dT for the host and inclusion compositions.[14]

It is obvious that wide-gap inclusions in the bulk of the host at distances from the surface exceeding the absorption depth for photons with $h\nu > E_{gi}$ are not photoactive and do not introduce additional maxima into the photoconductivity spectrum. However, these inclusions can strongly suppress the experimentally determined values of μ_h (due to the altered conditions for current transport through the crystal). It is important to take into account the decreased working volume of photoactive host when theoretically calculating quantum yields and photosensitivities of device structures.

When the parameters of the wide-gap inclusions are such that $G_i\tau_i < G_v\tau_v$, nonequilibrium carriers generated in the inclusions will recombine within them (without injection into the host) without making the sample photosensitive. On the other hand, diffusion- driven drainage and recombination of nonequilibrium charge carriers in the inclusions (i.e., gettering of these carriers from the adjacent host regions) will also be hindered by the presence of a potential barrier $\Delta E \approx |E_{gi} - E_{gv}|$, which, as previously, leads to exclusion of carriers from the photoactive volume of the host (for recombination-neutral surfaces).

We now discuss material with Hg-rich, narrow-gap inclusions, i.e., $E_{gi} < E_{gv}$ (see Fig. 1c). [Note that regions adjacent to Te inclusions are also Hg- rich (Fig. 1b).] Assume that $G_i\tau_i > G_v\tau_v$. When such crystals are illuminated by photons with $h\nu > E_{gv}$, photogeneration can take place in a surface layer one optical absorption depth thick, in both the host material and in the narrow-gap inclusions located in this layer. Since $\alpha_i \approx \alpha_{vs}$ in the layer[10] and $G_i = G_{vs}$ (where the label s indicates the surface layer of the sample), τ_i will be larger than τ_{vs}. In practice this case can occur in strongly compensated material (and also in crystals with $x > 0.23$, for which the nonequilibrium charge carrier lifetime is deter-

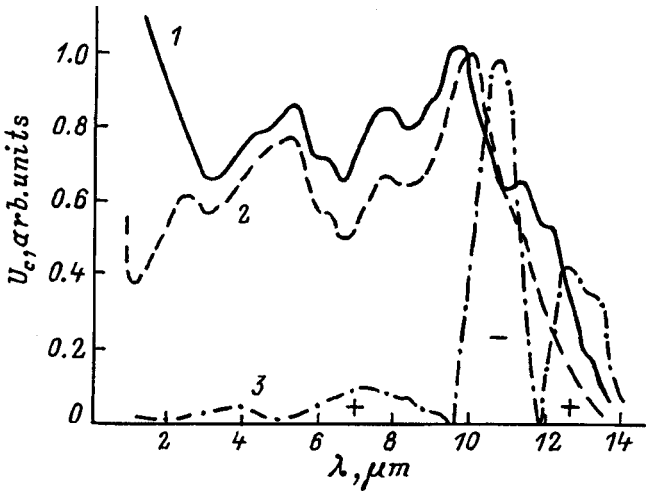

FIG. 4. Photosensitivity spectral distribution U_c for samples with narrow-gap and wide-gap inclusions for various bias polarities U_b: *1* — >0, *2* — <0, *3* — $=0$.

mined by the Shockley–Read mechanism in the host and by Auger processes in the narrow-gap inclusions[11,15]). When the photoactive volume is significant, these inclusions can make the crystal photosensitive. The photosensitivity of the sample in this spectral region can also be increased when nonequilibrium charge carriers can overcome the potential barrier $\Delta E \approx E_v - E_i$ and be injected into the host (when inclusions extend deep into the crystal, nonequilibrium charge carriers can be injected into the crystal bulk, thereby sensitizing the host). Low- temperature activation of photoconductivity may be related to this effect.

When the crystal is illuminated by photons in the spectral range $E_{gi} < h\nu < E_{gv}$, photogeneration of nonequilibrium charge carriers in the sample takes place primarily within the inclusions ($G_i \geqslant G_v$), and the condition $G_i\tau_i > G_v\tau_v$ can be satisfied even for $\tau_i < \tau_v$, which is normally the case for narrow-gap inclusions, leading to increased photosensitivity in this spectral range. Evidence for this is washing-out of the long-wavelength edge or the appearance of additional long-wavelength bands in the photoconductivity spectral distribution curves. When inclusions are present both with $x_i > x_v$ and $x_i < x_v$ (Figs. 1a–1c), which is normally observed in practice, the photoconductivity spectral characteristics will contain all the features discussed above. Figure 4 shows photoconductivity spectra for one such sample.

The shape of the photosensitivity spectral characteristic of nonuniform crystals, and of its long-wavelength edge, often depend on the magnitude and polarity of an applied bias U_b (Fig. 4, curves *1* and *2*). In a nonuniform material with a potential profile this effect can be due to generation of nonequilibrium charge-carrier pairs by photons with $h\nu < E_g$ in the neighborhood of barriers as a result of interband transitions with tunneling. The stronger the internal field in the barrier is, the farther into the infrared region the tail for photosensitivity extends. Chaging the magnitude or polarity of U_b changes the electric field of the barrier, shifting the low-energy edge of the photoconductivity toward higher or lower energies (the Franz–Keldysh effect).[8] The observed photovoltage (Fig. 4, curve *3*), whose magnitude and polarity depend on $h\nu$, may be related to the presence of opposing potential barriers in graded-gap regions of the sample.[16]

If the parameters of the narrow-gap inclusions are such that $G_i\tau_i < G_v\tau_v$ (which happens when $\tau_i \ll \tau_v$; in this case G_i can also exceed G_ν), the photosensitivity of the crystal falls off over the entire spectral range. This effect is observed in a rather large group of nonuniform crystals with equilibrium carrier concentrations in the range 3×10^{14} to $3\times10^{15}\,\mathrm{cm}^{-3}$, which have $\tau \leqslant 10^{-7}$ s, although the theoretical τ for interband Auger recombination is $\geqslant 10^{-6}$ s. This has not been explained.

CONCLUSIONS

We have analyzed generation-recombination activity of wide-gap and narrow-gap inclusions in a CdHgTe host as a function of the photoexcitation spectral range. We have found that the shape of the photoconductivity spectral characteristic is sensitive to the type of inclusion present in the matrix, with additional maxima appearing in the neighborhood of the fundamental absorption edge for wide-gap inclusions and washing-out of its long-wavelength edge for narrow-gap inclusions.

We have established that the shape of the photoconductivity spectra of nonuniform crystals depends on the magnitude and polarity of an applied bias voltage. We have observed wavelength-dependent, sign-alternating photovoltage, analogous to the photosensitivity spectra of opposing barriers in graded-gap layers.

[1] M. K. Sheĭnkman and A. Ya. Shik, Fiz. Tekh. Poluprovodn. **10**, 209 (1976) [Sov. Phys. Semicond. **10**, 128 (1976)].
[2] M. G. Mil'vidskiĭ and V. B. Osvenskiĭ, *Structural Defects in Semiconductor Single Crystals* (Metallurgiya, Moscow, 1984).
[3] M. G. Mil'vidskiĭ and V. B. Osvenskiĭ, *Structural Defects in Semiconductor Epitaxial Layers* (Metallurgiya, Moscow, 1985).
[4] A. I. Vlasenko, V. Z. Latuta, Yu. N. Gavrilyuk, A. V. Lyubchenko, and E. A. Sal'kov, Fiz. Tekh. Poluprovodn. **5**, 1013 (1979) [Sov. Phys. Semicond. **5**, 901 (1979)].
[5] N. N. Grigor'ev, L. A. Karachevtseva, K. R. Kurbanov, and A. V. Lyubchenko, Fiz. Tekh. Poluprovodn. **25**, 464 (1991) [Sov. Phys. Semicond. **25**, 280 (1991)].
[6] N. N. Grigor'ev, A. V. Lyubchenko, and E. A. Sal'kov, Ukr. Fiz. Zh. **34**, 1088 (1989).
[7] A. I. Vlasenko, A. V. Lyubchenko, and V. G. Chalaya, Fiz. Tekh. Poluprovodn. **30**, 377 (1996) [Sov. Phys. Semicond. **30**, 209 (1996)].
[8] J. I. Pankove, *Optical Processes in Semiconductors* (Prentice-Hall, Englewood Cliffs, N. J. 1971; Mir, Moscow, 1973).
[9] I. S. Virt, N. N. Grigor'ev, and A. V. Lyubchenko, Fiz. Tekh. Poluprovodn. **22**, 409 (1988) [Sov. Phys. Semicond. **22**, 251 (1988)].
[10] M. D. Blue, Phys. Rev. **134**, 226 (1964).
[11] A. I. Vlasenko, Yu. N. Gavrilyuk, A. V. Lyubchenko, and E. A. Sal'kov, Fiz. Tekh. Poluprovodn. **13**, 2180 (1979) [Sov. Phys. Semicond. **13**, 1274 (1979)].
[12] A. I. Vlasenko, Yu. N. Gavrilyuk, A. V. Lyubchenko, and E. A. Sal'kov, Ukr. Fiz. Zh. **25**, 431 (1980).
[13] M. P. Shchetinin, N. S. Baryshev, and I. S. Aver'yanov, Fiz. Tekh. Poluprovodn. **5**, 2350 (1971) [Sov. Phys. Semicond. **5**, 2059 (1971)].
[14] M. W. Scott, J. Appl. Phys. **40**, 4077 (1969).
[15] A. I. Vlasenko, Z. K. Vlasenko, and A. V. Lyubchenko, Fiz. Tekh. Poluprovodn. **31**, 1323 (1997) [Semiconductors **31**, 1280 (1997)].
[16] A. I. Vlasenko, Optoelectron. Semic. Tech. **31**, 191 (1996).

Translated by Frank J. Crowne

Theory of photovoltaic effects in crystals without an inversion center

R. Ya. Rasulov, Yu. E. Salenko, A. Tukhtamatov, T. Éski, and A. É. Avliyaev

Fergana State University, 712000 Fergana, Uzbekistan
(Submitted March 23, 1998; accepted for publication May 27, 1998)
Fiz. Tekh. Poluprovodn. **33**, 52–57 (January 1999)

Photon mechanisms of the shift and ballistic linear photovoltaic effects in semiconductors with a degenerate valence band are investigated theoretically. These mechanisms are attributed both to real-space hole shift in direct optical transitions between branches of the valence band and to the asymmetry of electron-phonon interaction, with allowance for Frölich electron-phonon interaction. The temperature and frequency dependences of the photocurrent are determined, and the results are compared with experimental data for *p*-type GaAs. The light absorption coefficient, the current due to entrainment of electrons by photons, and the shift linear photovoltaic (LPV) effect, all associated with direct optical transitions accompanied by electron spin flip, are calculated for crystals without an inversion center. Allowance is made for the contribution to the entrainment current from inclusion of the wave vector in the energy conservation law and in the momentum conservation law and for the interaction of the magnetic field of the light wave with the electron magnetic moment. The contribution of ''isotropization'' of the photocarrier distribution function to the shift LPV current in semiconductors with a complex valence band is calculated. It is shown that the scattering of photocarriers by *LO*-phonons in each stage of the cascade scattering process yields a current contribution. © *1999 American Institute of Physics.* [S1063-7826(99)01201-6]

INTRODUCTION

It has now been established that the momentum alignment of photoexcited carriers in crystals without an inversion center under the influence of linearly polarized radiation produces ordered motion, i.e., a photocurrent due to asymmetry of the scattering of carriers by phonons, photons, and other imperfections of the crystal structure.[1]

The currents generated by the shift and ballistic linear photovoltaic (LPV) effects in semiconductors with a degenerate valence band as a result of the asymmetric scattering of carriers by longitudinal optical (*LO*) phonons (phonon mechanism) have been investigated theoretically.[2,3] It was shown that the predominant mechanism of the effect in *p*-GaAs at a temperature $T>250\,\mathrm{K}$ and a hole density $p=10^{15}-10^{19}\,\mathrm{cm}^3$ in excitation by a CO_2 laser is transitions between the heavy-hole and light-hole branches, and that the temperature dependence of the photocurrent for the indicated mechanism is roughly described by the equation

$$j_\alpha = I\chi|\delta_{\alpha\beta\gamma}|e_\beta e_\gamma, \tag{1}$$

$$\chi(T)=p\left(\frac{E^*}{k_BT}\right)^{3/2}\exp\left(-\frac{E^*}{k_BT}\right)\frac{a_{\mathrm{phon}}N_\Omega+b_{\mathrm{phon}}(N_\Omega+1)}{2N_\Omega+1}. \tag{2}$$

Here $E^*=\hbar\omega m_2/(m_1-m_2)$, m_1 and m_2 are the effective masses of heavy and light holes, ω is the frequency, I is the intensity, **e** is the polarization vector of the exciting light, and N_Ω is the occupation number of *LO* phonons. The coefficients a_{phon} and b_{phon} in Eq. (1) depend on the parameters of the band structure, the electron-phonon interaction constants, and the light frequency.

Lyanda–Geller and Rasulov[3] have calculated numerically the current due to the phonon mechanism of the shift and ballistic LPV effects for *p*-GaAs and have compared the theoretical values of the coefficients a_{phon} and b_{phon} in Eq. (2) with experimental results. They noted an appreciable quantitative discrepancy between the theoretical and experimental temperature dependences of the photocurrent. The discrepancy can be attributed to the numerical calculations being carried out without regard for the contribution of the photon mechanism of the shift and ballistic LPV effects due to the presence of terms of different parities with respect to the wave vector **k** in the effective hole Hamiltonian $H(\mathbf{k})$ for the Γ_8 band. Estimates of this contribution in Ref. 4, based on then-available data on the coefficient D' characterizing the value of the **k**-cubed term in $H(\mathbf{k})$, have indicated that the role of the photon mechanism is smaller than that of the phonon mechanism. However, other data[5] show that the coefficient D' is 2.7 times the value assumed in Refs. 3 and 4. It is important, therefore, to calculate the photon mechanism of the shift and ballistic LPV effects, which is the objective of the present study. To make the problem complete, we also investigate the precession mechanism of the photovoltaic effects (photon entrainment due to the transfer of photon momentum to the system of carriers, and the shift LPV effect) in piezoelectric crystals.

PHOTON MECHANISM OF THE SHIFT AND BALLISTIC LINEAR PHOTOVOLTAIC EFFECTS

In addition to the phonon mechanism of the shift LPV effect, there is also a photon mechanism associated with real-space hole displacement in direct optical transitions between

branches of the valence band of GaAs. To calculate the current produced by this mechanism, we use the equation[2,6]

$$j_\alpha = -\frac{e^3 I e_\beta e_\gamma |\delta_{\alpha\beta\gamma}|}{2\pi m_0^2 \omega^2 \hbar c n_\omega} \int d\mathbf{k}\, \mathrm{Im}\left[P_{21}^{(\beta)*} \frac{\partial}{\partial k_\alpha} P_{21}^{(\alpha)} \right] \times f_{1\mathbf{k}} \delta(E_2 - E_1 - \hbar\omega). \quad (3)$$

Here n_ω is the refractive index of light, P_{21} is the matrix element of the momentum operator

$$\mathbf{P} = \frac{m_0}{\hbar} \nabla_{\mathbf{k}} \hat{H}, \quad (4)$$

$\hat{H}$ is the hole Hamiltonian, $E_l = \hbar^2 k^2/(2m_l)$ is the energy spectrum, m_l is the effective mass of holes of the lth branch ($l=2$ corresponds to the light-hole subband, and $l=1$ corresponds to the heavy-hole subband), and $\delta_{\alpha\beta\gamma}$ is an antisymmetric third-rank tensor; $\alpha, \beta, \gamma = x, y, z$.

From now on, in addition to the **k**-squared term

$$\hat{H} = \left(A + \frac{5}{4} B \right) k^2 - B(\mathbf{J}\cdot\mathbf{k})^2 \quad (5)$$

we also include in the Hamiltonian the k-cubed term

$$\hat{H}_3 = D' \mathbf{J}\cdot\mathbf{K} \quad (6)$$

and the term linear in **k**

$$\hat{H}_1 = \frac{4}{\sqrt{3}} k_0 \mathbf{V}\cdot\mathbf{k}, \quad (7)$$

where

$$K_\alpha = k_\alpha (k_{\alpha+1}^2 - k_{\alpha+2}^2), \quad V_\alpha = [J_\alpha (J_{\alpha+1}^2 - J_{\alpha+2}^2)].$$

Here J_α denotes the matrices of the operator of projection of the angular momentum in Γ_8 representation,[7] and

$$A \pm B = \hbar^2/(2m_{1,2}).$$

Now, making use of Eq. (4) with allowance for (5)–(7) and summing over all degenerate states, after several transformations we obtain

$$j_{\alpha,\nu}^{\mathrm{phot}} = e \frac{I}{\hbar\omega} K(\omega, T) L^{(\nu)} e_\beta e_\gamma |\delta_{\alpha\beta\gamma}|, \quad (8)$$

where

$$K(\omega, T) = \frac{e^2}{c\hbar n_\omega} f_0(E^*) \sqrt{\frac{\hbar\omega}{2B}} \quad (9)$$

is the light absorption coefficient associated with direct optical transitions of holes between the light-hole and heavy-hole branches of the semiconductor valence band, $f_0(E^*)$ is the equilibrium hole distribution function, $L^{(\nu)}$ is a quantity having units of length:

$$L^{(3)} = -\frac{D'}{2B}\left(1 + \frac{21}{16\pi} I_0 \right), \quad (10)$$

$$L^{(1)} = -\frac{k_0}{\hbar\omega}\left(1 + \frac{4}{\sqrt{3}} \frac{m_1 - m_2}{m_1 + m_2} \right), \quad (11)$$

$$I_0 = \int_{-1}^{+1} d\mu \int_0^{2\pi} \left[O_y^2 O_z^2 \sum_\alpha O_\alpha^2 (O_{\alpha+1}^2 - O_{\alpha+2}^2)^2 \right]^{1/2},$$

$$\mathbf{O} = \mathbf{k}/k \quad (12)$$

and the ratio $j_{\alpha,\nu}^{\mathrm{phot}}/K$ does not depend on the temperature.

We note that not only the contributions to the shift LPV current from the product of the linear term in **k** and the **k**-independent or **k**-squared term in the matrix element of the momentum operator, but also the contributions due to the perturbed part of the wave functions and splitting of the light-hole and heavy-hole subbands are included in the calculations. The inclusion of terms (5) and (6) in the Hamiltonian $\hat{H}$ leads to splitting of the light-hole subband:

$$E_l^{\pm} = \frac{\hbar^2 k^2}{2m_l} \pm D' k^3 \left[\sum_\alpha O_\alpha^2 (O_{\alpha+1}^2 - O_{\alpha+2}^2) \right]^{1/2} \quad (13)$$

(the heavy-hole subband does not split in this case), and the inclusion of (7) in $\hat{H}$ leads to identical splitting of both subbands:

$$E_l^{\pm} = \frac{\hbar^2 k^2}{2m_l} \pm \sqrt{3} k_0 k \sqrt{O_x^2 + O_y^2}. \quad (14)$$

The inclusion of splitting in the energy conservation law (in the argument of the δ-function) yields an additional contribution [the emergence of J_0 in Eq. (4)] to the shift LPV current in the first case and does not do so in the second case. The latter is attributable to the fact that the linear splitting $E_l(\mathbf{k})$ has no effect on the difference $E_2^+ - E_1^\pm$, which remains fixed.

It is evident from relation (8) that the temperature variation of the current due to the photon mechanism of the shift LPV effect is determined by the temperature dependence of the light absorption coefficient $K(T)$. The photon mechanism of the ballistic LPV effect is attributable to the asymmetric part of the probability $W^{(as)}$ of the optical transition of holes between the branches of the valence band. Here the probability $W^{(as)}$ contains odd-**k** terms, which are the result of the product of terms of different parities with respect to **k** in the matrix element of the electron-photon interaction operator.

Given Boltzmann statistics, the ballistic LPV current is determined primarily by eight functions Φ_m, which are proportional to the imaginary part of the product of the matrix elements of the momentum and electron-phonon interaction operators.[3] In addition to the **k**-squared terms in $H(\mathbf{k})$, we also take into account the **k**-cubed terms in calculating the current due to the photon mechanism of the ballistic LPV effect, and we restrict the problem to Frölich electron-phonon interaction.[2] Making transformations similar to those in Ref. 8, using the anticommutator expressions given in the Appendix [see Eq. (32) (Ref. 8)], and integrating over the solid angles of the wave vectors of the initial and final states Ω and ω', we obtain the equations for

TABLE I. Numerical values of the coefficients a_l and b_l (in nm) in *p*-GaAs for exciting light frequencies $\hbar\omega=117$ meV and $\hbar\omega=130$ meV at room temperature.

Photon energy, meV	Types of optical transitions: A a	A b	B a	B b	C a	C b	Ballistic a	Ballistic b	Shift a	Shift b	Total a	Total b
					Phonon mechanism							
117	−14.1	−2.7	15.3	4.0	−4.5	2.8	−2.3	4.1	−3.0	−3.0	−6.3	1.1
130	−15.3	−1.6	16.0	3.3	−4.7	2.8	−4.0	4.5	−2.0	−2.9	−6.3	1.6
					Photon mechanism							
117	0.326	−0.119	0.5	−0.06	−0.551	0.0	0.278	−0.2	0.2	0.2	0.467	0.04
130	0.318	−0.161	0.54	−0.05	−0.562	0.0	0.3	−0.17	0.3	0.3	0.482	0.09
					Resultant mechanism							
117	−13.77	−2.88	15.8	3.64	−5.05	2.8	−3.03	3.915	−2.81	−2.84	−5.83	1.1
130	−14.98	−1.77	16.59	3.35	−5.53	2.8	−3.7	4.33	−2.72	−2.72	−6.42	1.69

$$\overline{\Phi}_n=\langle k_\alpha\Phi_n\rangle \quad \text{and} \quad \overline{\Phi}'_n=\langle k'_\alpha\Phi_n\rangle_{\Omega\Omega'}, \tag{15}$$

$$\overline{\Phi}_1=\Phi_0[kk'^{-1}Q_1-(Q_0+2Q_2)/2], \quad \overline{\Phi}_2=\Phi_0(Q_0-Q_2),$$

$$\overline{\Phi}'_n=(-1)^n\overline{\Phi}_n(k\leftrightarrow k'), \quad n=1,2,$$

where

$$\Phi_0=\frac{32\pi^2}{5\hbar^2}BD'C^2U_L^2m_0^2(kk')^2,$$

$$Q_m=\frac{1}{2}\int_{-1}^{+1}P_m(x)(a-x)^{-1}dx, \tag{16}$$

P_m is a Legendre polynomial of order m, $a=(k^2+k'^2)/2kk'$, and U_L is the amplitude of the relative displacement of optical vibrations of the two sublattices,

Expressions for the current due to the photon mechanism of the ballistic LPV effect, calculated on the basis of the functions $\overline{\Phi}_n$ and $\overline{\Phi}'_n$ according to Eq. (8), are derived from Eq. (1) by replacing $Bd_0/\sqrt{3}$ with CD' and replacing a_{phon} and b_{phon} with a_{phot} and b_{phot}. The extremely cumbersome expressions for a_{phot} and b_{phot} are not given here.

COMPARISON WITH EXPERIMENT

For our subsequent quantitative calculations we use the following values for the parameters of GaAs: *LO*-phonon energy $\hbar\Omega=36$ eV; $m_1=0.51m_0$, $m_2=0.09m_0$; low-frequency and high-frequency dielectric constants $\varepsilon_0=12.5$ and $\varepsilon_\infty=10.9$; $|D'|=3.9\times10^{-23}$ eV·cm^3; $\rho=5.31$ g/cm^3.

We begin by estimating $L^{(\nu)}$. For different crystals the constant k_0 lies in the interval $(1-6)\times10^{-10}$ eV·cm (see, e.g., Ref. 5). For GaAs irradiated by a CO_2 laser ($\hbar\omega=0.12$ eV) these values correspond to $L_1^{(1)}=(0.2-1.4)\times10^{-8}$ cm$=(0.15-1)X_{\text{exp}}$, where $X_{\text{exp}}=0.17\times10^{-7}$ cm at room temperature. These estimates show that the contribution to the shift LPV current from the asymmetry of the photon processes due to relativistic terms linear in $\mathbf{k}$ in $\hat{H}$ are also comparable with the experimental values.

In the calculations of a_{phot} and b_{phot} we have allowed for the fact that when light is absorbed, the photons generate carriers with an anisotropic velocity distribution, which eventually begin to be scattered by phonons, by impurities, and by each other, depending on the energy, shifting in real space in each step of the cascade scattering process and yielding a corresponding contribution to the total photocurrent (see the Appendix). This current differs from the current generated in the scattering of holes from the initial state, not only by virtue of the collision-induced reduction in the degree of anisotropy of the distribution, but also because of the energy dependence of the average displacement. The ''partial'' photocurrents can have opposite signs in this case. The coefficients a_{phot} and b_{phot} for the shift and ballistic LPV currents due to the asymmetry of hole-photon interaction with inclusion of the squared and cubic terms in $\mathbf{k}$ in $H(\mathbf{k})$ and for the total current are given in Table I, where the letters *A*, *B*, and *C* refer to the processes *A*, *B*, and *C* discussed in Ref. 4 (the values of the coefficients a_{phon} and b_{phon} are taken from Ref. 3). Clearly, the ballistic and shift contributions of the photon mechanism to the current are comparable in order of magnitude, and these contributions partially cancel each other.[1)]

The calculated and experimental temperature dependences of the photocurrent for a *p*-type GaAs sample with a hole density $p=7.4\times10^{16}$ cm^{-3} are compared in Fig. 1. It is evident from the figure that the best agreement between theory and experiment occurs in the vicinity of room temperature, and allowance for the photon contribution to the photocurrent in the temperature range $T>200$ K diminishes the discrepancy between the theoretical and experimental results by 30%. It is important to note that the above theory of photon mechanisms in the shift and ballistic LPV effects for *p*-GaAs does not involve any fitting parameters.

PRECESSION MECHANISM OF PHOTOVOLTAIC EFFECTS IN THE CASE OF A SIMPLE BAND

It is a well-known fact[6] that spin splitting of the conduction band takes place in crystals without an inversion center; in crystals of cubic symmetry (O_h) it is proportional to k^3, and in gyrotropic crystals (symmetry D_3) it is proportional to k, where $\mathbf{k}$ is the electron wave vector. Spin-orbit interaction induces not only rippling of the conduction band, but also direct optical transitions of electrons between spin branches

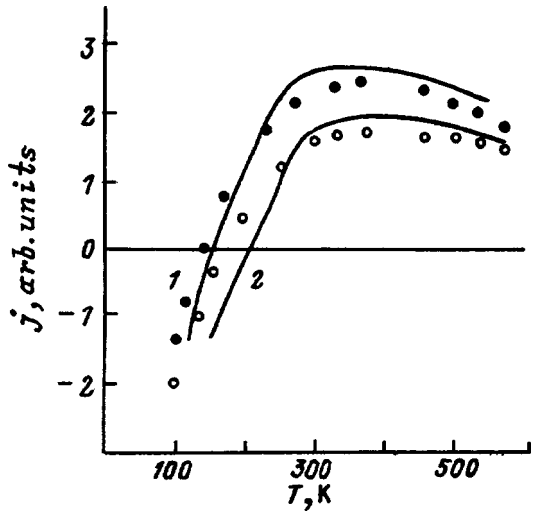

FIG. 1. Temperature dependence of the linear photovoltaic current for p-GaAs with a hole density $p=7.4\times10^{16}\,\mathrm{cm}^{-3}$. Wavelength: (*1*) $\lambda=10.6\,\mu$m; (*2*) $\lambda=9.5\,\mu$m. The points represent experimental data from Ref. 4, and the solid curves are calculated from the photon mechanism in the shift and ballistic linear photovoltaic effects.

at low temperatures and high hole densities, together with indirect optical transitions. It will be shown below that the possibility of such transitions leads to various optical and photovoltaic effects.

The state of conduction electrons in crystals of symmetry T_d is described by the Hamiltonian (see, e.g., Ref. 9 and the bibliography cited there)

$$\hat{H}=\frac{\hbar^2k^2}{2m_c}-\delta(\boldsymbol{\sigma}\mathbf{Q}), \tag{17}$$

and for tellurium[10]

$$\hat{H}=\frac{\hbar^2k^2}{2m_c}-\beta_c\sigma_zk_z+\alpha_c(\sigma_+k_-+\sigma_-k_+)+\delta_1(\sigma_+k_+^2+\sigma_-k_-^2)+i\delta_2k_+(k_-\sigma_+-k_+\sigma_-), \tag{18}$$

where

$\sigma_\pm=(\sigma_x\pm i\sigma_y)/2$, $k_\pm=k_x\pm ik_y$, $k_\perp^2=k_+k_-=k_x^2+k_y^2$,

$k_2=k_z^2+k_\perp^2$, $\mathbf{Q}=\mathbf{k}\times\boldsymbol{\pi}$, $\pi_i=k_{i+1}k_{i+2}$,

σ_α ($\alpha=x,y,z$) are the Pauli matrices, m_c is the effective mass of electrons at the bottom of the conduction band,

$$\delta_0=\hbar^3\gamma_c/2\sqrt{2m_c^3E_g},$$

E_g is the width of the band gap,[2)] and $\beta_c,\alpha_c,\delta_1$, and δ_2 are semiconductor band parameters characterizing the rippling of the energy spectrum, which is given by the relation

$$E_{\mathbf{k}}^{\pm}=\frac{\hbar^2k^2}{2m_c}\pm\Delta E. \tag{19}$$

Here $2\Delta E$ is the spin splitting:

$$\Delta E=\delta_0k^3\sqrt{f}$$

for III-V semiconductors;

$$\Delta E=\sqrt{\beta_c^2k_z^2+\alpha_c^2k_\perp^2}$$

for Te; $0\leqslant f\leqslant 1/4$,

$$f=O_z^2-O_z^4+O_x^2O_y^2(1-9O_z^2),\quad \mathbf{O}=\mathbf{k}/k.$$

We note that in tellurium the distortion of the electron energy spectrum in association with the last two terms in Eq. (2) is slight (see, e.g., Ref. 10).

The light absorption coefficient due to direct optical transitions with spin flip[3)] is given by the equation

$$K_{\mathrm{dir}}=\frac{e^2}{2\pi cn_\omega\hbar^2\omega}(1-e^{-\beta\hbar\omega})\times\int d^3\mathbf{k}|\mathbf{ep}_{\mathbf{k},\mathbf{k}}|^2f_0(E_{\mathbf{k}}^-)\delta(2\Delta E-\hbar\omega), \tag{20}$$

where $\beta^{-1}=k_BT$. For tellurium[4)] with σ-polarization ($\mathbf{e}\perp z$) we then have

$$K_{\mathrm{dir}}=\frac{e^2m_c\alpha_c^2}{4\pi cn_\omega\hbar^4\beta\beta_c\omega}e^{\beta E_F}(1-e^{-\beta\hbar\omega})\times\exp\beta\left(\frac{\hbar\omega}{2}-\frac{\hbar^2k_0^2}{2m_c}\right), \tag{21}$$

and for n-type III-V semiconductors the absorption coefficient is[5)]

$$K_{\mathrm{dir}}=\frac{e^2I'}{cn_\omega\omega\delta_0}(1-e^{-\beta\hbar\omega}), \tag{22}$$

where E_F is the chemical potential, $k_0=\hbar\omega/2\beta_c$, and

$$I'(\omega,T)=\frac{1}{4\pi}\int k\,dk\int d\,d\Omega f_0(E_{\mathbf{k}}^-)\delta(W_k-\sqrt{f}),$$

$$W_k=\hbar\omega/(2\delta_0k^3). \tag{23}$$

At low temperatures and in the presence of strong degeneracy electrons with momenta differing from the Fermi momentum $k_F\hbar$ by an amount of the order of $\delta_0m_ck_F^2\hbar$ can participate in optical transitions, including the direct kind, photon entrainment effects, and shift LPV effects involving spin flip, where

$$\delta=\delta_0\sqrt{2}/\sqrt{mE_g}$$

characterizes the intensity of spin-orbit interaction, and $m=2m_cm_v/(m_c+m_v)$, where m_v is the effective mass of holes at the top of the semiconductor valence band.

Calculations show that for strong degeneracy and low temperatures, i.e., in approximations where the density of electrons is defined as $n=k_F^3/3\pi^2$ (Ref. 9), for the z-component of the shift LPV current in n-type GaAs

$$J_z=e\frac{4e^2}{3cn_\omega\hbar}\frac{\delta_0(3\pi^2n)}{\hbar\omega}\frac{I}{\hbar\omega}(1-e^{-\beta\hbar\omega})e_xe_y, \tag{24}$$

and for tellurium

$$j_\alpha=-e\frac{e^2J_\alpha}{2\pi cn_\omega\hbar}\frac{I}{\hbar\omega}\frac{m_c\delta_1\delta_2}{\beta\hbar^3\omega\beta_\nu}f(\omega), \tag{25}$$

where

$$f(\omega)=e^{E_F\beta}\exp\beta\left(\frac{\hbar\omega}{2}-\frac{\hbar k_0^2}{2m_c}\right),$$

$$J_\alpha=[(|e_x|^2-|e_y|^2)\delta_{\alpha x}-(e_xe_y^*+e_ye_x^*)\delta_{\alpha y}].$$

Entrainment effects in *n*-type III-V semiconductors during direct transitions between spin branches were first investigated theoretically in Ref. 9 without regard for the contributions to the photon entrainment current due to the influence of the magnetic field of an electromagnetic wave on the electron magnetic moment[11] and due to inclusion of the photon wave vector ($\mathbf{q}$) in the momentum conservation law.[12] For these contributions we have the expression

$$\mathbf{J}_1=-\frac{7\pi}{3}\delta_0\frac{e^3(3\pi^2n)^{2/3}}{cn_\omega\hbar^2}\frac{I}{\hbar\omega}\mathbf{q}\tau_Fg, \tag{26}$$

which stems from the interaction described by the operator[11]

$$V_H=\frac{eA_0}{c\hbar}g\frac{\hbar^2}{2m_0}i\boldsymbol{\sigma}\cdot(\mathbf{q}\times\mathbf{e}), \tag{27}$$

where g is the electron Land factor, A_0 is the amplitude of the vector potential of the light wave, and

$$\mathbf{J}_2=-\frac{2\pi e}{m_c}K_{\rm dir}\tau_F\frac{\langle\mathbf{q}(\mathbf{k}\cdot\nabla_{\mathbf{k}}F)\delta(W_F-\sqrt{f})\rangle}{\langle F\delta(W_F-\sqrt{f})\rangle}. \tag{28}$$

The latter contribution arises when the photon momentum is taken into account in the momentum conservation laws, where the angle brackets $\langle\cdots\rangle$ signify angular averaging. Here $W_F=\hbar\omega/(2\delta_0k_F^3)$ is the reduced frequency, equal to the ratio of the photon energy to twice the maximum spin-orbit splitting energy in semiconductors of symmetry T_d (Ref. 9), and

$$F=k^{-4}(k^2-k_z^2)\{1-4W_F^{-2}k^{-6}[(k_x^2-k_y^2)^2-2k_x^2k_y^2]k_z^2\}. \tag{29}$$

The ratio of the shift LPV and photon entrainment currents in *n*-GaAs is equal to $4\sqrt{7}\,(3\pi^2n)^{1/3}/(3q\omega\tau_F)$, where $\tau_F=\tau(E=E_F)$. Here the photon energy is assumed to be approximately equal to the maximum spin-orbit splitting. The entrainment electron current density in Te can be written in the form

$$\mathbf{J}=-\frac{32}{3}e\frac{e^2}{cn_\omega\hbar}\frac{I}{\hbar\omega}\frac{\alpha_c^3(3\pi^2n)^{2/3}}{\hbar^3\omega^2}$$
$$\times\mathbf{q}\tau_F\left(1-\beta E_F+\frac{\partial\ln\tau_F}{\partial\ln E_F}+\frac{g}{24}\right). \tag{30}$$

We note that the inclusion of the photon wave vector in the momentum conservation law provides zero contribution to the photon entrainment current in Te. The possibilities of discriminating the currents due to the precession mechanisms of the photon entrainment and shift LPV effects occurring in both direct and indirect optical transitions are identical, so that for the shift LPV effect this problem must be treated exactly as in Ref. 9, where it is discussed for photon entrainment in semiconductors of symmetry T_d.

APPENDIX

We consider a semiconductor with a complex band. Let a charge carrier be situated in the lth subband of the mth level with energy $E_{l\mathbf{k}}$, and let the type of collision processes be characterized by the quantity $m_l=E_{l\mathbf{k}}/\hbar\Omega$, where $\hbar\Omega$ is the *LO*-phonon energy. The integral part of m_l is the number of *LO*-phonons emitted by the carrier. For $m_l>1$ the anisotropic part of the distribution function decreases as a result of scattering processes involving *LO*-phonons (and for $m_l<1$ it decreases on account of the scattering of carriers by acoustic phonons, impurities, etc., whose contribution we disregard). To calculate the distribution function, we expand it in Legendre polynomials $P_m(x)$, $x=\mathbf{k}\cdot\mathbf{k}'/kk'$:

$$f_{lk}^{(m)}=\sum_{n=0}^{2}b_{nl}^{(m)}P_n(x), \tag{A.1}$$

where $b_{0l}^{(m)}$ is a coefficient characterizing the density of carriers in the lth subband at the mth level, and $b_{1l}^{(m)}$ and $b_{2l}^{(m)}$ are coefficients characterizing the diagonal and off-diagonal (with respect to the band orders) contributions to the LPV current. Now the variation of the anisotropic part of the distribution function in transition from the state $(m',l',\mathbf{k}')$ to the state $(m,l,\mathbf{k})$ by virtue of the emission $(m'=m+1)$ and absorption $(m'=m-1)$ of an *LO*-phonon is given by the relation

$$\frac{b_{nl'}^{(m')}}{b_{0l}^{(m)}}=\frac{\int_{-1}^{+1}P_n(x)G_{l'l}(x)(z_{l'l}-x)^{-1}dx}{\int_{-1}^{+1}G_{l'l}(x)(z_{l'l}-x)^{-1}dx}. \tag{A.2}$$

Here[13]

$$G_{l'l}(x)=\frac{1}{2}[P_0+(-1)^{l+l'}P_2],\quad z_{l'l}=\frac{k_l^2+k_{l'}^2}{2k_lk_{l'}},$$

$$k_l=(2m_l^*E_{lm}\hbar^{-2})^{1/2},\quad k_{l'}=k_l(l\to l'), \tag{A.3}$$

$E_{lm}=E_{l\mathbf{k}}+m\hbar\Omega$, $E_{l'm'}$ are determined from the energy conservation law, $E_{l'm'}=E_{lm}\pm\hbar\Omega$, where the plus sign corresponds to absorption, and the minus sign to emission, of an *LO*-phonon; $m,m'=0,1,2,\ldots$. Substituting Eq. (33) into (32), we then have

$$\frac{b_{nl'}^{(m')}}{b_{ml}^{(m)}}=\frac{G_{l'l}^{(n)}(z_{l'l})}{G_{l'l}^{(0)}(z_{l'l})}, \tag{A.4}$$

where

$$G_{l'l}^{(0)}=\frac{1}{2}[Q_0^{(0)}+(-1)^{l+l'}(3Q_2^{(2)}-Q_0^{(2)})/2],$$

$$G_{l'l}^{(1)}=\frac{1}{2}[Q_1^{(0)}+(-1)^{l+l'}(3Q_3^{(2)}+2Q_1^{(2)})/5], \tag{A.5}$$

$$G_{l'l}^{(2)}=\frac{1}{2}[Q_3^{(0)}+(-1)^{l+l'}(36Q_4^{(2)}+55Q_2^{(2)}+14Q_0^{(2)})/105],$$

$$Q_n^{(n')}=Q_n^{(n')}(z_{l'l})=\int P_n(x)P_{n'}(x)(z_{l'l}-x)^{-1}dx.$$

Assuming that $l=l'$, for $n=2$ we at once obtain from Eq. (34) the expression derived in Ref. 14 to describe the decrease in the anisotropic part of the photoelectron distribution function in the conduction band. For a simple parabolic band we obtain the following expression from Eq. (34):

$$\frac{b_{1l}^{(m')}}{b_{1l}^{(m)}}=\frac{m+m'}{2\sqrt{mm'}}-\ln^{-1}\left|\frac{\sqrt{m'}+\sqrt{m}}{\sqrt{m'}-\sqrt{m}}\right|, \tag{A.6}$$

where m and m' are the carrier energies before and after the emission or absorption of an *LO*-phonon in units of $\hbar\Omega$.

We note that for large values of m (and m') the ratios b_{+1}/b_0 and b_{-1}/b_0 differ very little from one another. For example, if $E_m=10\hbar\Omega$, these ratios assume values of the order of 0.7 for gallium arsenide, implying that the anisotropic part of the distribution function in the first stage of the cascade scattering process decreases by a factor of 1.4.

[1)]The ratio obtained for the total current is $|a_{\text{tot}}|/|b_{\text{tot}}|\simeq 5$, in agreement with the experimental data, according to which $|a_{\text{tot}}|\gg|b_{\text{tot}}|$, whereas for the photon mechanism we have $|a_{\text{tot}}|/|b_{\text{tot}}|\simeq 10$.

[2)]The value of $|\gamma_c|$ determined from the spin relaxation time of electrons for gallium arsenide, according to Ref. 5, is equal to 0.022.

[3)]The photon entrainment effect and the linear photovoltaic effect have been investigated earlier without regard for spin flip.[8]

[4)]The spin-orbit splitting of the conduction band in Te is much greater than in III-V semiconductors. Consequently, a number of polarization optical and photovoltaic effects[9] can be detected by simpler methods.

[5)]An expression for $I'(\omega, T)$ has been derived previously[3] for the case of strong degeneracy.

[1] B. I. Sturman and V. J. Fridkin, *Photovoltaic Effect in Media Without a Center of Symmetry and Related Phenomena* [in Russian], Nauka, Moscow, 1992.
[2] E. L. Ivchenko, G. E. Pikus, and R. Ya. Rasulov, Fiz. Tverd. Tela (Leningrad) **26**, 3362 (1984) [Sov. Phys. Solid State **26**, 2020 (1984)].
[3] Yu. B. Lyanda-Geller and R. Ya. Rasulov, Fiz. Tverd. Tela (Leningrad) **27**, 945 (1985) [Sov. Phys. Solid State **27**, 577 (1985)].
[4] A. V. Andrianov, É. L. Ivchenko, G. E. Pikus, R. Ya. Rasulov, and I. D. Yaroshetskiĭ, Zh. Éksp. Teor. Fiz. **81**, 2080 (1981) [Sov. Phys. JETP **54**, 1105 (1981)].
[5] A. N. Titkov, V. I. Safarov, and G. Lampel, in *Proceedings of the 14th International Conference on the Physics of Semiconductors* (Edinburgh, 1978), p. 1031.
[6] V. I. Belinicher, E. L. Ivchenko, and B. I. Sturman, Zh. Éksp. Teor. Fiz. **83**, 649 (1982) [Sov. Phys. JETP **56**, 359 (1982)].
[7] G. L. Bir and G. E. Pikus, *Symmetry and Strain-Induced Effects in Semiconductors* (Israel Program for Scientific Translations, Jerusalem; Wiley, New York, 1975; Nauka, Moscow, 1972).
[8] R. Ya. Rasulov, Author's Abstract of Doctoral Dissertation [in Russian], St. Petersburg, 1993.
[9] S. B. Arifzhonov and A. M. Danishevskiĭ, Fiz. Tverd. Tela (Leningrad) **15**, 2626 (1973) [Sov. Phys. Solid State **15**, 1747 (1973)].
[10] E. L. Ivchenko and G. E. Pikus, Fiz. Tverd. Tela (Leningrad) **16**, 1933 (1974) [Sov. Phys. Solid State **16**, 1261 (1974)].
[11] F. T. Vas'ko, Fiz. Tekh. Poluprovodn. **18**, 86 (1984) [Sov. Phys. Semicond. **18**, 51 (1984)].
[12] É. Normantas, Fiz. Tekh. Poluprovodn. **16**, 2222 (1982) [Sov. Phys. Semicond. **16**, 1438 (1982)].
[13] G. L. Bir, É. Normantas, and G. E. Pikus, Fiz. Tverd. Tela (Leningrad) **4**, 1180 (1962) [Sov. Phys. Solid State **4**, 867 (1962)].
[14] B. P. Zakharchenya, D. I. Mirlin, V. I. Perel', and I. I. Reshina, Usp. Fiz. Nauk **136**, 459 (1982) [Sov. Phys. Usp. **25**, 143 (1982)].

Translated by James S. Wood

SEMICONDUCTOR STRUCTURES, INTERFACES AND SURFACES

Ultrashallow p^+-n junctions in Si(111): electron-beam diagnostics of the surface region

N. T. Bagraev, L. E. Klyachkin, and A. M. Malyarenko

A. F. Ioffe Physicotechnical Institute, Russian Academy of Sciences, 194021 St.Petersburg, Russia

A. A. Andronov and S. V. Robozerov

State Technical University of St. Petersburg, 195251 St. Petersburg, Russia

(Submitted April 22, 1998; accepted for publication April 23, 1998)
Fiz. Tekh. Poluprovodn. **33**, 58–63 (January 1999)

Ultrashallow p^+-n junctions fabricated in Si(111) are investigated by low- and intermediate-energy electron-beam probing of the surface region in order to determine how the crystallographic orientation of the silicon films affects the mechanisms for nonequilibrium diffusion of boron. A comparative study is made of p^+-n junctions made on both (111) and (100) silicon with regard to how the irradiation-induced conductivity depends on the energy of the primary electron beam, and also its distribution with area. Using this method, it is possible to determine how the probability of an electron-hole pair being separated by the electric field of the Si(111) and Si(100) p^+-n junctions varies with depth into the crystal, which experiments show is different, depending on whether diffusive motion of impurities is dominated by the kick-out or dissociative-vacancy mechanisms. It was found that for boron in silicon the kick-out type of diffusion mechanism is strongly enhanced in the [111] crystallographic direction, whereas diffusion in the [100] direction is primarily driven by vacancy mechanisms. It is shown that collection of nonequilibrium carriers in the p^+-n junction field is strongly enhanced when the diffusion profile consists of certain combinations of longitudinal and transverse quantum wells. [S1063-7826(99)01301-0]

1. INTRODUCTION

When single-crystal silicon acts as a getter of oxygen at a silicon-SiO_2 boundary, excess fluxes of vacancies or intrinsic interstitial atoms are generated at the boundary interface. As these defects migrate into the silicon, they drag impurity atoms along with them. Study of the distinctive features in the annealing and generation of these defects as they migrate could lead to practical use of this effect to obtain ultrashallow diffusion profiles of boron and phosphorus with a sharp boundary.[1,2] The depth and properties of ultrashallow diffusion- induced p^+-n junctions depends on the thickness of the predeposited oxide, the diffusion temperature, and the crystallographic orientation of the silicon single crystals. These parameters determine the intensity of the exchange interaction between doping impurities and intrinsic interstitial atoms and nonequilibrium vacancies, which stimulate impurity diffusion via either the kick-out or vacancy mechanisms, respectively.[1–4] In this paper we describe the results of our studies of how crystallographic anisotropy of these diffusion mechanisms influences the transport properties of nonequilibrium carriers in ultrashallow p^+-n junctions made in Si(100) and Si(111). Our experimental method is based on probing the surface region with low- and high-energy electrons,[5,6] which allows us to determine how the probability of separation of electron-hole pairs by the field of the p^+-n junction varies with depth into the Si crystal.

2. OBTAINING ULTRASHALLOW p^+-n JUNCTIONS IN SILICON

Ultrashallow p^+-n-junctions were made by diffusion of boron into *n*-type silicon single crystal films with a thickness of 350 μm and various resistivities: for Si(100), $\rho \cong 1.0$ and $20\,\Omega\cdot$cm, and for Si(111), $\rho \cong 5$ and $90\,\Omega\cdot$cm. The first step in fabicating the p^+-n junctions was to oxidize both sides of the film in dry oxygen at 1150 °C, after which circular windows 3 mm in diameter were opened in the oxide layer on the working side of the film by photolithography. These windows were then exposed to gas-phase boron, which was allowed to diffuse into the Si for a short time (4 min). In the course of these studies, we varied the diffusion temperature (800, 900, and 1100 °C) while holding the thickness of predeposited surface oxide constant. This procedure allowed us to simulate conditions for the kick-out and vacancy impurity diffusion mechanisms.[1,4] Making the thickness of predeposited oxide on both sides of the film greater than $d_0 \cong 0.44$ μm provided additional injection of vacancies at all the diffusion temperatures used.[3] The high concentrations of intrinsic interstitial atoms and vacancies responsible for dragging and braking the doping impurity

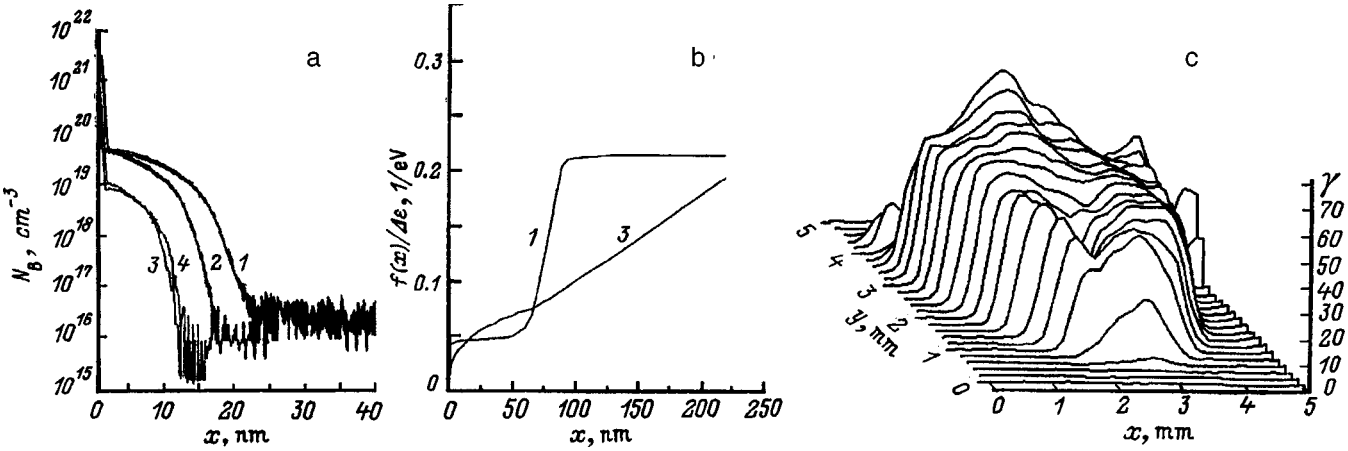

FIG. 1. Boron concentration profile N_B (a) and collection function (b) in silicon p^+-n structures obtained at $T_{dif}=1100$ °C. Film crystallographic orientations: *1, 2* — (111); *3, 4* — (100); original doping level of phosphorus substrate N(P), cm^{-3}: *1* — 9×10^{14}, *2* — 5×10^{13}, *3* — 5×10^{15}, *4* — 5×10^{14}. (c) sample raster image of the distribution of irradiation conductivity over the surface of the structure for excited electron energy $E_p=1800$ eV and N(P)$=5\times10^{13}$ cm^{-3}.

atoms were provided by adding dry oxygen and chlorine compounds to the boron-containing gas phase during the diffusion process. During the final stage of the fabrication process, ohmic contacts were made along the perimeter of the windows and from the back side of the films. The spatial distribution of boron concentration in these ultrashallow diffusion profiles was determined by secondary-ion mass spectrometry (SIMS).[1,2,7]

3. ELECTRON-BEAM DIAGNOSTICS OF SURFACE LAYERS OF SINGLE-CRYSTAL SILICON

The small diffusion depth of the p^+ profile (5–30 nm) in these ultrashallow p^+-n junctions favors the use of irradiation conductivity created by a focused electron beam to study them.[5,6] Varying the energy of the electron beam (E_p) in the range from 0.1 to 3.0 keV smoothly varies the probing depth from 2 to 250 nm.[5] Moreover, by scanning the electron beam along the area of the structure under study we can estimate the degree of uniformity of the doping impurity distribution within the diffusion window.[6] The experimental dependences of the irradiation conductivity on beam energy $\gamma(E_p)$ can be processed using regularizing algorithms from the theory of ill-posed problems, making it possible to recover the unknown collection function $f(x)$ for nonequilibrium carriers that enters into the integral equation

$$\gamma(E_p)=\int_0^\infty \frac{g(E_p,x)}{\Delta\varepsilon} f(x)\,dx, \qquad (1)$$

where $g(E_p,x)$ is the one-dimensional distribution of specific energy loss by primary electrons with respect to depth into the silicon, $\Delta\varepsilon$ is the average energy expended in generating a single electron-hole pair, and $f(x)$ is the collection function of the p^+-n junction,[5,8] which determines the number of electron-hole pairs excited at a depth x that are capable of contributing to the induced current. For irradiation by electrons with energies in the range 0.1 to 3.0 keV, the function $f(x)$ can be studied directly within the limits of the space-charge region of the p^+-n junction. The behavior of $f(x)$ in this region is related to the probability of separation of electron-hole pairs by the p^+-n junction field, and is determined primarily by the nonequilibrium carrier lifetime and electric-field distribution.

4. CHARACTERISTICS OF ULTRASHALLOW p^+-n JUNCTIONS ARISING FROM CRYSTALLOGRAPHIC ANISOTROPY OF THE MECHANISMS FOR NONEQUILIBRIUM IMPURITY DIFFUSION

Figures 1–3 show the results of our studies of ultrashallow p^+-n junctions formed at various diffusion temperatures on the surface of single- crystal Si films with (100) and (111) orientation and *n*- type conductivity. At temperatures of 1100 and 800 °C, boron penetrates into the single-crystal silicon under conditions dominated by kick-out and vacancy mechanisms for impurity diffusion (Figs. 1a and 2a).[1,2] In both cases the diffusion process is accelerated by an intense exchange interaction between impurity atoms and defects—intrinsic interstitial atoms in the first case and vacancies in the second.[1,2] The velocity of the diffusion leading edge is found to be a minimum at $T=900$ °C due to the approximately equal contributions of various diffusion mechanisms, which lead to complete elimination of intrinsic interstitial atoms and vacancies near the working surface of the silicon film (Fig. 3a). Diffusion profiles obtained under conditions of short-time nonequilibrium diffusion differ in shape from the classical profiles. The boron profile is ultrashallow, both when impurity diffusion is suppressed (Fig. 3a) and when it is accelerated (Figs. 1a and 2a), which is further evidence of the important role played by dragging of doping impurities by vacancies and intrinsic interstitial silicon atoms in impurity diffusion.

By diffusing boron into single-crystal silicon at $T=1100$ °C, i.e., under conditions where the dominant mechanism is the kick-out type, we ensure that the diffusion profile lies deeper in the crystal. However, the concentration of doping impurities on lattice sites (Fig. 1a) is lower than it is when the diffusion takes place at 800 °C, i.e., when vacancy-

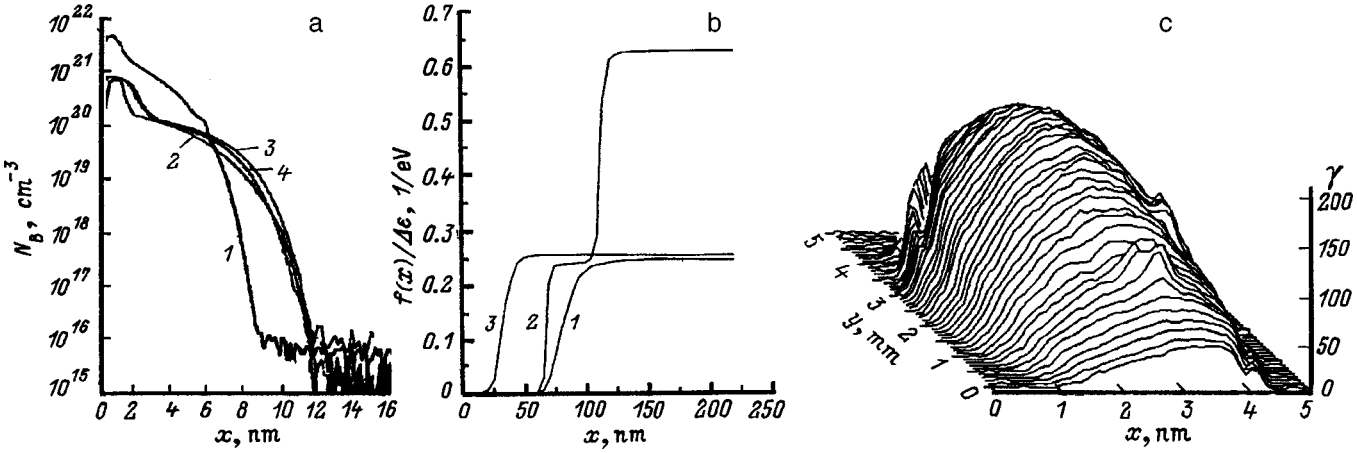

FIG. 2. Boron concentration profile N_B (a) and collection function (b) in silicon p^+-n structures obtained at $T_{diff}=800$ °C. Film crystallographic orientations: *1, 2* — (111); *3, 4* — (100); original doping level of phosphorus substrate N(P), cm^{-3}: *1* — 9×10^{14}, *2* — 5×10^{13}, *3* — 5×10^{15}, *4* — 3×10^{14}. (c) sample raster image of the distribution of irradiation conductivity over the surface of the structure for excited electron energy $E_p=1800$ eV and N(P)$=9\times10^{14}$ cm^{-3}.

related diffusion mechanisms operate (Fig. 2a).

A clear indicator[9,10] of how the kick-out type of diffusion mechanism is enhanced as the crystallographic orientation for the sample changes from (100) to (111) is the corresponding increase in the depth of the diffusion profile (Fig. 1a). Furthermore, the impurity diffusion coefficient depends on the charge state both of the diffusing impurity and the intrinsic interstitial silicon atom,[11] whereas their diffusion process is most effective in *n*- and *p*-type samples and is relatively suppressed in lightly doped silicon (Fig. 1a). This implies that a major contribution to the impurity-⟨interstitial silicon atom⟩ type of exchange interaction, on which the mechanism for the kick-out type of diffusion in a silicon lattice is based, comes from rearrangement involving a boron and an interstitial silicon ion:

$$(B_iV_{Si})^- + Si_i^+ \rightarrow Si_i^0 + B_s^0 . \qquad (2)$$

Here $(B_iV_{Si})^-$ is a center with symmetry C_{3V} (Ref. 12), whereas B_s^0 and $(B_iV_{Si})^+$ form centers with symmetries T_d and D_{2d} (Refs. 12 and 13).

Because rearrangement of negatively charged acceptors takes place predominantly along the [111] axis, this crystallographic direction determines the maximum effectiveness for nonequilibrium diffusion via stimulated injection of excess interstitial silicon atoms. It is noteworthy that the rate of reaction (2), which depends on the rate at which impurity and intrinsic ions are generated by trapping of electrons and holes from the conduction and valence bands, is in principle an indicator of the original degree of doping of the *n*-type silicon. Because the capture cross section for thermally excited electrons by boron acceptors

$$B_s^0 + e \rightarrow (B_iV_{Si})^- ,$$

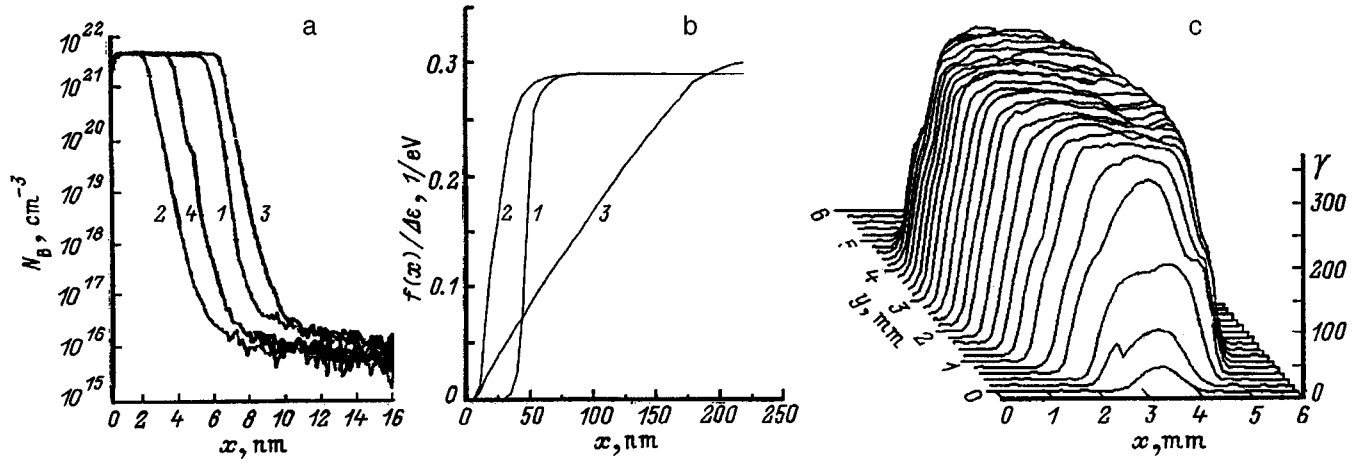

FIG. 3. Boron concentration profile N_B (a) and collection function (b) in silicon p^+-n structures obtained at $T_{diff}=900$ °C. Film crystallographic orientations: *1, 2* — (111); *3, 4* — (100); original doping level of phosphorus substrate N(P), cm^{-3}: *1* — 9×10^{14}, *2* — 5×10^{13}, *3* — 5×10^{15}, *4* — 3×10^{14}. (c) sample raster image of the distribution of irradiation conductivity over the surface of the structure for excited electron energy $E_p=1800$ eV and N(P)$=5\times10^{13}$ cm^{-3}.

is larger than the analogous capture cross section for amphoteric interstitial silicon

$$Si_i^0 + e \rightarrow Si_i^- ,$$

the most effective process is found to be an Auger process, which induces recombination of thermally excited carriers via the diffusing boron atoms dragged by the flux of interstitial silicon atoms:

$$2(e+h) + B_s^0 + Si_i^0 \rightarrow (B_i V_{Si})^- + Si_i^+ + e + h \rightarrow B_s^0 + Si_i^0 . \quad (3)$$

Therefore, reaction (2), which describes impurity diffusion accompanied by charging of the diffusive component, has its highest rate in heavily doped silicon of either conductivity type, due to the high probability for generation of thermally excited holes (see Fig. 1a). Consequently, nonequilibrium diffusion of boron in silicon films with crystallographic orientation (111) under conditions where the kick-out type of mechanism dominates can be enhanced by increasing the concentration of original donor impurities.

Electron-beam probing of $p^+ - n$ junctions obtained under conditions where the dominant mechanism for diffusion is the kick-out type shows that an increase in the collection function, which reflects the depth distribution of recombination-active centers, accompanies the increased depth of the diffusion p^+-profile as the crystallographic orientation of the film is changed from (100) to (111) (Fig. 1b). This is associated with enhancement of the excess fluxes of intrinsic interstitial atoms in the direction [111], which stimulates gettering in the bulk of the film and decreases the concentration of point defects that are centers of recombination for nonequilibrium carriers near the film's working surface. This improvement in the transport properties of nonequilibrium carriers is also reflected in the shape of their collection function (curve *1*, Fig. 1b), whose abrupt increase at $x \approx 50$ nm is connected with multiplication of holes and electrons within a diffusion profile that is a combination of longitudinal and transverse quantum wells.[14] A raster image of the distribution of excitation photoconductivity shows that the mobility of intrinsic interstitial atoms in Si(111) is sufficient for generation of a uniform $p^+ - n$ junction over the entire area of an open window (Fig. 1c). In contrast to analogous raster pictures of $p^+ - n$ junctions in Si(100),[6] the image obtained does not exhibit any suppression of excitation photoconductivity near the boundaries of the open window, due to the rapid annihilation of vacancies and intrinsic interstitial atoms that form continuously at the silicon-oxide boundary. This is connected with a lower average diffusion length of vacancies, one that is considerably lower in the [111] direction than it is for Si(100) films.[1,3,9,10]

The impurity concentration within these ultrashallow diffusion profiles increases at low diffusion temperatures (800 °C) under conditions where vacancy mechanisms for nonequilibrium impurity diffusion play a decisive role (Fig. 2a). Even though the diffusion temperature and oxide thickness favor the formation of a diffusion p^+-profile, $p^+ - n$ junctions obtained in Si(111) films are shallower than analogous $p^+ - n$ junctions created in Si(100), and not so uniformly distributed over the area of the open window (Figs. 2a and 2c; see Ref. 6). This behavior is also attributable to the fact that the [100] crystallographic direction in silicon is most favorable for motion of vacancies. Furthermore, the boron-vacancy exchange interaction weakens as the original concentration of phosphorus increases (see Fig. 2a, curves *1* and *2*). This implies that the position of the Fermi level in *n*-type silicon determines the rate of nonequilibrium impurity diffusion mediated by vacancy mechanisms involving the interaction of charged boron centers and ionized vacancies:

$$B_s^- + V_{Si}^+ \rightarrow V_{Si}^0 + B_s^0 . \quad (4)$$

Because the V^+ vacancy with energy $E_V + 0.13$ eV in silicon is a center with symmetry D_{2d} (Ref. 15), injection of excess vacancies most effectively accelerates impurity diffusion in the [100] direction. This process is primarily controlled by the generation of negatively charged boron centers ($E_V + 0.044$ eV) and positively charged vacancies via trapping of electrons and holes from the valence band:

$$B_s^0 + V_{Si}^0 \rightarrow (B_i V_{Si})^- + V_{Si}^0 + h \rightarrow (B_i V_{Si})^- + V_{Si}^+ \rightarrow V_{Si}^0 + B_s^0 . \quad (5)$$

Consequently, increasing the initial concentration of donor impurities decreases the concentration of positively charged vacancies, thereby braking the diffusion process when excess vacancies are injected (Fig. 2a). The decreased rate of impurity diffusion in the (111) direction also leads to the generation of vacancy complexes near the boundary of the $p^+ - n$ junction, which strongly decreases the lifetime of nonequilibrium carriers.[16,17] [In this case, the role of the back face of the film in suppressing impurity diffusion via oppositely-moving vacancy fluxes will be considerably weaker in Si(111) than in Si(100).] The discussion given here explains the increase in the ''dead layer'' region, reflected in the step-like shape of the collection function $f(x)$, in which excited electron-hole pairs do not participate in generating irradiation conductivity because of the small carrier lifetime and the presence of longitudinal quantum wells (parallel to the plane of the $p^+ - n$ junction) within the diffusion p^+- profile[6,14] (Fig. 2b). In certain cases the presence of a combination of longitudinal and transverse quantum wells[14] leads to a step-like shape for $f(x)$ (Fig. 2b, curve *2*) for the same reasons as when the kick-out type of impurity diffusion mechanism dominates (Fig. 1b).

The high doping impurity concentrations within the diffusion profile obtained when the mechanisms discussed above are equally effective indicate the important role of surface vacancy injection in creating $p^+ - n$ junctions (Fig. 3a). Nevertheless, the fact that the depth of the diffusion profile and concentration of shallow donors in *n*-type silicon both increase as the orientation is changed from (100) to (111) indicates a certain dominance of the kick-out type of impurity diffusion mechanism under these conditions ($T_{diff} = 900$ °C). Moreover, because the rate of diffusion is lower over the entire area where the $p^+ - n$ junction forms, it is possible to reach steady-state conditions. This makes it possible to obtain $p^+ - n$ junctions with doping impurity distributions that are independent of the crystallographic orientation of the film (see Fig. 3c of Ref. 6). The results of electron-beam probing demonstrate that the collection func-

tion increases under conditions of weak dominance by the kick-out type of diffusion mechanism at $T=900\,^{\circ}\mathrm{C}$ in Si(111) (Fig. 3b). Comparative analysis of the data given in Fig. 3b indicate that changing the crystallographic orientation of the silicon films from (100) to (111) increases the gettering efficiency of secondary defects from the region of the $p^{+}-n$ junction. Thus, $p^{+}-n$ junctions in Si(111) obtained under conditions where the diffusion mechanisms are equally effective collect excited nonequilibrium carriers most efficiently.

5. CONCLUSIONS

Electron-beam diagnostics of the surface region of ultrashallow diffusion $p^{+}-n$ junctions makes it possible to identify the role of crystallographic orientation of silicon films in the mechanisms for nonequilibrium impurity diffusion. It is observed that the kick-out type of diffusion mechanism is strongly enhanced in the [111] crystallographic direction, whereas the [100] direction favors impurity diffusion under conditions where vacancy mechanisms dominate. It is shown that collection of nonequilibrium carriers in the field of a $p^{+}-n$ junction can be strongly enhanced if the diffusion profile consists of certain combinations of longitudinal and transverse quantum wells.

This work was carried out in part with the support of the G. Soros International Science Fund (Project NTX300 in 1995), the State Committee of the Russian Federation on Higher Education (a grant for investigations in the areas of electronics and radio engineering), the State Program ''Physics of Solid-State Nanostructures'' (Project 97-1040), PTUMNE (Project 02.04.301.89.5.2) and the Federal Program ''Integration'' (Project 75 : 2.1).

[1] N. T. Bagraev, W. Gehlhoff, L. E. Klyachkin, and A. Naeser, Defect Diffus. Forum **143–147**, 1003 (1997).
[2] N. T. Bagraev, L. E. Klyachkin, and V. L. Sukhanov, Defect Diffus. Forum **103–105**, 192 (1993).
[3] W. Frank, U. Gosele, H. Mehrer, and A. Seeger, *Diffusion in Crystalline Solids* (Academic Press, 1984), p. 63.
[4] E. Antoncik, J. Electrochem. Soc. **141**, 3593 (1994).
[5] A. N. Andronov, N. T. Bagraev, L. E. Klyachkin, V. L. Sukhanov, S. V. Robozerov, and N. S. Faradzhev, Fiz. Tekh. Poluprovodn. **28**, 2049 (1994) [Semiconductors **28**, 1128 (1994)].
[6] A. N. Andronov, N. T. Bagraev, L. E. Klyachkin, and S. V. Robozerov, Fiz. Tekh. Poluprovodn. **32**, 137 (1998)) [Semiconductors **32**, 124 (1998)].
[7] P. S. Zalm, Rep. Prog. Phys. **58**, 1321 (1995).
[8] E. N. Patyshev and D. V. Kuzichev, Meas. Tech. No. 9, 3 (1991).
[9] S. Mizho and H. Higuchi, Jpn. J. Appl. Phys. **20**, 739 (1981).
[10] *Atomic Diffusion in Semiconductors*, edited by D. Shaw (Plenum Press, London, 1973; Mir, Moscow, 1975).
[11] R. B. Fair, Diffus. Defect Data **37**, 1 (1984).
[12] N. T. Bagraev, E. V. Vladimirskaya, V. E. Gasumyants, V. I. Kaĭdanov, V. V. Kveder, L. E. Klyachkin, A. M. Malyarenko, and E. I. Chaĭkina, Fiz. Tekh. Poluprovodn. **29**, 2133 (1995) [Semiconductors **29**, 1112 (1995)].
[13] D. E. Onopko, N. T. Bagraev, and A. I. Ryskin, Fiz. Tverd. Tela (St. Petersburg) **37**, 2376 (1995) [Phys. Solid State **37**, 1299 (1995)].
[14] N. T. Bagraev, W. Gehlhoff, L. E. Klyachkin, A. M. Malyarenko, and A. Naeser, Mater. Sci. Forum **258–263**, 1683 (1997).
[15] G. D. Watkins, *Deep Centers in Semiconductors*, edited by S. T. Pantelides (Gordon & Breach, New York, 1986), p. 87.
[16] N. T. Bagraev, I. S. Polovtsev, and K. Schmalz, Phys. Status Solidi A **113**, 233 (1989).
[17] K. Schmalz, F. -G. Kirscht, H. Klose, H. Richter, and K. Tittelbach-Helmrich, Phys. Status Solidi A **100**, 567 (1987).

Translated by Frank J. Crowne

Investigating the photosensitivity spectra of n-type GaAs–As_2Se_3 heterojunctions

I. P. Arzhanukhina, K. P. Kornev, and U. V. Seleznev

Kaliningrad State University, 236041 Kaliningrad, Russia
(Submitted May 5, 1997; accepted for publication June 30, 1998)
Fiz. Tekh. Poluprovodn. **33**, 64–67 (January 1999)

The spectral photoresponse characteristics of heterojunctions made with *n*-type GaAs and amorphous films of As_2Se_3 are investigated for various thicknesses of the chalcogenide-glass semiconductor film. Expressions are obtained for calculating the following quantities: the fraction of light absorbed in the chalcogenide-glass semiconductor; the fraction of light absorbed in the GaAs, taking into account multiple reflections within the structure; and their ratio. Light absorption in the structure is analyzed, and the origin of the heterostructure photoresponse is modeled. Experimental results are found to be in agreement with the theoretical calculations. © *1999 American Institute of Physics.* [S1063-7826(99)01401-5]

INTRODUCTION

The majority of papers devoted to investigating the properties of heterojunctions have dealt with heterojunctions based on crystalline materials. Such heterojunctions have already found application as radio-engineering elements, photodetectors, and injection lasers.[1,2] Recently, a search has begun for new heterostructure materials and concepts, including crystal-amorphous film heterojunctions.[3–5] These heterojunctions are interesting because it is possible to intentionally change their properties by changing the composition of the amorphous films. In this paper we will describe our studies of the photosensitivity spectrum of heterojunctions made with epitaxial *n*-GaAs and an amorphous film of As_2Se_3.

SAMPLE PREPARATION AND METHOD OF INVESTIGATION

In order to obtain the photosensitivity spectra of a *n*-GaAs–As_2Se_3 heterojunction, we first made a Al–*i*-GaAs–*n*-GaAs–As_2Se_3–Al structure. The heterojunctions were made from single-crystal samples of intrinsic gallium arsenide, on whose surface was grown an epitaxial layer with *n*-type conductivity. In all the samples, the carrier concentration in the epitaxial layers was of the order of $1\times10^{22}\,m^{-3}$. In order to obtain a heterojunction we deposited a layer of the chalcogenide glass semiconductor As_2Se_3 on the epitaxial layer of GaAs by thermal sputtering in vacuum. In making the heterojunctions we varied the thickness of the chalcogenide glass semiconductor (CGS) from 0.3 to 5 μm. We then deposited semitransparent but thick layers of aluminum on the film surface by vacuum sputtering. Before sputtering on the thick layer, we covered the central portion of the sample with a mask, beneath which the semitransparent layer of aluminum was preserved. This layer served simultaneously as a collector electrode and a window through which the heterostructure could be illuminated. We also deposited a thick layer of aluminum on the back side of the intrinsic GaAs substrate in order to contact the sample from the back.

Our method of investigating the photosensitivity spectra, and also our measurement apparatus, were described in our study[6] which was published previously. Measurements were made with both positive and negative voltages on the collector electrode. The magnitude of the voltage U_C could be varied from 0 to 20 V.

RESULTS

We investigated the photoresponse spectral characteristics of heterostructures with CGS film thicknesses of 0.3, 1, and 5 μm. By changing the film thickness we were able to vary the region of maximum sensitivity of the heterostructure. Figure 1 shows the photoresponse spectral characteristics of heterostructures with various CGS film thicknesses. These plots were obtained for $U_C=1$ V and are normalized to the value of the maximum photoresponse. For heterostructures with a CGS film thickness of 0.3 μm, the photoresponse spectral characteristic has one maximum in the range of optical photon energies of 1.4 eV. For a heterostructure with a CGS thickness of 1 μm, two maxima were observed in the photoresponse spectral characteristic, one at $h\nu=1.4$ eV and one at $h\nu=1.85$ eV. The peak associated with photoconductivity of gallium arsenide is virtually unobservable on the third curve, which was plotted for a heterostructure with a CGS film thickness of 5 μm; here the main contribution to the photoconductivity comes from the As_2Se_3. The photosensitivity maximum in this case lies in the range 1.9 eV (Fig. 1). The response curves obtained at high voltages on the collector electrode (Fig. 2) provide evidence that the photoresponse spectral characteristic of a heterostructure with an arsenic triselenide film thickness $d=1\,\mu$m is derived from the GaAs and As_2Se_3 photoconductivity. The curves shown in this figure clearly exhibit two peaks, one at photon energy $h\nu=$ 1.4 eV (the GaAs photoconductivity) and a second at photon energy $h\nu=$ 1.95 eV (the As_2Se_3 photoconductivity).

In investigating the photoresponse spectral characteristics of heterostructures with various thicknesses of the CGS film we can compare the experimental results with calculations that take into account absorption in the semiconductor layer with multiple reflections from the layer boundaries that

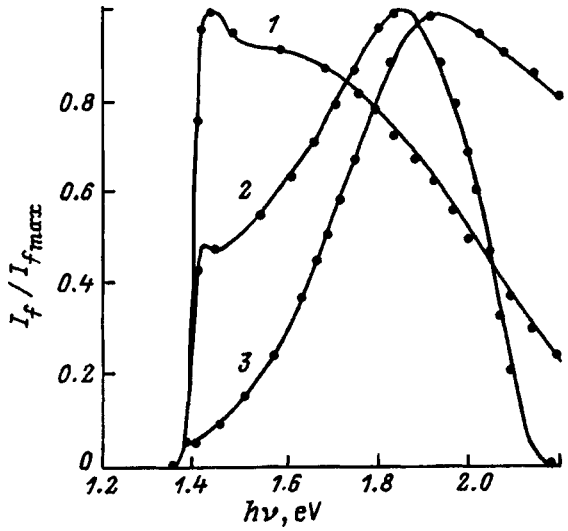

FIG. 1. Spectral characteristics of the photoresponse of an *n*-GaAs-arsenic triselenide heterostructure at various CGS film thicknesses d, μm: *1* — 0.3, *2* — 1, *3* — 5.

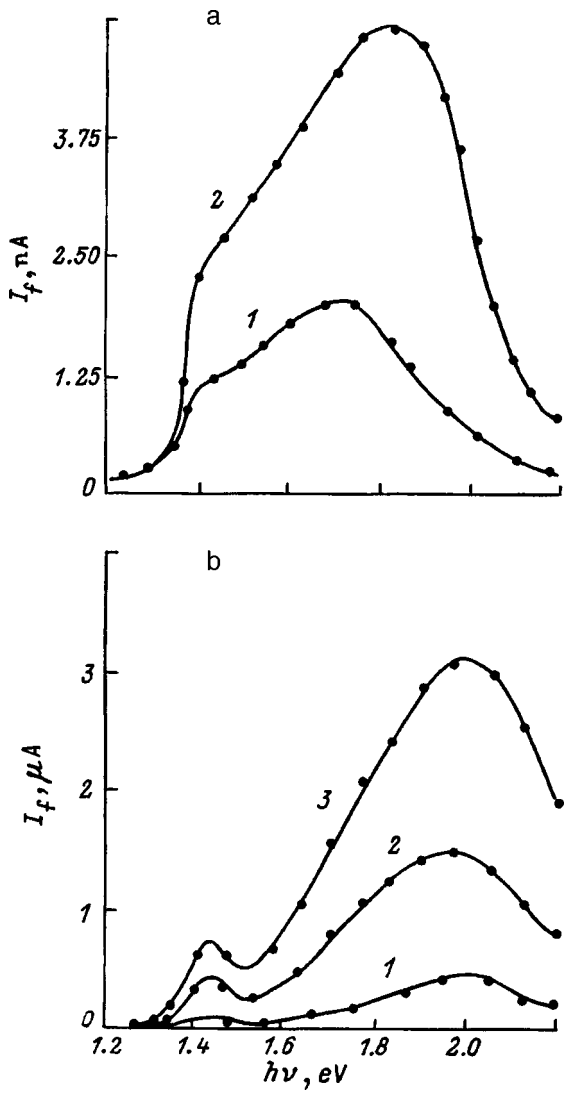

FIG. 2. Spectral characteristics of the photoresponse of an *n*-GaAs-arsenic triselenide heterostructure for negative polarity on the collecting electrode U_C, V: a) *1* — −0.5, *2* — −1; b) *1* — −4, *2* — −10, *3* — −20.

make up the heterostructure. The results of such calculations show that for a CGS film thickness $d=0.3\ \mu$m absorption in the arsenic triselenide is strong only at photon energies $h\nu>1.9$ eV, and hence the primary source of photoconductivity will be absorption in the GaAs over the entire range of photon energies for which the photoresponse spectral characteristics were measured (Fig. 1). Moreover, recombination processes play a significant role at moderate voltages on the collector, and therefore the distinctive features of the photoresponse spectral characteristics, as has been observed experimentally, are washed out. For samples with CGS film thickness $d=1\ \mu$m the transition from absorption in GaAs to absorption in As_2Se_3 takes place at $h\nu>1.7$ eV, and therefore the photoresponse spectral characteristic should exhibit both a region associated with GaAs photoconductivity and a region associated with As_2Se_3 photoconductivity, which is actually seen in the experimentally obtained photoresponse spectral characteristics. For thick films ($d=5\ \mu$m) absorption in the CGS becomes dominant at still lower photon energies, which should lead to an even more distinct region of As_2Se_3 photoconductivity in the photoresponse spectral characteristics of the heterostructure. Moreover, increasing the thickness of the As_2Se_3 film leads to an increase in its resistance, until at large thicknesses the resistance of the film makes the dominant contribution to the total resistance of the heterostructure. Therefore, the contribution of GaAs photoconductivity to the photoresponse spectral characteristic becomes small, although the region of GaAs photoconductivity is still observable on the photoresponse spectral characteristic (Fig. 1, curve *3*). The distinctive features discussed above are easily seen on curves obtained at high collector voltages, when the external field causes separation of carriers and recombination processes no longer modify the shape of the photoresponse spectral characteristic so strongly.

In studying the voltage dependence of the photoresponse spectral characteristics of these heterostructures, we scaled the curves to the same intensity of incident light over the entire voltage range. The resulting normalized curves, obtained for a CGS film thickness $d=1\ \mu$m and negative polarity on the collecting electrode, are shown in Fig. 2. For the curves corresponding to collector voltages of −0.5 V and −1 V the photocurrent increases rapidly in the photon energy range 1.3 to 1.4 eV, develops a shoulder at $h\nu=1.4$ eV, and then continues to increase more slowly. For voltages on the collecting electrode in the range −4 V to −20 V, the feature at $h\nu=1.43$ eV is no longer a shoulder, but rather a peak which is clearly distinguishable from the rest of the curve. At low collector voltages, the curves have their primary maxima at photon energies $h\nu=1.75$–1.8 eV; in this voltage range, the peak shifts toward higher photon energies with increasing collector voltage. For voltages in the range −4 to −20 V the peak is located at an energy $h\nu=1.97$ eV. For negative polarity on the collecting electrode the photocurrent corresponds to motion of positive charge towards the collecting electrode for all the cases investigated.

For all the photoresponse spectral characteristics measured at zero or positive potential on the collecting electrode,

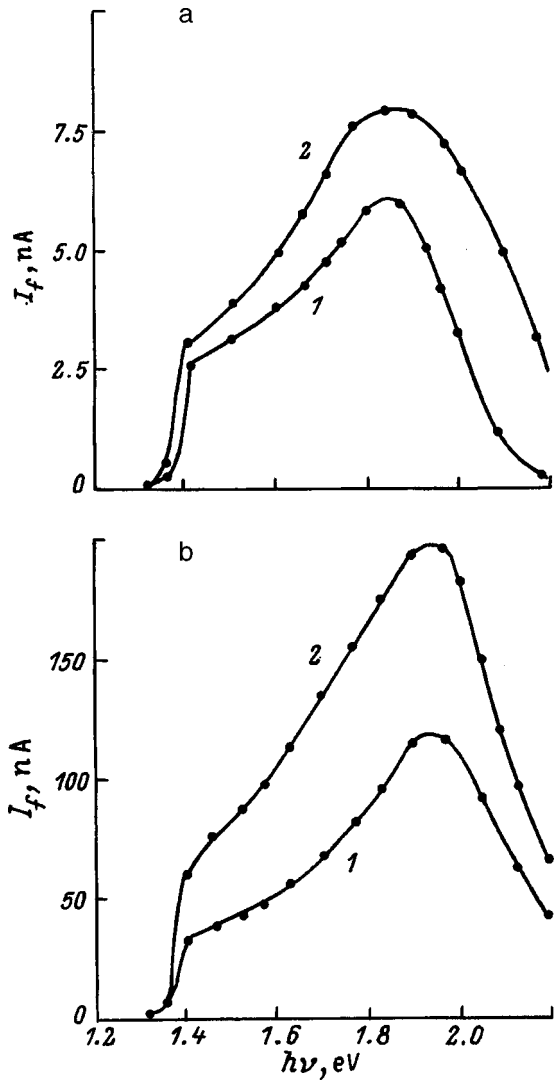

FIG. 3. Spectral characteristics of the photoresponse of an *n*-GaAs-arsenic triselenide heterostructure for positive polarity on the collecting electrode U_C, V: a) *1* — 0, *2* — 1; b) *1* — 3, *2* — 4.

the corresponding photocurrent consists of motion of electrons toward the collector while holes move toward the thick aluminum layer on the back side of the heterostructure. Because the mobility of holes in CGS is considerably higher than that of electrons, it is the motion of holes in these materials that determines the direction of current through the heterostructure. Figure 3 shows photoresponse spectral characteristics obtained at voltages from 0 to 4 V on the collector. The curves were measured for a CGS film thickness $d=1\,\mu$m. At low positive voltages (0.5, 1 V) the photocurrent is larger in magnitude than the photocurrent for the same negative-polarity voltage. At voltages above 4 V the photocurrent for a given negative-polarity voltage on the collector is much highr than the photocurrent for the same positive-polarity voltage.

For zero external voltage on the heterostructure, and also at low collector voltages ($U_C\sim 1$ V), the photoresponse spectral characteristics exhibit a rapid increase in photocurrent in the range of quantum energies $1.3<h\nu<1.4$ eV, and a shoulder at $h\nu=1.4$ eV. As the photon energy continues to increase, the photocurrent increases more slowly and reaches a maximum at $h\nu=1.8$ eV. In this range of collector voltages, reversing the polarity produces only a slight change in the magnitude of the photocurrent.

Increasing the voltage on the collector electrode to 3 V causes a rapid increase in the magnitude of the photocurrent (by roughly a factor of 30). Any further increase in the voltage is also accompanied by a considerable increase in the photocurrent. Increasing the collector voltage not only increases the photocurrent but also changes the shape of the photoresponse spectral characteristics. At high voltages the ratio of the photocurrent at its maximum to the photocurrent near the shoulder at $h\nu=1.4$ eV increases, and the position of the primary maximum shifts. While for low collector voltages the maximum is located at $h\nu=1.8$ eV, at high voltages it shifts toward photon energies $h\nu=1.9$–1.95 eV. This shift is analogous to that observed for the negative-polarity case.

The appearance of a photocurrent with no external voltage applied to the heterostructure is explained by the fact that the photogenerated carriers are separated by fields near the barriers that arise in the heterostructure at the boundaries of the contacting materials. Evidence for this occurrence is the fact that at moderate positive voltages ($U_C\sim 1$ V) the magnitude of the photocurrent differs only slightly from its magnitude in the absence of an external voltage (Fig. 3). As the positive voltage applied to the collector is increased further, the photocurrent increases rapidly. In this case the photocarriers are being separated by the external field. Thus, as long as the external field is small compared to the fields near the boundary in the heterostructure, the direction and magnitude of the current is primarily determined by internal barriers. Additional confirmation is the fact that for small negative biases on the collector the photocurrent is considerably smaller than for positive voltages of the same magnitude. In this case it is noteworthy that the photocurrent maximum increases with increasing negative voltage on the collector more rapidly than it does for increasing positive voltage (Figs. 2 and 3). Thus, at a voltage of -4 V on the collector the maximum value of the photocurrent is roughly 2.5 times larger than at a voltage of $+4$ V. Since the maximum value of the photocurrent lies in the region determined by photoconductivity of the CGS film, this is easily explained by the fact that the majority carriers in CGS are holes. For negative voltages on the collector, the photogenerated holes arrive immediately at the collector electrode from the CGS. In GaAs the mobility of electrons is larger than that of holes; consequently, the recombination processes will play a smaller role, and therefore the photocurrent will be larger. In the range of photon energies $h\nu=1.4$ eV, when light is absorbed not in the CGS but rather in the GaAs, the magnitudes of the photocurrent at voltages -4 and $+4$ V on the collector are nearly the same (Fig. 3). In this case, the asymmetry of the hole and electron mobilities in As_2Se_3 and GaAs does not play a decisive role, since in GaAs electrons can move both towards the thick aluminum layer (''$-$'' on the collector), and towards the CGS film (''$+$'' on the collector) where they then can recombine with holes.

In the range of photon energies $1.0<h\nu<1.4$ eV we observe a photocurrent for negative polarity on the collector

that is not present for positive polarity. The presence of this photocurrent can be explained by photoemission of holes from the thick Al layer on the back side of the heterostructure. For negative voltages on the collector, these photoemitted holes can reach the collector through the GaAs and As_2Se_3. Hole photoemission was observed in studies of potential barriers at an Al–GaAs boundary in Ref. 7.

CONCLUSIONS

In this paper we have proposed a model for the origin of photoresponse in GaAs–As_2Se_3 heterostructures. We have shown that the shape of the photoresponse spectral characteristics of these heterostructures is determined by the thickness of the amorphous As_2Se_3 layer. At film thicknesses of 0.3 μm and smaller, the photoresponse spectral characteristics are determined primarily by absorption in the GaAs. At a film thickness of 1 μm both the GaAs and As_2Se_3 contribute to the photoresponse spectral characteristics, while for a film thickness of 5 μm and larger the primary role is played by absorption in the As_2Se_3.

We have found that when a positive-polarity voltage is applied to the aluminum electrode on the GaAs side, the shape of the photoresponse spectral characteristics is nearly independent of the magnitude of the voltage. For negative-polarity voltages, the magnitude of the peak associated with the GaAs photoconductivity increases with increasing absolute value of the voltage. The increase in photocurrent is more rapid for increasing negative-polarity voltages than it is for positive-polarity voltages.

When there is no external voltage applied to the heterostructure, and for low positive voltages ($U_C < 1$ V), the photogenerated carriers are separated at barriers that are present in the heterostructure. At higher voltages the carriers are separated by the external field.

[1] A. G. Milnes and D. Feucht, *Heterojunctions and Metal-Semiconductor Junctions* (Academic Press, New York, 1972; Mir, Moscow, 1975, p. 12.).
[2] A. V. Anshon, I. A. Karpovich, and A. A. Safronov, Izv. Vuzov Fizika **29**, No. 8, 112 (1986).
[3] V. Venkataraman, Curr. Sci. **67**, 855 (1994).
[4] M. A. Iovu, M. S. Iovu, A. A. Simashkevich, D. I. Tsiulyanu, and S. D. Shutov, *Mater. Conf. ''Amorphous Semiconductors–80''* (Kishinev, 1980), p. 120.
[5] A. M. Andriesh, E. A. Akimova, V. V. Bivol, E. G. Khancevskaya, M. S. Iovu, S. A. Malkov, and V. I. Verlan, Int. J. Electron. **77**, 339 (1904).
[6] K. P. Kornev, Dep. VINITI 1986, N8021–B8.
[7] A. S. Kochemirovskiĭ and K. P. Kornev, *Abstracts from Proc. All-Union Conference on ''Glassy Semiconductors''* (Leningrad, 1985), p. 80.

Translated by Frank J. Crowne

Thermally stimulated currents and instabilities of the photoresponse in PbTe(In) alloys at low temperatures

B. A. Akimov, V. A. Bogoyavlenskiĭ, L. I. Ryabova, V. N. Vasil'kov, and E. I. Slyn'ko

M. V. Lomonosov Moscow State University, 119899 Moscow, Russia
(Submitted May 5, 1998; accepted for publication May 19, 1998)
Fiz. Tekh. Poluprovodn. **33**, 9–12 (January 1999)

The photoelectric properties of $Pb_{1-X-Y}Sn_XGe_YTe(In)$ epitaxial films ($0.06<X<0.2$, $0.08<Y<0.12$) with In concentrations of 0.5–1 at. % on BaF_2 substrates are investigated in the temperature range 4.2 K$<T<$30 K. Thermally stimulated single current (TSC) peaks are observed at $T\sim 6-14$ K. It is established that a magnetic field up to 5 T slightly shifts the peaks essentially without affecting their profile. The TSC peaks and the electrothermal instabilities observed at $T<15$ K are attributed to the excitation of electrons from metastable states into the conduction band. © *1999 American Institute of Physics.* [S1063-7826(99)00201-X]

INTRODUCTION

Solid solutions based on In-doped PbTe are intriguing objects for investigations of unusual impurity states in semiconductors.[1] Applied aspects of the problem are associated with the fabrication of photodetection devices utilizing these compounds for the infrared range of the spectrum.[2,3]

It has been established that the introduction of 0.5–2.0 at. % In in PbTe has the effect of fixing the Fermi level at 70 meV above the bottom of the conduction band and also of improving the homogeneity of the electrical properties of single crystals. At temperatures $T<T_C\sim 20$ K long-time relaxations of the electron distributions are observed in PbTe(In) upon departure from the equilibrium state.[1]

The Fermi level can be stabilized in the band gaps of $Pb_{1-X}Sn_XTe(In)$ (Ref. 1), $Pb_{1-X}Mn_XTe(In)$ (Ref. 4), and $Pb_{1-X}Ge_XTe(In)$ (Ref. 5). For the fabrication of photodetection devices from these alloys it is preferable to use epitaxial films, which can be prepared by hot-wall epitaxy and molecular-beam epitaxy, including fabrication on silicon with transition layers.[6] Liberal possibilities for varying the parameters of the energy spectrum are afforded in the investigation of $Pb_{1-X-Y}Sn_XGe_YTe(In)$ alloys.[7] However, the principal advantage of these solid solutions is that the persistent photoconductivity sets in at the highest temperature of any investigated PbTe(In) alloys: $T_C\sim 36$ K (Ref. 2).

According to prevailing notions, an In impurity in PbTe and in alloys containing it induces the formation of deep *DX*-like centers. Such centers are described by configuration diagrams[4,8,9] for a three-level system $E_C-E_1-E_2$. The E_C level corresponds to the bottom of the conduction band, and E_1 corresponds to a metastable one-electron state. The Fermi level is stabilized on the basis of the two-electron E_2 level. The metallic state occurs in the alloy for $E_2>E_C$, and the dielectric state occurs for $E_2<E_C$. In the latter case the thermal activation energy E_A of the system conductivity corresponds to E_2-E_C transitions. According to existing data, this quantity increases in $Pb_{1-X-Y}Sn_XGe_YTe(In)$ alloys as X and Y are increased.[7] In the dielectric state the E_1 level can be situated either higher or lower than the E_C level.

Here we report a series of experiments on the kinetic characteristics of nonequilibrium processes with the objective of discerning and analyzing characteristic features of the metastable states of impurity centers in $Pb_{1-X-Y}Sn_XGe_YTe(In)$ alloys.

INVESTIGATED SAMPLES AND HIGHLIGHTS OF THE EXPERIMENTAL PROCEDURE

Epitaxial films of composition $Pb_{1-X-Y}Sn_XGe_YTe(In)$ were prepared by hot-wall epitaxy on BaF_2 substrates.[2] The mixture used for synthesis came in three compositions: $X=0.06$, $Y=0.08$, $C_{In}=1\%$; $X=0.1$, $Y=0.1$, $C_{In}=0.5\%$; $X=0.2$, $Y=0.12$, $C_{In}=1\%$. The temperature regime in the chamber was maintained in such a way as to keep the substrate temperature fixed at 380 °C with a gradient not to exceed 1–3 °C in the reaction zone. The growth of the film lasted 7–8 h under these very nearly equilibrium conditions. The thickness of the resulting films varied from 1 μm to 6 μm in this case. Plots of the temperature dependence of the normalized resistances of the films, recorded with the samples completely shielded against phonon radiation and in IR illumination, are shown in Fig. 1. All the samples had a high photosensitivity (the resistance varied from four to six orders of magnitude at 4.2 K) and a thermal activation energy E_A in the range from 4 meV to 44 meV. The variation of E_A is attributable to the variation of the compositions of the film and the raw mixture in the course of several successive synthesis procedures after the mixture of fixed composition.

In the present study, for the most part, we used a standard thermal-activation current spectroscopy technique, whose details are described, for example, in Ref. 10.

EXPERIMENTAL RESULTS

Typical profiles of the thermally stimulated current (TSC) curves are shown in Fig. 2 for a film with activation energy $E_A\sim 35$ meV. A film sample with 1×2 mm was cooled down to 4.2 K and was illuminated with IR radiation from a miniature incandescent lamp with a maximum radiation power up to 30 mW. The voltage on the sample was

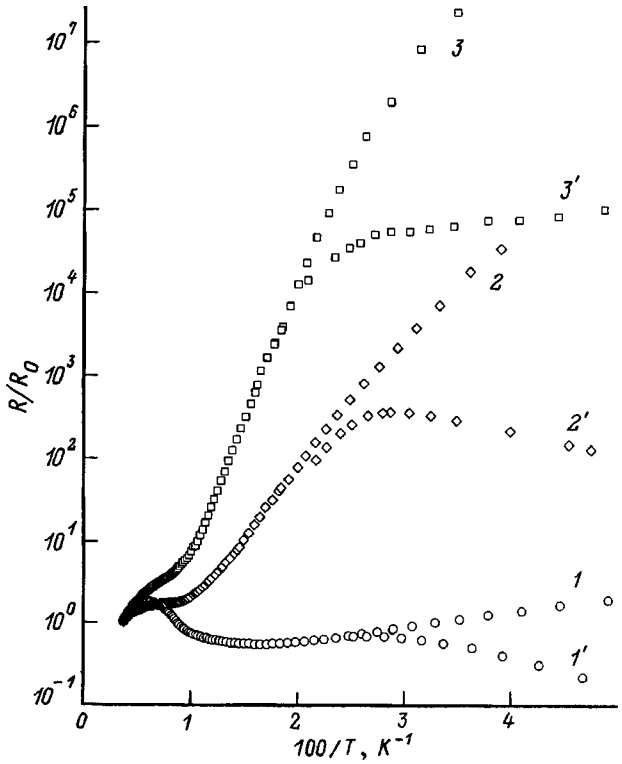

FIG. 1. Temperature dependence of the resistance of $Pb_{1-X-Y}Sn_XGe_YTe(In)$ film samples having various activation energies at low temperatures with shielding (*1, 2, 3*) and with IR illumination (*1′, 2′, 3′*).

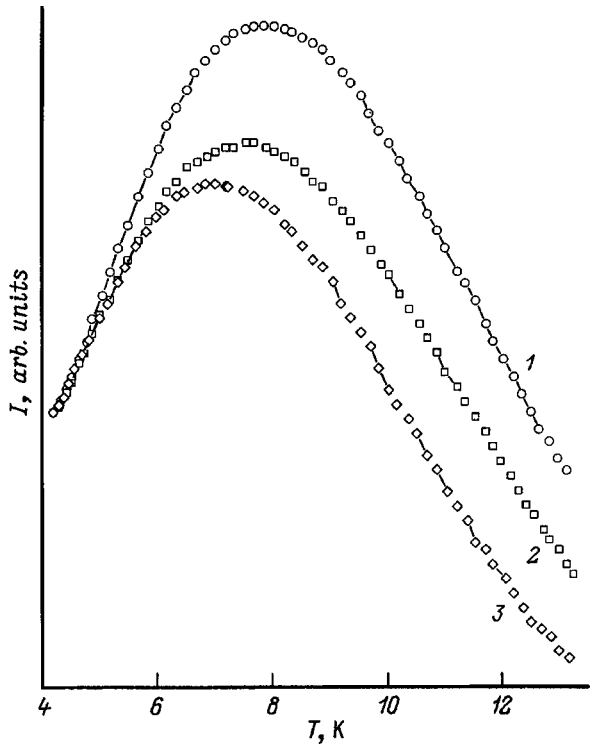

FIG. 3. Plots of the temperature dependence of thermally stimulated currents in zero field (*1*) and in magnetic fields: (*2*) $H=1$ T; (*3*) $H=5$ T.

fixed at the 1-V level, and the current was recorded in the sample circuit. The illumination was then turned off, and prolonged (to several tens of minutes) relaxation of the photocurrent I was observed. Segment *1–2* of the *I-t* curves in Fig. 2 corresponds to a certain finite relaxation stage. Under the conditions of residual relaxation of the photocurrent, at the time corresponding to point *2* the sample began to heat up at the rate of 1–3 K/s. In this stage TSC peaks were recorded with maxima in the interval from 6 K to 14 K, and the shape of the peaks depended on the heating regime. Curves *2–5* and *2*, *3′*, *4*, and *5′* in Fig. 2 correspond to heating of the sample at rates of 1 K/s and 2 K/s, respectively. In the vicinity of point *4* the current I almost attained its dark-field value. In segments *4–5* and *4–5*' a characteristic increase in the current is observed in connection with the thermal activation of conductivity even with shielding.

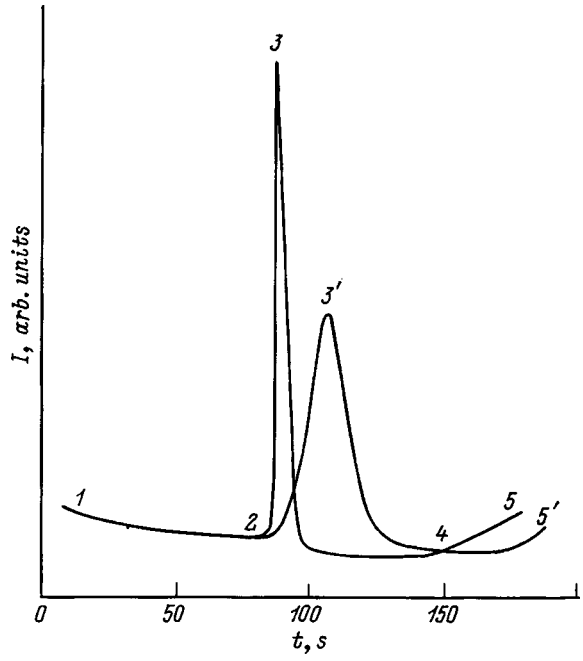

FIG. 2. Typical profiles of automatic traces of thermally stimulated currents in the investigated films (see text).

In contrast with abundant existing data,[10] TSC peak are observed in the investigated systems at substantially lower temperatures. It is evident from the data in Fig. 2 that the TSC peak is unique and does not have any individual prominent features.

Earlier papers[11,12] have called attention to the extraordinary behavior of the properties of metastable (paramagnetic) centers in PbTE-based alloys containing In and Ga impurities. In the present study, therefore, we have investigated the distinctive features of the TSC peaks in magnetic fields up to 5 T. We have established that the TSC amplitude decreases in a magnetic field, while the maxima of the peaks shift very slightly toward lower temperatures (Fig. 3).

When the applied voltage on the film is increased (to 5 V) in continuous illumination, quasiperiodic current oscillations are observed (Fig. 4, the edge of curve *1*). Oscillations of this kind have been studied previously in detail for metastable states in PbTe(Ga).[13] Curve *2* in Fig. 4 describes the short-time variation of the ambient temperature from 4.2 K to 15 K at the maximum. Here, all other conditions

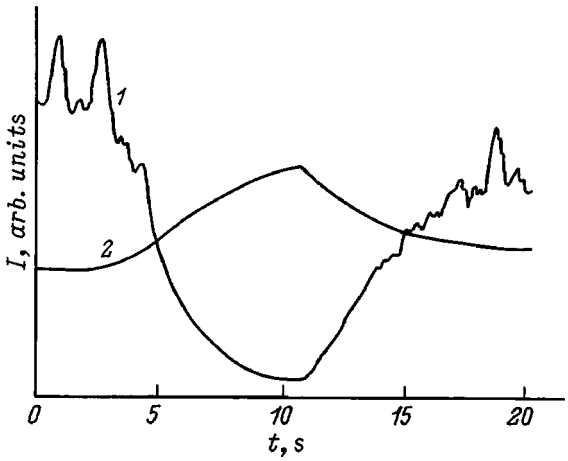

FIG. 4. Electrothermal instabilities of the current in the sample circuit (*1*) and their transformation when the ambient temperature is changed (*2*).

being equal, the variations of the current through the sample decrease, and the instabilities vanish.

A bistability effect has been observed in an investigation of the photoresponse of the samples at 4.2 K. It was found that when the illumination intensity is sufficiently small, additional excitation must be introduced in the system to increase the photocurrent at voltages up to 3 V. This can be done by raising the temperature of the sample or by illuminating it with radiation from a second source. The general scheme of the experiment was as follows. The sample was exposed to weak illumination at 4.2 K, and then the illumination was turned off. At a certain time following the start of relaxation of the photocurrent the light was turned back on, but this subsequent illumination had absolutely no influence on the relaxation. Next, after a certain time, either the sample heater or the second IR source was turned on. It was established that the sample becomes photosensitive again when it reaches a temperature of 6 K, and the above-described cycle is reversibly reproduced from then on.

DISCUSSION OF THE RESULTS

The experimental results can be interpreted within the framework of the previously described deep-center model. Unfortunately, only a phenomenological description of the effects can be proposed, because of the complexity of the investigated multicomponent systems and because of the onset of phase transition in the investigated temperature interval.

The most logical hypothesis appears to be that the TSC peaks correspond to transitions of charge carriers between the metastable E_1 level and the conduction band. The light excitation of the system causes electrons to be excited from the E_2 level into the conduction band. Metastable electronic states with the E_1 level are induced in this case. As the electron distributions relax, a certain number of centers with energy E_1 remain occupied. Heating of the sample causes electrons localized at these centers to be thermally excited into the conduction band. Here the sample conductivity increases at the start of heating, and the E_1 levels begin to depopulate. The rate of transitions of band electrons to the E_2 level is found to be higher than the rate of their secondary trapping at the E_1 level. This effect can be attributed to the much higher number of states at the E_2 level than at the E_1 level. A further increase in temperature is accompanied by depopulation of both the conduction band and the E_1 level. In the dynamics the entire process described here then produces a TSC peak. The description of such processes is similar to the well-known thermal stimulated currents in wide-gap semiconductors,[10] and all that remains is to trace the analogy between the known sticking levels and the metastable E_1 states.

The qualitative result is that a unique TSC peak is observed with a maximum at extremely low temperatures 6–14 K. The peak shifts in a magnetic field, but does not split. Exact quantitative calculations of the position of the E_1 level are difficult to perform in the TSC method, but approximate estimates give transition energies of the order of 10–20 meV. The same energies can be obtained by analyzing the patterns of the electrothermal stabilities at various temperatures according to the procedure in Ref. 13. It is also natural to view the existence of the instabilities themselves as qualitative confirmation of the proposed model.

We note that observation of a single TSC peak can provide information about the phase transition in $Pb_{1-X-Y}Sn_XGe_YTe$(In) films. It is evident from Fig. 1 that the resistance-temperature curves do not exhibit any prominent features. The data, taken collectively, indicate that phase transition can be suppressed in the investigated systems. Neither should the opposite situation be dismissed, with the large splitting of equivalent valleys, so that only one lower valley emerges as the E_C level.

The position of the E_1 level depends on the composition of the alloy. The observation of this level for $E_1 > E_C$ is most likely possible if allowance is made for the existence of a barrier in configuration space between this level and the conduction band.[4,9] Methodologically, however, the observation of this phenomenon in alloys with a low activation energy (to 10 meV) is complicated by the fact that the presence of sources having a temperature higher than 15 K in the chamber, together with the sample, imparts a substantial photoconductivity to the films. At higher activation energies (above 40 meV) the photocurrent relaxes so rapidly that it is impossible to record the TSC. Consequently, data obtained in the intermediate interval of activation energies must be deemed the most reliable.

Difficulties are still encountered in the interpretation of experiments on the bistability of the photoresponse and on the magnetic field dependence of the profiles and positions of the TSC peaks.

In closing, we note an important consequence of the reported investigations. The existence of metastable states which can be partially populated in illumination does in fact imply that long-wavelength photodetection devices with the preexcitation of metastable states can be constructed on the basis of the investigated alloys.

This work has been supported in part by the Russian Fund for Fundamental Research, Grants No. 96-02-16275-a and No. 96-15-96500.

[1] B. A. Akimov, A. V. Dmitriev, D. R. Khokhlov, and L. I. Ryabova, Phys. Status Solidi A **137**, 9 (1993).
[2] V. F. Chishko, V. T. Hryapov, I. L. Kasatkin, V. V. Osipov, E. I. Slyn'ko, O. V. Smolin, and V. V. Tretinik, Infrared Phys. **33**, 197 (1993).
[3] B. A. Akimov, L. I. Ryabova, V. N. Shumskiy, and N. I. Petikov, Infrared Phys. **34**, 375 (1993).
[4] B. A. Akimov, N. A. L'vova, and L. I. Ryabova, Fiz. Tekh. Poluprovodn. **30**, 1647 (1996) [Semiconductors **30**, 861 (1996)].
[5] Kh. A. Abdullin and A. I. Lebedev, JETP Lett. **39**, 325 (1984).
[6] H. Zogg, S. Blunier, T. Hoshino, C. Maissen, J. Masek, and A. N. Tiwari, IEEE Trans. Electron Devices **ED-38**, 1110 (1991).
[7] Kh. A. Abdullin and A. I. Lebedev, Fiz. Tekh. Poluprovodn. **19**, 1725 (1985) [Sov. Phys. Semicond. **19**, 1061 (1985)].
[8] Z. Wilamovski, T. Suski, and W. Jantsh, Acta Phys. Pol. A **82**, 561 (1992).
[9] B. A. Akimov, A. V. Albul, and L. I. Ryabova, Fiz. Tekh. Poluprovodn. **29**, 2158 (1995) [Semiconductors **29**, 1125 (1995)].
[10] Yu. A. Gorokhovskiĭ and G. A. Bordovskiĭ, *Thermal-Activation Spectroscopy of High-Resistance Semiconductors and Dielectrics* [in Russian], Nauka, Moscow, 1991.
[11] B. A. Akimov, A. V. Nikorich, D. R. Khokhlov, and S. N. Chesnokov, Fiz. Tekh. Poluprovodn. **23**, 668 (1989) [Sov. Phys. Semicond. **23**, 418 (1989)].
[12] A. V. Vasil'ev, B. A. Volkov, T. N. Voloshok, and S. V. Kuvshinnikov, in *Proceedings of the 23rd International Conference on the Physics of Semiconductors*, Vol. 4 (Berlin, 1996), p. 3009.
[13] B. A. Akimov, N. B. Brandt, A. V. Albul, and L. I. Ryabova, Fiz. Tekh. Poluprovodn. **31**, 133 (1997) [Semiconductors **31**, 100 (1997)].

Translated by James S. Wood

LOW-DIMENSIONAL SYSTEMS

Charging of deep-level centers and negative persistent photoconductivity in modulation-doped AlGaAs/GaAs heterostructures

V. I. Borisov, V. A. Sablikov, I. V. Borisova, and A. I. Chmil'

Institute of Radio Engineering and Electronics, Russian Academy of Sciences, 141120 Fryazino, Russia
(Submitted August 14, 1997; accepted for publication April 14, 1998)
Fiz. Tekh. Poluprovodn. **33**, 68–74 (January 1999)

The relaxation kinetics of persistent photoconductivity in AlGaAs / GaAs modulation-doped heterostructures due to charging of $EL2$- and DX-centers is investigated over a wide range of temperatures and excitation photon energies. The light-induced charging of these deep centers was found to lead to accumulation of positive and negative localized charges, which give rise to positive and negative persistent photoconductivities, respectively. These positive and negative charges are accumulated in different parts of the heterostructure. Their different characteristic times, and the different temperature dependences of these times, result in nonmonotonic time and temperature dependences of the persistent photoconductivity. Charging of $EL2$-centers in the GaAs buffer layer leads to negative persistent conductivity in the temperature range $180-300$ K, while the negative photoconductivity observed at the temperatures below 180 K is caused by excited states of DX-centers in the n^+-AlGaAs. © *1999 American Institute of Physics.* [S1063-7826(99)01501-X]

1. INTRODUCTION

It is well known that structural defects with deep levels can strongly influence the concentration and mobility of electrons in semiconductors, thereby becoming an important factor in determining the electronic characteristics of these semiconductors and structures based on them. Their influence is derived from the fact that charge can accumulate at deep level centers, which changes the potential well of the structure. Well-known defects with deep levels in epitaxial layers of GaAs and AlGaAs include $EL2$-centers in GaAs and DX centers in AlGaAs. $EL2$-centers in GaAs are complexes of an antisite defect As_{Ga} and an acceptor impurity, which create deep donor levels.[1] The concentration of $EL2$-centers is determined by how the structure was grown and thermally processed. $EL2$ centers are usually present in structures grown by chemical deposition from metallorganic compound vapors (MOVPE); however, they are also observed in structures grown by molecular beam epitaxy.[2] DX-centers form when AlGaAs is doped with donor impurities as a result of a substitutional impurity atom being excited into a metastable state.[3] Both DX and $EL2$ centers are characterized by extremely low probabilities for thermal ejection of the electrons they trap, and therefore a considerable nonequilibrium charge can accumulate in them.

In this study our goal was to investigate photoinduced processes that charge the deep levels at $EL2$- and DX-centers in AlGaAs/GaAs modulation-doped heterostructures (MDH) and their effect on the relaxation of persistent photoconductivity under conditions where this conductivity is primarily determined by two-dimensional electrons, whose concentration is changed by the charging of deep levels. Photoconductivity in MDH has been widely studied recently.[4–6] The most striking effect connected with charging of deep levels is the appearance of negative photoconductivity, which is observed at the time of illumination, and negative persistent photoconductivity (NPP), which is observed after the light is switched off. Negative photoconductivity was observed in structures with a two-dimensional hole gas[4] at 4.2 K, while NPP was observed in MDH with two-dimensional electrons at temperatures of 170 to 300 K (Ref. 5). Its appearance is associated with charging of $EL2$-centers in the GaAs buffer layer.

In this paper we investigate in detail the relaxation kinetics of photoconductivity in MDH within the temperature range 80 to 300 K and for a wide range of photon energies. As a result, we establish that there are two mechanisms for NPP. One acts at temperatures of 180 to 300 K, and is associated with charging of $EL2$-centers in the GaAs buffer layer, which takes place uniformly over the layer thickness: In the center portion of the layer, the $EL2$-centers are emptied of electrons and a positive charge accumulates on the impurities, which is responsible for the positive persistent photoconductivity. Near the boundary of the space-charge layer with the thick buffer, filling of the $EL2$-centers by electrons takes place, a consequence of which is the appearance of NPP. The second NPP mechanism acts at temperatures of 120 to 180 K. It is caused by charging of DX-centers in the strongly doped n^+-AlGaAs.

2. EXPERIMENT

The investigations were carried out on AlGaAs/GaAs MDH grown by molecular beam epitaxy on a substrate made

of semi-insulating GaAs. Thicknesses and doping of the layers were as follows: an undoped GaAs layer with thickness $\sim 1\mu$m and residual concentration of shallow acceptors $\sim 10^{15}$ cm^{-3}; a strongly doped layer of n^+Al$_x$Ga$_{1-x}$As($x \approx 0.25$) with thickness ~50 nm and a donor concentration of $\sim 10^{18}$ cm^{-3}; and a spacer layer with thickness ~15 nm. The surface of the sample was shielded from contact with the environment by a thin (~50 nm) layer of undoped GaAs. The concentration and mobility of the two-dimensional electrons at 77 K were: $n_{2D} \approx 5 \times 10^{11}$ cm^{-2} and $\mu_{2D} \approx 10^5$ cm^2/(V·s). Contacts to the sample were made by melt-diffusing In into it in hydrogen atmosphere; the distance between contacts was 2 to 5 mm.

In making the measurements, the samples were placed in a cryostat of the circulating type with an optical window. After each low-temperature measurement, the sample was heated to room temperature, and then slowly (at a rate of 1 to 4 K/s) cooled in order to make the next measurement.

In order to study the relaxation of the photoconductivity, we illuminated the samples with light pulses with durations from ~1 ms to 1 s. As light sources we used an AL-119A infrared light-emitting diode (photon energy $h\nu = 1.33$ eV, power $P \approx 40$ mW) and an LGN-207A helium-neon laser ($h\nu = 1.97$ eV, $P \approx 1.5$ mW). We used an MDR-3 monochromator ($h\nu =$ 0.62–2.05 eV) to measure the spectral dependence. Light from the light-emitting diode was pulse-modulated by feeding the diode voltage pulses, while an electromechanical modulator was used to modulate the light from the laser or monochromator. In the first case, the fall time was determined by the time required to switch off the diode ($< 1.5\,\mu$s), while in the second case it was determined by the time for switching on and switching off the light, which did not exceed 1 ms.

Figure 1 shows typical photoconductivity kinetics curves over a wide range of temperatures. The variation of the photoconductivity represented by these curves exhibits certain characteristic features both within the illumination time and during the relaxation period, in the course of which the sign of the persistent photoconductivity changes from positive to negative. The shapes of these curves reveal that there are two temperature intervals: 180 to 300 K (see Fig. 1a) and 80 to 180 K (see Fig. 1b) in which the characteristic relaxation times are different. As the measurement temperature decreases from room temperature to liquid-nitrogen temperature, the characteristic time it takes the photoconductivity to relax after switching off the light increases strongly, and at a temperature of ~180 K NPP nearly disappears. As the temperature decreases further, a new NPP segment arises with a considerably smaller characteristic time, which also increases strongly under cooling. This indicates that two types of capture center are involved in the relaxation. The first type, which lies deeper in energy, dominates the relaxation kinetics of the photoconductivity for temperatures in the range 180 to 300 K, while the second, shallower center dominates at low temperatures. Judging from the magnitude of the NPP effect, the number of centers of the second type is larger than the first. We have established that defects of the first kind are $EL2$-centers, while defects of the second kind are probably DX-centers.

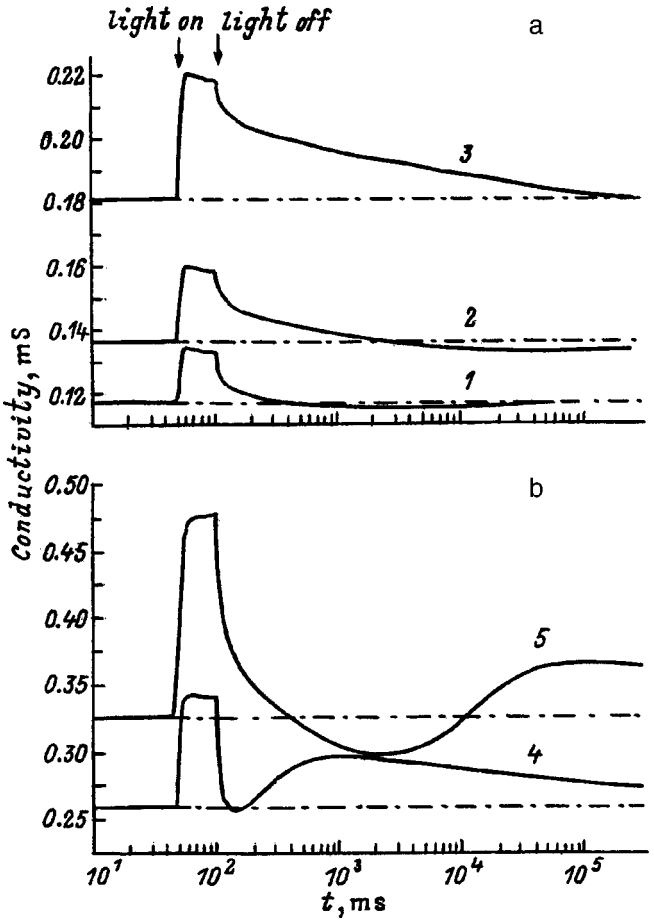

FIG. 1. Relaxation of photoconductivity in two temperature ranges. a—T = 292 (*1*), 250 (*2*), and 200 K (*3*). b—T = 160 (*4*) and 140 K (*5*). Photon energy $h\nu = 1.33$ eV.

3. CHARGING OF *EL2*-CENTERS

In the temperature range 180 to 300 K, the behavior of the photoconductivity deppends strongly on the photon energy. When $h\nu$ is less than the band gap of GaAs, long-period relaxation of the photoconductivity and NPP are observed (Fig. 1a). When it is greater, i.e., when interband absorption can occur, the photoconductivity $\Delta\sigma/\sigma_0$ relaxes within a short time, i.e., there is little positive persistent photoconductivity, whereas the NPP amplitude is nearly the same as it is under illumination by impurity-energy photons (Fig. 2). This implies that illumination by the latter empties electrons from $EL2$-centers in a certain portion of the buffer layer, resulting in positive persistent photoconductivity, and leaves the $EL2$-centers in the rest of the buffer layer occupied by electrons. However, illumination with interband light can only fill the $EL2$-centers with electrons, and hence there is no positive persistent photoconductivity.

Another fact that is important for clarifying the nature of these effects involves the spectral dependence and photoconductivity kinetics within the illumination time. The spectral dependence of the photoconductivity $\Delta\sigma/\sigma_0$ (Fig. 3) correlates qualitatively with the changes in the photoionization cross section of $EL2$-centers reported in Ref. 7. Photoconductivity first appears at $h\nu \approx$ 0.6 eV, which is probably connected with ionization of unmonitored defects. At

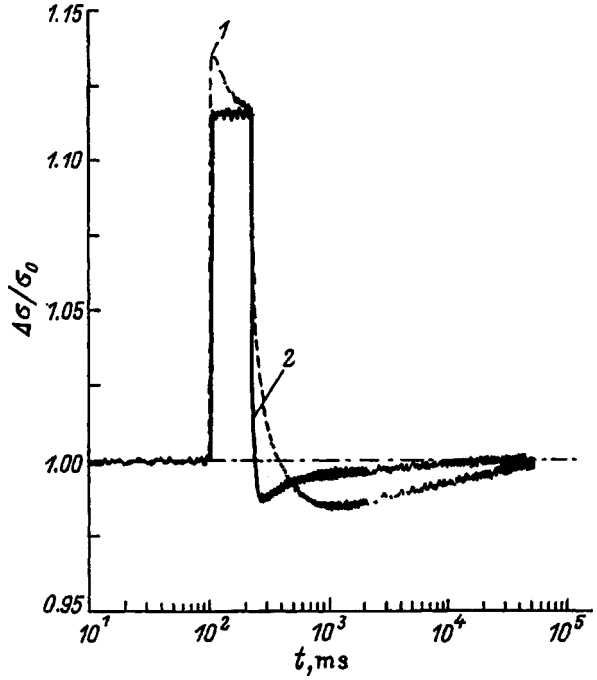

FIG. 2. Relaxation of photoconductivity excited by pulsed light with impurity-energy photons $h\nu = 1.33$ eV (*1*) and interband-energy photons $h\nu = 1.97$ eV (*2*). $T = 292$ K.

$h\nu \approx 0.75$ eV the light can induce transitions of electrons from the valence band to the $EL2$-centers. This causes negative charge to begin to accumulate at these centers, which in turn decreases the concentration of electrons in the quantum well. As $h\nu$ increases further, the ionization cross section of $EL2$- centers increases rapidly, which transfers electrons to the conduction band. These photoinduced electrons enter the quantum well and increase the conductivity. A similar effect is apparent in the photoconductivity dynamics during illumination by photons with $h\nu = 1.33$ eV (Fig. 1a): After the

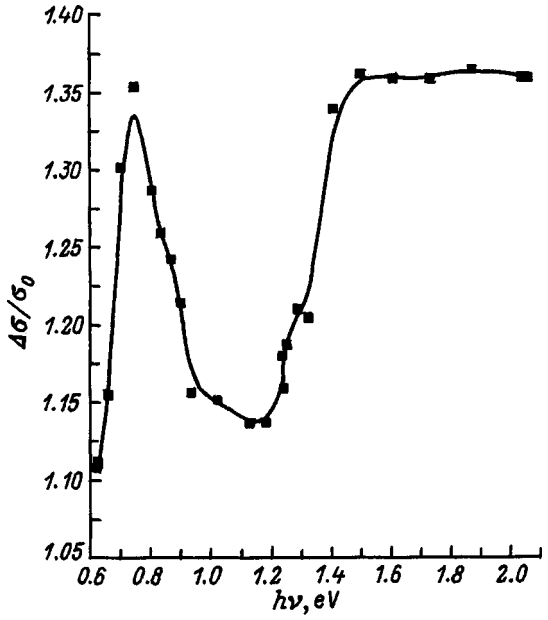

FIG. 3. Spectral dependence of photoconductivity. $T = 292$ K.

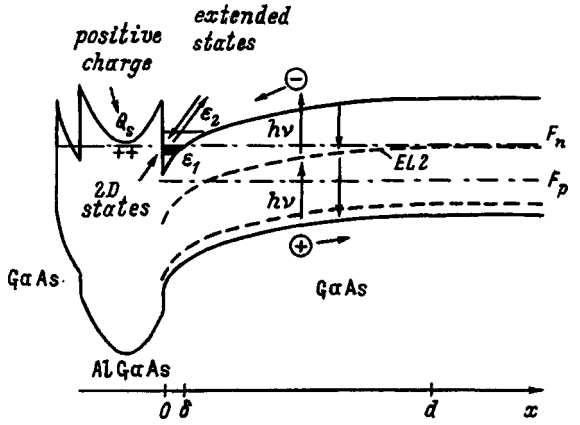

FIG. 4. Band diagram of heterostructure.

increase in conductivity connected with emptying of $EL2$ centers in the center portion of the space-charge layer, there must be a decrease due to photoinduced filling of $EL2$-centers by electrons at the edge of the space-charge layer, where the equilibrium occupation of centers by electrons is lower than the photoinduced occupation.

4. SPATIAL DISTRIBUTION OF PHOTOINDUCED CHARGE IN *EL2*-CENTERS

Persistent photoconductivity is caused by nonequilibrium electrons in the quantum well, whose concentration after the light is switched off is determined by the nonequilibrium charge on the deep centers. The presence of positive and negative photoconductivity implies that positive and negative charges accumulate at the centers in different regions of the GaAs buffer layer. In order to estimate the magnitude of the persistent photoconductivity and understand the kinetics of its relaxation, it is necessary to know the spatial distribution of photoionized charge of the $EL2$-centers over the GaAs layer thickness and the activation energy for emptying them.

The nonequilibrium filling of $EL2$-centers by electrons under illumination is determined by two factors: direct electron transitions induced by absorption of impurity-energy photons, and redistribution of the electronic conductivity in the buffer layer, which takes place due to photoinduced changes in the potential (Fig. 4). We find the distribution of charge in the buffer layer by solving the Poisson equation:

$$\frac{\partial^2 \varphi}{\partial x^2} = \frac{4\pi e}{\varepsilon}[n(x) + N_a - N_t^+(x) - p(x)], \tag{1}$$

where $n(x)$ is the electron concentration, $p(x)$ is the hole concentration, N_a is the concentration of shallow acceptors, and N_t^+ is the concentration of positively charged $EL2$-centers. This concentration N_t^+ is determined by the equations of charging kinetics, with whose help we can express N_t^+ in terms of the concentration of free charge carriers and the flux of photons Φ as

$$N_t^+ = N\left(1 + \frac{\sigma_p \Phi + e_p + c_n n}{\sigma_n \Phi + e_n + c_p p}\right)^{-1}, \tag{2}$$

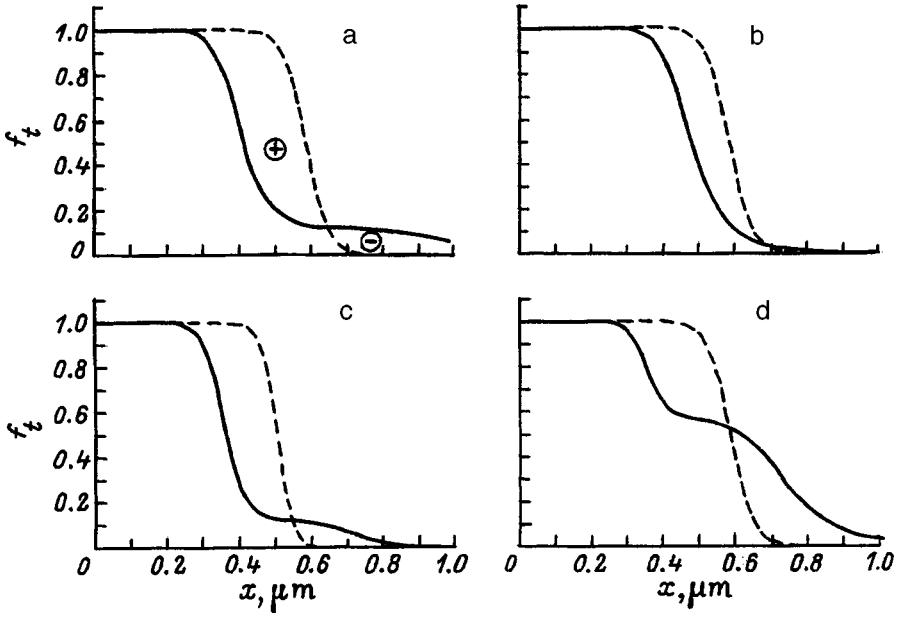

FIG. 5. Plots of occupation of $EL2$-centers f_t versus buffer layer thickness x during illumination (solid curve) and in darkness (dashed curve). a: $N_t=1.3\times10^{15}\,\mathrm{cm}^{-3}$, $n_0=10^2\,\mathrm{cm}^{-3}$, $h\nu=1.33\,\mathrm{eV}$. b: $N_t=1.3\times10^{15}\,\mathrm{cm}^{-3}$, $n_0=10^8\,\mathrm{cm}^{-3}$, $h\nu=1.33\,\mathrm{eV}$. c: $N_t=1.0\times10^{15}\,\mathrm{cm}^{-3}$, $n_0=10^2\,\mathrm{cm}^{-3}$, $h\nu=1.33\,\mathrm{eV}$. d: $N_t=1.3\times10^{15}\,\mathrm{cm}^{-3}$, $n_0=10^2\,\mathrm{cm}^{-3}$, $h\nu=1.0\,\mathrm{eV}$. In all cases $N_a=1.5\times10^{15}\,\mathrm{cm}^{-3}$, $T=250\,\mathrm{K}$.

where σ_n and σ_p are cross sections for electron transitions from an $EL2$-center to the conduction band and from the valence band to an $EL2$-center, e_n and e_p are coefficients of thermal emission of electrons from the center to the conduction band and holes to the valence band, and c_n and c_p are capture coefficients.

The distribution of the concentrations $n(x)$ and $p(x)$ is determined by the condition of quasiequilibrium (i.e., constancy of the quasi-Fermi levels F_n and F_p) transverse to the buffer layer. In this case, for holes and also for electrons in the bulk of the buffer layer we can use expressions derived from the Boltzmann distribution:

$$n=n_0\,\exp\{e\varphi(x)/k_BT\},\quad p=p_0\,\exp\{-e\varphi(x)/k_BT\}, \tag{3}$$

where n_0 and p_0 are concentrations of electrons and holes far from the heterojunction, which are related by the condition of electrical neutrality:

$$n_0+N_a-N_t^+(n_0,p_0)-p_0=0. \tag{4}$$

The concentration n_0 of minority carriers is determined by the effective lifetime, and consequently depends on the rate of recombination at the boundary with the substrate and on transport of electrons in the plane of the heterostructure to the current contacts. Henceforth we will treat the magnitude of n_0 as a variable, and choose it in such a way as to achieve the best agreement with measurements. For a fixed n_0 we determine p_0 from Eq. (4), and thus find the quasi- Fermi levels.

In solving the Poisson equation, we model the two-dimensional electron gas in the quantum well as a layer of thickness d with a uniform distribution of electron density. Taking into account the lowest quantum level E_1, the surface electron concentration n_s is determined from the expression

$$n_s=D_sk_BT\ln\left[1+\exp\left(\frac{F_n+e\varphi_s-E_1}{k_BT}\right)\right], \tag{5}$$

where D_s is the two-dimensional density of states, and φ_s is the potential at the heterojunction relative to the bulk. The thickness d and energy E_1 are calculated using the model of a triangular quantum well.[8]

The boundary condition at the left boundary of the buffer layer was formulated by assuming that the charge Q_s in the layer of strongly doped AlGaAs does not change under illumination. We justify this assumption by noting that at high temperatures the long-period relaxation of the photoconductivity is connected with charging of the $EL2$-centers in the GaAs, whereas the DX-centers in the AlGaAs charge much more rapidly.

Results of these calculations are shown in Fig. 5, where we plot the spatial distribution of the population of $EL2$-centers $f_t=N_e/N_t$ in the equilibrium state (the dashed curves) and under illumination. In these calculations we used values of the photoionization cross section of $EL2$-centers taken from Ref. 7: $\sigma_n=1.5\times10^{-16}\,\mathrm{cm}^2$ and $\sigma_p=2\times10^{-17}\,\mathrm{cm}^2$ for $h\nu=1.33\,\mathrm{eV}$, and $\sigma_n=4\times10^{-17}\,\mathrm{cm}^2$ and $\sigma_p=5\times10^{-17}\,\mathrm{cm}^2$ for $h\nu=1.0\,\mathrm{eV}$. Following Ref. 9, we calculated the capture and thermal emission coefficients from the following expressions: $c_n=1.5\times10^{-8}T^{1/2}\exp(-0.066/k_BT)$, $c_p=1.9\times10^{-12}T^{1/2}$, $e_n=2.83\times10^7T^2\exp(-0.814/k_BT)$, and $e_p=3.3\times10^4T^2\exp(-0.813/k_BT)$. Here the capture coefficients c_n and c_p in units of $[\mathrm{cm}^3/\mathrm{s}]$ and emission coefficients e_n and e_p in units of $[\mathrm{s}^{-1}]$ were obtained by substituting T in [K] and k_BT in [eV]. An optical flux of $\Phi=10^{17}\,\mathrm{cm}^{-2}\cdot\mathrm{s}^{-1}$ was used.

It is clear from Fig. 5a that light removes electrons from the $EL2$-centers in the central portion of the buffer layer ($0.3<x<0.65\,\mu\mathrm{m}$), resulting in an accumulation of photoinduced positive charge. At the edge of the space-charge layer ($x>0.7\,\mu\mathrm{m}$) the $EL2$-centers are occupied by electrons, and here a negative charge accumulates. The nonequilibrium charge accumulated in the buffer is compensated by nonequilibrium electrons in the quantum well, thereby affecting the photoconductivity. When the light is switched off, the

nonequilibrium charge in the buffer relaxes as follows. The positive charge is neutralized by electrons ejected by the quantum well into the buffer and trapped by $EL2$-centers. This involves a broad spectrum of activation energies; hence, no well-defined activation energy is observed during the relaxation of the positive persistent photoconductivity. Relaxation of the negative charge, which is responsible for NPP, takes place by thermal ejection of electrons from $EL2$-centers into the conduction band. The activation energy of this process is higher than the energy for thermal ejection from the quantum well; therefore, it is slower. The characteristic relaxation time for NPP is determined by the quantity e_n, which according to calculations at $T=250$ K equals $7\times10^{-5}\,\mathrm{s}^{-1}$, which is close to the observed relaxation time.

The magnitude of positive and negative charge accumulated in deep centers during illumination allows us to estimate the values of positive and negative persistent photoconductivity that can be observed experimentally. Thus, according to Fig. 5a, the surface concentration of accumulated positive charge is $\sim2.4\times10^{10}\,\mathrm{cm}^{-2}$, while the negative charge is $\sim2\times10^{9}\,\mathrm{cm}^{-2}$. If we take into account that the equilibrium concentration of two-dimensional electrons is $\sim5\times10^{11}\,\mathrm{cm}^{-2}$, then the positive persistent photoconductivity is ~5% of the equilibrium photoconductivity and the NPP is ~0.5%, which agrees with experiment. Here it is worth noting that this ratio of values of positive and negative persistent photoconductivity is achieved by choosing the degree of compensation, i.e., the ratio N_t/N_a, and the electron concentration n_0. If n_0 is greatly increased, e.g., by a factor of 10^2 (see Fig. 5a), to $\sim10^8\,\mathrm{cm}^{-3}$, the NPP decreases by more than an order of magnitude (see Fig. 5b). The fact that the concentration of nonequilibrium electrons in the bulk of the buffer layer turns out to be so low implies that in this structure the potential barrier in the buffer layer is probably short-circuited, because the contacts used to measure the photocurrent short out the rear surface of the buffer (adjacent to the substrate) and the two-dimensional electron layer. Decreasing the degree of compensation (i.e., decreasing the ratio N_t/N_a) also leads to a significant decrease in the magnitude of the NPP (see Fig. 5c).

The NPP effect is strongly modified when the ratio of $EL2$-center ionization cross sections σ_p/σ_n is changed. Specifically, increasing this ratio leads to an increase in NPP. This situation is illustrated by Fig. 5d, where we plot the calculated center population under illumination by photons with $h\nu=1.0$ eV.

5. LOW-TEMPERATURE NPP (CHARGING OF *DX*-CENTERS)

At temperatures below 180 K, the relaxation of DX-center photoconductivity is qualitatively similar to the $EL2$-center case discussed above (Fig. 2b). The primary quantitative difference arises from the fact that at low temperatures the activation energy of DX-centers is smaller in magnitude. Another difference is the large number of defects in the AlGaAs layer compared with $EL2$-centers, and hence the larger persistent photoconductivity.

The main features of the low-temperature decay kinetics

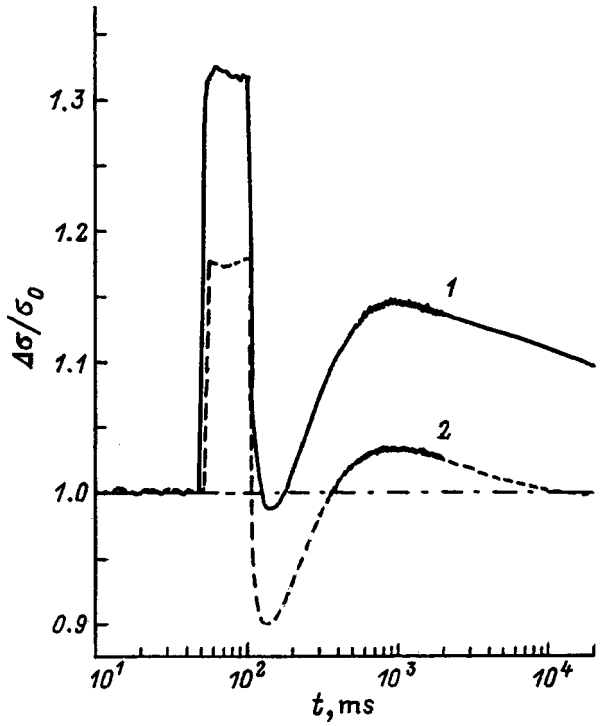

FIG. 6. Relaxation of photoconductivity excited by impurity-energy photons $h\nu=1.33$ eV (*1*) and interband-energy photons $h\nu=1.97$ eV (*2*). $T=160$ K.

of the photoconductivity $\Delta\sigma/\sigma_0$ can be seen in Fig. 6, which shows the relaxation for interband and impurity photoexcitation. It is clear that the increase in photon energy, and thus the absorption coefficient of light, leads not to an increase in photoconductivity, which we would naturally expect, but rather to a decrease. This implies that the photoconductivity is primarily due to absorption of impurity-energy photons. At $h\nu=1.33$ eV the photoconductivity is found to be larger because light penetrates deeper into the sample and causes ionization of $EL2$-centers over a larger portion of the space-charge layer. In this case the contribution of $EL2$-centers to the photoconductivity is almost time-independent since the temperature is low. Consequently, the nonmonotonic relaxation of the photoconductivity in Fig. 6 is due to charging of impurities in the AlGaAs layer, where the primary defects are DX-centers.

The main effect of charging DX-centers at moderate temperatures (~150 K) is NPP, which, as far as we know, has not been discussed previously. We assume that the NPP effect in this case is related to metastable excitation of states of the DX centers. Known states of a DX-center are: the (singly charged) ground state DX^-, a neutral state DX^0 (the result of a single photoionization), and an ionized state DX^+. In this state, the DX-center can be converted into a shallow-donor state N^+.[3,10] It has been established elsewhere[10] that a high energy barrier inhibits the thermal ionization of the DX^0 state to the N^+ state, so that photoexcitation of DX^- states results in an accumulation of centers in the state DX^0, which have one electron apiece. After the light is switched off, free electrons start to be trapped by the defects, forming DX^- centers. If we assume that this trapping occurs more rapidly than thermal ionization of the equilibrium DX^0

states, then the DX^- centers that form bind more electrons than are generated by the light. As a result, the quasi-Fermi level for electrons in the AlGaAs is lowered, causing a backflow of electrons from the quantum well to the AlGaAs layer. This results in NPP, which relaxes at the same rate as thermal ionization of the DX^0 states. Unfortunately, there is not enough data available at present on the photoexcitation and relaxation of states of DX-centers to allow us to analyze this NPP mechanism quantitatively.

6. CONCLUSIONS

Our studies of photoconductivity relaxation kinetics in the temperature range 80 to 300 K and photon energy range from 0.6 to 2.1 eV for the excitation light has led to the following results.

1. In modulation-doped AlGaAs/GaAs heterostructures there are two processes that lead to negative persistent photoconductivity. One of them, which operates in the temperature range 180 to 300 K, is caused by charging of $EL2$-centers. The other is observed at lower temperatures (below 180 K), and is associated with excited states of DX-centers.

2. Photoinduced charging of deep centers can lead to accumulation of positive and negative charge and in this way causes positive and negative persistent photoconductivity, respectively.

3. These positive and negative impurity center charges accumulate in different portions of the heterostructure buffer layer and are characterized by different relaxation times, which also have different temperature dependences. This leads to nonmonotonic time and temperature dependences of the persistent photoconductivity.

This work was supported by the Russian Fund for Fundamental Research (Grant No. 97-02-17999).

[1] T. Hariu, T. Sato, H. Komori, and K. Matsushita, J. Appl. Phys. **61**, 1068 (1987).
[2] A. Kitagawa, A. Usami, T. Wada, Yu. Tokuda, and H. Kano, J. Appl. Phys. **61**, 1215 (1987).
[3] P. M. Mooney and T. N. Theis, Comments Condens. Matter Phys. **16**, 167 (1992).
[4] M. J. Chou, D. C. Tsui, and G. Weimann, Appl. Phys. Lett. **47**, 609 (1985).
[5] H. Peterson, H. J. Grimmeiss, A. L. Powell, C. C. Button, J. S. Roberts, and P. I. Rockett, J. Appl. Phys. **74**, 5596 (1993).
[6] A. J. Shields, J. L. Osborne, M. J. Simmons, D. A. Ritchie, and M. Pepper, Semicond. Sci. Technol. **4**, 890 (1996).
[7] P. Silverberg, P. Oming, and L. Samuelson, Appl. Phys. Lett. **52**, 1689 (1988).
[8] M. Shur, *GaAs Devices and Circuits* (Plenum Press, New York/London, 1987; *Modern Devices Based on Gallium Arsenide*, Mir, 1991).
[9] J. S. Blakemore, J. Phys. Chem. Solids **49**, 627 (1988).
[10] L. Dobaczewski and P. Kaczor, Phys. Rev. Lett. **66**, 68 (1991).

Translated by Frank J. Crowne

Conductivity of thin nanocrystalline silicon films

V. G. Golubev, L. E. Morozova, A. B. Pevtsov, and N. A. Feoktistov

A. F. Ioffe Physicotechnical Institute, Russian Academy of Sciences, 194021 St.Petersburg, Russia
(Submitted May 26, 1998; accepted for publication May 27, 1998)
Fiz. Tekh. Poluprovodn. **33**, 75–78 (January 1999)

It is shown in this paper that thin (200–250 Å) hydrogenated nanocrystalline silicon films have low longitudinal conductivity, comparable to that of undoped amorphous silicon, and high transverse conductivity. These films can be used as doping layers in barrier structures with low surface current leakage. It was found that film conductivity decreases by 8–10 orders of magnitude along the layer as the layer thickness is reduced from 1500 to 200 Å. The observed dependence of the conductivity on thickness can be explained (in terms of percolation theory) by destruction of a percolation cluster made up of nanocrystallites as the layer thickness is decreased. [S1063-7826(99)01601-4]

There are a number of devices based on hydrogenated amorphous silicon (a-Si:H) and nanocrystalline silicon (nc-Si:H) that need low-conductivity doping layers along the film surface. This is true of, e.g., vidicons, low-light photoelements,[1] and space-time optical modulators.[2] In these devices it is necessary to prevent leakage of current along the doping layers of the $p-i-n$ structures. This can be partially achieved by decreasing the level of doping of the p- and n-layers. However, decreasing the concentration of doping impurities leads to degradation of the parameters of the $n-i$ or $p-i$ barrier, and accordingly to degradation of the loading characteristics of the photoelements and the photosensitivity and speed of the space-time optical modulator.

In this paper we show that thin (200–250 Å) nanocrystalline silicon films used as doping layers possess low leakage along the surface.

These synthetic films essentially consist of a system of crystalline quantum dots embedded in an amorphous host. The nanocrystallite-amorphous host interface is a heterojunction with a tunneling insulator.[3] The crystallites can have sizes from 20 to 100 Å, and their volume fraction varies in the range from 0– 50%.[4–7] On the other hand, it was shown in Refs. 7 and 8 that the abrupt change in conductivity observed in nanocrystalline silicon as the volume fraction of the crystallites increases can be explained within the framework of a phenomenological representation taken from percolation theory which does not involve the consideration of quantum effects. The volume fraction of nanocrystallites, upon reaching a critical value of the order of 16% in nanocrystalline silicon, for example, forms a percolation cluster made up of nanocrystallites, and the conductivity of the film rises abruptly. In this case, the current percolates through the system of nanocrystallites, which possess a conductivity more than an order of magnitude higher than the amorphous host. If the volume fraction is below the critical value, which corresponds to the percolation threshold, a percolation cluster does not form and the conductivity is determined by the properties of the amorphous phase.

However, it is incorrect to treat thin films, i.e., whose thickness is comparable to the size of a crystallite, as three-dimensional systems in percolation theory problems. Note that two-dimensional systems (with respect to the size of a crystallite) require considerably larger volume fractions of nanocrystallites to create a percolation cluster: it is known[8] that for the conducting hard-sphere model the percolation threshold is reached when the critical volume fraction occupied by spheres is roughly 16% for a three-dimensional system and 50% for a two-dimensional system. Thus, thin (quasi-two-dimensional) films of nc-Si:H, in which a bulk percolation cluster has not formed, i.e., there is no high longitudinal conductivity present, and which at the same time have a fairly high transverse conductivity (determined by the properties of individual crystallites and the heterojunctions between them) can be used as doping layers for $p-i-n$ structures.

Nanocrystalline silicon is made by plasma-enhanced chemical vapor deposition, or PE CVD, from silane strongly diluted with hydrogen.[4] The parameters for the fabrication process are as follows: concentration of silane in hydrogen 2–3%, working pressure of the mixture 0.2–0.4 Torr, outflow of working mixture 10–20 cm^3/min, substrate temperature 200–300 °C, rf power density 0.3 to 1 W/cm^2, and frequency 17 MHz.

The films were deposited by standard diode PECVD, in which an rf voltage is applied to an rf electrode with the substrate located on a heated second electrode. This heated electrode is grounded with respect to the rf component and can be given a dc negative bias of 0–300 V. For *in situ* monitoring of the growth rate and optical parameters of the film, we used laser interferometry with the laser beam normal to the substrate. To obtain doped films of nanocrystalline n-type nc-Si:H, phosphene is added to the gas mixture [with $PH_3/(SiH_4+PH_3)\sim 1\%$].

Both quartz and crystalline silicon were used as substrates. The growth rate of the film was 0.3 to 1.0 Å/s. The volume fraction and dimensions of the crystallites, determined by numerically processing Raman scattering spectra with allowance for spatially confined phonons,[7] were $\sim 30\%$ and ~ 40 Å, respectively. Film thicknesses ranged from 1500 to 200 Å.

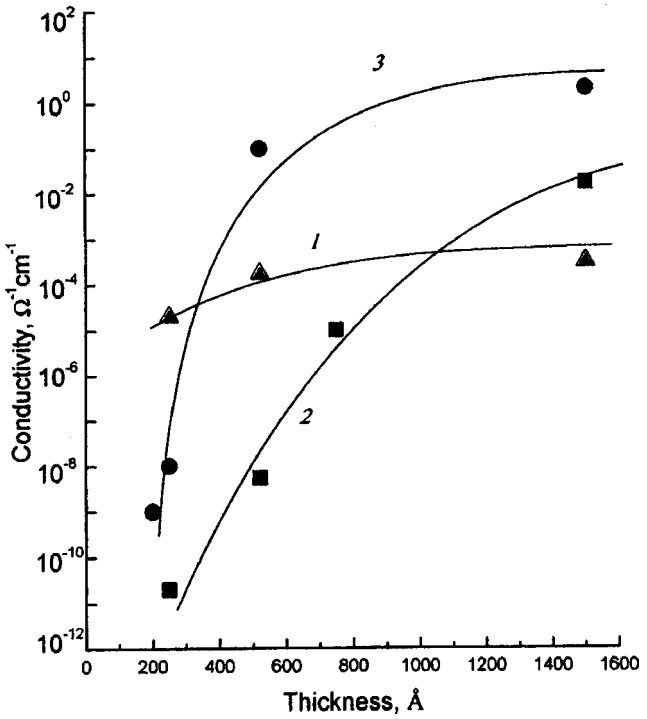

FIG. 1. Plots of conductivity versus thickness for nanocrystalline (*2*, *3*) and amorphous (*1*) silicon films doped (*1*, *3*) and undoped (*2*) with phosphorus.

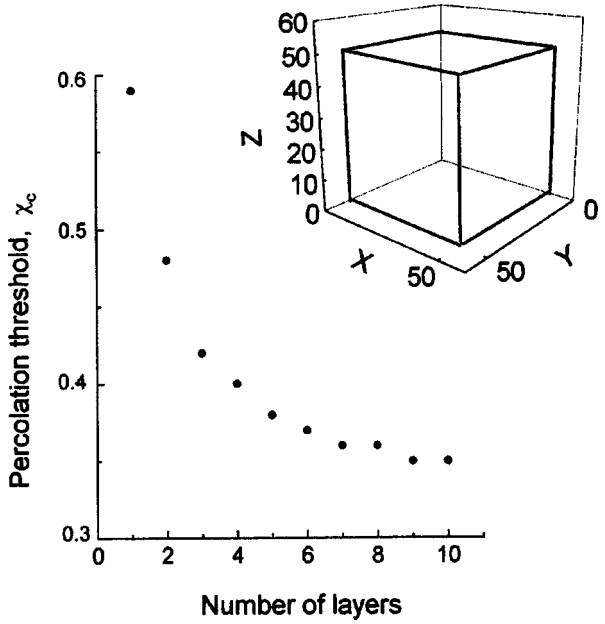

FIG. 2. Calculated dependence of the magnitude of the percolation threshold χ_c in the longitudinal (X, Y) direction for a simple cubic lattice on the number of lattice layers in the transverse (X, Z) direction. Calculations were made for a cube consisting of $50\times50\times50$ sites (see the inset) and a step of 1 in the directions X, Z.

Doped layers of *a*-Si : H were also fabricated in order to compare the thickness dependence of the conductivity for nanocrystalline and amorphous films. The corresponding deposition took place at silane concentrations in the gas mixture of more than 10% and decreased rf power density (<0.1 W/cm^2). The conductivity of the samples was measured in a planar configuration between deposited silver paste electrodes about 3 mm long and separated by a distance of order 1 mm.

Figure 1 shows the thickness dependence of the conductivity for films with various compositions: nanocrystalline films, both undoped and doped with phosphorus, and also weakly doped amorphous films ($PH_3/SiH_4\sim0.01\%$). It is clear from this figure that the nanocrystalline films exhibit a very strong dependence of the conductivity on thickness, with the magnitude of the conductivity decreasing by more than nine orders of magnitude as the thickness decreases from 1500 to 200 Å. At the same time, varying the thickness of the amorphous layers within the same limits changes the conductivity by less than an order of magnitude. This difference in behavior of the conductivities of nanocrystalline and amorphous films allows us to associate the observed decrease in conductivity in thin films of *nc*-Si : H with the destruction of a percolation cluster as the system goes from three-dimensional to quasi-two-dimensional with respect to the size of a crystallite. In fact, if the diameter of the nanocrystallites is 30 to 40 Å, only 5–6 nanocrystallites can fit in the transverse direction with respect to the substrate for a film with thickness 200–250 Å. At the same time, the film can accommodate more than 10^5 crystallites in the longitudinal direction.

In order to confirm this interpretation, we used the Monte Carlo method to numerically calculate the percolation threshold χ_c for the site problem ($\chi_c=W/\eta$, where W is the critical volume fraction, and η is the packing density). In these calculations we assumed a simple cubic lattice. The magnitudes of the percolation threshold in the limiting cases of bulk ($50\times50\times50$) and planar ($50\times50\times1$) lattices (see the inset in Fig. 2) came to 0.31 and 0.59 respectively, which coincide with values of χ_c reported in the literature[9] for simple cubic and square lattices. The calculated dependence of χ_c on the number of layers of the lattice along the directions X, Y (longitudinal conductivity) is shown in Fig. 2.

From this analysis it follows that in thin films (less than 10 crystallite diameters) a percolation cluster will not appear in the longitudinal direction until the volume fraction of the nanocrystalline phase exceeds a critical value that is larger that the value for the three-dimensional case ($\sim16\%$). As we have already noted, this value is bounded from above by the value for a planar (two-dimensional) system, or $\sim50\%$. Thus, from the point of view of percolation theory, we should treat films of *nc*-*a*-Si : H as quasi-two-dimensional when their thickness becomes comparable to the size of a nanocrystallite.

Our estimates indicate that the volume fraction of nanocrystallites in these samples is $\sim30\%$; this is virtually independent of the film thickness, i.e., considerably smaller than the critical value of 50% for percolation in the two-dimensional case. This result is in agreement with our interpretation of the observed giant falloff in conductivity, i.e., that it is due to destruction of a percolation cluster during the transition from bulk to a thin quasi-two-dimensional layer of *nc*-Si : H (thin with respect to the size of a nanocrystallite).

Let us now consider the behavior of the conductivity transverse to the layer. Our calculations show that in thin

layers (of order 5–6 crystallite diameters) the transverse conductivity should rise rapidly due to the increased probability for the formation of a percolation cluster of nanocrystallites from the upper electrode to the lower. However, we emphasize at the outset that in these experimental studies the area of the upper titanium contact was $\sim 10^{-3}\,\mathrm{cm}^2$, so that for films that are about 1000 Å thick the measured transverse resistance will substantially exceed the resistance of the lower titanium electrode ($\sim 10\,\Omega$) only for conductivity values less than $10^{-4}\,\Omega^{-1}\mathrm{cm}^{-1}$. This quantity limits the maximum values of transverse conductivity observed in experiment.

This analysis allows us to estimate the volume fraction of crystallites in a film of *nc*-Si:H, for which considerable anisotropy in the conductivity appears. However, it does not allow us to obtain the analytic dependence of the conductivity on film thickness. In order to explain the specific form of this function, we probably must invoke the same considerations as the authors of the monograph Ref. 10 did in deriving their analytic expression for the dependence of hopping conductivity on layer thickness.

It is interesting to note that the longitudinal conductivity of a phosphorus-doped *nc*-Si:H film with thickness of 200–250 Å is only an order of magnitude higher than that of undoped nanocrystalline *nc*-Si:H, and is considerably lower than the conductivity of weakly doped *a*-Si:H. In considering this result, we must take into account that nanocrystalline films are grown under fabrication conditions that differ greatly from the standard PECVD conditions used to obtain amorphous silicon, which can lead to an increased concentration of defects in the amorphous phase. On the one hand, this circumstance will facilitate the growth of the nanocrystalline phase since it decreases the energy barrier for nucleation of crystallites due to the increased static disorder in the amorphous medium,[6] while on the other hand it makes the doping the amorphous host less effective. Moreover, the atomic impurities are themselves additional centers for formation of crystallite seeds. Because of this circumstance, we can argue that the distribution of doping impurity in the film should be strongly nonuniform and concentrated in the nanocrystalline phase. Since for thin (200–250 Å) layers the volume fraction of crystallites is insufficient for a percolation cluster to appear, the conductivity of the heterophase films in the longitudinal direction will be determined by the properties of the low-conductivity amorphous phase.

Thus, we have investigated the dependence of the conductivity of hydrogenated nanocrystalline silicon films on thickness. The conductivity along the layer decreases by 8–10 orders of magnitude as the thickness decreases from 1500 to 200 Å. The observed thickness dependence of the longitudinal conductivity is interpreted in the framework of percolation theory and is associated with destruction of a percolation cluster as the film thickness decreases. The thin (200–250 Å) films of *nc*-Si:H we have obtained could be used as doped layers in $p-i-n$ structures, where it is necessary to decrease the current leakage along the layer surface while preserving a rather high value of transverse conductivity.

This work was carried out with the financial support of the Russian Fund for Fundamental Research (Project No. 98-02-17350) and the Minister of Science and Technology Program ''Physics of Solid-State Nanostructures''. (Project No. 96-1012).

[1] *Amorphous Semiconductors and Devices Based on Them*, edited by I. Khamakavi [Metallurgiya, Moscow, 1986].
[2] N. I. Ivanova, N. A. Feoktistov, A. N. Chaika, A. P. Onokhov, and A. B. Pevtsov, Mol. Cryst. Liq. Cryst. **282**, 315 (1996).
[3] G. Y. Hu, R. F. O'Connel, Y. L. He, and M. B. Yu, J. Appl. Phys. **78**, 3945 (1995).
[4] T. Hamasaki, H. Kurata, M. Hirose, and Y. Osaka, Appl. Phys. Lett. **37**, 1084 (1980).
[5] X. Liu, S. Tong, L. Wang, G. Chen, and X. Bao, J. Appl. Phys. **78**, 6143 (1995).
[6] A. B. Pevtsov, V. Yu. Davydov, N. A. Feoktistov, and V. G. Karpov, Phys. Rev. B **52**, 955 (1995).
[7] V. G. Golubev, V. Yu. Davydov, A. V. Medvedev, A. B. Pevtsov, and N. A. Feoktistov, Fiz. Tverd. Tela (St. Petersburg) **39**, 1348 (1997) [Phys. Solid State **39**, 1197 (1997)].
[8] R. Tsu, J. Gonsalez-Hernandez, S. S. Chao, S. C. Lee, and K. Tanaka, Appl. Phys. Lett. **40**, 534 (1982).
[9] J. M. Ziman, *Models of Disorder: The Theoretical Physics of Homogeneously Disordered Systems* (Cambridge Univ. Press, Cambridge, 1979; Mir, Moscow, 1982).
[10] V. I. Shklovskiĭ and A. L. Efros, *Electronic Properties of Doped Semiconductors* (Nauka, Moscow, 1979), Ch. 9, p. 276 (Springer-Verlag, New York, 1984).

Translated by Frank J. Crowne

Vertical screening in doped, intentionally disordered semiconductor superlattices

I. P. Zvyagin and M. A. Ormont

Physics Department, M. V. Lomonosov Moscow State University, 119899 Moscow, Russia
(Submitted May 5, 1998; accepted for publication June 4, 1998)
Fiz. Tekh. Poluprovodn. **33**, 79–82 (January 1999)

The energy spectrum of electrons in doped, intentionally disordered superlattices is calculated with allowance for the Coulomb fields generated by the redistribution of electrons among the quantum wells. An approach based on density functional theory is used in conjunction with a numerical technique to investigate the influence of screening on the vertical disorder, in particular, on the distribution of quantum-well levels in such structures. It is shown that screening shifts the maximum of the distribution and significantly decreases its width; this effect can result in delocalization of the electronic states governing the vertical conductivity of the structure.
 [S1063-7826(99)01701-9]

INTRODUCTION

There has been growing interest lately in the properties of the vertical conductivity of intentionally disordered superlattices (IDSLs), i.e., structures containing quantum wells in which the distribution of quantum-well levels can actually be controlled by regulating the thicknesses of the layers during growth. Experimental studies of GaAs/GaAlAs IDSLs, preeminently by optical methods, have been reported in several papers.[1–3] They comprise model quasi-one-dimensional systems useful for investigating the influence of the magnitude and type of disorder on the energy spectrum and kinetic properties. In particular, for short-period superlattices containing only a few wells it has been found possible to acquire information about vertical (in the direction of the superlattice growth axis) transport of photoexcited nonequilibrium charge carriers.[1] Richter *et al.*[4] have performed direct electrical measurements of the temperature dependence of the vertical conductivity of IDSLs which were doped uniformly throughout their volume with silicon and which contained on the order of 10^2 wells, where random fluctuations of the widths of the wells created a Gaussian distribution of quantum-well levels. The results of the measurements in Ref. 4 have disclosed several nontrivial anomalies of the vertical conductivity at low temperatures; in particular, it has been found that the vertical conductivity depends weakly on the temperature (quasimetallic behavior), even in the presence of large disorder, when the specified width of the random distribution of quantum-well levels is significantly greater than the miniband width, and it is reasonable to assume that all miniband states are localized. To explain this anomaly in the behavior of the vertical conductivity, the authors of Ref. 4 hypothesized that it is related to the influence of Coulomb fields produced by a redistribution of electrons among the wells on the energy spectrum of the doped superlattice. In this paper we calculate the ground state of doped IDSLs at low temperatures and investigate the dependence of its characteristics on the parameters of the superlattice and on the doping level.

STATEMENT OF THE PROBLEM

We consider a system of quantum wells separated by barriers of constant width with a Gaussian distribution of quantum-well levels calculated in the isolated-well approximation. All electrons with donors inside the barriers transfer into the quantum-well regions, producing electric fields, which cause the levels to shift; this effect necessitates a self-consistent solution of the problem of calculating the electric fields and the distribution of electrons among the wells of the superlattice. We confine the discussion to narrow quantum wells and slight overlap of the wave functions of adjacent wells; we can then restrict the discussion entirely to the lowest quantum-well subband and assume approximately that the charge of the carriers in a quantum well are localized in-plane (this model is analogous to the Vischer–Richter model of charged layers used in the investigation of screening due to longitudinal charge redistribution in the layers[5]).

As long as we are concerned with the region of moderately low dopant concentrations, we can disregard exchange-correlation effects and stay within the Hartree approximation (for low concentrations exchange-correlation effects can be appreciable and result in the formation of superstructures and structural rearrangement of the energy spectrum[4,6]). To calculate the spectrum with allowance for the redistribution of electrons among the quantum wells, it is convenient to use an approach based on density functional theory.[7] Specifically, following Refs. 4 and 6, we write the energy of the system at $T=0$ K, $E[n]$ as a density functional $n(z)=\Sigma_i \nu_i \delta(z-id)$, where ν_i is the two-dimensional density of electrons in the ith layer, and d is the period of the superlattice (the confining potential is taken into account here in the choice of basis). We note that the functional $E[n]$ is simply a function of many variables $\nu=\{\nu_i\}$ in the given situation. We have

$$E(\nu)=\sum_i E_i^{(0)}\nu_i+\sum_i (\nu_i^2/2\rho_0) + (1/2)\sum_{i,j} V_{ij}(\nu_i-\nu_0)(\nu_j-\nu_0), \quad (1)$$

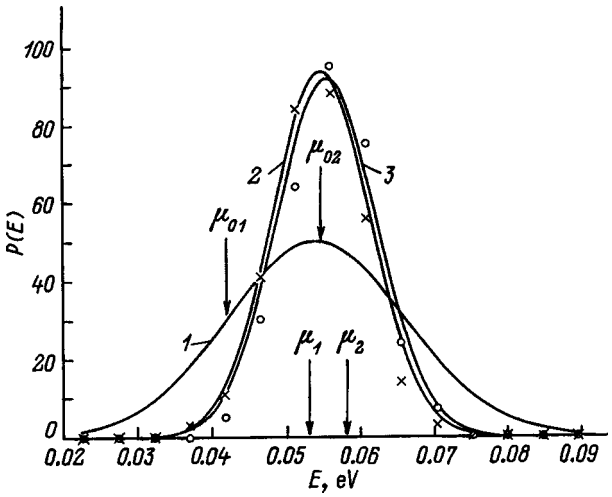

FIG. 1. Distribution functions of quantum-well levels in intentionally disordered superlattices, calculated with allowance for the Coulomb fields generated by the spatial redistribution of electrons. (*1*) Gaussian bare distribution function (3); (*2*) Gaussian approximation of the results of calculations (○) at a dopant concentration $1\times10^{17}\,\mathrm{cm}^{-3}$, and curve *3* is the same for calculations (×) at a concentration of $5\times10^{17}\,\mathrm{cm}^{-3}$. The arrows indicate the positions of the Fermi levels μ_1 and μ_2; ν_{01} and ν_{02} denote the positions of the Fermi levels calculated at the indicated concentrations without regard for the Coulomb fields associated with redistribution of the charges.

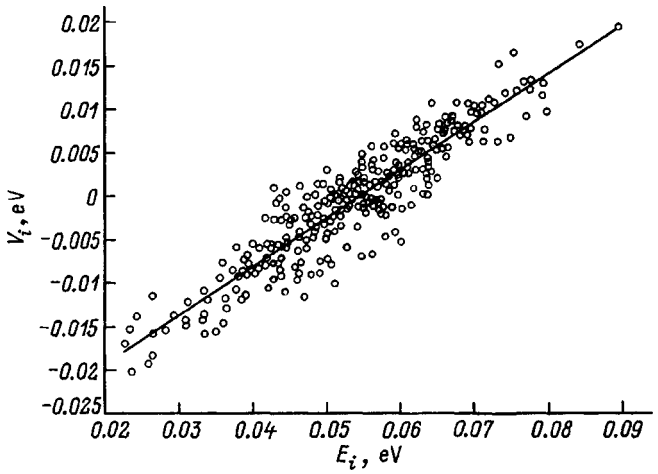

FIG. 2. Dependence of the shifts of the quantum-well levels due to the redistribution of electrons on the energies of the bare levels $E_i^{(0)}$ for a Gaussian distribution of the levels at $N_d=10^{17}\,\mathrm{cm}^{-3}$. The solid curve corresponds to the linear approximation (4).

where $E_i^{(0)}$ is the energy level in the ith well in the absence of free electrons, ρ_0 is the two-dimensional density of states in the well, $V_{ij}=-2\pi e^2 d|i-j|/\varepsilon$, $\nu_0=N_d d$ is the average two-dimensional electron density in the layer, and N_d is the dopant concentration. The distribution of electrons among the quantum wells for the ground state of the system can be determined by minimizing $E(\nu)$ subject to the additional condition $\Sigma_i(\nu_i-\nu_0)=0$. The corresponding conditions of the minimum of $E(\nu)$ have the form

$$E_i^{(0)}+\nu_i/\rho_0+\sum_j V_{ij}(\nu_j-\nu_0)+\mu=0, \tag{2}$$

where μ is a Lagrange multiplier (chemical potential of the system), which is determined from the condition $\Sigma_i(\nu_i-\nu_0)=0$.

RESULTS OF THE CALCULATIONS

The results of the numerical solution of the system of equations (2) are shown in Figs. 1 and 2. The distributions of the renormalized levels E_i are calculated with allowance for the Coulomb fields produced by the redistribution of carriers among the wells for a given bare Gaussian distribution of the quantum-well levels

$$P(E_i^{(0)})=(1/\sqrt{2\pi}w)\exp\{-(E_i^{(0)}-E_m)^2/2w^2\} \tag{3}$$

(Fig. 1, curve *1*) for various doping levels; Fig. 1 shows the distributions of the E_i levels for $N_d=10^{17}\,\mathrm{cm}^{-3}$ (curve *2*) and $N_d=5\times10^{17}\,\mathrm{cm}^{-3}$ (curve *3*). The following parameters are used in the calculations: $\rho_0=3\times10^{13}\,\mathrm{eV}^{-1}\cdot\mathrm{cm}^{-3}$, $w=15\,\mathrm{meV}$, $\varepsilon=10$, and $d=33$ Å. The character of the variation of the spectrum of quantum-well levels is readily established by analyzing the shifts of the levels relative to their bare positions; the shift of the E_i level in the ith well relative to the bare level $E_i-E_i^{(0)}=V_i$ is dictated by the potential energy of the electric field V_i at the site of the ith well. The dependence of V_i on the position of the $E_i^{(0)}$ level for curve *2* in Fig. 1 ($N_d=10^{17}\,\mathrm{cm}^{-3}$) is shown in Fig. 2. The figure clearly reveals a trend of the quantum-well levels to shift toward the renormalized Fermi level μ. The dependence $V_i(E_i^{(0)})$ can be approximated by the equation

$$E_i-E_i^{(0)}=A(E_i^{(0)}-\mu), \tag{4}$$

where $A\approx0.55$. If the approximation (4) is adopted for the ''average'' shift of the bare level, the distribution function of the renormalized levels also has a Gaussian form of half-width $w_1=Aw$ with the shifted maximum $E_m=E_m^{(0)}+A(E_m^{(0)}-\mu)$.

It is evident that Coulomb effects lead to a significant decrease in the width of the distribution function and a shift of the Fermi level. To gain insight into the physical reasons for the modification of the energy spectrum of quantum-well levels as described by relation (4), we recall that the depth of a quantum-well level in a superlattice with one ''defective'' quantum well having a different width from the ''regular'' wells of the superlattice decreases by the factor $\beta=1+4\pi e^2\rho_0 d/\varepsilon$ as a result of vertical screening due to charge redistribution among the wells. For the above-indicated values of the parameters we have $\beta\approx1.9$, i.e., the average slope A in Eq. (4) is essentially the same as $1/\beta$. The scatter of the level shifts relative to the linear approximation (4) is attributable to the significant bearing of fluctuations of wells of the immediate environment on any one given well. This interpretation is corroborated by a calculation of the renormalization of the level spectrum for an ensemble of superlattices, each of which contains only one ''defective'' well, with the same level distribution as the bare distribution $P(E_i^{(0)})$. For such an ensemble Eq. (4) is satisfied exactly, and the random scatter of the level shifts is zero.

Strictly speaking, the pattern of shifting of levels situated above and below the Fermi level is not symmetric about μ; i.e., the distributions of the shifts above and below μ are

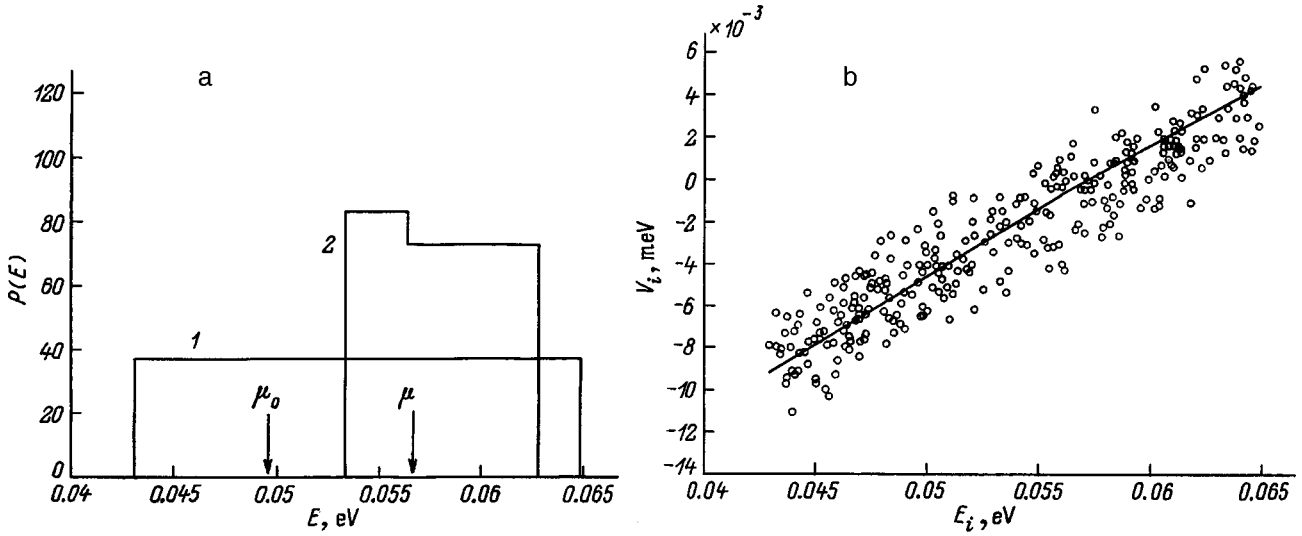

FIG. 3. Modification of the distribution function of the quantum-well levels $P(E_i^{(0)}=[1](1/2w)\Theta\{w-|E_i^{(0)}-E_0|\}$ due to the Coulomb fields generated by the redistribution of electrons among the quantum wells ($N_d=10^{17}$ cm^{-3}, $w=22$ meV). (a) Function $P(E_i^{(0)})$ (curve *1*) and the distribution function (curve *2*) obtained from it by piecewise-linear approximation of the distribution of shifts of the quantum-well levels (line with a kink in Fig. 3b); (b) dependence of the shifts of the quantum-well levels on the bare energies of the levels.

approximated by linear functions of the type (4) with several different coefficients A. Because of the strong energy dependence of the Gaussian distribution function, this asymmetry has little effect on the form of the renormalized distribution function. The asymmetry of the shifts becomes obvious, however, for a slowly varying distribution function. Figures 3a and 3b show the results of calculations for a bare level distribution function that is constant in a certain energy interval and is equal to zero outside it:

$$P(E_i^{(0)})=(1/2w)\Theta\{w-|E_i^{(0)}-E_0|\} \tag{5}$$

(this function is represented by curve *1* in Fig. 3a). The dependence of the shifts of the quantum-well levels on the bare energies of the levels for this case is shown in Fig. 3b. Both in the region $E_i^{(0)}<\mu$ and in the region $E_i^{(0)}>\mu$ the level shifts can be approximated ''on the average'' by linear functions of type (3) with slopes A_1 and A_2, respectively. Here $A_1>A_2$, i.e., the slope for $E_i^{(0)}<\mu$ is somewhat larger than for $E_i^{(0)}>\mu$. For this reason the level distribution function exhibits a characteristic increase at energies lower than μ (curve *2* in Fig. 3a is generated by a piecewise-linear approximation of the distribution shown in Fig. 3b).

DISCUSSION OF THE RESULTS

Thus, the doping of IDSLs not only imparts a simple shift to the Fermi level, but also significantly alters the positions of the quantum-well levels that correspond to the minima of the subbands in the individual wells. The levels of adjacent levels merge as a result, and this process has the effect of, on the one hand, diminishing the disorder governed by the factor β and, on the other, increasing the overlap integrals of the electron wave functions of adjacent wells, i.e., the effective miniband width. These two factors account for the trend, discerned in measurements of the vertical conductivity of doped superlattices with vertical disorder, toward the delocalization of electronic states in the direction of the axis of the superlattices.[5]

This work has received financial support from the Russian Fund for Fundamental Research (Grant 97-02-17334) and the Ministry of Education (Fundamental Natural Sciences Grant 97-0-7.1-174).

[1] A. Chomette, B. Deveaud, A. Regreny, and G. Bastard, Phys. Rev. Lett. **57**, 1464 (1986).
[2] T. Yamamoto, M. Kasu, S. Noda, and A. Sasaki, J. Appl. Phys. **68**, 5318 (1990).
[3] E. Tuncel and L. Pavesi, Philos. Mag. **65**, 213 (1992).
[4] G. Richter, W. Stolz, P. Thomas, S. Koch, K. Maschke, and I. P. Zvyagin, Superlattices Microstruct. **22**, No 4, 475 (1997).
[5] P. B. Vischer and L. V. Falikov, Phys. Rev. B **3**, 2541 (1971).
[6] I. P. Zvyagin, Zh. Éksp. Teor. Fiz. **114**, No. 3(9) (1998) [JETP **87**, 594 (1998)].
[7] W. Kohn and P. Vashishta, in *Theory of the Inhomogeneous Electron Gas*, edited by S. Lundqvist and N. H. March (Plenum Press, New York, 1983; Mir, Moscow, 1987).

Translated by James S. Wood

Optical intersubband transitions in strained quantum wells utilizing $In_{1-x}Ga_xAs/InP$ solid solutions

S. A. Stoklitskiĭ, V. N. Murzin, and Yu. A. Mityagin

P. N. Lebedev Physics Institute, Russian Academy of Sciences, 117924 Moscow, Russia

B. Monemar and P. O. Holtz

Linköping University, S-58183 Linköping, Sweden

(Submitted June 3, 1998; accepted for publication June 5, 1998)
Fiz. Tekh. Poluprovodn. **33**, 83–90 (January 1999)

Infrared absorption in strained *p*-type $In_{1-x}Ga_xAs/InP$ quantum wells is investigated for both possible types of strain (tensile and compressive). It is observed that the normal-incidence absorption increases considerably under compressive strain (when the ground state is a heavy-hole state) and decreases under tensile strain (when the ground state is a light-hole state). The peak absorption in the compressed quantum well can attain very large values, on the order of $5000\,cm^{-1}$ at a hole density $\sim 10^{12}\,cm^{-2}$; this attribute makes ''compressed'' *p*-type quantum wells attractive for IR detection applications. © *1999 American Institute of Physics.* [S1063-7826(99)01801-3]

1. INTRODUCTION

The fundamental properties and applied aspects of semiconductor quantum-well structures utilizing GaAs/AlGaAs, InGaAs/AlGaAs, and InGaAs/InP compounds have been the subject of intensive research in recent years.[1–10] One of the more promising applied trends bears on the utilization of such structures as infrared and far-infrared radiation detectors. Optical intersubband absorption in quantum wells is attributable to transitions between localized states in the quantum well or between a localized state of the quantum well and delocalized states above the quantum barrier. Conventional *n*-type quantum wells[1–4] have alluring properties from the standpoint of IR detection, such as low carrier mass and high mobility. In this case, however, the quantum-mechanical selection rule forbids optical transitions at normal incidence and requires the presence of an electric field component perpendicular to the plane of the two-dimensional electron gas (quantum well). The efficient generation of a perpendicularly polarized electromagnetic wave requires special methods, for example, the formation of structures on the surface of the semiconductor (grooving or a planar metallic grid). A more promising means in this regard is afforded by *p*-type quantum wells, which have been receiving ever-increasing attention lately.[5–10] Owing to the quantum-mechanical mixing of light-hole and heavy-hole states, optical transitions between states in quantum wells with *p*-type conductivity are allowed for an electromagnetic wave at normal incidence, facilitating the fabrication of IR detectors.[11–14]

Since the energy spectrum, wave functions, and matrix elements of hole-state optical transitions in quantum wells are highly sensitive to deformations of the crystal lattice,[15,16] IR properties can be effectively controlled by the application of external uniaxial compression or ''built-in'' strain (stressed structures). The effects of built-in stress produced by mismatch of the substrate and quantum well lattice parameters have been investigated theoretically[7,17] and experimentally[10] in GaInAs/AlInAs systems. Xie *et al.*[7] have theoretically predicted a substantial increase in IR absorption in a strained system of composition $Ga_{0.7}In_{0.3}As/Al_{0.48}In_{0.52}As$, which corresponds to tension of the quantum well material.

In this paper we report the results of an experimental study of the effect of a built-in strain on infrared absorption in quantum wells based on $In_{1-x}Ga_xAs/InP$. The cases of tension ($x>0.47$) and compression ($x<0.47$) are examined. In Sec. 2 we briefly describe the theory of quantum hole states and IR absorption in stressed quantum wells with allowance for the error in the parameters of the valence band in the quantum well and the barrier. In Sec. 3 we present the results of numerical calculations of the matrix elements of the optical transitions for various polarizations of light. The results of calculations of the absorption spectra of IR radiation are discussed in Secs. 4 and 5.

2. ENERGY SPECTRUM AND OPTICAL TRANSITIONS IN STRESSED QUANTUM WELLS

In this paper we discuss a typical strained structure (quantum well) formed by a layer of semiconductor material (solid solution) $In_{1-x}Ga_xAs$ with band gap $E_g(x)=0.5-1.0\,eV$, contained between two insulating InP barrier layers, which is characterized by a considerably larger band gap (1.4 eV). By varying the atomic fraction of gallium x in the well layer it is possible to alter the physical parameters (including the lattice constant a) and to control the strain created in the zone of the $In_{1-x}Ga_xAs/InP$ interface (exact matching of the well and barrier lattice parameters and, accordingly, zero strain are achieved for $x\approx 0.47$). We assume

below that the elastic stress generated by mismatch of the well and barrier lattice constants a_w and a_b are localized entirely in the quantum well layer.

For the ensuing analysis we choose the direction of growth of the semiconductor structure (perpendicular to the plane of the layers) as the z axis. The energies and wave functions of the valence band states can be obtained by solving the following system of equations by the effective mass method:[14–20]

$$\sum_{\nu} [H_{\mu\nu}+V_h(z)\delta_{\mu\nu}]F_{\nu}(k_{\parallel},z)=E(k_{\parallel})F_{\mu}(k_{\parallel},z), \qquad (1)$$

where the indices μ and ν denote the Bloch states $|3/2, 3/2\rangle$, $|3/2, 1/2\rangle$, $|3/2, -1/2\rangle$, $|3/2, -3/2\rangle$, respectively, $H_{\mu\nu}$ is the 4×4 Luttinger Hamiltonian, and $V_h(z)$ is the potential of the quantum well. Since the quantum well potential $V_h(z)$ is a function of the coordinates, the wave vector k_z in Eq. (1) must be replaced by the operator $(1/i)(\partial/\partial z)$. The components of the wave functions $F_{\mu}(\mathbf{k}_{\parallel}, \mathbf{r})$ have the form

$$F_{\mu}(\mathbf{k}_{\parallel}, \mathbf{r})=F_{\mu}(\mathbf{k}_{\parallel}, z)\exp(i\mathbf{k}_{\parallel}, \mathbf{r}_{\parallel}), \qquad (2)$$

where $\mathbf{k}_{\parallel}$ denotes the hole wave vector in the plane of the quantum well.

Since the parameters of the effective mass tensor in Eq. (1) are functions of the coordinates, all operators of the form $A(z)(\partial^2/\partial z^2)$ and $B(z)(\partial/\partial z)$ in the Luttinger Hamiltonian must be replaced by the symmetrized expressions $(\partial/\partial z)A(z)(\partial/\partial z)$ and $1/2[B(z)(\partial/\partial z)+(\partial/\partial z)B(z)]$ to ensure the Hermitian property.[22]

We invoke the unitary transformation[18,20,15,16] for block 2×2 diagonalization of the initial 4×4 Luttinger Hamiltonian. We also use the axial (relative to the z axis) approximation[18,20] for simplicity. The transformed Hamiltonian $H_{\mu\nu}$ can be written in the form[15,16]

$$H_{\mu\nu}=\begin{bmatrix} H^U & 0 \\ 0 & H^L \end{bmatrix}, \qquad (3)$$

where

$$H^U=\begin{bmatrix} H^U_{11} & H^U_{12} \\ H^U_{21} & H^U_{22} \end{bmatrix},$$

$$H^U_{11}=\frac{\hbar^2}{2m_0}\times\left[(\gamma_1+\gamma_2)k_{\parallel}^2+\frac{1}{i}\frac{\partial}{\partial z}(\gamma_1-2\gamma_2)\frac{1}{i}\frac{\partial}{\partial z}+\xi\right],$$

$$H^U_{12}=\frac{\hbar^2}{2m_0}\times\left[\sqrt{3}\gamma k_{\parallel}^2-i\sqrt{3}k_{\parallel}\left(\gamma_3\frac{1}{i}\frac{\partial}{\partial z}+\frac{1}{i}\frac{\partial}{\partial z}\gamma_3\right)\right],$$

$$H^U_{21}=\frac{\hbar^2}{2m_0}\times\left[\sqrt{3}\gamma k_{\parallel}^2+i\sqrt{3}k_{\parallel}\left(\gamma_3\frac{1}{i}\frac{\partial}{\partial z}+\frac{1}{i}\frac{\partial}{\partial z}\gamma_3\right)\right],$$

$$H^U_{22}=\frac{\hbar^2}{2m_0}\times\left[(\gamma_1-\gamma_2)k_{\parallel}^2+\frac{1}{i}\frac{\partial}{\partial z}(\gamma_1+2\gamma_2)\frac{1}{i}\frac{\partial}{\partial z}+\xi\right], \qquad (4)$$

$$H^L=\begin{bmatrix} H^L_{11} & H^L_{12} \\ H^L_{21} & H^L_{22} \end{bmatrix},$$

$$H^L_{11}=\frac{\hbar^2}{2m_0}\times\left[(\gamma_1-\gamma_2)k_{\parallel}^2+\frac{1}{i}\frac{\partial}{\partial z}(\gamma_1-2\gamma_2)\frac{1}{i}\frac{\partial}{\partial z}+\xi\right],$$

$$H^L_{12}=\frac{\hbar^2}{2m_0}\times\left[\sqrt{3}\gamma k_{\parallel}^2-i\sqrt{3}k_{\parallel}\left(\gamma_3\frac{1}{i}\frac{\partial}{\partial z}+\frac{1}{i}\frac{\partial}{\partial z}\gamma_3\right)\right],$$

$$H^L_{21}=\frac{\hbar^2}{2m_0}\times\left[\sqrt{3}\gamma k_{\parallel}^2+i\sqrt{3}k_{\parallel}\left(\gamma_3\frac{1}{i}\frac{\partial}{\partial z}+\frac{1}{i}\frac{\partial}{\partial z}\gamma_3\right)\right],$$

$$H^L_{22}=\frac{\hbar^2}{2m_0}\times\left[(\gamma_1+\gamma_2)k_{\parallel}^2+\frac{1}{i}\frac{\partial}{\partial z}(\gamma_1+2\gamma_2)\frac{1}{i}\frac{\partial}{\partial z}+\xi\right]. \qquad (5)$$

In the case of a strained quantum structure (e.g., $In_{1-x}Ga_xAs$ with the lattice constant $a(x)$, grown on InP with the lattice constant a_0) the stress energy ξ in Eqs. (5) can be expressed in terms of the biaxial strain $\varepsilon=[a_0-a(x)]/a(x)$ as $\xi=-b[1+2c_{12}/c_{11})]\varepsilon$. The hole potential energy is written in the form[15,16]

$$V_h(z)=\begin{cases} 2a_v\left(1-\dfrac{c_{12}}{c_{11}}\right)\varepsilon & \text{hydrostatic strain energy} \\ & \text{in the well region,} \\ \Delta E_v & \text{in the barrier region,} \end{cases} \qquad (6)$$

where ΔE_v is the height of the quantum barrier.

The conditions for matching the solutions at the quantum well-barrier interface can be obtained by integrating Eqs. (1) in the region close to the interface. The explicit boundary conditions express the requirement of continuity of the column functions[15,16,22]

$$\begin{bmatrix} F_1(z) \\ F_2(z) \end{bmatrix}, \quad \begin{bmatrix} F_3(z) \\ F_4(z) \end{bmatrix} \qquad (7)$$

and

$$\begin{bmatrix} (\gamma_1-2\gamma_2)\dfrac{\partial}{\partial z} & \sqrt{3}\gamma_3 k_{\parallel} \\ -\sqrt{3}\gamma_3 k_{\parallel} & (\gamma_1+2\gamma_2)\dfrac{\partial}{\partial z} \end{bmatrix}\begin{bmatrix} F_1(z) \\ F_2(z) \end{bmatrix},$$

$$\begin{bmatrix} (\gamma_1+2\gamma_2)\dfrac{\partial}{\partial z} & \sqrt{3}\gamma_3 k_{\parallel} \\ -\sqrt{3}\gamma_3 k_{\parallel} & (\gamma_1-2\gamma_2)\dfrac{\partial}{\partial z} \end{bmatrix}\begin{bmatrix} F_3(z) \\ F_4(z) \end{bmatrix}. \qquad (8)$$

The absorption coefficient for optical transitions between hole subbands n and n' is given by the expression

$$\alpha_{nn'}(\omega)=\frac{4\pi^2e^2}{n_0\omega c\Omega}\sum_{k_{\parallel}}[f_n(k_{\parallel})-f_{n'}(k_{\parallel})] \times|\langle n'|\mathbf{e}\cdot\hat{\mathbf{v}}|n\rangle|^2\delta(E_{n'}-E_n-\hbar\omega), \qquad (9)$$

where n_0 is the refractive index, $\mathbf{e}$ is the light polarization vector, and $f_n(k_{\parallel})$ is the hole distribution function. In the envelope function approximation the hole velocity operator can be specified as

$$\hat{\mathbf{v}}=\frac{1}{\hbar}\frac{\partial H}{\partial \mathbf{k}}. \tag{10}$$

The final result for the velocity components can be written in the form

$$\hat{v}_{\parallel}=\begin{bmatrix} \hat{v}_{\parallel}^{U} & 0 \\ 0 & \hat{v}_{\parallel}^{L} \end{bmatrix}, \quad \begin{bmatrix} \hat{v}_{z}^{U} & 0 \\ 0 & \hat{v}_{z}^{L} \end{bmatrix}, \tag{11}$$

where the operators $v_{\parallel}^{U}$ and v_{z}^{U} have the symmetrized Hermitian form

$$v_{\parallel}^{U}=\frac{\hbar}{2m_0}\begin{bmatrix} 2k_{\parallel}(\gamma_1+\gamma_2) & 2\sqrt{3}\overline{\gamma k}_{\parallel}-\sqrt{3}\frac{1}{i}\left(\gamma_3\frac{1}{i}\frac{\partial}{\partial z}+\frac{1}{i}\frac{\partial}{\partial z}\gamma_3\right) \\ 2\sqrt{3}\overline{\gamma k}_{\parallel}+\sqrt{3}\frac{1}{i}\left(\gamma_3\frac{1}{i}\frac{\partial}{\partial z}+\frac{1}{i}\frac{\partial}{\partial z}\gamma_3\right) & 2k_{\parallel}(\gamma_1-\gamma_2) \end{bmatrix}, \tag{12}$$

$$v_{z}^{U}=\frac{\hbar}{2m_0}\begin{bmatrix} \frac{1}{i}\frac{\partial}{\partial z}(\gamma_1-2\gamma_2)+(\gamma_1-2\gamma_2)\frac{1}{i}\frac{\partial}{\partial z} & -i2\sqrt{3}\gamma_3 k_{\parallel} \\ +i2\sqrt{3}\gamma_3 k_{\parallel} & \frac{1}{i}\frac{\partial}{\partial z}(\gamma_1+2\gamma_2)+(\gamma_1+2\gamma_2)\frac{1}{i}\frac{\partial}{\partial z} \end{bmatrix}, \tag{13}$$

and $v_{\parallel}^{L}$ and v_{z}^{L} are the Hermitian conjugates of the operators $v_{\parallel}^{U}$ and v_{z}^{U}, respectively. The matrix elements $m_0\langle n'|\mathbf{e}\cdot\hat{\mathbf{v}}|n\rangle$ can be written in the form[14]

$$m_0\mathbf{e}\cdot\hat{\mathbf{v}}_{nn'}=m_0\langle n'|\mathbf{e}\hat{\mathbf{v}}|n\rangle=\mathbf{e}\sum_{\nu\nu'}(\mathbf{P}_{\nu\nu'}O_{\nu\nu'}^{nn'}+\mathbf{Q}_{\nu\nu'}D_{\nu\nu'}^{nn'}), \tag{14}$$

where the coefficients of the matrices $\mathbf{P}_{\nu\nu'}\mathbf{Q}_{\nu\nu'}$ can be obtained directly from Eqs. (13) and (14). The elements of the overlap matrix $O_{\nu\nu'}^{nn'}$ and the dipole matrix $D_{\nu\nu'}^{nn'}$ are defined as

$$O_{\nu\nu'}^{nn'}=\int F_{\nu'}^{*}F_{\nu}dz \tag{15}$$

and

$$D_{\nu\nu'}^{nn'}=\int F_{\nu'}^{*}\left(A(z)\frac{1}{i}\frac{\partial}{\partial z}+\frac{1}{i}\frac{\partial}{\partial z}A(z)F_{\nu}\right)dz$$
$$=\int A(z)\left[F_{\nu'}^{*}\frac{1}{i}\frac{\partial F_{\nu}}{\partial z}+F_{\nu}\left(\frac{1}{i}\frac{\partial F_{\nu'}}{\partial z}\right)^{*}\right]dz. \tag{16}$$

Note that the matrix $\mathbf{P}_{\nu\nu'}$ is linear in $k_{\parallel}$, and $\mathbf{Q}_{\nu\nu'}$ does not depend on $k_{\parallel}$ (Ref. 14).

3. HOLE ENERGY SPECTRUM AND MATRIX ELEMENTS OF OPTICAL TRANSITIONS IN STRAINED QUANTUM WELLS

The physical parameters used for the materials GaAs, InAs, and InP in the calculations are summarized in Table I.[15,16,27] All the materials for the solid solution $In_{1-x}Ga_xAs$ have been calculated by linear interpolation of the parameters of InAs and GaAs with the exception of the width of the band gap for the strained material $E_g(In_{1-x}Ga_xAs)=0.418+0.614x+0.487x^2$ eV (Refs. 15 and 16). A difficult quantity to determine in analyzing the effects of strain in quantum structures is the partial distribution of the elastic potentials and the energy barriers between the valence and conduction bands. In our calculations we have used the simple model described in Refs. 15 and 16. The fraction of the hydrostatic potential associated with the valence band is assumed to be 1/3 ($a_v=a/3$), and the height of the potential barrier for holes is taken to be $\Delta E_v=0.64\Delta E_g$. The energy spectrum and the wave functions are calculated by the propagation matrix method.[15,16]

Figures 1a and 1b show the calculated structure of the hole states for a quantum well (80 Å) having the composition $In_{1-x}Ga_xAs/InP$ for various atomic fractions of Ga (x). For the unstrained quantum well the first hole subband $H1$ is the lowest, because heavy holes have a large effective mass in the direction of the growth axis of the structure (quantum-well effect). With the onset of compression ($x<0.47$) the energy of heavy-hole states decreases, and the energy of light-hole states increases under the influence of the shear potential. It is evident from Fig. 1a that the effective mass of the lowest state in the plane of the quantum well is ''facilitated'' in this case.

In the case of a tensile-strained structure ($x>0.47$) the deformation potential lowers the energy of light-hole states and raises the energy of heavy-hole states, ''competing''

TABLE I. Physical parameters of semiconductor materials GaAs, InAs, and InP.

Parameter	GaAs	InAs	InP
Lattice constant a, Å	5.653	6.058	5.869
Band gap E_g, eV	1.519	0.418	1.424
γ_1	6.85	20.4	4.95
γ_2	2.1	8.3	1.65
γ_3	2.9	9.1	2.35
c_{11}, 10^{11} dyn/cm^2	11.89	8.83	10.11
c_{12}, 10^{11} dyn/cm^2	5.38	4.53	5.61
a_c-a_v, eV	−9.77	−6.0	−8.6
b, eV	−1.7	−1.8	−2.0

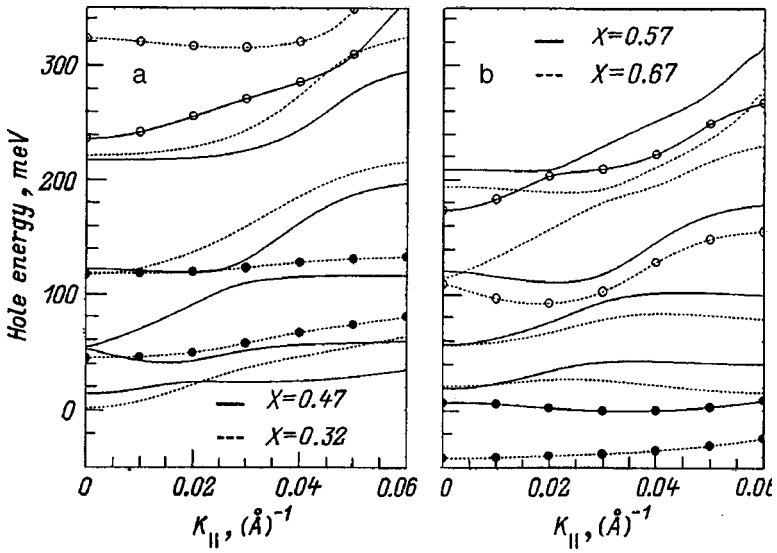

FIG. 1. Structure of the valence band $E(k_{\|})$ for an $In_{1-x}Ga_xAs/InP$ quantum well of width 80 Å, calculated for various compositions: (a) $x=0.47$ (zero mismatch of the lattice parameters for the barrier and quantum well materials), $x=0.32$ (compressive strain); (b) $x=0.57$, $x=0.32$ (tensile strain). Light-hole states are marked.

with the quantum-well effect and resulting in strong interaction and mixing of states of the lower subbands $H1$ and $L1$ in the ''transition'' composition interval ($x\cong 0.5-0.6$). This phenomenon produces a region of negative effective masses in the plane of the quantum well. With a further increase in the tensile strain, the light-hole subband becomes the ground state, characterized by a ''heavy'' mass in the plane of the quantum well.

The results of calculations of the probabilities of optical transitions (squares of the moduli of the matrix elements

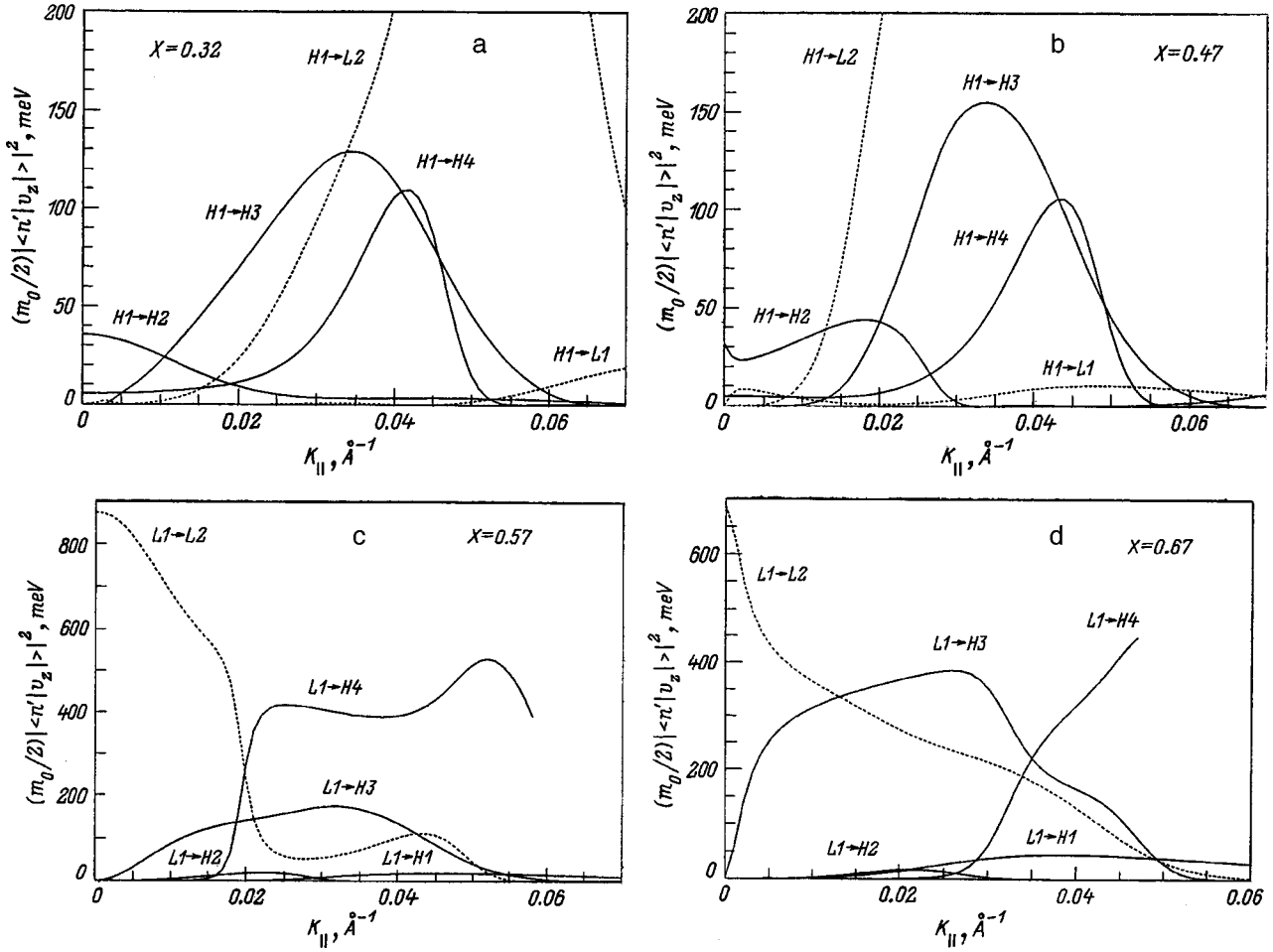

FIG. 2. Calculated values of the squares of the moduli of the dipole matrix elements $(m_0/2)|\langle n|v_z|n'\rangle|^2$ for z-polarization optical transitions and various $In_{1-x}Ga_xAs/InP$ compositions: (a) $x=0.32$ (compression); (b) $x=0.47$ (no strain); (c, d) $x=0.57$ (tension), $x=0.67$ (tension). Width of the well 80 Å.

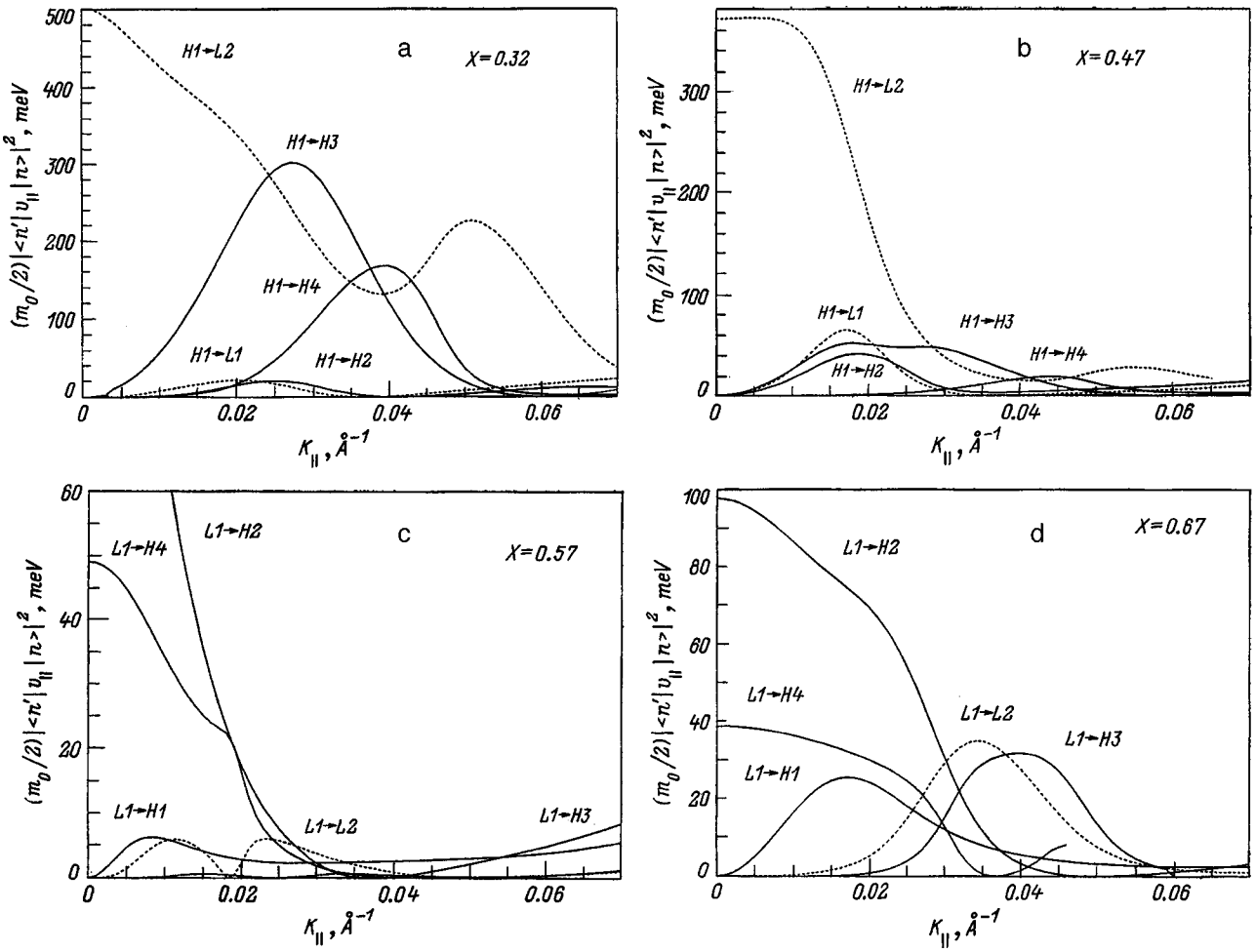

FIG. 3. Calculated values of the squares of the moduli of the dipole matrix elements $(m_0/2)|\langle n|v_z|n'\rangle|^2$ for x-polarization optical transitions and various $In_{1-x}Ga_xAs/InP$ compositions: (a) $x=0.32$ (compression); (b) $x=0.47$ (no strain); (c, d) $x=0.57$ (tension), $x=0.67$ (tension). Width of the well 80 Å.

$m_0\mathbf{e}\cdot\hat{\mathbf{v}}_{nn'}=m_0\langle n'|\mathbf{e}\cdot\hat{\mathbf{v}}|n\rangle$ are shown in Fig. 2 (the vector $\mathbf{e}$ is parallel to the z axis — z-polarization) and Fig. 3 (light at normal incidence, the vector $\mathbf{e}$ is parallel to the plane of the quantum well — x-polarization) as functions of the modulus of the wave vector $k_{\parallel}$. The results are shown only for transitions from the ground state, because the latter is usually the only filled state in typical experimental situations. The selection rules for various intersubband transitions can be inferred from an analysis of Eqs. (12)–(14). The probabilities of transitions for wave vectors in the vicinity of $k_{\parallel}=0$ are given by the matrix elements $\mathbf{Q}_{vv'}$.

It is evident from Figs. 2 and 3 that the selection rules differ markedly for different polarizations. For small values of the wave vector $k_{\parallel}$ the dominant transitions are parity-allowed intersubband transitions between *HH* and *LH* states ($H1\rightarrow L2$ or $L1\rightarrow H2, H4$) in the case of x-polarization and in-band transitions ($H1\rightarrow H2$, $H1\rightarrow H4$, or $L1\rightarrow L2$) in the case of z-polarization. The matrix elements of the intersubband transitions increase considerably when the ground state is a light-hole state (under tensile strain), because the probability of such transitions is inversely proportional to the square of the effective mass in the z-direction.

For x-polarization, as is evident from Fig. 3, the probabilities of intersubband transitions in the vicinity of $k_{\parallel}=0$ increase significantly if the ground state is a heavy-hole state. This property is associated with the different degrees of penetration of the wave functions of the light-hole and heavy-hole ground states $F_v(z)$ into the region of the quantum barrier. Figure 4 bears witness to the fact that the light-hole wave function is considerably ''smoother,'' which accounts for the smaller dipole matrix elements $D_{vv'}^{nn'}$.

As the wave vector $k_{\parallel}$ increases, the heavy-hole and light-hole states mix, and transitions between any states become possible. For sufficiently large $K_{\parallel}$ both matrices $\mathbf{P}_{vv'}$ and $\mathbf{Q}_{vv'}$ contribute to the transition probability. Looking at the important case of light at normal incidence (x-polarization), we can see that all the transition probabilities increase substantially in compression (Ga content $x<0.47$), when the ground state is a heavy-hole state. In contrast, the optical transition matrix elements decrease in tension ($x>0.47$), when the ground state is a light-hole state. It is evident from Fig. 3c that the transition probabilities are especially small in the interval of compositions $x\cong 0.5-0.6$, when the lowest state is highly mixed. The above-described influence of stress on optical transitions is easy to understand when the variation of the effective mass in the plane of the quantum well is taken into account. Since the transition probability $w_{nn'}$ for x-polarization is governed by the matrix

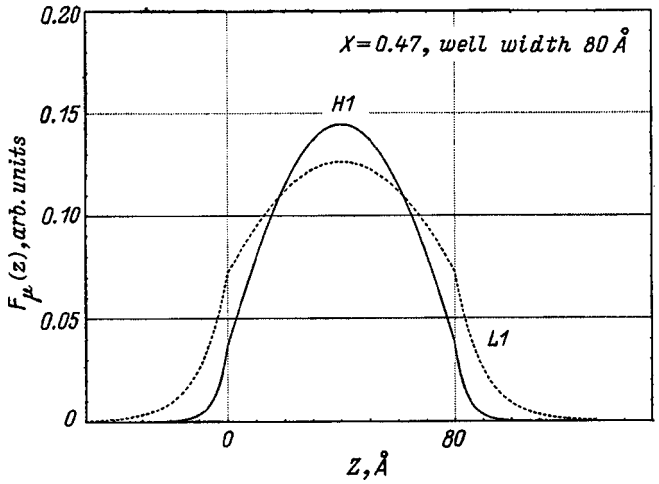

FIG. 4. Calculated wave functions for the lower heavy-hole and light-hole states in an unstrained $In_{1-x}Ga_xAs/InP$ quantum well, $x=0.47$, $k_\parallel=0$, $w=80$ Å.

elements $\langle n'|\mathbf{e}\cdot\hat{v}_x|n\rangle$, in the first approximation we can write $w_{nn'}(k_\parallel)\sim v_{xn}(k_\parallel)=\partial E_n(k_\parallel)/\partial k_\parallel$. As a matter of fact, a comparison of Figs. 2 and 3 with Fig. 1 reveals that high transition probabilities correspond to a large inverse effective mass $\partial E_1(k_\parallel)/\partial k_\parallel$ in the presence of compressive strain (heavy-hole ground state), and low transition probabilities correspond to small values of $\partial E_1(k_\parallel)/\partial k_\parallel$ (light-hole ground state).

The variance of the ground state $\partial E_1(k_\parallel)/\partial k_\parallel$ is particularly small for strong mixing of the lower states ($x\sim 0.5-0.6$), which drastically reduces the absorption of light at normal incidence. We also mention two other factors that significantly affect the intensity of hole intersubband optical absorption in the InGaAs system: an increase in the Luttinger parameters and an increase in the depth of the quantum well when the In fraction $(1-x)$ is increased ($\Delta E_v=390$ meV for $x=0.47$, and $\Delta E_v=486$ meV for $x=0.32$).

Consequently, the intensity of optical intersubband transition in strained quantum wells increases significantly for the *x*-polarization (normal incidence of light), when the ground state is a heavy-hole state, and for the *z*-polarization, when the ground state is a light-hole state.

4. INTERSUBBAND ABSORPTION SPECTRA IN A STRAINED $In_{1-x}Ga_xAs/InP$ QUANTUM WELL

To determine the absorption coefficient, it is necessary to sum the intensities of transitions between the individual *m*th and *n*th subbands:

$$\alpha(\omega)=\sum_{m,n}\alpha_{mn}(\omega). \tag{17}$$

In this paper we consider the case of zero temperature for simplicity, assuming that the distribution function in Eq. (9) has the values $f(k_\parallel)=1$ for $E<E_f$ and $f(k_\parallel)=0$ for $E>E_f$. The following replacement of the δ-function is made in Eq. (9) in calculations of the normalized Lorentz function: $\delta(E)=(\Gamma/2\pi)(E^2+\Gamma^2/4)^{-1}$ with a typical width of the contour $\Gamma=8$ meV. To investigate the effects of stress, we calculate the normal-incidence spectra for an 80 Å $In_{1-x}Ga_xAs/InP$ quantum well for various values of the parameter *x*. In the integration over $k_\parallel$ the two-dimensional hole density in the quantum well is assumed to be fixed and equal to 10^{12} cm^{-2}.

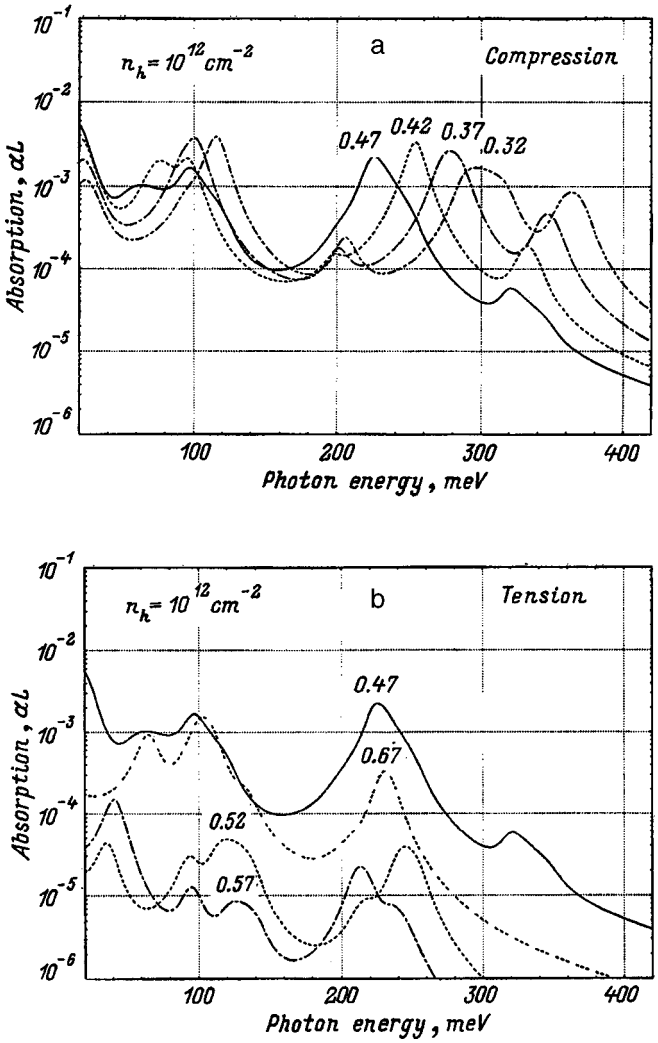

FIG. 5. Optical absorption spectra in a quantum well at normal incidence for various $In_{1-x}Ga_xAs/InP$ compositions at $T=0$ K. (a) $x=0.47$ (unstrained lattice), $x=0.42, 0.37, 0.32$ (compression); (b) $x=0.47$ (unstrained lattice), $x=0.52, 0.57, 0.67$ (tension). The hole density is constant and equal to 10^{12} cm^{-2}.

The calculated normal-incidence spectra for various compositions of the $In_{1-x}Ga_xAs$ system are shown in Figs. 5a and 5b. The spectra have a similar appearance for the unstrained ($x=0.47$) and compressed ($x<0.47$) lattices (see Fig. 5a), and the dominant transitions are $H1\rightarrow H3$ ($h\nu\sim 100$ meV) and $H1\rightarrow L2$ ($h\nu\sim 200-300$ meV). The absorption in the spectral region $h\nu\sim 100$ meV ($\lambda\sim 10\,\mu$m), which is important from the applications point of view, increases significantly as the compression is increased, owing to an increase in the dipole matrix elements of the optical transitions (see the preceding section). It is evident from Fig. 5a that the peak absorption coefficient attains values $\alpha L\sim 0.005$, which correspond to large bulk absorption

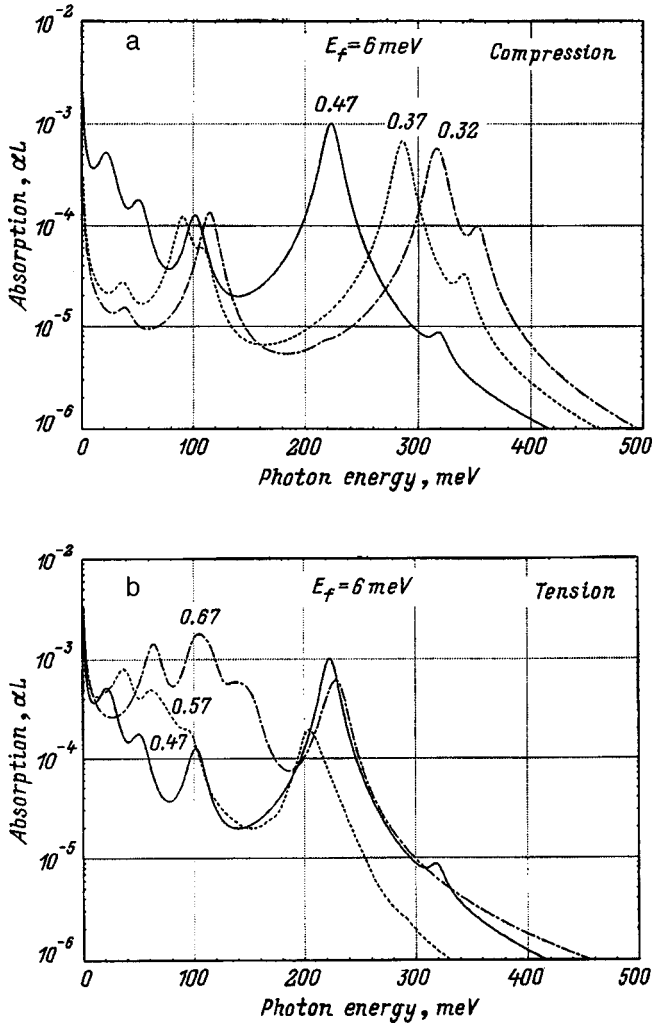

FIG. 6. Optical absorption spectra in a quantum well at normal incidence for various $In_{1-x}Ga_xAs/InP$ compositions at $T=0$ K. (a) $x=0.47$ (unstrained lattice), $x=0.37, 0.32$ (compression); (b) $x=0.47$ (unstrained lattice), $x=0.57, 0.67$ (tension). The Fermi level is constant and equal to 6 meV.

$\alpha=aL/L\sim 6000\,\mathrm{cm}^{-1}$. The pronounced shift of the dominant $H1\rightarrow L2$ peak toward higher frequencies is caused by an increase in the energy gap between the heavy-hole and light-hole subbands.

The pattern changes radically in tensile strain ($x>0.47$). It is evident from Fig. 5b that the total IR absorption in a highly tensile-strained quantum well ($x=0.67$) is much lower than in the unstrained structure, consistent with the smaller values of the optical matrix elements (see Fig. 3d). It is evident from Fig. 3c that the optical transition probabilities drop sharply in the presence of small tensile strains ($x=0.5-0.6$). The observed effect is obviously attributable to strong interaction and mixing of the lower hole states $L1$ and $H1$ (''anticrossing''; see Fig. 1b), which causes the optical matrix elements to decrease considerably (see the preceding section). Moreover, the strong mixing of hole states produces an electronlike effective mass near the origin in *k*-space (Refs. 21,15, and 16 As a result, at low temperatures holes occupy the lowest energy states for nonzero values of the wave vector $k_{\|}=0.03-0.04\,\text{Å}^{-1}$, where the matrix elements are much smaller than for $k_{\|}\sim 0$. With a further increase in the tension ($x>0.6$) the pure light-hole state emerges as the ground state, and the transitions $L1\rightarrow H3$ and $L1\rightarrow H4$ become dominant.

The results discussed above have been obtained on the assumption of a constant two-dimensional hole density ($10^{12}\,\mathrm{cm}^{-2}$). In some papers the influence of strain on the optical absorption has been analyzed on the assumption of a fixed Fermi level.[7] To compare the results of the two different approaches, we also calculate the absorption coefficients for a fixed energy of the hole Fermi level (6 meV), which corresponds to a variation of the two-dimensional density of the hole gas in the interval $10^{11}-10^{12}\,\mathrm{cm}^{-2}$ (Fig. 6). It is evident from Fig. 6b that when the Fermi level is fixed, the IR absorption in the tensile-strained quantum well increases considerably at photon energies of the order of 100 meV, exactly as in Ref. 7. It is obvious that the observed increase in the absorption is associated with an increase in the density of states of the lower light-hole subband (see Fig. 1b) (at a fixed Fermi level of 6 meV the variation of the atomic fraction of Ga from 0.47 to 0.67 corresponds to an increase in the hole density n_h from $2.5\times 10^{11}\,\mathrm{cm}^{-2}$ to $2.2\times 10^{12}\,\mathrm{cm}^{-2}$). Thus, a comparison of the absorption spectra calculated at a fixed Fermi level reveals primarily a significant variation of the density of states of the lower hole subband. Since the hole density in typical quantum structures created for infrared applications depends on the doping level of the quantum well region and not on the built-in strain, the analysis of the absorption spectra calculated at a fixed hole density is deemed more suitable.

Calculations of the absorption spectra for various fixed hole densities in the range $n_h=10^{10}-10^{12}\,\mathrm{cm}^{-2}$ and Fermi levels $E_f=5-20$ meV reveal qualitatively the same strain dependences as above.

5. CONCLUSIONS

We have conducted a theoretical investigation of infrared absorption in strained *p*-type $In_{1-x}Ga_xAs/InP$ quantum wells for both possible types of strain (tension and compression). We have found that the absorption at normal incidence increases considerably under compressive strain (when the ground state has a heavy-hole character) and decreases in tensile deformation (when the ground state is a light-hole state). The peak absorption in the quantum well in compression can attain very large values of the order of $5000\,\mathrm{cm}^{-1}$ at hole densities $\sim 10^{12}\,\mathrm{cm}^{-2}$, lending a definite appeal to the application of ''compressed'' *p*-type quantum wells for IR detection.

This work has received financial support from the Russian Fund for Fundamental Research (No. 96-02-18593) and the FTNS Interindustrial Scientific-Technical Program (No. 97-1048).

[1] B. F. Levine, R. J. Malik, J. Walker, K. K. Choi, C. G. Bethea, D. A. Kleinman, and J. M. Vandenberg, Appl. Phys. Lett. **50**, 273 (1987).
[2] L. S. Yu and S. S. Li, Appl. Phys. Lett. **59**, 1332 (1991).
[3] G. Hasnain, B. F. Levine, C. G. Bethea, R. A. Logan, J. Walker, and R. J. Malik, Appl. Phys. Lett. **54**, 2515 (1989).
[4] J. Y. Andersson and L. Lundqvist, J. Appl. Phys. **71**, 3600 (1992).
[5] B. F. Levine, S. D. Gunapala, J. M. Kuo, S. S. Pei, and S. Hui, Appl. Phys. Lett. **59**, 1864 (1991).

[6] S. D. Gunapala, B. F. Levin, D. Ritter, R. Hamm, and M. B. Panish, J. Appl. Phys. **71**, 2458 (1992).
[7] H. Xie, J. Katz, and W. I. Wang, Appl. Phys. Lett. **59**, 3601 (1991).
[8] H. Xie, J. Katz, W. I. Wang, and Y. C. Chang, J. Appl. Phys. **71**, 2844 (1992).
[9] J. Katz, Y. Zhang, and W. L. Wang, Electron. Lett. **28**, 932 (1992).
[10] Y. H. Wang, Sheng S. Li., J. Chu, and Pin Ho, Appl. Phys. Lett. **64**, 727 (1994).
[11] P. Man and D. S. Pan, Appl. Phys. Lett. **61**, 2799 (1992).
[12] L. C. Chiu, J. S. Smith, S. Margalit, A. Yariv, and A. Y. Cho, Infrared Phys. **23**, 93 (1983).
[13] A. Pinczuk, D. Heiman, R. Sooryakuman, A. C. Gossard, and W. Wiegmann, Surf. Sci. **170**, 573 (1986).
[14] Y. C. Chang and R. B. James, Phys. Rev. B **39**, 12 672 (1989).
[15] S. L. Chuang, Phys. Rev. B **43**, 9649 (1991).
[16] C. Y.-P. Chao and S. L. Chuang, Phys. Rev. B **46**, 4110 (1992).
[17] S. A. Stoklitsky, P. O. Holtz, B. Monemar, Q. X. Zhao, and T. Lundström, Appl. Phys. Lett. **65**, 1706 (1994).
[18] J. M. Luttinger and W. Kohn, Phys. Rev. **97**, 869 (1955).
[19] D. A. Broido and L. J. Sham, Phys. Rev. B **31**, 888 (1985).
[20] M. Altarelli, U. Ekenberg, and A. Fasolino, Phys. Rev. B **32**, 5138 (1985).
[21] R. Eppenga, M. F. H. Schuurmans, and S. Colak, Phys. Rev. B **36**, 1554 (1987).
[22] A. Twardowsky and C. Herman, Phys. Rev. B **35**, 8144 (1987).
[23] L. C. Andreani, A. Pasquarello, and F. Bassani, Phys. Rev. B **36**, 5887 (1987).
[24] R. Eppenga, M. F. H. Schuurmans, and S. Colak, Phys. Rev. B **36**, 1554 (1987).
[25] K. Suzuki and J. C. Hensel, Phys. Rev. B **9**, 4184 (1974).
[26] A. G. Petrov and A. Shik, Phys. Rev. B **48**, 11 883 (1993).
[27] Landolt-Börnstein, *Numerical Data and Functional Relationship in Science and Technology*, New Series, edited by K.-H. Hellwege, Group III, Vol. 17A (Springer-Verlag, Berlin, 1982); Groups III–V, Vol. 22A (Springer-Verlag, Berlin, 1986).

Translated by James S. Wood

Influence of composition and anneal conditions on the optical properties of (In, Ga)As quantum dots in an (Al, Ga)As matrix

Zhao Zhen, D. A. Bedarev, B. V. Volovik, N. N. Ledentsov, A. V. Lunev, M. V. Maksimov, A. F. Tsatsul'nikov, A. Yu. Egorov, A. E. Zhukov, A. R. Kovsh, V. M. Ustinov, and P. S. Kop'ev

A. F. Ioffe Physicotechnical Institute, Russian Academy of Sciences, 194021 St. Petersburg, Russia
(Submitted June 10, 1998; accepted for publication June 11, 1998)
Fiz. Tekh. Poluprovodn. **33**, 91–96 (January 1999)

The optical properties of structures containing InGaAs quantum dots in GaAs and AlGaAs matrices grown by molecular-beam epitaxy are investigated. It is shown that increasing the In content in the quantum dots has the effect of raising the energy of carrier localization and increasing the energy distance between the ground state and the excited states of carriers in the quantum dots. An investigation of the influence of postgrowth annealing on the optical properties of the structures shows that the formation of vertically coupled quantum dots and the use of a wide-gap AlGaAs matrix enhances the thermal stability of the structures. Moreover, high-temperature (830 °C) thermal annealing can improve the quality of the AlGaAs layers in structures with vertically coupled InGaAs quantum dots in an AlGaAs matrix. The results demonstrate the feasibility of using postgrowth annealing to improve the characteristics of quantum dot lasers. © *1999 American Institute of Physics.* [S1063-7826(99)01901-8]

1. INTRODUCTION

The growth of structures with ordered arrays of In(Ga)As quantum dots in an (Al)GaAs matrix and their investigation are pursuits of great current importance in today's physics and technology of semiconductors.[1–3] The most intensive research is aimed at the formation of quantum dots by the spontaneous morphological transformation of strained layers as they are deposited onto the surface of a crystal having a different lattice constant. There is interest both in fundamental studies of the physical properties associated with size quantization and in the feasibility of device applications for such structures.[3,4] For example, lasers have now been fabricated using quantum dots in the system InGaAs/AlGaAs (Ref. 5), which is characterized by extremely high temperature stability of the threshold current,[6] exceeding the theoretical limit for quantum-well lasers.[7]

It has been shown in several papers[2,3] that the formation of dense ($>5\times10^{10}\,\mathrm{cm}^{-3}$) arrays of coherent InGaAs quantum dots on the surface of GaAs or (Al, Ga)As in molecular-beam epitaxy takes place only under certain growth conditions. For example, the ratio of the fluxes of arsenic to gallium atoms should not exceed 5–10, and the surface temperature is usually held in the interval 450−500 °C. Growth at higher substrate temperatures leads to a drastic reduction in the density of the quantum dot array, an increase in the probability for the formation of dissociated clusters, and the reevaporation of In atoms from the surface. Consequently, the deposition of quantum dots and their initial overgrowth (capping) by the matrix material (GaAs or AlGaAs) must take place at relatively low substrate temperatures. On the other hand, we know that the growth of high-quality GaAs and especially AlGaAs layers requires that substantially higher substrate temperatures (600−700 °C) be maintained to preclude the formation of point defects. Hence, the optimum temperature for the deposition of quantum dots and their initial overgrowth does not coincide with the optimum temperature for growth of GaAs and AlGaAs. Two fundamental questions arise in this regard: Is it impossible to improve the quality of wide-gap barriers by postgrowth annealing of the structures and, on the other hand, does not the growth of passive regions of a laser at elevated temperatures influence the geometrical dimensions, composition, and shape of the quantum dots.

To address these issues, we have undertaken an investigation of the thermal stability of quantum dots by means of postgrowth annealing. It has been shown previously[8–10] that the high-temperature thermal annealing of InAs quantum dots in GaAs shifts the emission line of the quantum dot structures toward higher photon energies (the phenomenon of disordering of quantum dots as a result of the diffusion of atoms across the quantum dot boundary at high temperatures), but does not significantly improve the luminescence characteristics of the structures. The quantum dots increase in size, thereby lowering the average In concentration; this behavior has been confirmed by transmission electron microscope data.[10] Moreover, the quantum dot photoluminescence line narrows as a result of the weaker influence of variance of the quantum dot size on the optical transition energy as size of the quantum dots increases. A decrease in the energy of carrier localization in quantum dots increases the probability of thermal emission of carriers and, in the case of laser applications, raises the threshold current and detracts from the temperature stability of the device. Consequently, a detailed study of the influence of annealing processes on the properties of structures containing quantum dot arrays is necessary in order to optimize the regimes of growth and postgrowth processing of laser structures. So far, however, struc-

TABLE I. Conditions of quantum dot formation.

Sample	No. of quantum dot tiers	In content, x	InGaAs thickness, Å	Matrix	T_g, °C	T_o, °C
1	1	0.23	66	$Al_{0.15}Ga_{0.85}As$	500	600
2	1	0.37	22	$Al_{0.15}Ga_{0.85}As$	500	600
3	1	0.50	17	$Al_{0.15}Ga_{0.85}As$	500	600
4	3	0.50	12	$Al_{0.15}Ga_{0.85}As$	485	700
5	1	0.37	22	GaAs	500	600
6	1	0.50	17	GaAs	500	600
7	1	1.0	8	GaAs	500	600
8	6	0.55	12	GaAs	500	600

tures involving InAs quantum dots in a GaAs matrix have been investigated for the most part, whereas currently the best results in terms of the performance characteristics of quantum dot lasers have been achieved for (In, Ga)As quantum dots in an (Al, Ga)As matrix. This fact mandates the need for detailed studies of the influence of postgrowth annealing on the properties of the structures in this system specifically and also for the assessment of common patterns and differences in comparison with the case of InAs and InGaAs quantum dots in GaAs.

2. EXPERIMENT

The investigated samples were grown by molecular-beam epitaxy on GaAs(100) substrates. In structures with $In_xGa_{1-x}As$ quantum dots in GaAs and $Al_{0.15}Ga_{0.85}As$ matrices, AlAs/GaAs superlattices were grown after the deposition of a GaAs buffer layer to prevent carrier leakage into the substrate. This operation was followed by the deposition of a GaAs or $Al_{0.15}Ga_{0.85}As$ layer of thickness 100 nm. Then the active zone was grown. The indium content, the effective thicknesses of the InGaAs layer, and the quantum dot deposition temperature (T_g) are shown in Table I. Since the critical thickness at which quantum dots begin to form increases as the mole fraction of InAs (x) is decreased, the effective thickness of the InGaAs layer was decreased for samples having a lower x. After the deposition of the quantum dots and a 100-Å GaAs ($Al_{0.15}Ga_{0.85}As$) layer the growth temperature was raised, and a GaAs ($Al_{0.15}Ga_{0.85}As$) layer and an AlAs/GaAs superlattice were grown to prevent surface recombination. The overgrowth temperatures (T_o) are also given in Table I.

We have also grown samples containing several quantum dot layers. The growth conditions for these samples corresponded to those for the samples with a single layer of quantum dots. The active zone consisted of three or six quantum dot layers separated by 50-Å barriers of the matrix material. Since the total quantity of InGaAs in these structures had been increased, the InGaAs layer thickness was diminished in the upper quantum dot layers to prevent dislocations from forming. The mole fraction of InAs, the effective thickness of the InGaAs layer, the quantum dot deposition temperature, and the overgrowth temperature for these structures are also given in Table I

Photoluminescence was excited by an Ar^+ laser beam (wavelength $\lambda = 514.5$ nm and power density $P = 100$ W/cm^2). The luminescence signal was recorded by a cooled photomultiplier or a germanium *p-i-n* photodiode. The samples were annealed in a hydrogen atmosphere for various durations at temperatures of $600-850$ °C.

3. RESULTS AND DISCUSSION

Figure 1 shows the photoluminescence spectra of samples with various mole fractions of InAs (x) in an AlGaAs matrix at various temperatures. It is important to note that a variation of the mole fraction of InAs alters the mismatch between the lattice parameters and, accordingly, changes the dimensions and shape of the quantum dots. The formation of quantum dots for all the structures was monitored according to the variation of the fast-electron diffraction pattern. It is evident from Fig. 1 that increasing x from 0.23 to 0.37 causes the photoluminescence band (QD) to shift ~ 65 meV toward lower photon energies. A further increase in x does not produce any appreciable shift of the photoluminescence line. In addition, the photoluminescence bandwidth increases. Another prominent feature is the fact that when the temperature is raised, the decrease in the total photoluminescence intensity of a sample with $In_{0.23}Ga_{0.77}As$ quantum dots is far more pronounced than for structures having a high concentration x. This behavior of the photoluminescence can be explained as follows. An increase in the mole fraction of InAs causes the energy of carrier localization in the quantum dots to increase, and this process, in turn, has the effect of shifting the photoluminescence line toward lower photon energies. As a result, the geometrical dimensions of the quantum dots also influence the electron spectrum and the optical transition energy, thereby increasing the nonuniform broadening of the emission line. Moreover, an increase in the degree of carrier localization lowers the probability for the thermal emission of carriers and thus weakens the temperature dependence of the photoluminescence intensity.

An increase in the temperature leads to the suppression of new lines (QD*) on the short-wavelength side of the spectrum, owing to the increase in the population of excited quantum dot states. For a structure with $x = 0.23$ the energy distance between the QD and QD* optical transition lines is ~ 45 meV. For a sample with $x = 0.5$ this distance increases to ~ 90 meV. In the case of the structure with $x = 0.5$ no appreciable change in the profile of the spectrum is observed up to room temperature. However, this result can also be

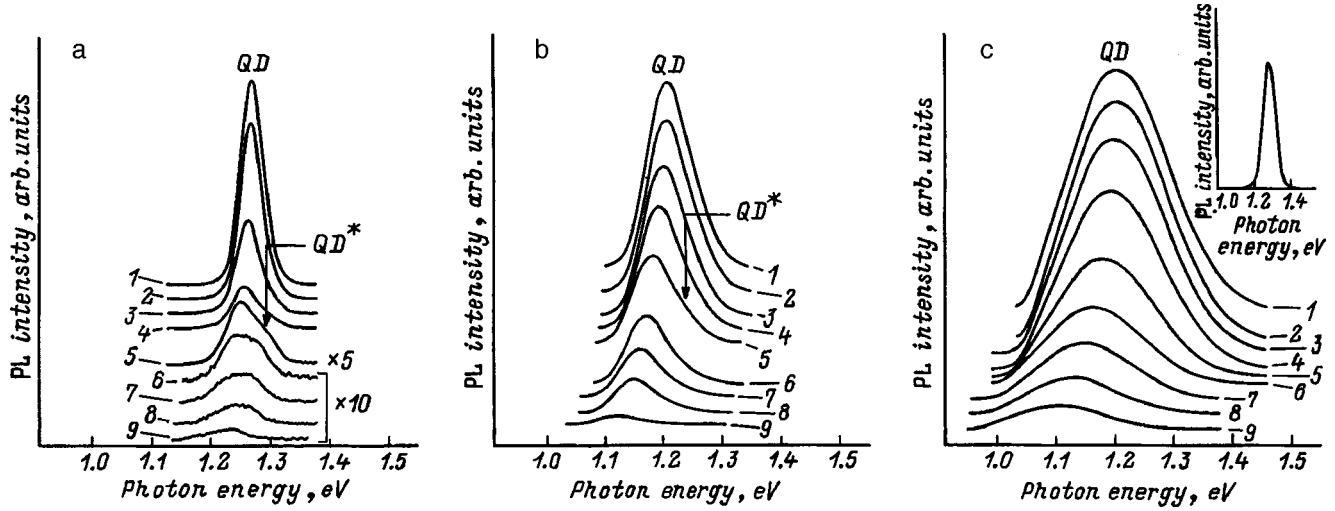

FIG. 1. Photoluminescence spectra of samples containing quantum dots with different mole fractions of InAs in an $Al_{0.15}Ga_{0.85}As$ matrix at various temperatures. (a) Sample 1: (*1*) $T=15$ K; (*2*) 40 K; (*3*) 70 K; (*4*) 100 K; (*5*) 140 K; (*6*) 180 K; (*7*) 210 K; (*8*) 240 K; (*9*) 280 K. (b) Sample 2: (*1*) $T=15$ K; (*2*) 40 K; (*3*) 70 K; (*4*) 100 K; (*5*) 140 K; (*6*) 180 K; (*7*) 210 K; (*8*) 240 K; (*9*) 300 K. (c) Sample 3: (*1*) $T=15$ K; (*2*) 40 K; (*3*) 70 K; (*4*) 100 K; (*5*) 140 K; (*6*) 180 K; (*7*) 210 K; (*8*) 250 K; (*9*) 300 K. Inset: photoluminescence spectrum of sample 4 at $T=77$ K.

identified with an increase in the photoluminescence bandwidth and the masking of new lines by nonuniform broadening. Consequently, an increase in x further weakens the temperature dependence of the shape of the photoluminescence spectrum.

The following conclusion can be drawn from our results. For the investigated samples the quantum dots in a structure with $x=0.5$ are characterized by the maximum degree of carrier localization and a substantial energy distance between the ground stae and the excited electron states. These attributes make such structures promising for applications as the active zone of semiconductor injection lasers. However, the large photoluminescence bandwidth (~ 180 meV) can work against the attainment of low threshold current densities. It has been shown[11,12] that one way to monitor and regulate the size and shape of quantum dots is by replication, i.e., by depositing several tiers of quantum dots separated by narrow (of the order of the height of the quantum dot) (Al)GaAs barriers. The inset in Fig. 1 shows the photoluminescence spectrum of a sample with three $In_{0.5}Ga_{0.5}As$ quantum dots in an $Al_{0.15}Ga_{0.85}As$ matrix. Clearly the photoluminescence spectrum has narrowed considerably to ~ 75 eV, indicating that the system of quantum dots has become more homogeneous in vertical allocation. The small shift of the photoluminescence maximum toward shorter wavelengths for the given structure is probably attributable to the smaller effective thickness of the InGaAs layer in each successive deposition cycle.

It has been shown[12,13] that a wide-gap AlGaAs matrix can be used to enhance carrier localization in quantum dots and thereby lower substantially the threshold current density in injection lasers. We have investigated the postgrowth annealing of structures with quantum dots in GaAs and AlGaAs matrices with a view toward studying the influence of the matrix material and the In content on the thermal stability of quantum dots. Figure 2 shows photoluminescence spectra recorded before and after the postgrowth annealing of samples containing InGaAs quantum dots with various In concentrations in a GaAs matrix. The anneal temperature was maintained at $T_a=700\,^\circ$C, and the anneal time was 30 min or 90 min. It is evident that the photoluminescence

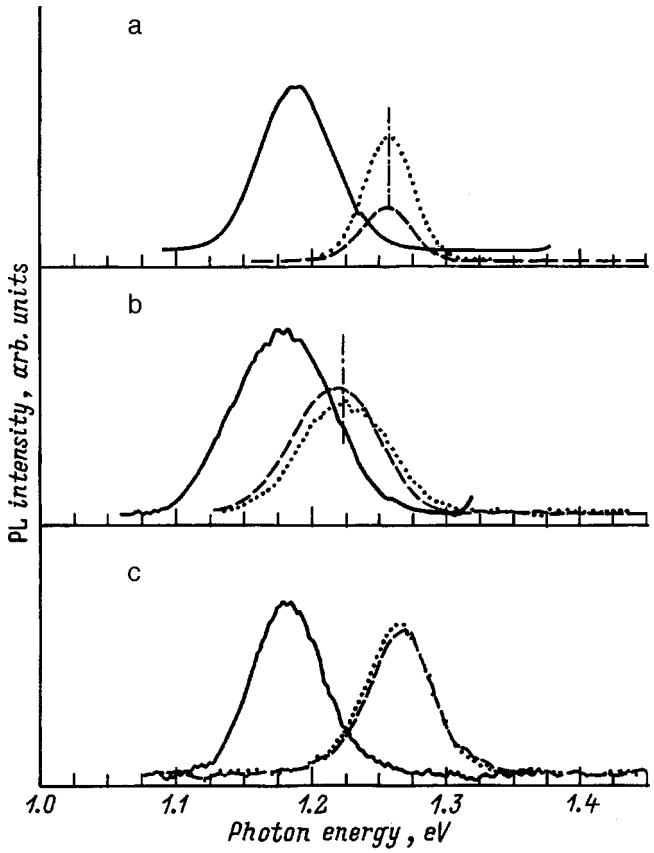

FIG. 2. Photoluminescence spectra of samples containing quantum dots with different mole fractions of InAs in a GaAs matrix without annealing (solid curves) and after 30-min (dashed curves) and 90-min (dotted curves) anneals at $T_a=700\,^\circ$C. Measurement temperature $T=77$ K. (a) Sample 5; (b) sample 6; (c) sample 7.

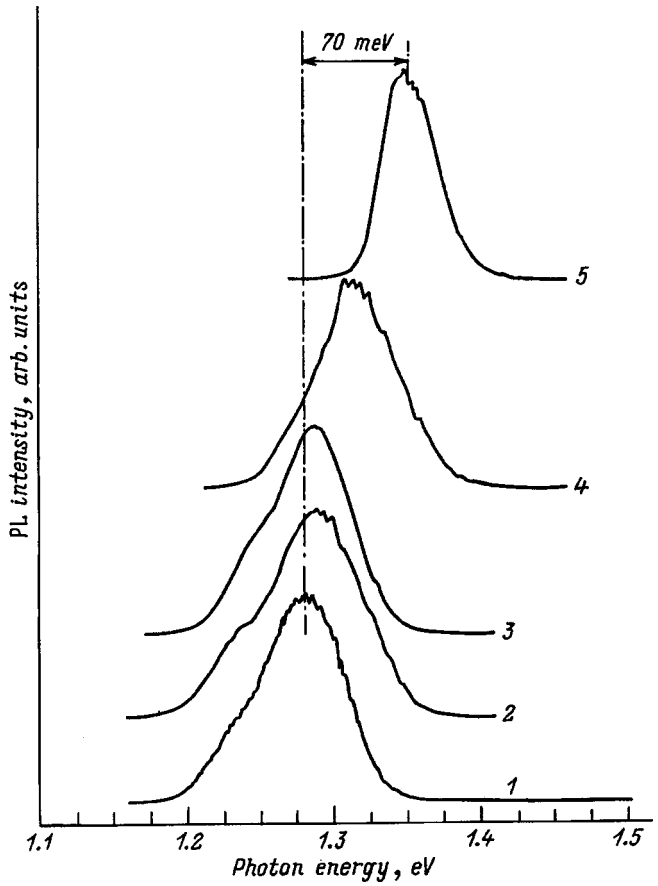

FIG. 3. Photoluminescence spectra of a structure without annealing (*1*) and after a 30-min anneal at various temperatures: (*2*) $T_a = 700$ K; (*3*) 750 K; (*4*) 800 K; (*5*) 850 K. Measurement temperature $T = 77$ K.

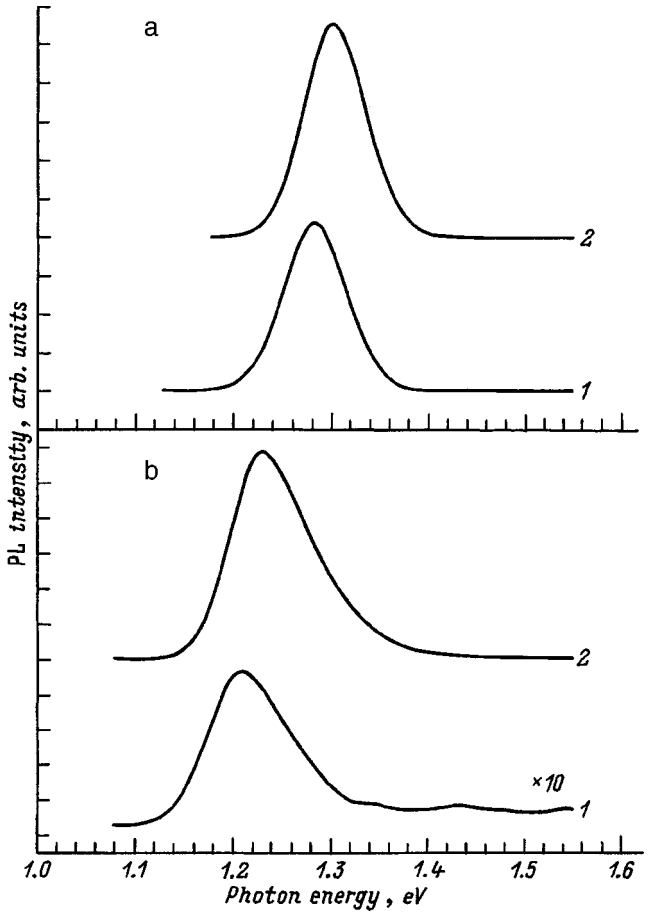

FIG. 4. Photoluminescence spectra of structure 4 without annealing (*1*) and after a 30-min anneal at $T_a = 850\,^\circ$C (*2*). Measurement temperature: (a) $T = 77$ K; (b) $T = 300$ K.

line shifts toward higher photon energies after annealing, independently of the In content in the quantum dots. This phenomenon has been observed by many research groups[8,9] and, as mentioned above, is attributed to the diffusion of In and Ga atoms across the quantum dot boundary, which lowers the effective In content in the quantum dots. We note, first of all, that the smallest shift of the photoluminescence peak occurs for $In_{0.5}Ga_{0.5}As$ quantum dots. Second, the spectra recorded after 30-min and 90-min anneals scarcely differ at all. At 700 °C, therefore, the diffusion processes have a short duration, and any subsequent changes are of little significance. Since the adopted anneal conditions are consistent with the conditions for the high-temperature growth of wide-gap emitters in injection lasers, this result is indicative of a major modification of the shape and dimensions of the quantum dots in a GaAs matrix in the active zone of lasers.

The results of previous studies[12,13] have shown that structures with several tiers of quantum dots separated by narrow (of the order of the dot height) barriers (so-called structure with vertically coupled quantum dots) can be used not only to diminish the size variance, but also to achieve greater gain in lasers and to prevent gain saturation in lasing through the ground state in quantum dots. Figure 3 shows the photoluminescence spectra for a structure with vertically coupled InGaAs quantum dots in a GaAs matrix under various anneal conditions. We see that only for anneal temperatures $T_a > 800\,^\circ$C does the short-wavelength shift of the photoluminescence line for such a structure become appreciable, whereas annealing at lower temperatures leaves the position of the line essentially unchanged. We therefore assume that structures with vertically coupled quantum dots have greater thermal stability. This result is probably attributable to an effective increase in the size of the carrier localization zone in the case of vertically coupled dots. Diffusion processes, which tend to ''smear'' the quantum dot boundaries, now exert a far weaker influence on the quantum dot electron spectrum and, hence, on the optical transition energy. This result shows that high-temperature emitter growth, at which the density of point defects is small and the optical properties of the structure change only slightly, can be employed in growing laser structures with an active zone utilizing vertically coupled quantum dots.

We have shown previously[11] that the high-temperature annealing of structures containing InGaAs quantum dots in an AlGaAs matrix influences the optical characteristics of the structures to a lesser extent than structures with quantum dots in a GaAs matrix. Figure 4 shows the photoluminescence spectra of structures containing vertically coupled InGaAs quantum dots in an $Al_{0.15}Ga_{0.85}As$ matrix. We note that for the structure with quantum dots in the system $InGaAs/Al_{0.15}Ga_{0.85}As$ the top AlGaAs capping layer was

grown at a temperature of 700 °C. During growth, therefore, the structure was subjected to a 10-min anneal at higher temperatures than in the annealing of structures with quantum dots in a GaAs matrix. It is evident that for this structure a 30-min postgrowth anneal at the temperature $T_a = 830$ °C slightly shifts the photoluminescence line (by 20 meV) toward higher photon energies without altering the low-temperature photoluminescence intensity or the linewidth. This outcome is probably attributable to the suppression of diffusion processes by virtue of the lower mobility of Al atoms. On the other hand, annealing significantly increases the photoluminescence intensity at a temperature of 300 K. We attribute this phenomenon to a significant decrease in the density of point defects in the AlGaAs layer immediately adjacent to the quantum dots, which was deposited at a low temperature. The result is a decrease in the probability of nonradiative recombination at room temperature.

We have thus shown that the high-temperature thermal annealing of structures containing vertically coupled InGaAs quantum dots in an AlGaAs matrix can significantly improve the quality of the structure, essentially without affecting the energy of carrier localization in the quantum dots relative to the barrier. This result also shows that annealing during the growth of laser structures with InGaAs quantum dots in AlGaAs can be augmented with postgrowth annealing at higher temperatures, thereby improving the characteristics of the laser structures.

4. CONCLUSIONS

We have investigated the influence of the mole fraction of InAs and high-temperature postgrowth thermal annealing on the luminescence properties of structures containing InGaAs quantum dots in GaAs and AlGaAs matrices. We have shown that increasing the mole fraction of InAs from 0.23 to 0.5 for quantum dots in an AlGaAs matrix raises the energy of carrier localization in the quantum dots and increases the energy distance between the ground state and the excited states. Nonuniform broadening of the photoluminescence line increases as the mole fraction of InAs is increased, but it can be diminished by depositing several planes of quantum dots separated by narrow barriers to improve the size uniformity of the quantum dots and stimulate effective electronic interaction between the quantum dots in adjacent tiers. Furthermore, the replication of quantum dot layers separated by thin barriers enhances the thermal stability of the structures in comparison with those containing a single layer of quantum dots. For structures with InGaAs quantum dots in an AlGaAs matrix the quality of the AlGaAs layers can be improved by high-temperature annealing ($T_a = 830$ °C), essentially without altering the energy spectrum of the structure. These results demonstrate the feasibility of using postgrowth annealing to improve the quality of laser structures.

In different stages this work has received support from the Russian Fund for Fundamental Research, the Volkswagen Foundation (No. 1/73-631), and the International Association for the Promotion of Cooperation with Scientists from the Independent States of the Former Soviet Union (INTAS Grant 96-0467).

[1] L. Goldstein, F. Glass, J. Y. Marzin, M. N. Charasse, and G. Le Roux, Appl. Phys. Lett. **47**, 1099 (1985).
[2] M. Moison, F. Houzay, F. Barthe, L. Leprince, E. Andre, and O. Vatel, Appl. Phys. Lett. **64**, 196 (1994).
[3] P. M. Petroff and S. P. Den Baars, Superlattices Microstruct. **15**, 15 (1994).
[4] N. N. Ledentsov, M. Grundmann, N. Kirstaedter, O. Schmidt, R. Heitz, J. Bohrer, D. Bimberg, V. M. Ustinov, V. A. Shchukin, P. S. Kop'ev, Zh. I. Alferov, S. S. Ruvimov, A. O. Kosogov, P. Werner, U. Richter, U. Gösele, and J. Heydenreich, Solid-State Electron. **40**, 785 (1996).
[5] N. Kirstaedter, N. N. Ledentsov, M. Grundmann, D. Bimberg, V. M. Ustinov, S. S. Ruvimov, M. V. Maximov, P. S. Kop'ev, Zh. I. Alferov, U. Richter, P. Werner, U. Gösele, and J. Heydenreich, Electron. Lett. **30**, 1416 (1994).
[6] M. V. Maximov, I. V. Kochnev, Yu. M. Shernyakov, S. V. Zaitsev, N. Yu. Gordeev, A. F. Tsatsul'nikov, A. V. Sakharov, I. L. Krestnikov, P. S. Kop'ev, Zh. I. Alferov, N. N. Ledentsov, D. Bimberg, A. O. Kosogov, P. Werner, and U. Gösele, in *International Symposium on the Formation, Physics, and Device Application of Quantum Dot Structures* (Sapporo, Japan, 1996) [Jpn. J. Appl. Phys. **36**, Part 1, 4221 (1997)].
[7] Y. Arakawa and H. Sakaki, Appl. Phys. Lett. **40**, 939 (1982).
[8] R. Leon, Y. Kim, C. Jagadish, M. Gal, J. Zou, and D. J. H. Cockayne, Appl. Phys. Lett. **69**, 1888 (1997).
[9] S. Malik, C. Roberts, R. Murray, and M. Pate, Appl. Phys. Lett. **71**, 1987 (1997).
[10] A. O. Kosogov, P. Werner, U. Gösele, N. N. Ledentsov, D. Bimberg, V. M. Ustinov, A. Yu. Egorov, A. E. Zhukov, P. S. Kop'ev, N. A. Bert, and Zh. I. Alferov, Appl. Phys. Lett. **69**, 3072 (1996).
[11] B. V. Volovik, M. V. Maximov, A. V. Sakharov, I. V. Kochnev, N. N. Ledentsov, A. F. Tsatsul'nikov, P. S. Kop'ev, Zh. I. Alferov, D. Bimberg, A. O. Kosogov, and P. Werner, in *Seventh European Workshop on Metal-Organic Vapor-Phase Epitaxy and Related Growth Techniques* (Berlin, Germany, 1997) (workshop booklet).
[12] N. N. Ledentsov, V. A. Shchukin, M. Grundmann, N. Kirstaedter, J. Böhrer, O. Schmidt, D. Bimberg, V. M. Ustinov, A. Yu. Egorov, A. E. Zhukov, P. S. Kop'ev, S. V. Zaitsev, N. Yu. Gordeev, Zh. I. Alferov, A. I. Borovkov, A. O. Kosogov, S. S. Ruvimov, P. Werner, U. Gösele, and J. Heydenreich, Phys. Rev. B **54**, 8743 (1996).
[13] V. M. Ustinov, A. Yu. Egorov, A. R. Kovsh, A. E. Zhukov, M. V. Maximov, A. F. Tsatsul'nikov, N. Yu. Gordeev, S. V. Zaitsev, Yu. M. Shernuakov, N. A. Bert, P. S. Kop'ev, Zh. I. Alferov, N. N. Ledentsov, J. Bohrer, D. Bimberg, A. O. Kosogov, P. Werner, and U. Gösele, J. Cryst. Growth **175/176**, 689 (1997).

Translated by James S. Wood

Nonradiative recombination at shallow bound states in quantum-confined systems in an electric field

É. P. Sinyavskiĭ and A. M. Rusanov

Institute of Applied Physics, Academy of Sciences of Moldavia, 277028 Kishinev, Moldavia
(Submitted November 3, 1997; accepted for publication June 30, 1998)
Fiz. Tekh. Poluprovodn. **33**, 97–100 (January 1999)

The one-phonon recombination of carriers at shallow impurity states in parabolic quantum wells in a longitudinal electric field is investigated. It is shown that one-phonon recombination processes are more active in quantum-confined systems than in the bulk material. The possibility of electrically induced one-phonon transfer in a confined system is discussed. © *1999 American Institute of Physics.* [S1063-7826(99)02001-3]

1. In doped, quantum-confined systems (quantum films and single quantum wells) the onset of resonance states in an allowed band[1] and the existence of size-induced bound states[2,3] (bound states that do not exist in the bulk material) can significantly influence kinetic phenomena.

If an electric field of strength F is directed along the spatial quantization axis, the band electron energy for parabolic quantum wells is given by the relation

$$E_{n\mathbf{k}_\perp}=\frac{\hbar^2\mathbf{k}_\perp^2}{2m}+\hbar\omega\left(n+\frac{1}{2}\right)-\Delta, \tag{1}$$

where $\hbar\omega$ is the spatial quantization energy — if E_c is the depth of a quantum well of width d, then $\hbar\omega=[8\hbar^2E_c/md^2]^{1/2}$, $\hbar\mathbf{k}_\perp$ is the quasimomentum of an electron of mass m in the plane perpendicular to the spatial quantization axis, and $\Delta=e^2F^2/2m\omega^2$. It follows directly from Eq. (1) that a static electric field merely shifts the carrier energy into the forbidden range, so that carrier heating effects do not occur.

With present-day technology utilizing computers to monitor the molecular-beam shutter it is possible to generate various profiles of the potential of quantum wells. An artificial parabolic quantum well was first obtained by Gossard[5] in the confined system GaAs/Al_xGa_{1-x}As. In the system Al_xGa_{1-x}As/GaAs Wang *et al.*[6] have created high-quality parabolic wells, in which they clearly observed optical transitions from high quantum-well levels at $d=4500$ Å. Equivalent quantum-well levels occur for sufficiently wide parabolic wells, making systems of this kind highly promising for optoelectronic device applications. For GaAs/Al_xGa_{1-x}As parabolic well parameters $E_c=0.255$ eV and $m=0.06m_0$ it is found that $\hbar\omega=4.6$ meV for $d=3\times10^3$ Å.

We can infer from the form of the electron potential energy $U(z)=(m\omega^2/2)z^2-eFz$ that the minimum of the potential of a parabolic quantum well in a longitudinal electric field shifts in the opposite direction from **F** (the displacement $d_0=eF/m\omega^2$) and drops by the amount Δ. This behavior of the parabolic well potential in an external field specifically affects nonradiative carrier trapping in quantum-confined systems. If an impurity is located at the center of a quantum well, the overlap of the wave functions of band electrons and bound states decreases as **F** increases, thereby lowering the recombination rate. But if the potential energy minimum approaches a local center as **F** is increased, the increase in the overlap integral of the free-carrier and bound-state wave functions causes the recombination rate to increase. In quantum-confined systems, therefore, a static electric field can significantly influence processes of nonradiative trapping of free carriers.

In the present article we investigate the characteristics of single-phonon trapping of carriers by shallow impurity states in a parabolic quantum well in a longitudinal electric field. We discuss in detail the influence of scattered waves on nonradiative recombination time.

2. In the zero-range potential model the wave function $\Psi_s(\mathbf{r})$ and the bound-state energy E of the parabolic well in the presence of a longitudinal electric field are known.[4] In particular, if E_0 is the zero-field binding energy in the bulk material, then for $E_0/\hbar\omega\gg1$

$$E=-E_0-\frac{\hbar\omega}{2}+\hbar\omega\frac{\xi^2}{2};\quad \xi^2=\frac{m\omega}{\hbar}(z_0+d_0)^2. \tag{2}$$

The impurity is situated at the point with coordinates $\mathbf{r}_0(0,0,z_0)$.

The band-electron wave function is determined from the Lippmann-Schwinger equation and in the zero-range potential model[7] is described by the relation

$$\Psi_{n\mathbf{k}_\perp}(\mathbf{r})=\Psi^{(0)}_{n\mathbf{k}_\perp}(\mathbf{r})+\frac{V_0\tilde{\Psi}^{(0)}_{n\mathbf{k}_\perp}(z_0)}{1-V_0\tilde{G}_{n\mathbf{k}_\perp}(z_0;z_0)}G_{n\mathbf{k}_\perp}(\mathbf{r},z_0), \tag{3}$$

$$\tilde{A}(z_0;z_0)=\left[1+x\frac{\partial}{\partial x}+y\frac{\partial}{\partial y}+(z-z_0)\frac{\partial}{\partial z}\right]A(\mathbf{r},z_0)\Big|_{\substack{x=y=0\\z=z_0}},$$

where V_0 is the power of the potential well, corresponding to E_0. The second term in Eq. (3) is the result of taking scattered waves into account; it will be shown below that scattering determines the magnitude and temperature dependence of one-phonon recombination.

For a parabolic well in a longitudinal electric field

$$\Psi^{(0)}_{n\mathbf{k}_\perp}(\mathbf{r})=\frac{1}{\sqrt{L_x}L_y}\left(\frac{\lambda}{\pi}\right)^{1/4}\frac{e^{i(\mathbf{k}_\perp\boldsymbol{\rho})}}{\sqrt{2^n n!}}\times\exp\left\{-\frac{\lambda}{2}(z+d_0)^2\right\}H_n\left[\frac{\lambda}{2}(z+d_0)\right]. \quad (4)$$

Here $\lambda=m\omega/\hbar$, $(\mathbf{k}_\perp\cdot\boldsymbol{\rho})=k_x x+k_y y$, $H_n(z)$ denotes Hermite polynomials, $G_{n\mathbf{k}_\perp}(\mathbf{r},z_0)$ is the Green's function,

$$G_{n\mathbf{k}_\perp}(\mathbf{r},z_0)=\sum_{\nu,\mathbf{p}_\perp}\frac{\Psi^{(0)}_{\nu\mathbf{p}_\perp}(\mathbf{r})\Psi^{(0)*}_{\nu\mathbf{p}_\perp}(z_0)}{E_{\nu\mathbf{p}_\perp}-E_{n\mathbf{k}_\perp}+i\delta},\quad \delta\to+0,$$

and L_x and L_y are the dimensions of the quantum well along the x and y axes, respectively. The following inequalities are assumed to hold in our subsequent calculations:

$$\frac{eFd}{8E_c}\ll 1,\quad \sqrt{\frac{m\omega}{\hbar}}\frac{d}{2}>1,\quad \frac{e^2F^2d^2}{E_c}<E.$$

The first inequality implies that we are considering electric fields of such a magnitude that many quantum-well levels are retained in the shifted quadratic potential of the quantum well. The satisfaction of the second inequality means that we can use quantum oscillator wave functions in a static electric field for the ensuing calculations. The last inequality implies that tunneling processes of an electron from a bound state to the continuous spectrum do not occur in an external field. We calculate the matrix element

$$M_{s,\mathbf{k}_\perp n}=\int\Psi^*_s(\mathbf{r})e^{i\mathbf{q}\cdot\mathbf{r}}\Psi_{n\mathbf{k}_\perp}(\mathbf{r})d\mathbf{r}$$

($\mathbf{q}$ is the phonon wave vector) for the low-temperature case, when electrons are situated in the lower quantum-well conduction band ($n=0$). If the thickness of the quantum well is such that $E/\hbar\omega\gg 1$, we have

$$|M_{s,\mathbf{k}0}|^2\cong\frac{1}{L_xL_y}\left(\frac{2}{\varepsilon_0}\frac{\hbar}{m\omega}\sqrt{\frac{2\pi}{\varepsilon_0}}\right)e^{-\xi^2}\times\frac{[1-\sqrt{1+(qa_0)^2}]^2}{[1+(qa_0)^2]^2|1-V_0\tilde{G}_{\mathbf{k}_\perp 0}(z_0,z_0)|^2}, \quad (5)$$

$$E_0=\frac{\hbar^2}{2ma_0^2};\quad \varepsilon_0=\frac{E_0}{\hbar\omega}+\frac{1}{2}.$$

The Green's function $\tilde{G}_\varepsilon(z_0,z_0)$ is calculated in the usual way.[7] As a result, we obtain ($\varepsilon<1$)

$$1-V_0\tilde{G}_\varepsilon(z_0,z_0)=1+\left(\frac{\hbar\omega}{2\pi E_0}\right)^{1/2}\left\{I_0(\xi)-\sqrt{2\pi(1-\varepsilon)}+\exp(-\xi^2)\ln\frac{1-\varepsilon}{\varepsilon}+i\pi\exp(-\xi^2)\right\}, \quad (6)$$

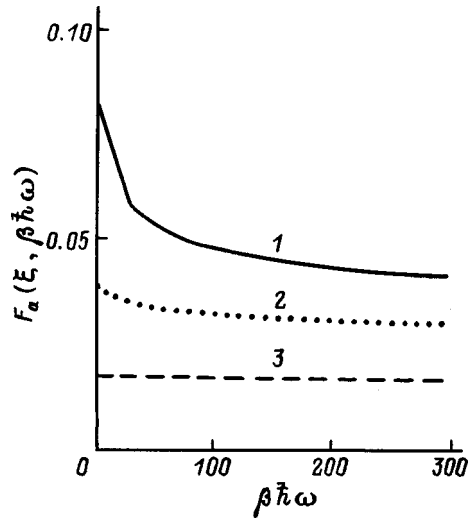

FIG. 1. Temperature dependence of the probability of one-phonon transfer (in arbitrary units) of an electron to shallow impurities with the emission of an acoustic phonon. (*1*) $\xi^2=0$; (*2*) $\xi^2=1$; (*3*) $\xi^2=2$.

$$I_0(\xi)=\int_0^\infty\frac{d\tau}{\tau}e^{\tau\varepsilon}\left\{\frac{\exp[2\xi^2/(e^\tau+1)]}{\sqrt{1-e^{-2\tau}}}-1-e^{-\tau}\left[\frac{\exp(\xi^2)}{\sqrt{2\tau}}-1\right]\right\}\exp(-\xi^2).$$

The values of ε ($\varepsilon=\hbar\mathbf{k}_\perp^2/2m\omega$) for which the real part of expression (6) vanishes determine the size-impurity states. But if the imaginary part of (6) is much smaller than unity, the size-impurity states strongly influence nonradiative recombination processes.

3. We now consider the transition of an electron from the conduction band to a local state with the emission of an acoustic phonon of energy $\hbar\omega_q=\hbar\upsilon$ (υ is the sound velocity in the semiconductor material). Using Eq. (5), we obtain the following expression for the nonradiative trapping time when the natural inequality $m\upsilon^2/E_0\ll 1$ holds:

$$\frac{1}{\tau_{ak}}=\frac{1}{\tau^0_{ak}}F_a(\xi,\beta\hbar\omega)\frac{4}{\pi^2}\left[\frac{\hbar\omega}{E_d}\right]^{1/2}; \quad (7)$$

$$\frac{1}{\tau^0_{ak}}\cong\frac{\pi^2n_sE_1^2}{2m\rho\upsilon^3a_0};$$

$$F_a(\xi,\beta\hbar\omega)=\exp(-\xi^2)\int_0^\infty\frac{e^{-\hbar\omega\beta\tau}\hbar\omega\beta}{|1-V_0\tilde{G}_\tau(z_0,z_0)|^2}d\tau;$$

$$E_d=\hbar^2/md^2,$$

where n_s is the density of local centers, E_1 is the deformation potential constant, ρ is the density of the crystal, $\beta=1/k_0T$, T is the absolute temperature, and $\tau^{(0)}_{ak}$ is the lifetime for the bulk material.[8] The temperature dependence of $F_a(\xi,\beta\hbar\omega)$ for various values of ξ^2 is shown in Fig. 1. Curves *1*, *2*, and *3* are plotted for $\xi^2=0,1,2$, respectively, and $(\hbar\omega/2\pi E_0)^{1/2}=0.1$. The temperature dependence of the lifetime in connection with the emission of an acoustic phonon is the result of taking into account scattering by the

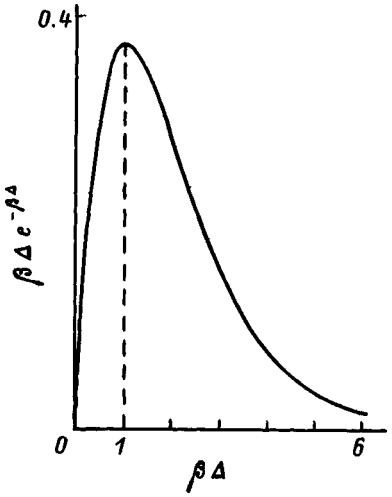

FIG. 2. Temperature dependence of the reciprocal carrier trapping time (in arbitrary units) in a bound state with the emission of an optical phonon.

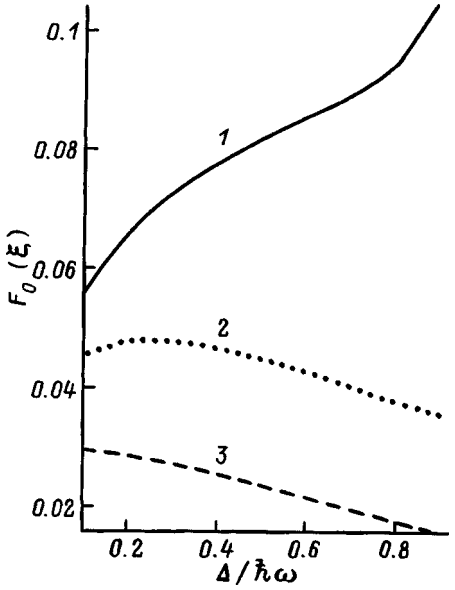

FIG. 3. Dependence of the probability of transfer of an electron (in arbitrary units) to a bound state with the emission of an optical phonon on the field shift $\Delta=\hbar\omega_0-E$. (*1*) $\xi^2=0$; (*2*) $\xi^2=1$; (*3*) $\xi^2=2$.

short-range potential [second term in Eq. (3)]. Since $(\hbar\omega/E_d)\gg 1$ for realistic parabolic well thicknesses ($d\approx 3\times 10^3$ Å), one-phonon recombination processes can be more active in the quantum well than in the bulk material. For typical parameters of GaAs/AlGaAs parabolic wells ($m=0.06m_0$, $E_1=5$ eV, $v=5\times 10^5$ cm/s, $E_c=0.255$ eV) together with $E=0.02$ eV, $n_s=10^{15}\,\mathrm{cm}^{-3}$, $d=3\times 10^3$ Å, $\xi=0$, and $T=20$ K we have $\tau_{ak}\approx 3.6\times 10^{-11}$ s ($\tau_{ak}^{(0)}\approx 0.6\times 10^{-10}$ s). As ξ^2 increases (implying an increase in the electric field if the impurity is located at the center of the well), τ_{ak} increases, because the minimum of the potential energy moves away from the impurity site, diminishing electron-impurity interaction.

The carrier trapping time from the lower quantum-well conduction band to a bound state with the emission of an optical phonon of energy $\hbar\omega_0$ can be calculated analogously:

$$\frac{1}{\tau_{0n}}=\frac{1}{\tau_{0n}^{(0)}}\frac{(3\pi-8)}{2\pi}\left(\frac{\hbar\omega_0}{E_0}\right)\left(\frac{\hbar\omega}{E_d\beta\Delta}\right)^{1/2}F_0(\xi). \tag{8}$$

Here we have the notation

$$\frac{1}{\tau_{0n}^{(0)}}=\frac{4\pi\sqrt{\pi}e^2C_0\beta\hbar n_s}{m}\sqrt{\beta\Delta}\,\mathrm{e}^{-\beta\Delta},$$

$$F_0(\xi)=\mathrm{e}^{-\xi^2}\frac{1}{|1-V_0\tilde{G}_{\Delta/\hbar\omega}(z_0,z_0)|^2},$$

$$C_0^{-1}=\tilde{\varepsilon}_0^{-1}+\varepsilon_\infty^{-1},\quad \Delta=\hbar\omega_0-E\geqslant 0;$$

$\tilde{\varepsilon}_0$ and ε_∞ are the low-frequency and high-frequency permittivities of the medium, respectively, and $\tau_{0n}^{(0)}$ is the nonradiative trapping time of a band electron in the bulk material.[9] It follows directly from Eq. (8) that $1/\tau_{0n}$ exhibits a nonmonotonic dependence on T as the temperature increases (Fig. 2). The dependence of $F_0(\xi)$ on $\Delta/\hbar\omega$ for various values of ξ^2 ($\xi^2=0,1,2$ for curves *1*, *2*, and *3*, respectively) and $(\hbar\omega/2\pi E_0)^{1/2}=0.1$ is shown in Fig. 3. It follows from this figure that τ_{0n} increases as the electric field increases (provided that the impurity is located at the center of the parabolic well), owing to the diminution of electron-impurity interaction. For $\hbar\omega_0=0.02$ eV, $C_0=1.48\times 10^{-2}$, $n_s=10^{15}\,\mathrm{cm}^{-3}$, $\Delta=0.01$ eV, and $T=20$ K ($d=3\times 10^3$ Å) we have $\tau_{an}=10^{-11}$ s ($\tau_{an}^{(0)}\approx 2.5\times 10^{-11}$ s). Consequently, the lifetime associated with the emission of an optical phonon in a parabolic quantum well can be shorter (under like conditions) than in the bulk material. For zero electric field ($F=0$) the quantity ξ^2 depends only on the position of the impurity in the parabolic well [see Eq. (2)]. If the impurity is situated at the center of the quantum well ($\xi=0$), the processes of nonradiative recombination with the emission of an optical phonon are more active than in the bulk material. When the impurity is farther from the center of the well, the overlap of the bound-state wave functions and the continuous spectrum diminishes, resulting in the phenomenon of lifetime ''stretching'' [the presence of the factor $\exp(-\xi^2)$ in Eqs. (7) and (8)].

If $E>\hbar\omega_0$, processes involving the emission of a single optical phonon are impossible, and only low-probability two-phonon processes occur. However, as F is increased, the bound-state energy decreases [see Eq. (2)] and, beginning with a certain threshold F_{cr}, E can become smaller than $\hbar\omega_0$, so that one-phonon trapping processes are allowed. Such electric field-induced one-phonon recombination processes can significantly influence the kinetic properties of quantum wells. The critical electric field F_{cr} is determined from the natural condition

$$\frac{\hbar\omega}{2}\xi^2=E-\hbar\omega_0.$$

For $E=0.025$ eV, $\hbar\omega_0=0.02$ eV, and $d=2\times 10^3$ Å we have $F_{\mathrm{cr}}=10^4$ V/cm.

[1] A. V. Chaplik, Fiz. Tekh. Poluprovodn. **5**, 1900 (1971) [Sov. Phys. Semicond. **5**, 1651 (1971)].
[2] É. P. Sinyavskiĭ and E. Yu. Kanarovskiĭ, Fiz. Tverd. Tela (Leningrad) **34**, 737 (1992) [Sov. Phys. Solid State **34**, 395 (1992)].
[3] A. A. Pakhomov, K. V. Khalipov, and I. N. Yassievich, Fiz. Tekh. Poluprovodn. **30**, 1387 (1996) [Semiconductors **30**, 730 (1996)].
[4] É. P. Sinyavskiĭ and E. Yu. Kanarovskiĭ, Fiz. Tverd. Tela (St. Petersburg) **37**, 2639 (1995) [Phys. Solid State **37**, 1450 (1995)].
[5] A. C. Gossard, in *Institute of Physics Conference Series*, No. 69, edited by E. H. Roderick (IOP Publ., Bristol, 1983), p. 1.
[6] S. M. Wang, G. Treideris, W. Q. Chen, and T. G. Andersson, Appl. Phys. Lett. **62**, 61 (1993).
[7] Yu. N. Demkov and V. N. Ostrovskiĭ, *Zero-Range Potentials and Their Applications in Atomic Physics* (Plenum Press, New York, 1988; Izd. Leningrad Gos. Univ., Leningrad, 1975).
[8] E. B. Gol'dgur and R. I. Rabinovich, Zh. Éksp. Teor. Fiz. **84**, 1109 (1983) [Sov. Phys. JETP **57**, 643 (1983)].
[9] É. P. Sinyavskiĭ and E. Yu. Safronov, Fiz. Tekh. Poluprovodn. **24**, 1299 (1990) [Sov. Phys. Semicond. **24**, 816 (1990)].

Translated by James S. Wood

Radiative tunneling recombination and luminescence of trapezoidal δ-doped superlattices

V. V. Osipov and A. Yu. Selyakov

''Orion'' State Scientific Center of the Russian Federation, 111123 Moscow, Russia

M. Foygel

South Dakota School of Mines and Technology, Rapid City, SD 57701-3995, USA

(Submitted June 16, 1998; accepted for publication June 30, 1998)
Fiz. Tekh. Poluprovodn. **33**, 101–105 (January 1999)

Radiative recombination is investigated in the authors' previously proposed δ-doped superlattice, which can be grown from one of several well-known single-crystal semiconductors of the type InSb, InAs, or GaAs. The energy diagram of the superlattice consists of alternating trapezoidal *n*-type and *p*-type potential wells for electrons and holes. An equation for the radiative recombination rate is derived for such a trapezoidal superlattice, and it is shown that, owing to the spatial separation of electrons and holes, the radiative lifetime can attain values of the order of 1 ms, and that it depends weakly on the temperature. This result is attributable to the fact that radiative recombination in a trapezoidal superlattice is governed by optical tunneling transitions of electrons from states near the bottom of the *n*-type wells to states near the bottom of the *p*-type wells. An expression is obtained for the luminescence spectrum of the superlattice, where the spectral maximum corresponds to a photon energy much smaller than the width of the semiconductor band gap and can be situated in the far-infrared range. It is noted that such a trapezoidal superlattice can be an efficient converter of thermal radiation into very long-wavelength radiation.
[S1063-7826(99)02101-8]

1. We have previously[1–3] proposed a trapezoidal δ-doped superlattice (TSL) and analyzed its interband absorption spectra. This type of TSL can be grown from any of the better-known homogenous single-crystal semiconductors. A superstrong built-in electric field is produced in the thin regions between the oppositely charged δ-doped layers of the TSL. We have shown[1,4] that InSb and InAs TSLs absorb radiation efficiently up to the far-infrared range as a result of the Franz–Keldysh effect[5,6]. Notably, in classical doped superlattices of the *n-i-p-i* type, proposed in the eighties and investigated by Neustroev and Osipov,[7–10] nonequilibrium electrons and holes can acquire extremely long lifetimes by virtue of their spatial separation, but far-IR radiation is weakly absorbed in them.[11,12] Another phenomenon that occurs in TSLs is the spatial separation of nonequilibrium electrons and holes, making it reasonable to expect that the nonequilibrium carriers in them will also be capable of attaining long lifetimes. In contrast with classical doped superlattices, however, the recombination of spatially separated electrons and holes is dictated mainly by diagonal (indirect in real space) radiative tunneling transitions, because of the presence of thin regions endowed with a superstrong electric field in the TSL. In this paper we derive expressions for the nonequilibrium carrier lifetime, the radiative recombination rate, and the luminescence spectrum governed by such transitions due to radiative tunneling, and we investigate the statistics of electrons and holes in a TSL.

2. A TSL is formed in a single-crystal nondegenerate semiconductor by alternating δ-doped donor and acceptor layers characterized by surface densities of atoms σ_d and σ_a, respectively. One period of the TSL spans two pairs of such oppositely charged δ-doped layers, and the energy diagram of the TSL consists of alternating trapezoidal potential wells for electrons and holes (see Fig. 1). We refer to the latter as *n*-type and *p*-type wells, respectively. We have previously[1] analyzed the conditions that must be satisfied by the parameters of the TSL.

In equilibrium, of course, the law of mass action holds at each point of the TSL for nondegenerate electrons and holes: $np=n_i^2=N_cN_v\exp\{-E_g/kT\}$, where N_c and N_v are the effective densities of states in the conduction and valence bands, respectively; n_i is the carrier density in the intrinsic semiconductor, E_g is the width of the semiconductor band gap , k is the Boltzmann constant, and T is the absolute temperature. However, the longitudinal conductivity of the TSL and the recombination rate in it depend on the spatially separated nonequilibrium carriers or, more precisely, on the numbers of electrons and holes in the *n*-type and *p*-type wells, respectively. The widths of these wells l_d and l_a satisfy the conditions[1] $\alpha_{\text{eff}}l_d \ll 1$ and $\alpha_{\text{eff}}l_a \ll 1$, where α_{eff} is the effective (averaged over the period) long-wavelength IR absorption coefficient in the TSL. Consequently, the Fermi quasilevel F_n or F_p for electrons or holes can be regarded as independent of the coordinate in each *n*-type or *p*-type potential well. Moreover, for the investigated TSL we have $l_d, l_a \gg l_{ad}$ (see Fig. 1), and the height of the potential barrier

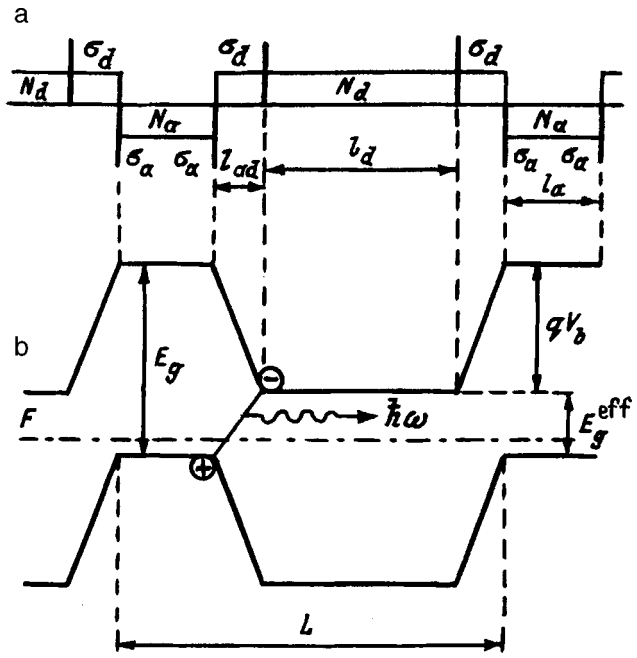

FIG. 1. Doping profile (a) and energy diagram (b) of a trapezoidal δ-doped superlattice. (a) σ_d and σ_a are the surface densities of atoms in the δ-doped donor-type and acceptor-type layers, respectively; N_d and N_a are the donor and acceptor densities, and l_d, l_a, and l_{ad} are the thicknesses of the TSL layers; (b) the arrow indicates the tunneling (indirect in real space) electron-hole recombination with the emission of a photon of energy $\hbar\omega \simeq E_g^{\text{eff}}$, where E_g^{eff} is the effective width of the TSL band gap.

satisfies the condition $qV_b \gg kT$ (q is the electron charge), so that within small error limits the numbers of nondegenerate electrons (N) and holes (P) in the corresponding potential wells per unit area are

$$N = N_c l_d \exp\{(F_n - E_g)/kT\},$$
$$P = N_v l_a \exp\{(qV_b - F_p)/kT\}, \quad (1)$$

where F_n and F_p are referred to the edge of the valence band in an n-type potential well, and the numbers N and P have the dimensions of surface density. In thermodynamic equilibrium it follows from Eq. (1) that

$$NP = N_c N_v l_d l_a \exp\{(qV_b - E_g)/kT\} \equiv N_i^2. \quad (2)$$

Consequently, the numbers of separated nondegenerate electrons and holes localized in n-type and p-type potential wells of the TSL, respectively, are formally governed by the statistics of the nondegenerate electron gas in a certain homogeneous narrow-gap semiconductor with a band gap having an effective width $E_g^{\text{eff}} = E_g - qV_b$. This result is to be expected, because E_g^{eff} characterizes the long-wavelength threshold of interband absorption of radiation in the TSL; i.e., it is also the effective optical width of the TSL band gap.[1–4]

It follows from the periodicity of the TSL that the electroneutrality condition must hold for each period, i.e., $P + N_d l_d + 2\sigma_d = N + N_a l_a + 2\sigma_a$. When $N_d l_d + 2\sigma_d - N_a l_a - 2\sigma_a \ll N_i$, the relation $N = P = N_i$ holds, and such a TSL is aptly called intrinsic. In reality, σ_d and σ_a are much larger than $N_d l_d$ and $N_a l_a$ and are not equal to each other. For example, when $\sigma_a > \sigma_d$, we have $P = 2(\sigma_a - \sigma_d) \gg N_i$. In the given TSL σ_a and σ_d are approximately equal to $(2-5)\times 10^{12}\,\text{cm}^{-2}$, and the thickness of the p-type well is $l_a \simeq 100$ Å (Ref. 1), so that the hole density in the p-type well can be of the order of $10^{18}\,\text{cm}^{-3}$, which comes close to N_v for InSb.

3. The radiative recombination of nonequilibrium carriers in the TSL is determined by radiative tunneling transitions, indirect in real space, of electrons from n-type wells into p-type wells. For nondegenerate electrons and holes the corresponding radiative recombination rate can be written in the form

$$R_r = \mathcal{A} NP. \quad (3)$$

The differential radiative recombination rate is $R = R_r - G_t$, where G_t is the rate of thermal generation of carriers. In thermodynamic equilibrium $R_{r0} = G_t = \mathcal{A} N_0 P_0 = \mathcal{A} N_i^2$, where N_0 and P_0 are the equilibrium numbers of electrons and holes in n-type and p-type potential wells, respectively, and N_i^2 is given by Eq. (2). Let the increments ΔN and ΔP of the carrier densities in the potential wells be small in comparison with their equilibrium values. Then, taking into account the relations $\Delta N = \Delta P$ and $G_t = \mathcal{A} N_i^2$ and relying on Eq. (3), we can write R in the form $R = \mathcal{A}\Delta N(N_0 + P_0) \equiv \Delta N/\tau_R$; i.e., the radiative lifetime of nonequilibrium carriers is

$$\tau_R = N_i^2/G_t(N_0 + P_0), \quad (4)$$

and the radiative recombination rate is

$$R_r = G_t NP N_i^{-2}. \quad (5)$$

Enlisting an idea of Van Roosbroeck and Shockley,[13] we can write the rate of thermal generation of carriers in one period L of the TSL per unit area of the face in thermodynamic equilibrium in the form

$$G_t = L \int_0^\infty v_g \alpha_{\text{eff}}(\hbar\omega) \frac{d[N(\hbar\omega)]}{d(\hbar\omega)} d(\hbar\omega), \quad (6)$$

where $v_g = c/\tilde{n}$ is the group velocity of photons in the semiconductor, $\tilde{n}$ is the refractive index of the semiconductor, c is the speed of light in empty space, $\hbar\omega$ is the photon energy, $N(\omega)$ is the number of equilibrium photons, determined from Planck's formula, $\alpha_{\text{eff}}(\hbar\omega)$ represents the average over the TSL period of the long-wavelength absorption coefficient $\alpha(\hbar\omega)$ due to the Franz–Keldysh effect[5,6,14] in the regions occupied by the built-in electric field of the TSL. We have shown previously[1] that

$$\alpha_{\text{eff}} = 2\alpha(\hbar\omega)(\hbar\omega - E_g^{\text{eff}})/qEL, \quad (7)$$

where

$$\alpha(\hbar\omega) = \pi\mathcal{R}\sqrt{\hbar\omega_E} \int_\beta^\infty \text{Ai}^2(x)\,dx, \quad (8)$$

$\mathcal{R} = (2\mu/\hbar^2)^{3/2}(2q^2P_{cv}^2)/(m^2 c\tilde{n}\omega)$, $\omega_E = (qE)^{2/3}/(2\mu\hbar)^{1/3}$, $\beta = (E_g - \hbar\omega)/\hbar\omega_E$, and $E = 4\pi q\sigma/\varepsilon$ is the electric field between the oppositely charged δ-doped layers (ε is the dielectric constant of the semiconductor), $\sigma = \sigma_d = \sigma_a$, m is the free-electron mass, $\mu^{-1} = m_c^{-1} + m_v^{-1}$ is the reduced effec-

tive mass, $\mathrm{Ai}(x)$ is an Airy function, P_{cv} is the interband matrix element of the momentum operator and for semiconductors exhibiting Kane dispersion is given by the expression $P_{cv}^2 = m^2 E_g(E_g+\Delta_{so})/3m_c(E_g+\frac{2}{3}\Delta_{so})$, and Δ_{so} is the spin-orbit splitting.[15] We have shown[1] that superstrong electric fields can be generated in a TSL, where the long-wavelength electronic absorption is governed by tunneling optical transitions of electrons mainly from the heavy-hole subband of the conduction band (in contrast with moderately high fields, where the electronic absorption is governed by light holes[5,6,14]). In this case the far-IR absorption coefficient in the superstrong electric field regions of the TSL is close to the interband absorption coefficient and is weakly frequency-dependent up to a photon energy of the order of E_g^{eff}. We note that the effective optical band gap $E_g^{\mathrm{eff}} \ll E_g$ in the investigated TSLs, and the light-hole spectrum in the corresponding potential wells is highly quantized, so that light holes do not contribute to the absorption of far-IR radiation with $\hbar\omega \simeq E_g^{\mathrm{eff}}$. The long-wavelength absorption coefficient in the superstrong electric fields is given by the equation[1]

$$\alpha(\hbar\omega) = \Gamma^2(2/3)\mathcal{R}\sqrt{\hbar\omega_E}/4\pi, \tag{9}$$

where $\mu \simeq m_c$, and $\Gamma(x)$ is the gamma function. Substituting the Planck distribution into Eq. (6), we obtain

$$G_t = \frac{2\tilde{n}^2}{\pi^2 c^2 \hbar^3 qE}\int_{E_g^{\mathrm{eff}}}^{E_g}(\hbar\omega)^2(\hbar\omega - E_g^{\mathrm{eff}})\alpha(\hbar\omega) \times \exp\{-\hbar\omega/kT\}d(\hbar\omega) = \frac{2\tilde{n}^2}{\pi^2 c^2\hbar^3 qE}\exp\left\{-\frac{E_g^{\mathrm{eff}}}{kT}\right\} \times \int_0^{\infty}\alpha(E_g^{\mathrm{eff}}+\mathcal{E})(E_g^{\mathrm{eff}}+\mathcal{E})^2\mathcal{E}\exp\left\{-\frac{\mathcal{E}}{kT}\right\}d\mathcal{E}. \tag{10}$$

Here we have made allowance for the fact that $E_g^{\mathrm{eff}} \gg kT$ and $E_g \gg E_g^{\mathrm{eff}}$. It is evident from Eq. (9) that in very strong electric fields the electronic absorption coefficient $\alpha(E_g^{\mathrm{eff}}+\mathcal{E})$ is high for $\mathcal{E}=0$, depends weakly on E_g^{eff}, and at moderately high temperatures is a much smoother function of $\mathcal{E}$ than $\exp\{-\mathcal{E}/kT\}$. We can take advantage of these properties to estimate the integral in Eq. (10), whereupon we obtain

$$G_t = \frac{2(\tilde{n}kTE_g^{\mathrm{eff}})^2}{\pi^2 c^2\hbar^3 qE}\alpha(E_g^{\mathrm{eff}})\exp\left(-\frac{E_g^{\mathrm{eff}}}{kT}\right). \tag{11}$$

Equations (11), (5), (4), and (2) give the radiative tunneling recombination rate and the corresponding lifetime. The lifetime is

$$\tau_R = \frac{\pi^2 c^2\hbar^3 qE}{2(\tilde{n}kTE_g^{\mathrm{eff}})^2}\frac{N_c N_v l_d l_a}{N_0+P_0}\alpha(E_g^{\mathrm{eff}})^{-1}. \tag{12}$$

It is evident from Eq. (12) that the radiative tunneling recombination time τ_R in the TSL depends comparatively weakly on the temperature, in contrast with classical doped superlattices, where the carrier lifetime $\tau_R \propto \exp\{qV_b/kT\}$ (Refs. 7–10). Here τ_R increases with decreasing electronic absorption α of photons with energy $\hbar\omega = E_g^{\mathrm{eff}} \ll E_g$. In real TSLs the surface densities of dopant atoms in the δ-doped layers cannot be rigorously determined, and the scatter of σ_d and σ_a therefore leads to fluctuations of E_g^{eff} in different periods of the TSL. However, this scatter of E_g^{eff} should not have a significant effect on the values of τ_R because, according to (9), in strong electric fields $\alpha \propto (E_g^{\mathrm{eff}})^{-1}$ [the coefficient $\mathcal{R} \propto \omega^{-1} \propto (E_g^{\mathrm{eff}})^{-1}$], so that, according to (12), the dependence of τ_R on E_g^{eff} is relatively weak.

4. We now interpret the results. Obviously, nondegenerate electrons and holes have characteristic energies that coincide (to within kT) with the energies of the bottoms of the *n*-type and *p*-type potential wells, respectively (Fig. 1). As they recombine by radiative tunneling, they emit a photon with energy $\hbar\omega \simeq E_g^{\mathrm{eff}} + kT$, so that the absorption coefficient for such photons must determine the radiative recombination rate in the TSL. This assertion essentially follows from Eqs. (10), (11), and (5). It also implies that the superstrong electric field condition[1] in the given situation is $E \gg E_0 \equiv (q\hbar)^{-1}(2\mu)^{1/2}(E_g)^{3/2}$. When this condition is satisfied, the absorption is at a maximum and is given by Eq. (9).

We have shown[1] that an InSb TSL with parameters $\sigma = 5\times10^{12}\,\mathrm{cm}^{-2}$, $l_a = 42$ Å, $l_d = 233$ Å, and $l_{ad} = 33$ Å has $E_g^{\mathrm{eff}} \simeq 0.05$ eV, which corresponds to the long-wavelength absorption threshold $\lambda_{co} = 25\,\mu$m. A calculation of the lifetime from Eq. (12) using the expressions for α (9) (which is valid for $E \gg E_0$) gives the following for a TSL with the indicated parameters: $\tau_R = 10^{-4}[2N_i/(N_0+P_0)]$ s, where $N_i = 1.7\times10^9\,\mathrm{cm}^{-2}$ at $T = 77$ K. In the given TSL, however, the built-in field $E \approx E_0$, i.e., one cannot possibly interpret that the strong electric field condition is satisfied. A calculation of the lifetime from Eq. (12) using the value of α evaluated numerically from the general equation (8) gives $\tau_R = (3.6\times10^{-4})[2N_i/(N_0+P_0)]$ s. The lifetime attains a maximum $\tau_{Ri} = 360\,\mu$s in an intrinsic TSL. The same lifetime is encountered in an InAs TSL with parameters such that $\lambda_{co} = 25\,\mu$m (Ref. 4). The radiative recombination time can be several orders of magnitude shorter in extrinsic, nondegenerate TSLs with $P_0 \approx N_v I_a$. It is clear that the built-in electric field E diminishes as σ decreases (and as l_{ad} increases accordingly), so that the electronic absorption decreases, while the radiative tunneling lifetime in the TSL increases and can attain huge values.

5. We now discuss the luminescence of the TSL. According to Eqs. (5) and (10), the spectral density of the recombination radiation is

$$S(\omega, E_g^{\mathrm{eff}}) = \frac{NP}{N_i^2}\frac{2\tilde{n}^2\hbar\omega^3}{\pi^2 c^2 qE}(\hbar\omega - E_g^{\mathrm{eff}})\alpha(\omega)\exp\left(-\frac{\hbar\omega}{kT}\right). \tag{13}$$

According to Eq. (13), the luminescence spectrum comprises a narrow line having a half-width of the order of kT and a maximum corresponding to $\hbar\omega = E_g^{\mathrm{eff}} + kT$. It follows, therefore, that the luminescence spectral density, in contrast with the radiative tunneling lifetime, depends exponentially on E_g^{eff}. As mentioned, E_g^{eff} varies from one period to the next, owing to technological scatter of the TSL parameters. It is natural to assume that the fluctuations of E_g^{eff} fit a Gaussian distribution $\mathcal{P}(E_g^{\mathrm{eff}}) = \exp\{-(E_g^{\mathrm{eff}} - E_{g0}^{\mathrm{eff}})^2/2\Delta\}/\sqrt{2\pi\Delta}$ with

mean E_{g0}^{eff} and variance Δ. Averaging Eq. (13) over this distribution, we find that the luminescence spectrum of a real TSL can be written in the form

$$\overline{S(\omega,E_g^{\text{eff}})}=\int_0^{\hbar\omega} S(\omega,E_g^{\text{eff}})\mathcal{P}(E_g^{\text{eff}})dE_g^{\text{eff}}$$

$$=\frac{NP}{N_i^2}\frac{\tilde{n}^2\hbar\omega^3\alpha(\omega)}{\pi^2c^2qE}\exp\left(-\frac{\hbar\omega}{kT}\right)\left\{(\hbar\omega-E_{g0}^{\text{eff}})\right.$$

$$\times\left[\operatorname{erf}\left(\frac{\hbar\omega-E_{g0}^{\text{eff}}}{\sqrt{2\Delta}}\right)+\operatorname{erf}\left(\frac{E_{g0}^{\text{eff}}}{\sqrt{2\Delta}}\right)\right]$$

$$+\sqrt{\frac{2\Delta}{\pi}}\left[\exp\left(-\frac{(\hbar\omega-E_{g0}^{\text{eff}})^2}{2\Delta}\right)\right.$$

$$\left.\left.-\exp\left(-\frac{(E_{g0}^{\text{eff}})^2}{2\Delta}\right)\right]\right\}, \qquad (14)$$

where $\operatorname{erf}(x)$ is the probability integral. It is evident from this equation that the half-width of the luminescence spectrum is approximately equal to kT for $\Delta<kT$ and depends on Δ in the opposite case. The scatter of E_g^{eff} among the periods of the TSL can therefore be assessed from the width of the luminescence spectrum.

6. We have thus established that the radiative lifetime of nonequilibrium carriers in a TSL, depending on its parameters, can vary over a wide range and attain enormous values because of the spatial separation of electrons and holes. Estimates show that Shockley-Read recombination is strongly suppressed in TSLs for this reason. Owing to the tunneling nature of recombination, the radiative lifetime depends relatively weakly on the temperature. Such a TSL therefore holds considerable promise for the design of photodetectors operating over a broad range in the far infrared. Indeed, we have shown in a preceding paper that an InSb TSL absorbs radiation efficiently in the wavelength range up to $25-100\,\mu$m (Ref. 1). We have learned that the luminescence spectral maximum corresponds to a photon energy $\hbar\omega\simeq E_g^{\text{eff}}\ll E_g$ (Fig. 1) and lies in the far-IR range, and its position can be varied between wide limits by varying the parameters of the TSL. The radiative lifetime in the TSL is a minimum in this case; i.e., luminescence is most efficient in a TSL whose parameters are such that the built-in electric fields in it are superstrong, and the density of holes (or electrons) is large. We emphasize that a TSL having such parameters and existing at a sufficiently low temperature is an efficient converter of room-temperature ($T\simeq 300$ K) thermal radiation into very far-infrared radiation.

The research described in this publication was made possible in part by Award #RE1-287 of the U.S. Civilian Research and Development Foundation for the Independent States of the Former Soviet Union (CRDF).

[1] V. V. Osipov, A. Yu. Selyakov, and M. Foygel, Fiz. Tekh. Poluprovodn. **32**, 221 (1998) [Semiconductors **32**, 201 (1998)].
[2] V. V. Osipov and A. Yu. Selyakov, in *Proceedings of the Third All-Russian Conference on the Physics of Semiconductors* [in Russian] (RIIS FIAN, Moscow, 1997), p. 81.
[3] V. V. Osipov, A. Yu. Selyakov, and M. Foygel, in *Proceedings of the 1997 International Semiconductor Device Research Symposium* (Charlottesville, USA, 1997) p. 277.
[4] V. V. Osipov, A. Yu. Selyakov, and M. Foygel, Phys. Status Solidi B **205**, 32 (1998).
[5] W. Franz, Z. Naturforsch. Teil A **13**, 484 (1958).
[6] L. V. Keldysh, Zh. Éksp. Teor. Fiz. **34**, 1138 (1958) [Sov. Phys. JETP **7**, 788 (1958)].
[7] L. N. Neustroev, V. V. Osipov, and V. A. Kholodnov, Fiz. Tekh. Poluprovodn. **14**, 939 (1980) [Sov. Phys. Semicond. **14**, 553 (1980)].
[8] L. N. Neustroev and V. V. Osipov, Fiz. Tekh. Poluprovodn. **14**, 1186 (1980) [Sov. Phys. Semicond. **14**, 701 (1980)].
[9] L. N. Neustroev and V. V. Osipov, Mikroélektronika **9**, 99 (1980).
[10] L. N. Neustroev and V. V. Osipov, Fiz. Tekh. Poluprovodn. **15**, 1068 (1981) [Sov. Phys. Semicond. **15**, 615 (1981)].
[11] J. Maserjian, F. J. Grunthaner, and C. T. Elliott, Infrared Phys. **30**, 27 (1990).
[12] M. Foygel, E. Brenden, J. H. Seguin, and V. V. Osipov, Phys. Status Solidi B **203**, 255 (1997).
[13] W. Van Roosbroeck and W. Shockley, Phys. Rev. **94**, 1558 (1954).
[14] A. I. Anselm, *Introduction to Semiconductor Theory* (Prentice-Hall, Englewood Cliffs, N.J., 1981; Nauka, Moscow, 1978).
[15] *Semiconductors and Semimetals*, Vol. 3: *Optical Properties of III-V Compounds*, edited by R. K. Willardson and A. C. Beer (Academic Press, New York, 1967; Mir, Moscow, 1970).

Translated by James S. Wood

Influence of thermal annealing on the intensity of the 1.54-μm photoluminescence band in erbium-doped amorphous hydrogenated silicon

A. A. Andreev, V. B. Voronkov, V. G. Golubev, A. V. Medvedev, and A. B. Pevtsov

A. F. Ioffe Physicotechnical Institute, Russian Academy of Sciences, 194021 St. Petersburg, Russia
(Submitted April 28, 1998; accepted for publication April 28, 1998)
Fiz. Tekh. Poluprovodn. **33**, 106–109 (January 1999)

Erbium-doped *a*-Si:H films are prepared by magnetron sputtering of a Si-Er target at a deposition temperature of 200 °C. The films are then subjected to cumulative thermal annealing. A sharp increase ($\sim$50-fold) in the photoluminescence intensity at a wavelength of 1.54 μm is observed after a 15-min anneal at 300 °C in a nitrogen atmosphere. At an anneal temperature $\geqslant$500 °C the photoluminescence signal decreases essentially to zero. The influence of thermal annealing processes is discussed in the context of the model of partial transformation of the structural network of amorphous *a*-Si(Er):H films. [S1063-7826(99)02201-2]

INTRODUCTION

The last decade has witnessed a consistent preoccupation with semiconductor materials doped with rare-earth metals (REMs), in keeping with the development of fiber-optic communication techniques.[1] These materials are intriguing in that REM ions in semiconductors behave like efficient in-center, narrowband infrared emitters. In particular, for the trivalent erbium ion (Er^{3+}) the radiative optical transition ${}^4I_{13/2} \rightarrow {}^4I_{15/2}(4f^{11})$ takes place at a wavelength of 1.54 μm, which corresponds to minimum attenuation and dispersion in quartz optical fibers.[2] The principal advantage of erbium-doped materials is the weak dependence of the radiation wavelength on the host matrix to the erbium dopant, the excitation conditions, and the temperature. The combination of these properties, which have important bearing on optical engineering, with the feasibility of the electronic pumping of REM ions in semiconductor structures opens the door to the design of amplifiers and generators of highly monochromatic, thermally stable radiation.

In recent years considerable attention has been devoted to the preparation of erbium-doped single-crystalline silicon.[3] Silicon is the principal material used in semiconductor electronics, but it is shunned as an optoelectronic material because of its indirect-band energy structure, which is a hindrance to efficient interband radiative recombination. The possibility of obtaining light-emitting structures using erbium-doped silicon holds considerable promise for the implementation of optoelectronic integrated circuits based entirely on silicon technology. The fabrication of silicon optoelectronic devices is further beset by a number of problems, mainly the low limit of attainable densities of optically active erbium ions and strong temperature extinction of the radiation intensity at a wavelength of 1.54 μm.

The above-stated problems can be solved by using erbium-doped amorphous hydrogenated silicon *a*-Si(Er):H. First, the electronic properties of this kind of material meet the requirements imposed on semiconductor devices. Second, the *a*-Si(Er):H thin-film deposition technology is highly sophisticated and compatible with silicon integrated-circuit technology. Third, *a*-Si(Er):H exhibits a high intensity and weak temperature extinction of photoluminescence at a wavelength of 1.54 μm in comparison with crystalline silicon.[4,5] Nonetheless, many problems pertaining to optimization of the production of efficiently radiating *a*-Si(Er):H have yet to be solved completely. One such problem is the influence of thermal annealing of *a*-Si(Er):H films to improve the emission properties of Er^{3+} ions.

The objective of the present study is to investigate the influence of thermal annealing on the intensity of 1.54-μm photoluminescence and the physicochemical processes accompanying this treatment. The main efforts are aimed at obtaining films whose deposition and subsequent annealing to stimulate maximum enhancement of the photoluminescence intensity take place at $T \leqslant 300$ °C. This endeavor is of fundamental value from the standpoint of compatibility with silicon integrated-circuit technology.

EXPERIMENTAL PROCEDURE

The *a*-Si(Er):H films were deposited by cosputtering of Si and Er targets with simultaneous decomposition of the reactive gas in the plasma of a dc magnetron discharge. The magnetron system was of the planar type and utilized SmCo permanent magnets. One target of diameter 60 mm was made from a *p*-type Si plate with a resistivity $\rho = 10-15\ \Omega \cdot$cm. The zone of intense sputtering was carefully overlaid with high-resistance intrinsic silicon wafers with $\rho > \text{k}\Omega \cdot$cm. This structure inhibited the generation of surface charges on the target and ensured stable burning of the discharge. An Er target in the form of one or two wafers having dimensions 9×1 mm^2 was placed in the zone of intense discharge in the gap between the high-resistance silicon wafers in the radial direction. The target-substrate distance was 60 mm. The Ar sputtering gas and the reactive gas with components in the ratio $[SiH_4]/[SiH_4 + H_2] = 20\%$ were delivered from differ-

ent sources. The partial pressure of the silane-hydrogen mixture in the discharge chamber was $\sim 1.5\times 10^{-3}$ Torr, and the Ar pressure was $\sim(8-30)\times 10^{-3}$ Torr. The minimum oxygen content depended on the tightness of the vacuum system. The discharge current was chosen near the threshold of stable burning and was varied in the interval 15–30 mA. The substrate temperature was 200 °C. The substrates were made of alkali-free glass, fused quartz, and crystalline silicon. The deposited layers had thicknesses of $0.5-1.0\ \mu$m.

The properties of the films were monitored according to the following set of optical parameters: the energy position and slope of the optical absorption curve and the Urbach characteristic energy. By varying the conditions of the technological process and the ratio of the areas of the erbium wafers and the silicon target it was possible to obtain films with a set of parameters close to the standard characteristics of *a*-Si:H: $E_g=1.7$ eV, $B=700\ \mathrm{cm^{-1}\cdot eV^{-1/2}}$, and $E_0=60$ meV. Here E_g is the optical width of the band gap as determined by the Tauc procedure, and E_0 is the Urbach parameter.

The amorphousness of the films was monitored against Raman spectra. Only a wide band centered around $480\ \mathrm{cm^{-1}}$, typical of a purely amorphous film structure, was observed for both the as-prepared and the thermally annealed layers.

The impurity concentration in the films was determined by secondary-ion mass spectrometry (SIMS) and for Er had a value $\sim 5\times 10^{20}\ \mathrm{cm^{-3}}$. The oxygen concentration from natural leakage into the reactor also did not exceed $5\times 10^{20}\ \mathrm{cm^{-3}}$.

The photoluminescence was investigated during excitation by an Ar^+ laser operating at a wavelength of 488 nm at liquid-nitrogen temperature and room temperature. The receiver was a cooled germanium photodiode. The measurement channel comprised a high-sensitivity narrow band amplifier, a phase detector, and a computer.

RESULTS AND DISCUSSION

The amplitude of the photoluminescence peak at $\lambda=1.54\ \mu$m was no more than four or five times the noise level in the as-prepared samples. It is important to note that variation of the set of technological parameters did not produce any radical changes in the photoluminescence signal. It was found, however, that a decrease in the growth rate of the layers to less than 1 Å/s tended to increase the photoluminescence intensity. A possible explanation for such behavior is the nonequilibrium of the investigated system. The additional technological operation of thermal annealing of the films was therefore instigated. They were annealed by incrementing the temperature in sequential steps (cumulative process) in a nitrogen atmosphere at standard pressure. In the first step the temperature was set equal to $T_a=300$ °C for a duration of 15 min. The sample was then cooled to room temperature and annealed repeatedly at $T_a=400$ °C for 15 min. The temperature in the successive steps was $T_a=500$, 600, and 700 °C.

The results of the influence of thermal annealing on the photoluminescence are shown in Fig. 1. The first annealing

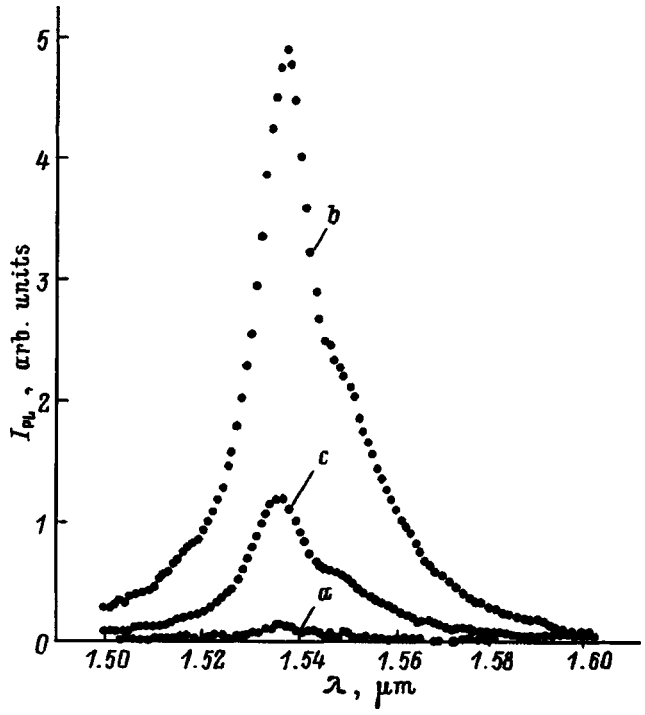

FIG. 1. Photoluminescence spectra of *a*-Si(Er):H at $T=77$ K plotted as a function of the cumulative annealing temperature. (a) as-prepared sample; (b) annealing at $T_a=300$ °C; (c) annealing at $T_a=300$ °C+400 °C. The annealing procedure is explained in the text.

step already produces a sharp, approximately 50-fold increase in the photoluminescence intensity (I_{PL}). However, the next annealing step at $T_a=400$ °C causes the intensity of the photoluminescence peak to decrease. The third annealing step causes the signal to decrease or vanish altogether, depending on the specific characteristics of the originally prescribed technological deposition regime. This behavior of the photoluminescence in *a*-Si(Er):H has been established previously.[6–8] In Ref. 6, however, the object of investigation was *a*-Si:H prepared by plasma-enhanced chemical vapor deposition (PECVD) and doped by erbium ion implantation. Cumulative annealing was carried out for 2 h. The investigated material in Refs. 7 and 8 was *a*-Si(Er):H prepared by rf cathode sputtering of Si and Er in an argon and hydrogen atmosphere. Cumulative annealing was carried out in an argon atmosphere for 15 min. It is known from practice in the deposition of *a*-Si:H that a change of technology leads to the production of somewhat different structural modifications of *a*-Si:H. Accordingly, a difference shows up in the behavior of the photoluminescence as a function of the anneal temperature (Fig. 2). In our case attention is called to the critical nature of the choice of anneal temperature, as opposed to Ref. 6, where the temperature interval of effective annealing is more spread out, and in Ref. 7 it is shifted into the region of higher temperatures, ~500 °C.

We also note that efficient photoluminescence has been observed after annealing at $T_a=300$ °C in *a*-Si(Er):H prepared by a standard PECVD procedure using the fluorine-containing metal-organic complex $\mathrm{Er(HFA)_3\cdot DME}$[HFA=$\mathrm{CF_3C(O)CHC(O)CF_3}$, DME=$\mathrm{CH_3OCH_2CH_2OCH_3}$] (Refs. 9 and 10).

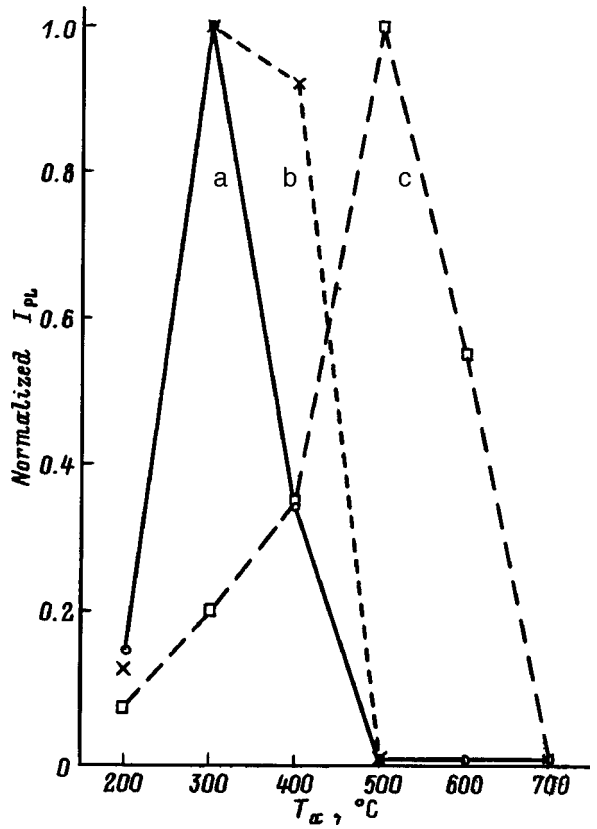

FIG. 2. Normalized photoluminescence intensity at $\lambda = 1.54$ μm as a function of the anneal temperature. (a) data of the present study at a measurement temperature $T = 77$ K; (b) data of Ref. 6, $T = 295$ K; (c) data of Ref. 7, $T = 77$ K.

The physics of the structural transformation processes taking place in thermal annealing is well understood. It has been established that the breaking of Si–H–Si bonds, the liberation of hydrogen, and its efficient diffusion and partial separation take place in the structural network of *a*-Si:H in the temperature interval 300–400 °C (Refs. 11 and 12). The structural network acquires an additional degree of freedom for partial reorganization in this case. If the structure is initially insufficiently close to equilibrium, structural transformation during thermal annealing leads to more complete saturation of the chemical bonds for all constituent components of the lattice, including erbium and residual oxygen.

It is a well-known fact[2,3] that erbium in silicon can exist both in a silicon environment $\langle \mathrm{Si}(12) \rangle$ and in an oxygen environment $\langle \mathrm{O}(6) \rangle$. Only in the latter case, however, is the configuration of the erbium environment optimal for the formation of an optically active center that emits efficiently at a wavelength of 1.54 μm. In light of these considerations, to account for the abrupt increase in the photoluminescence intensity, we can assume that the potential instability of the structural network of *a*-Si:H is conducive to a decrease in the density of nonradiative recombination centers and to a change in the nearest-neighbor environment of erbium. An important factor here could be the property of erbium as an oxygen getter. In other words, as far as erbium is concerned, the Er–O bond could be preferred over the Er–Si bond. Atomically ionized hydrogen diffusing efficiently at 300 °C and filling the structural network of *a*-Si(Er):H in a concentration up to 10% can act as a catalyst for this process. The narrowness of the region of structural transformation in annealing in our case attests to the narrowness of the distribution of heights of the diffusion barriers for mobile impurities. This conclusion is corroborated by the small width of the photoluminescence peak. The set of structural defects in implanted samples,[6] judging from all appearances, is more diverse, so that the interval of optimal thermal annealing is broader and shifts toward higher temperatures. In regard to the distinctly nonequilibrium method of rf cosputtering,[7,8] the dominant type of bond in this case is found in the stronger passivating Si–H bonds, whose breaking temperature corresponds roughly to 500 °C. The decrease of the photoluminescence intensity essentially to zero in our films at $T \geqslant 500$ °C is attributable to the loss of hydrogen by the material and, as a result, a high concentration of dangling bonds, which are centers of nonradiative recombination of electron-hole pairs formed by the pump source.

We also note that the problem of obtaining the optimal density of optically active Er^{3+} ions can be solved only in conjunction with metered predoping of the films with oxygen. The erbium and hydrogen concentrations in our films were approximately equal, whereas the optimal ligand environment for erbium ions, as mentioned, consists of six oxygen atoms.

CONCLUSIONS

We have thus shown that *a*-Si(Er):H films emitting radiation at a wavelength $\lambda = 1.54$ μm with optical parameters close to those of standard amorphous hydrogenated silicon can be prepared by the magnetron cosputtering of Si and Er in an argon-silane atmosphere with strong dilution of the silane with hydrogen. We have discovered that the photoluminescence intensity increases approximately 50-fold after thermal annealing of the films. It should be noted that both deposition and optimal thermal annealing have been carried out at low temperatures: 200 °C and 300 °C, respectively, making it possible to reconcile the technological process developed in this study with standard silicon electronic technology. We have proposed a mechanism for the structural transformation of the amorphous *a*-Si:H network during annealing as the mechanism responsible for the observed enhancement of the photoluminescence intensity.

This work has received support from the Russian Fund for Fundamental Research (Project No. 98-02-17350).

[1] *Rare Earth Doped Semiconductors II*, edited by S. Coffa, A. Polman, and R. N. Schwartz (MRS, Pittsburgh, 1996) [Mater. Res. Soc. Symp. Proc. **422**, 1 (1996)].
[2] A. Polman, J. Appl. Phys. **82**, 1 (1997).
[3] N. A. Sobolev, Fiz. Tekh. Poluprovodn. **29**, 1153 (1995) [Semiconductors **29**, 595 (1995)].
[4] M. S. Bresler, O. B. Gusev, V. Kh. Kudoyarova, A. N. Kuznetsov, P. E. Pak, E. I. Terukov, I. N. Yassievich, and B. P. Zaharchenya, Appl. Phys. Lett. **67**, 3599 (1995).
[5] E. I. Terukov, V. Kh. Kudoyarova, M. M. Mezdrogina, and V. G. Golubev, Fiz. Tekh. Poluprovodn. **30**, 820 (1996) [Semiconductors **30**, 440 (1996)].
[6] J. H. Shin, R. Serna, G. N. Hoven, A. Polman, W. G. J. H. M. Sark, and A. M. Vredenberg, Appl. Phys. Lett. **68**, 997 (1996).

[7] A. R. Zanatta and L. A. O. Nunes, Appl. Phys. Lett. **70**, 511 (1997).
[8] A. R. Zanatta and L. A. O. Nunes, Appl. Phys. Lett. **71**, 3679 (1997).
[9] V. B. Voronkov, V. G. Golubev, N. I. Gorshkov, A. V. Medvedev, A. B. Pevtsov, D. N. Suglobov, and N. A. Feoktistov, Pis'ma Zh. Tekh. Fiz. **24**(13), 8 (1998) [Tech. Phys. Lett. **24**, 502 (1998)].
[10] V. B. Voronkov, V. G. Golubev, N. I. Gorshkov, A. V. Medvedev, A. B. Pevtsov, D. N. Suglobov, and N. A. Feoktistov, Fiz. Tverd. Tela (St. Petersburg) **40**, 1433 (1998) [Phys. Solid State **40**, 1301 (1998)].
[11] W. Beyer, in *Tetrahedrally-Bonded Amorphous Semiconductors*, edited by D. Adler and H. Fritzsche (Plenum Press, New York, 1985), p. 129.
[12] W. B. Jackson and S. B. Zhang, in *Transport, Correlation, and Structural Defects*, edited by H. Fritzsche (World Scientific Publ., Singapore, 1990), p. 63.

Translated by James S. Wood

Amorphous hydrogenated silicon films exhibiting enhanced photosensitivity

O. A. Golikova and M. M. Kazanin

A. F. Ioffe Physicotechnical Institute, Russian Academy of Sciences, 194021 St. Petersburg, Russia
(Submitted April 10, 1998; accepted for publication April 15, 1998)
Fiz. Tekh. Poluprovodn. **33**, 110–113 (January 1999)

Amorphous hydrogenated silicon (*a*-Si:H) films with photoconductivities as high as 10^6, i.e., exceeding the photoconductivity of ''standard'' *a*-Si:H by two orders of magnitude, are investigated. The dark conductivity (σ_d) of the films has an activation energy $\Delta E = 0.85 - 1.1$ eV. The photoconductivity σ_{ph} is measured at a photocarrier generation rate of $10^{19}\,\text{cm}^{-3}\cdot\text{s}^{-1}$ and photon energy $\varepsilon = 2$ eV. Several distinctive characteristics are ascertained in the behavior of σ_{ph} and σ_d as functions of ΔE and also in the spectral curve and decay kinetics of σ_{ph} during prolonged illumination. It is concluded that the investigated material holds major promise for photovoltaic device applications. © *1999 American Institute of Physics.* [S1063-7826(99)02301-7]

1. INTRODUCTION

A well-known characteristic of intrinsic amorphous silicon (*a*-Si:H) is the activation energy of the dark conductivity (σ_d) $\Delta E = (\varepsilon_c - \varepsilon_F)_{T=0} = 0.85$ eV (ε_c is the edge of the conduction band, and ε_F is the Fermi level), and its room-temperature photoconductivity ($\sigma_{\text{ph}}/\sigma_d$) is approximately equal to 10^4 (the photoconductivity σ_{ph} is evaluated for a carrier generation rate $G = 10^{19}\,\text{cm}^{-3}\cdot\text{s}^{-1}$ and an incident-light photon energy $\hbar\omega = 2$ eV, Ref. 1). More recently, however, there have been reports of the preparation of intrinsic *a*-Si:H with $\sigma_{\text{ph}}/\sigma_d \simeq 10^6$ (Refs. 2–5). The authors of Refs. 2–4 have attributed the elevated value of $\sigma_{\text{ph}}/\sigma_d$ to the presence of ordered-structure domains with dimensions of the order of 1 nm in the amorphous matrix. In Refs. 2–4 *a*-Si:H films were deposited by plasma-enhanced chemical vapor deposition using an rf glow discharge (rf PECVD) from strongly hydrogen-diluted SiH_4. In contrast, Azuma *et al.*,[5] after preparing films by ESR-assisted remote hydrogen plasma deposition[6] from SiH_2Cl_2, have attributed the high values of $\sigma_{\text{ph}}/\sigma_d$ observed by them to the formation of voids with a filling ratio of 2–4 vol. %. In their opinion, the presence of voids tends to reduce the local voltages in the Si structural network and, in turn, to lower the density of defects (dangling Si–Si bonds).

Departing from Refs. 2–5, we have investigated amorphous hydrogenated silicon with a high photoconductivity, deposited by rf PECVD from 100% SiH_4 with variation of the position of the Fermi level: $\Delta E = 0.85 - 1.10$ eV. The objective of the study is to obtain information about the electronic properties of the material, which, in our opinion, would be useful in lending insight into the factors responsible for the enhanced photoconductivity.

2. EXPERIMENTAL RESULTS

Figures 1 and 2 show σ_d and σ_{ph} ($T = 300$ K) as functions of ΔE for ''standard'' *a*-Si:H having a photoconductivity ($\sigma_{\text{ph}}/\sigma_d$) close to 10^4 at $\Delta E = 0.85 - 1.1$ eV and also for *a*-Si:H having a high photoconductivity — according to the data of our study and Refs. 2–4. Also shown in the figure are data for an *a*-Si:H sample prepared in Ref. 7 by hot-wire deposition from $Si:H_4$ (the objective of Ref. 7 was to obtain and investigate nanocrystalline silicon samples, and silane-hydrogen mixtures were used for this purpose). The authors of Ref. 5 give only the ratio $\sigma_{\text{ph}}/\sigma_d$, but not the separate photoconductivities or ΔE.

It follows from Fig. 1 that the points corresponding to the high-photoconductivity *a*-Si:H samples prepared by different techniques fit the general curve for *a*-Si:H. The relation $\sigma_d = e\mu N \exp(\gamma/k)\exp(-\Delta E/kT)$ is well known; here μ is the mobility of electrons in the conduction band, N is the number of states in this band in the interval of energies of the order of kT, and γ is the temperature coefficient of the gap $\varepsilon_c - \varepsilon_F$. Assuming that N and γ are constant, we infer from the results in Fig. 1 that the mobility μ in high-photoconductivity *a*-Si:H does not depend on ΔE and is approximately an order of magnitude higher than in standard *a*-Si:H.

We now analyze the photoconductivity data (Fig. 2). We know that for standard *a*-Si:H σ_{ph} decreases monotonically as ΔE increases, where the density of defects N_D increases in the interval $\Delta E = 0.85 - 1.10$ eV, and the dependence of σ_{ph} on N_D can be written as $\sigma_{\text{ph}} \sim 1/N_D$ (Ref. 1). For high-photoconductivity *a*-Si:H, on the other hand, the σ_{ph} data are too scattered for the dependence of σ_{ph} on ΔE to be determined. Since $\sigma_{\text{ph}} \sim \mu\tau$ (τ is the electron lifetime) and $\mu \cong$ const, it is obvious that the scatter of $\sigma_{\text{ph}}(\Delta E)$ is caused by the scatter of the lifetimes τ, which nonetheless are much longer than the lifetimes τ in the standard *a*-Si:H. All other conditions being equal, therefore, $\sigma_{\text{ph}}/\sigma_d \sim \tau$, so that when τ increases approximately by a factor of 10^2, the defect density N_D can be expected to decrease accordingly. This behavior suggests the existence of additional recombination centers, whose density is not directly related to the position of the Fermi level.

Investigations of the defect density in films with enhanced photoconductivity by the constant-photocurrent method have shown that for $\Delta E = \text{const}$ the density N_D de-

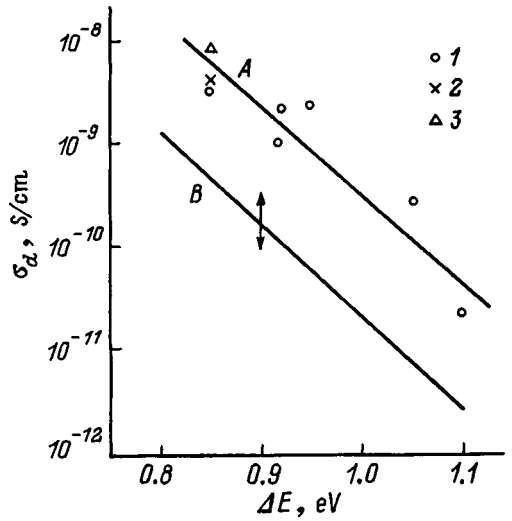

FIG. 1. Dependence of the dark conductivity σ_d at $T=300$ K on its activation energy ΔE. (*A*) ''Standard''*a*-Si:H; (*B*) *a*-Si:H with an enhanced photoconductivity. The experimental points represent data from: (*1*) our study; (*2*) Refs. 2–4; (*3*) Ref. 7.

creases by less than an order of magnitude relative to the defect density in the standard *a*-Si:H. It is ascertained from the absorption spectra in Fig. 3 that for the film endowed with the largest ratio $\sigma_{\rm ph}/\sigma_d$ of all the films prepared by us (3×10^6), for which $\Delta E=1.05$ eV, the defect density is $N_D=10^{16}\,\mathrm{cm}^{-3}$, whereas for the standard *a*-Si:H films (with the same position of ε_F) we have $N_D=5\times10^{16}\,\mathrm{cm}^{-3}$. It is important to note the situation reported in Refs. 2–4, where N_D was observed to decrease in a high-photoconductivity

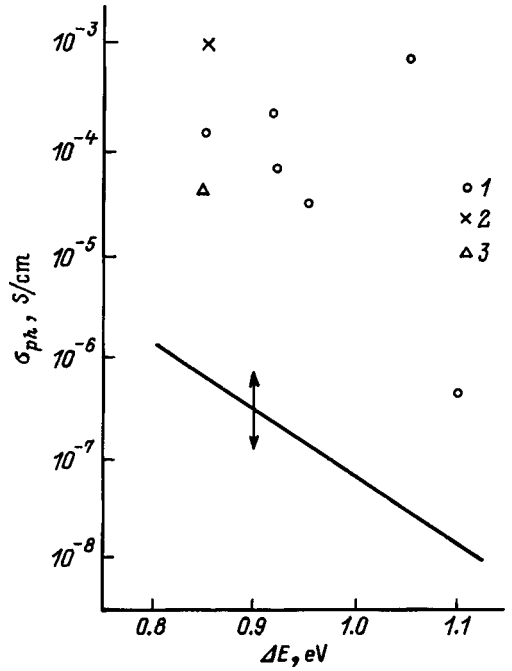

FIG. 2. Dependence of the photoconductivity $\sigma_{\rm ph}$ at $T=300$ K ($G=10^{19}\,\mathrm{cm}^{-3}\cdot\mathrm{s}^{-1}$, $\varepsilon=2$ eV) on the dark-conductivity activation energy ΔE. The solid line is plotted for standard *a*-Si:H; the experimental points are plotted for *a*-Si:H with an enhanced photoconductivity ($\sigma_{\rm ph}/\sigma_d$) from data in: (*1*) our study; (*2*) Refs. 2–4; (*3*) Ref. 7.

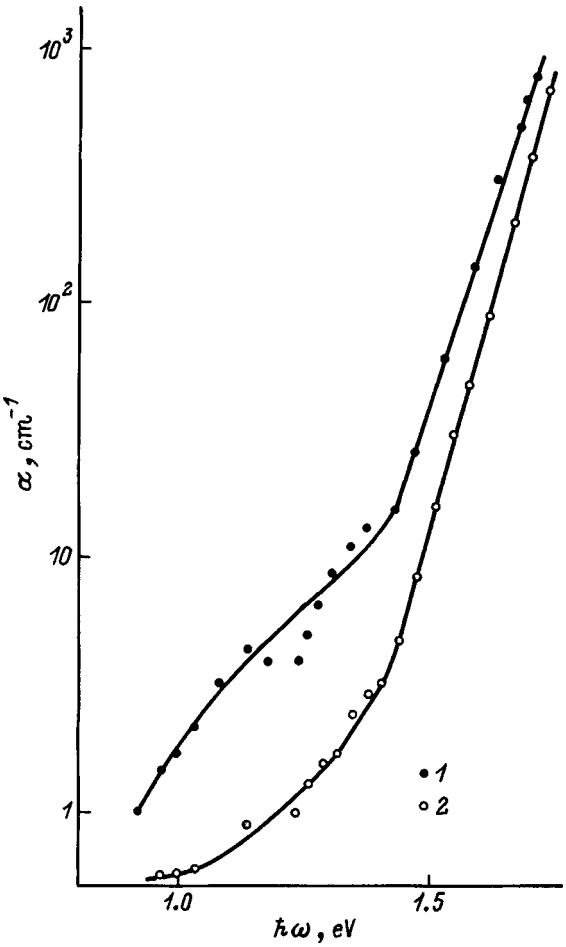

FIG. 3. Absorption spectra for a standard *a*-Si:H film (*1*) and for a high-photoconductivity film at $\Delta E=1.05$ eV (*2*).

film from the value of N_D in standard *a*-Si:H, but also within order-of-magnitude limits. The authors of Ref. 5, on the other hand, have found for their films that $N_D=(2-5)\times10^{15}\,\mathrm{cm}^{-3}$, which is close to the minimum density N_D attained in standard *a*-Si:H (Ref. 1). Consequently, there is no foundation for a radical decrease in N_D in films having an enhanced photoconductivity.

The results of experimental studies of the current-illuminance diagram for our films with a high photoconductivity $\sigma_{\rm ph}/\sigma_d$ show that the current-illuminance diagram at the wavelength of the incident light, 630 nm, is described by a power law with power exponent close to unity; this behavior is inherent in standard *a*-Si:H with a low defect density. The spectral curve, on the other hand, has a distinctive feature in the presence of a secondary maximum at 540 nm, in addition to the maximum at 620 nm (Fig. 4).

Figure 5 shows the dependence of the relative variation of $\sigma_{\rm ph}$ on the elapsed time during a total 5-h exposure to light having a power $W=100\,\mathrm{mW/cm}^2$ and $\lambda<0.9\,\mu$m at room temperature. Three films were investigated with close values of ΔE (0.89–0.92 eV). The first film, deposited at a temperature $T_s=380\,^\circ$C, had a high photoconductivity and contained 8 at. % hydrogen.[1)] The other two films were standard *a*-Si:H deposited at $T_s=380$ and 300 °C and contained 4 at. % and 8 at. % hydrogen, respectively.[8] It is evident that

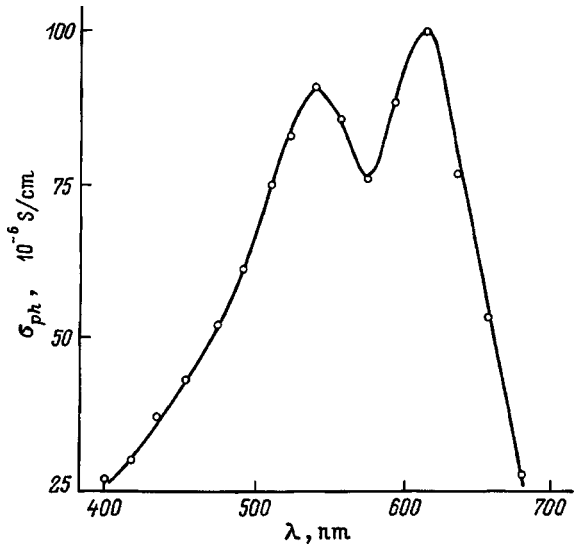

FIG. 4. Spectral curve of the photoconductivity of an *a*-Si:H film having an enhanced photoconductivity $\sigma_{\rm ph}/\sigma_d$.

the kinetics of the decay of $\sigma_{\rm ph}$ accelerates as the hydrogen content is increased. On the other hand, for the high-photoconductivity film $\sigma_{\rm ph}$ decreases much more rapidly than the value of $\sigma_{\rm ph}$ for standard *a*-Si:H with the same hydrogen content. After illumination, however, the value of $\sigma_{\rm ph}$ for this film is approximately an order of magnitude higher than the photoconductivity of the standard film. We note that similar facts affecting the decay kinetics of $\sigma_{\rm ph}$ in exposure to light have also been established in studies of high-photoconductivity films.[2–4]

3. DISCUSSION OF THE RESULTS

For films with an enhanced photoconductivity $\sigma_{\rm ph}/\sigma_d$ we now briefly summarize their main properties that differ from the properties of standard *a*-Si:H films (in either case for $\Delta E = 0.85 - 1.1$ eV):

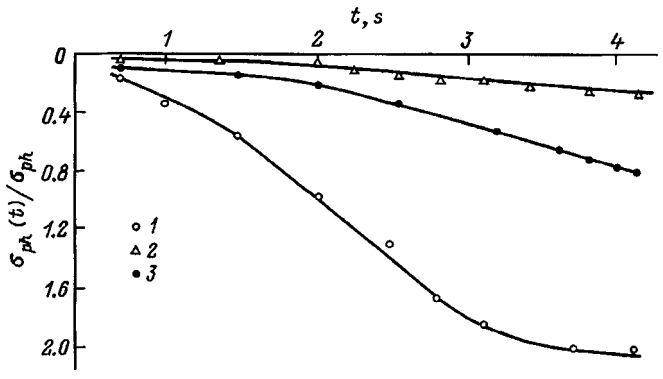

FIG. 5. Relative variation of the photoconductivity $\sigma_{\rm ph}(t)/\sigma_{\rm ph}$ as a function of the illumination time (t) for $W = 100$ mW/cm^2, $\lambda < 0.9$ μm for: (*1*) films having an enhanced photoconductivity; (*2*) standard films. Hydrogen content: (*1*) 8 at. %; (*2*) 4 at. %; (*3*) 8 at. %.

• an order-of-magnitude higher electron mobility independent of ΔE;

• a lengthened (by as much as two orders of magnitude) electron lifetime, in contrast with the less than order-of-magnitude increase in the defect density determined by the constant photocurrent method;

• a large scatter of the lifetimes τ as ΔE is varied;

• an excess hydrogen content in comparison with the hydrogen content of standard *a*-Si:H at the same film deposition temperature;

• accelerated decay kinetics of $\sigma_{\rm ph}$ under the influence of prolonged illumination in comparison with that observed for standard *a*-Si:H with the same hydrogen content;

• two maxima on the spectral curve, one the same as for standard *a*-Si:H, and the other observed at a higher energy (2.3 eV), which is close to the width of the band gap E_g for nanocrystalline silicon.[9]

The sum-total of these properties indicates that our investigated films are structurally similar to the films described in Refs. 2–4: The *a*-Si:H matrix contains small-size (nanometer-order) crystalline silicon inclusions whose boundaries are passivated in varying degrees by excess (at a given deposition temperature) hydrogen. Since a characteristic band in the Raman spectra (at $\sim 520\,{\rm cm}^{-1}$) for the given films is not observed, we conclude that the dimensions of the crystalline inclusions do not exceed 7 nm (Ref. 10). If both phases contribute to carrier transport processes, the electron lifetime τ is found to be far more sensitive than the mobility μ to the presence of nanocrystalline inclusions and also to the degree of hydrogen passivation of their boundaries. Hydrogen at the inclusion boundaries probably forms weaker bonds with Si than hydrogen in the amorphous phase; this conjecture is supported by the accelerated kinetics of $\sigma_{\rm ph}$ under the influence of prolonged illumination.

4. CONCLUSIONS

Hydrogenated silicon films with photosensitivities of the order of 10^6, prepared by different technologies in different laboratories, are new and important objects of investigation. The primary need from the scientific point of view is for further research on their distinctive structural characteristics, and next in priority is the construction of electron-transport and photoconduction models; obviously the discussion in Sec. III is merely phenomenological in character. We note that a model of electron transport in films containing an amorphous phase and a crystalline phase is nonexistent at present.[11] From the application standpoint, films having a high photoconductivity $\sigma_{\rm ph}/\sigma_d$ are of unquestionable interest for the design of photovoltaic devices.[2–4] Indeed, despite the higher ''degradation rate'' of $\sigma_{\rm ph}$, it still has a higher value after prolonged illumination than the photoconductivity $\sigma_{\rm ph}$ for standard *a*-Si:H.

We wish to thank Dr. Pere Roca i Cabarrocas (École Polytechnique, France) for sending preprints.

This work has received support from the International Association for the Promotion of Cooperation with Scientists from the Independent States of the Former Soviet Union (INTAS Grant N 931916).

[1)]The hydrogen content in the film was determined by V. Kh. Kudoyarova using infrared spectroscopy.

[1] O. A. Golikova, Fiz. Tekh. Poluprovodn. **31**, 281 (1997) [Semiconductors **31**, 228 (1997)].
[2] P. Roca i Cabarrocas, S. Hamma, P. St'ahel, C. Longeaurd, J. P. Kleider, R. Meaudre, and M. Meaudre, in *Proceedings of the 14th European Photovoltaic Solar Energy Conference* (Barcelona, July, 1997), P5A, p. 20.
[3] P. St'ahel, S. Hamma, P. Sladek, and P. Roca i Cabarrocas, in *Abstracts of the 17th International Conference on Amorphous and Microcrystalline Semiconductors (ICAMS 17)* (Budapest, August, 1997), Th-B214.
[4] P. Roca i Cabarrocas, S. Hamma, S. N. Sharma, G. Viera, E. Bertran, and J. Costa, in *Abstracts of the 17th International Conference on Amorphous and Microcrystalline Semiconductors (ICAMS 17)* (Budapest, August, 1997), Th-B3/5.
[5] M. Azuma, T. Yokoi, and I. Shimizu, in *Abstracts of the 16th International Conference on Amorphous Semiconductors (ICAS 16)* (Kobe, Japan, September, 1995), Mo-BO3-2.
[6] V. L. Dalal, M. Leonard, and G. Baldwin, J. Non-Cryst. Solids **164-166**, 71 (1993).
[7] B. Brogueira, V. Chu, and J. P. Conde, Mater. Res. Soc. Symp. Proc. **377**, 57 (1995).
[8] O. A. Golikova, M. M. Kazanin, O. I. Kon'kov, V. Kh. Kudoyarova, and E. I. Terukov, Fiz. Tekh. Poluprovodn. **30**, 405 (1996) [Semiconductors **30**, 226 (1996)].
[9] A. A. Andreev, B. Y. Averbaouch, P. Mavlyanov, S. B. Aldabergenova, M. Albrecht, D. Stenkamp, G. Frank, and H. P. Stenk, in *Abstracts of the 17th International Conference on Amorphous and Microcrystalline Semiconductors (ICAMS 17)* (Budapest, August, 1997), Fr-A215.
[10] T. Okada, T. Twaki, K. Yamomoto, H. Kasahara, and K. Abe, Solid State Commun. **49**, 809 (1984).
[11] D. Ruff, H. Mell, L. Tolf, G. Huhn, I. Silber, and W. Fuhs, in *Abstracts of the 17th International Conference on Amorphous and Microcrystalline Semiconductors (ICAMS 17)* (Budapest, August, 1997), Th-P9/21.

Translated by James S. Wood